

SEISMOLOGICAL STUDIES USING OBSERVED AND SYNTHETIC WAVEFORMS

Thesis by

Rhett Giffen Butler

In Partial Fulfillment of the Requirements

for the Degree of

Doctor of Philosophy

California Institute of Technology

Pasadena, California

1979

(Submitted May 17, 1979)

**TO**

**KIM MARIE**

ACKNOWLEDGEMENTS

I wish to begin by saluting the spirit of the Seismo Lab, an entity which has inspired contagious enthusiasm in geophysics to many of us. I have thoroughly enjoyed my stay here. The open atmosphere of interaction and exchange of ideas has been immensely beneficial to me. To the faculty, staff, and my fellow students I would like to extend my heartfelt thanks.

I have benefited greatly from my association with Don Heloberger, Don Anderson, and Hiroo Kanamori. Their particular inspiration, encouragement, knowledge, and guidance have been a continual resource for me. I wish also to thank L. J. Burdick, Charles Langston, Larry Ruff, Robert Hart, George Mellman, and Dave Harkrider for stimulating discussion, enthusiasm, and advice.

For their collaborating efforts on parts of the research presented in this thesis I am grateful to Charles Langston, Robert Hart, Larry Ruff and Gordon Stewart. I thank Florence Heloberger for her contribution of earthquake data in Chapter IV.

For their assistance in the preparation of the final draft of this thesis, I thank Barbara Valencia and Gail Nichols for typing the manuscript and Lazlo Lenches for drafting and organizing the figures.

To my parents I wish to express my appreciation and gratitude for their unceasing interest in my education.

To Kim Marie Roberts I wish to express a special thanks for the love, encouragement, and moral support she has provided me while writing this thesis.

I have received the generous support of the Fannie and John Hertz Foundation during most of my tenure as a graduate student at Caltech. This research was supported in part by the National Science Foundation under grant numbers EAR 76-14262, EAR 77-13641, EAR 78-14786; by the United States Geological Survey under contract numbers 14-08-0001-16776, 14-08-0001-17631; and by the Advanced Research Projects Agency of the Department of Defense under contract numbers F44620-72-C-0078, F49620-77-C-0022, F49620-79-C-0012.

ABSTRACT

Application of waveforms to four topics in seismology is presented. Detailed waveform analyses of three earthquakes are reported in Chapter I. The Oroville, California earthquake of 8/1/75 has a north-south striking, westward dipping normal fault mechanism with a small component of left-lateral motion. A surface wave seismic moment of  $1.9 \times 10^{25}$  dyne-cm. is a factor of 3 greater than the teleseismic body wave determination. Slow deformations on the Oroville fault may explain the enhanced excitation of the surface waves. The Tangshan, China earthquake of 7/27/76 and its principal aftershock represent a complex intraplate event sequence with strike-slip, normal, and thrust faulting. The main shock was a bilateral strike-slip event, striking  $N40^{\circ}E$ , with a seismic moment of  $1.8 \times 10^{27}$  dyne-cm. Associated thrusting occurred concurrently with the main shock. The principal aftershock was an oblique, normal double event, striking approximately perpendicular to the main event, with a seismic moment of  $8 \times 10^{26}$  dyne-cm. The 4/26/73 Hawaii earthquake is a subcrustal, double event. The events are consistent with left-lateral strike-slip motion on an echelon southward dipping faults. Evidence of lateral heterogeneity in the Hawaii source region is suggested by incompatibility between and azimuthal amplitude anomalies associated with the P and SH data.

In Chapter II shear travel times are obtained by a waveform correlation technique. A total of 87 SH travel-times are measured from the 1968 Borrego Mountain, California and 1973 Hawaii earthquakes. The Borrego data have a trend toward faster travel times at  $40^{\circ}$ , but show an overall 6 second slow baseline with respect to the Jeffreys-Bullen

Table. The Hawaii data contain large azimuthal scatter suggesting lateral heterogeneity in the near source region. The shear phase SS is modeled using a Hilbert transform to mimic distortion incurred at an internal caustic in its propagation. Significant variation is found in SS travel time residuals for paths reflected under the Canadian shield. A correlation of the variation with tectonic sub-province is suggested. Differential travel times of multiple ScS determined by waveform cross-correlation are shown to contain a systematic bias late with respect to conventional visual onset timing methods. The timing bias for  $ScS_2$ -ScS differential times ranges between 2.2 and 3.8 seconds late, and depends upon the average  $Q_\beta$  of the mantle.

In Chapter III direct body waves and fundamental surface waves are calculated for a credible, hypothetical great earthquake on the San Andreas fault. Amplitudes and durations of long period ground motion ( $T > 1$  second) are found for a receiver in downtown Los Angeles. Calculations are carried out for various epicenters, dislocation profiles, and time functions. Ground motion from Love radiation is found to be most important with peak-to-peak amplitudes up to 14 cm. and durations up to 5 minutes.

Chapter IV presents a study of short period P wave amplitudes from nuclear explosions in the Soviet Union recorded by WWSSN stations in the United States. Thirty-four events in five test sites are analyzed. A well-defined amplitude pattern is obtained for each source region. A pattern of lateral variation of amplitude in the United States is obtained for a northern azimuth of approach. Stations in the western United States do not show systematically lower amplitudes than eastern

stations, in contrast to previous studies. A preliminary data set of earthquakes in the Kurile Islands and South America indicate the amplitude pattern in the U.S. varies azimuthally.

TABLE OF CONTENTS

	<u>Page</u>
Acknowledgements.....	iii
Abstract.....	v
Table of Contents.....	viii
General Introduction.....	1
CHAPTER I      Application of Waveform Analysis Techniques for the Determination of Source Parameters for Three Earthquakes	
Section I.1      Waveform Analysis of the August 1, 1975 Oroville Earthquake	
Abstract.....	9
Introduction.....	10
Body Wave Data and Analysis.....	11
Body Wave Discussion.....	29
Body Wave Summary.....	30
Surface Wave Data and Analysis.....	31
Surface Wave Discussion.....	39
Surface Wave Summary.....	43
Ultra-long Period Body Wave Analysis	43
Ultra-long Period Body Wave Summary.	55
References.....	58
Section I.2      The July 27, 1976 Tangshan, China Earthquake - A Complex Sequence of Intraplate Events	
Abstract.....	60
Introduction.....	61
Seismological Data.....	62
Surface Wave Analysis.....	69

TABLE OF CONTENTS

(Continued)

	<u>Page</u>
Body Wave Analysis.....	71
Discussion.....	80
Conclusion.....	84
References.....	85
 Section I.3      Body Wave Analysis of the April 26, 1973 Hawaiian Earthquake	
Abstract.....	88
Introduction.....	88
Data Analysis.....	89
Discussion.....	109
References.....	114
 CHAPTER II      Travel Times of Shear Phases Using Waveform Correlation	
 Section II.1      Shear Wave Travel-Times from Two Well-Constrained Earthquakes	
Abstract.....	117
Introduction.....	117
Travel-Times.....	119
Discussion.....	137
References.....	141
 Section II.2      Shear Wave Travel-Times From SS	
Abstract.....	143
Introduction.....	143

TABLE OF CONTENTS

(Continued)

	<u>Page</u>
Review of SS.....	145
Travel-Times.....	149
Discussion.....	163
References.....	174
 Section II.3    A Source of Bias in Multiple ScS	
Travel-Times	
Abstract.....	179
Introduction.....	179
Determination of the Effect for ScS	180
Implications.....	184
References.....	188
 CHAPTER III    Long Period Ground Motion From A Great Earthquake	
Abstract.....	191
Introduction.....	191
The Model.....	193
Body Waves.....	204
Surface Waves.....	208
Discussion.....	216
Summary.....	223
References.....	225

TABLE OF CONTENTS

(Continued)

	<u>Page</u>
CHAPTER IV    An Amplitude Study of Russian Nuclear Events for WWSSN Stations in the United States	
Abstract.....	231
Introduction.....	231
Nature of the Study.....	233
Data.....	242
Source Comparisons.....	247
Amplitude Variation at Receiver...	254
Preliminary Results for Earthquake Sources.....	262
Summary.....	269
References.....	272
Appendix A    Map of WWSSN Stations.....	274

## GENERAL INTRODUCTION

Waveforms are both the natural resources and the tools that the seismologist uses in the study of the earth. Earthquakes generate a broad spectrum of seismic energy from high frequency strong ground motion to free oscillations of the earth with periods of nearly an hour. These waves recorded on a variety of instruments from accelerographs to tidal gravimeters are the fundamental data set from which we extract information to infer the structure, nature, and processes of the earth's interior. Waveforms are seismological tools in the application and use of synthetic seismograms in geophysical problems. Synthetic waveforms may be calculated by a number of methods in seismological modeling situations and directly compared with observed waveforms. The agreement between observations and synthetics provides powerful constraints upon model assumptions and can yield insight toward ways of improving a model. The four chapters of the thesis are an eclectic collection of topics in seismology studied by means of waveforms.

Chapter I presents an application of waveform analysis techniques in the study of three earthquakes to determine source parameters. The August 1, 1975 Oroville, California earthquake, although a relatively small event by seismological standards ( $M_L = 5.7$ ) received enhanced interest due to its proximity to the Oroville reservoir. A small foreshock immediately preceding the main shock masked the focal mechanism from the local stations. Long period teleseismic body waves and surface waves are analyzed to constrain the source parameters. An anomalously large excitation of surface waves relative to the body waves suggests the source included a component of slow deformation. Body phases

recorded on an ultra-long period seismometer at Pasadena are modeled to shed further light on the long period characteristics of the Oroville source.

The Tangshan, China earthquake of July 27, 1976 and its principal aftershock, which occurred fifteen hours after the main event, resulted in the loss of life of over 650,000 persons in north-east China. The city of Tangshan with a population of 1.6 million was virtually destroyed and extensive damage was suffered throughout the densely populated surrounding region. Without diminishing the significance of the event in human terms the Tangshan event represents the largest continental intraplate earthquake since the establishment of the World Wide Standardized Seismic Network. Long period surface waves are analyzed to constrain the overall faulting parameters and seismic moments of the main shock and principal aftershock. Teleseismic body waves are used to detail the faulting process. The complexity of the earthquake sequence is compared with the 1976 Guatemala earthquake, a large interplate event. Reasons for the enormously high casualties and destruction are offered in the discussion. As no local data or details of faulting were initially provided by the Chinese government, the study of the Tangshan event provided a blind test of teleseismic source analysis techniques.

The April 26, 1973 Hawaii earthquake was a  $M_s = 6.2$  subcrustal event occurring on the northeast coast of the island of Hawaii near Hilo. The event generated a number of high quality observations of shear phases at seismic recording stations throughout the world. As good control of the epicenter was provided by the local seismic array,

the event offered an opportunity to measure shear travel times from the middle of the Pacific plate. An analysis is made of the teleseismic body waves to determine focal parameters and a source time function for the earthquake. The Hawaii source is used in Chapter II in an S wave travel time study and in an analysis of waveforms and travel times of the shear phase SS.

Chapter II considers waveform correlation techniques in the measurement of travel times of shear phases. The difficulty in determining the precise arrival times of teleseismic shear waves, a well known problem in observational seismology is addressed in the first section. This difficulty arises largely from the fact that shear waves are secondary arrivals on the seismogram and the onset of the S wave pulse is often obscured by precursory arrivals. This difficulty is further compounded by the relatively low Q of most teleseismic S waves. Thus high frequencies are preferentially removed from the pulse and the resulting arrival has a somewhat emergent onset. To overcome these difficulties a waveform correlation between the observed shear wave and a synthetic shear wave is adopted to obtain a reliable onset time of the observation. Travel times of 87 SH shear waves are measured for two intermediate size earthquakes, the 1968 Borrego Mountain and 1973 Hawaii earthquakes. Synthetic shear waves for the waveform correlation are generated using source time functions previously determined by body wave analyses of the events.

Section 2 of Chapter II presents results in the development of the seismic shear phase SS as an earth reconnaissance tool. SS is a shear wave which reflects once off the earth's free surface at the

midpoint of its propagation, thus sampling an intermediary portion of the earth between the source and the receiver. High quality SS observations are obtained from the earthquakes used in the previous S study. SS is a distorted phase due to an internal caustic in its propagation. In generating synthetic SS, the distortion effects are modeled by Hilbert transformation of the undistorted pulses. Travel times are obtained by the waveform correlation method. Travel times of SS and differential SS-S travel times are presented and discussed in the context of lateral heterogeneity in the earth's upper mantle.

Section 3 of Chapter II considers the effect of seismic attenuation on the measurement of differential travel times obtained by cross-correlation methods. If two seismic phases have suffered different amounts of attenuation, the more attenuated phase will have a broader waveform. Cross-correlation timing between the phases will be greater than timing based upon the visual onsets of the phases. The implications of this effect are discussed for differential travel times of multiple ScS.

Chapter III presents a model of long period ground motion from a great earthquake. Long period ground motions ( $T > 1$  second) have little effect on ordinary structures. However, high-rise buildings, oil tanks, suspension bridges, reservoirs, and off-shore oil drilling platforms have natural resonances which lie in the long period ranges. Synthetic direct body waves and fundamental surface waves are generated for a hypothetical great earthquake on the San Andreas fault. The ground response is calculated for a receiver in downtown Los Angeles from epicenters at Parkfield, Palmdale, and San Bernardino. Smooth

and non-smooth rupture processes are considered. Uncertainties in the complexity of the rupture, velocity structure, and effects of lateral heterogeneity preclude definitive results. However, tentative conclusions of the nature of long period ground motion from a great earthquake may be reached for such gross parameters as overall amplitudes and durations.

Chapter IV reports a study of short period amplitude variations observed by stations of the World Wide Standardized Seismograph Network in the United States for a data set of nuclear explosions from five test sites in the Soviet Union. Previous studies of lateral amplitude variations in the United States using earthquakes have reported that short period (1 sec) magnitudes of events in the western United States tend to be about 0.5 magnitude units (a factor of three) lower than in the central and eastern United States. The implication of this result has been that attenuation or dissipation of seismic energy is regionally greater in the tectonic, younger west than in the stable central and eastern United States. The amplitude results for the explosion data set presented are interpreted in terms of source effects at the test sites and receiver effects in the United States. The effect of signal amplification for stations situated on low velocity sediments is considered. The individual test sites have stable amplitude patterns, although some systematic differences are observed between sites. Combining the amplitude data from the five test sites to judge receiver effects, it is noted that although amplitude variations are observed among the stations, no systematic regional differences between the western United States and the central and east

are suggested in the data. To provide an indication of the azimuthal characteristics of the amplitude pattern, preliminary data are presented in a study of amplitude patterns in the United States from carefully selected earthquakes in the Kurile Islands and South America.

Most of the results presented have been or are in the process of being published: Chapter I (Langston and Butler, 1976; Hart, Butler and Kanamori, 1977; Butler, Stewart, and Kanamori, 1979), Chapter II (Hart and Butler, 1977; Butler, 1979; Butler, 1977), Chapter III (Butler and Kanamori, 1979), Chapter IV (Butler and Ruff, 1979).

REFERENCES

- Butler, R. (1977). A source of bias in multiple ScS differential times determined by waveform correlation, Geophys Res. Lett. 4, 593.
- Butler, R. (1979). Shear wave travel times from SS, submitted to Bull. Seism. Soc. Am.
- Butler, R. and H. Kanamori (1979). Long period ground motion from a great earthquake, submitted to Bull. Seism. Soc. Am.
- Butler, R. and L. Ruff (1979). An amplitude study of Russian nuclear events for WWSSN stations in the United States, in preparation.
- Butler, R., G. S. Stewart, and H. Kanamori (1979). The July 27, 1976 Tangshan, China earthquake - a complex sequence of intraplate events, Bull. Seism. Soc. Am., 69, 207.
- Hart, R. S. and R. Butler (1978). Shear wave travel times and amplitudes for two well-constrained earthquakes, Bull. Seism. Soc. Am., 68, 973.
- Hart, R. S., R. Butler, and H. Kanamori (1977). Surface wave constraints on the August 1, 1976 Oroville earthquake, Bull. Seism. Soc. Am. 67, 1.
- Langston, C. A. and R. Butler (1976). Focal mechanism of the August 1, 1975 Oroville earthquake, Bull. Seism. Soc. Am., 66, 111.

**CHAPTER I**

**APPLICATION OF WAVEFORM ANALYSIS TECHNIQUES  
FOR THE DETERMINATION OF SOURCE PARAMETERS  
FOR THREE EARTHQUAKES**

SECTION I.1 WAVEFORM ANALYSIS OF THE AUGUST 1, 1975 OROVILLE EARTHQUAKEABSTRACT

Long period teleseismic P and S waves from the WWSS and Canadian networks are modeled to determine the focal parameters for the August 1, 1975 Oroville earthquake. Using the techniques of P first motions, waveform synthesis, and phase identification the focal parameters are determined as follows: dip  $65^\circ$ ; rake  $-70^\circ$ ; strike  $180^\circ$ ; depth  $5.5 \pm 1.5$  km; moment  $5.7 \pm 2.0 \times 10^{24}$  dyne-cm; and a symmetric triangular time function 3 sec in duration. This is a north-south striking, westward dipping, normal fault with a small component of left-lateral motion. The time separation between the small foreshock and mainshock appears to be 6.5 sec rather than 8.1 sec as previously determined.

Observations of Love and Rayleigh waves on WWSSN and Canadian Network seismograms have been used to place additional constraints upon the source parameters of the event. The 20 second surface wave magnitude is 5.6. The surface wave radiation pattern is consistent with the focal parameters determined by the body wave study. The seismic moment from the surface waves of this event was determined to be  $1.9 \times 10^{25}$  dyne-cm by both time domain and long period ( $T \geq 50$  sec.) spectral amplitude determination. This moment value is significantly greater than that determined by the body wave analysis.

Body and surface waves recorded on an ultra-long period seismograph at Pasadena 660 km from Oroville are modeled to obtain a third moment estimate for the earthquake. A range of moments between the teleseismic body and surface wave determinations is obtained from a variation in the rake of the fault and the duration of the source time function. An

extended 12 second "tail" appended to the three second time function of the teleseismic body waves can provide fairly good agreement among the moment estimates for Oroville from the three data sets.

#### INTRODUCTION

The August 1, 1975 earthquake at Oroville, California --  $M_L = 5.9$  (average of PAS and BKS);  $m_b = 5.9$  (USGS);  $M_s = 5.6$  (average of 25 WWSS and Canadian network stations) -- is a relatively small event by seismological standards. Interest in the event, however, has been considerably enhanced due the proximity of the epicenter to the Oroville reservoir. It is the intent of this section not to speculate on any causal relationship of the earthquake to the reservoir, but rather to provide constraints upon the faulting mechanism and seismic moment of the event.

The main Oroville shock had some peculiarities which effectively thwarted standard location and focal mechanism techniques using nearby stations. As reported by Morrison, et al. (1976), a magnitude 4.5 foreshock preceeded the mainshock by 8.1 seconds. Consequently, the location of the mainshock, although inferred to be at the same place as the foreshock, was hard to pin down. The foreshock was also large enough to obscure local P first motions, so that the faulting mechanism was also unknown until sufficient aftershock data were processed to get an indirect look at the fault plane (Bufe, et al., 1976; Ryall and VanWormer, 1975; Lahr et al., 1976). Because of these reasons, and also since the event was well recorded at teleseismic ranges, a body waveform analysis was carried out to determine estimates of the orientation, depth, time function, and seismic moment parameters for the earthquake.

The long period surface wave radiation from this event as recorded at WWSSN and Canadian Network stations is examined in order to place further constraints upon the source mechanism. Events of this rather small magnitude ( $M_s = 5.6$ ) do not ordinarily generate substantial long period ( $T \geq 30$  sec.) surface waves. The Oroville surface waves, however, have quite large amplitudes at these periods. This has allowed us to not only confirm the source geometry determined by the body wave analysis, but also to compute the long period seismic moment and stress drop for this event. In doing so, we have determined that for long period energy, the earthquake source is characterized by substantially different parameters than those determined using teleseismic body wave data.

The apparent difference between the teleseismic body wave and surface wave moments of the event importuned a desire to obtain an independent moment estimate for the event. The horizontal components of the ultra-long period Gilman seismometer at Pasadena 660 km from Oroville recorded fairly simple radial P and SH arrivals from the Oroville earthquake. The Gilman instrument has a peak response of at about 80 seconds period and offered an opportunity to look at the long period body wave radiation from Oroville. Radial P and SH arrivals are modeled by the generalized ray method. Moment estimates are found to be sensitive to the source parameters and the duration of the source time function.

#### Body Wave Data and Analysis

Immediately after the earthquake, requests for the long and short period vertical components from each station in the WWSS and Canadian networks were sent out with excellent response from most. This particular component was requested primarily because of a travel time study being

conducted for the region. Fortunately, in view of the clear long period P and S waves observed, some stations sent the horizontal components also. These turned out to be very helpful in constraining the focal mechanism.

Before any waveform interpretation could be done, however, the extent of interference of the foreshock with the mainshock had to be determined. Figure I.1.1 shows the short period vertical component for the station MSO. This is one of the few teleseismic stations where the foreshock is clearly recorded, and only because MSO is relatively close to the epicenter. The long period component shows little interference between the shocks at this particular distance. For more distant stations the foreshock is virtually always in the noise, even on the short period components. Figure I.1.1 also demonstrates what we infer to be a relative timing error of approximately 1.5 sec between the foreshock and mainshock. Where the foreshock and the P wave for the mainshock can be clearly seen, the timing observed is closer to 6.5 seconds rather than the 8.1 seconds reported by Morrison, et al., (1976). An explanation for this discrepancy will be given in the discussion in light of the focal mechanism.

Focal parameters for the main event were determined by a multi-staged process; each stage representing an increase in resolution for some particular set of parameters or some individual parameter.

Figure I.1.2 shows the distribution of P wave first motions on an equal area projection of the lower half of the focal sphere. Table I.1.1 cites the stations used in this study. Basically, the first motions indicate normal faulting but the various orientation angles are

TABLE OF CONTENTS.

SECTION	PAGE
General	1
Voltage Diagrams	7
Auto Transformers	9
Transformer Design	10
APPENDICES	
I Electrostatic Measurements	12
II Network Diagram	13
III Notes on Tables	14
ADDENDA of Original Data	
Outline	15
Group I (A)	18
II (B)	21
III (C)	21
IV (D)	24

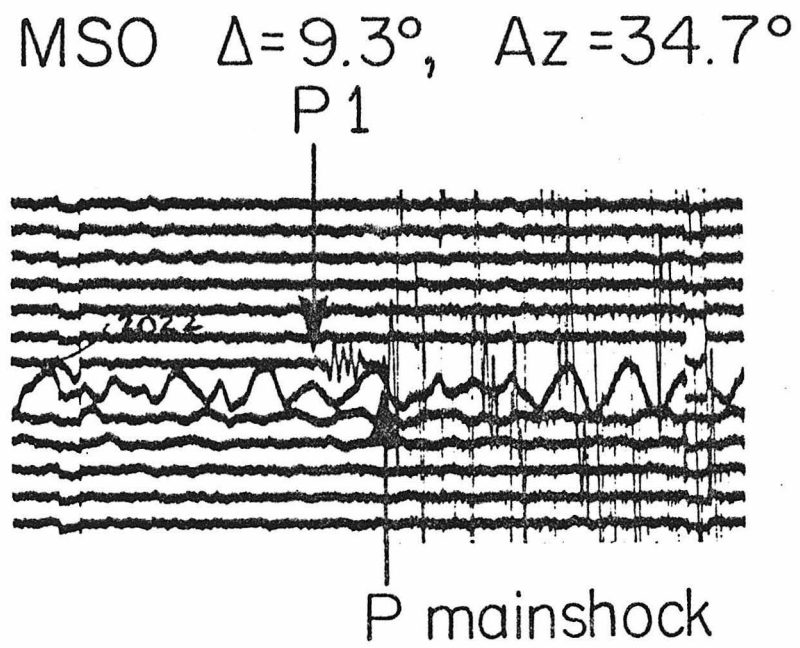


Figure I.1.1 Copy of the short period vertical component at MSO showing the foreshock and mainshock P arrivals.

TABLE I.1.1

## WWSSN AND CANADIAN STATIONS USED IN THIS STUDY

(C - compression; D - dilatation)

<u>STATION</u>	<u><math>\Delta</math> (°)</u>	<u>AZ (°)</u>	<u>P FIRST MOTION</u>	<u>MOMENT (<math>\times 10^{24}</math> dyne-cm)</u>
ALE	47.20	8.9	D	5.0
BLC	29.08	22.8	D	
EDM	14.88	19.6	D	
FBC	39.33	34.2	D	4.6
FCC	26.11	33.2	D	
FFC	20.18	34.4	D	
FSJ	15.09	354.0	D	
MBC	36.90	0.9	D	
MNT	35.48	64.2	D	3.9
OTT	34.02	64.7	D	3.2
PHC	11.98	341.8	(D)	
PNT	9.97	7.6	D	
RES	37.44	11.3	D	
SCH	39.26	48.4	D	7.4
SES	13.26	30.9	D	
STJ	49.10	56.7	D	6.5
VIC	9.16	352.4	D	
YKC	23.46	8.3	D	
LHC	24.79	58.2	D	
INK	24.92	347.2	D	
AAM	28.67	71.9	D	
ANP	92.84	306.0	D	

TABLE I.1.1

(Continued)

<u>STATION</u>	<u><math>\Delta</math> (°)</u>	<u>AZ (°)</u>	<u>P FIRST MOTION</u>	<u>MOMENT</u> <u>(<math>\times 10^{24}</math> dyne-cm)</u>
AQU	88.93	31.6	D	
ARE	72.64	129.5	D	8.0
ATU	96.64	26.9	D	
BHP	48.23	117.5	D	4.6
BKS	1.65	198.1	(D)	
BLA	32.18	80.7	D	3.0
BOG	55.12	116.3	D	
CAR	56.28	105.3	D	
COP	77.49	24.7	D	
DAL	21.06	100.5	D	
ESK	72.01	31.9	D	
GOL	12.53	83.7	C	
GSC	5.63	135.9	D	
HNR	87.14	255.4	D	
JCT	19.94	110.0	D	
KEV	68.70	11.2	D	
KIP	35.88	250.7	(C)	reported
LPB	74.75	127.0	D	5.5
LPS	37.93	122.2	D	
LUB	16.89	104.2	D	
MAT	74.65	304.7	D	7.1
MSO	9.25	34.7	D	
NNA	65.96	131.0	D	6.7
NUR	76.62	16.4	D	

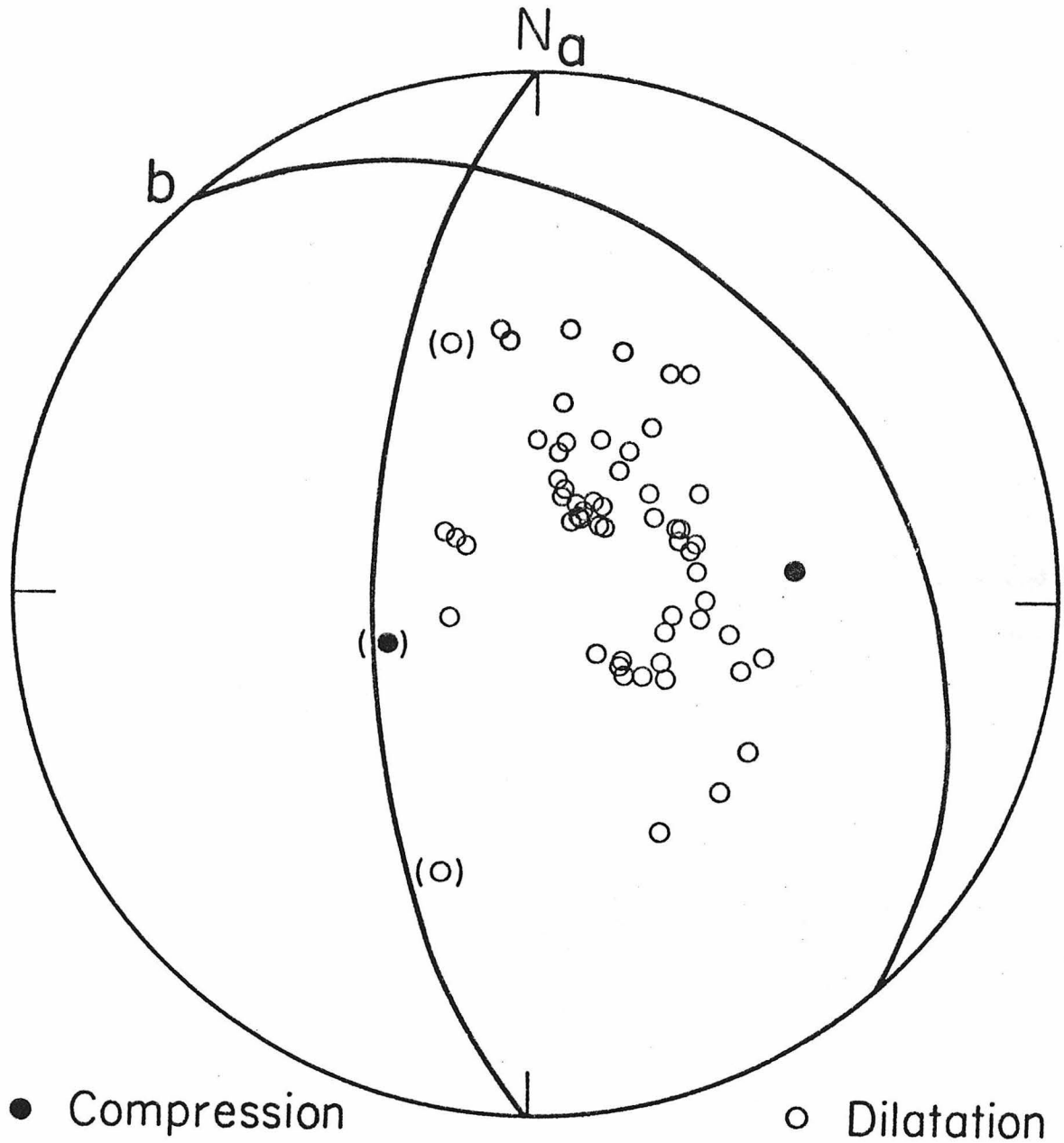
TABLE I.1.1

(Continued)

<u>STATION</u>	<u><math>\Delta</math> (o)</u>	<u>AZ (o)</u>	<u>P FIRST MOTION</u>	<u>MOMENT</u> <u>(x10<sup>24</sup> dyne-cm)</u>
OXF	26.10	90.7	D	
PTO	79.27	45.0	D	
SCP	33.20	73.4	D	
SHA	28.61	97.4	D	
SHK	79.41	306.0	D	11.0
SJG	52.18	97.4	D	6.0
STU	82.00	30.3	D	
TOL	82.61	43.5	D	6.2
TRI	86.30	29.6	D	
TUC	11.29	125.8	D	
UME	72.72	16.7	D	
VAL	71.19	37.5	D	
WES	37.66	68.9	D	3.1
PAS	5.96	151.5	D	

av. = 5.7

 $\sigma = 2.0$



Plane "a":  $\delta=65^\circ$ ,  $\lambda=-70^\circ$ ,  $\theta=180^\circ$

Plane "b":  $\delta=32^\circ$ ,  $\lambda=-110^\circ$ ,  $\theta=319^\circ$

Figure I.1.2 Equal area projection of the lower half of the focal sphere showing the P first motions. The brackets, '( )', indicate questionable readings.

unconstrained by  $\pm 30^\circ$  or more. In order to constrain the orientation and also determine the depth, time function, and moment, long period P waves were examined at ranges greater than  $30^\circ$  but less than  $90^\circ$  to avoid upper mantle and core structural complications. By modeling the P waveform in the time domain, source information can be extracted by examining the timing, shape, and relative amplitudes of the phases P, pP, and sP, assuming that the local source crustal structure is known. The computational techniques and conventions are described in detail by Langston and Helmberger (1975) and by Helmberger (1974) and will only be touched upon.

A synthetic seismogram is computed by first calculating the sum of ray responses for an imbedded point dislocation, of some orientation and depth, in a layered elastic medium. An area normalized dislocation time function is assumed and the displacement seismogram convolved with a Q operator (Futterman, 1962; Carpenter, 1966) and the 15-100 instrument impulse response to produce the final synthetic. This is then compared directly with the observation. The far-field time function assumed in this study is a simple triangular pulse parameterized by the rise and fall-off times ( $\delta t_1$  and  $\delta t_2$ ). The T/Q parameters assumed are 1.0 and 4.0 for P and S waves, respectively. Comparison between the observed seismogram and synthetic is done by trial-error and by a formal generalized inverse. The particulars of this generalized inverse are described in detail by Langston (1976).

The P waveforms chosen for study were processed in the manner described by Langston (1976). Eighteen long period P waves were used and are shown as the top seismograms, at each station, in Figure I.1.3.

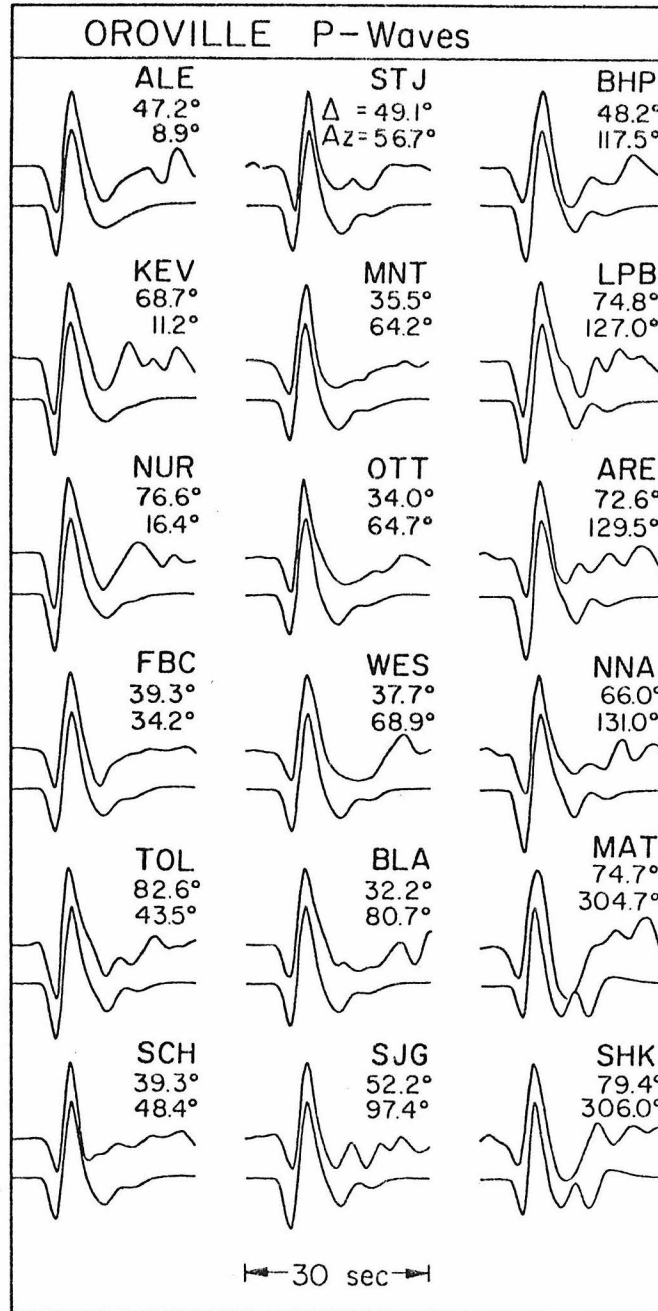


Figure I.1.3 Observed and synthetic long period waveforms for the 18 stations used. Each seismogram pair consists of the observed on top and computed directly below for each station.

This station distribution represents the best azimuthal variation possible with the long period data set. Pacific azimuths are not included because of very poor signal quality and the scarcity of stations at those azimuths and the specified range interval. The waveforms exhibited in Figure I.1.3 are very simple in character. Distortion due to the instrument response is relatively minor for these particular seismograms so it is easy to identify the polarities of the major arrivals. Every station shows a dilatational first arrival with a major compression directly behind it. Examining the strength and polarity of the radiation pattern from a shallow, normal dip-slip, point dislocation in a typical continental crust predicts that the combined phases of pP and sP should be compressional and larger than the dilatational P wave. Using this hypothesis several models were constructed with very satisfactory results. The crustal model assumed in this procedure is taken from Eaton (1966) and is displayed in Table I.1.2.

Good fits to the P waves were obtained by using a point dislocation with a depth of 5 km, dip of  $65^\circ$  W, and a symmetric triangular time function 3 seconds in duration. The depth is controlled by the interference of P and pP and the dip by their amplitude ratios. It was quickly apparent, however, that the strike and rake remained unconstrained to the same degree as found by the first motion study. An inversion was attempted to see if the small differences these parameters have on the data set were resolvable, but the same story emerged. The starting model turned out to be the best model with 'resolution' matrix indicating that the strike and rake were very poorly constrained.

TABLE I.1.2

## OROVILLE CRUST MODEL

<u><math>\alpha</math> (km/sec)</u>	<u><math>\beta</math> (km/sec)</u>	<u><math>\rho</math> (gm/cm<sup>3</sup>)</u>	<u>Th (km)</u>
6.0	3.5	2.7	10.0
6.8	3.9	2.8	10.0
8.0	4.6	3.3	---

In an effort to constrain these parameters the few S waves were examined. The horizontal components were digitized and then rotated into the ray azimuth. The left half of Figure I.1.4 show these data. This particular S wave data set has many problematic characteristics, as do most S waveforms. First, SJG has some long period noise (T ~60 sec) and the signal is relatively small. However, since a rotation is insensitive to baseline shifts when relative waveshapes are considered, long period drift should contribute very little error in the rotation. MAT and TRI exhibit complicated arrivals after the first 10 seconds which are, presumably, core phases and S-coupled  $P_L$  waves (Helmberger and Engen, 1974). Of the four, NNA has the best rotation due to ideal range, good back azimuth, and high amplitude SH. Even considering these problems, valuable information about the source is contained in the first 10 seconds due to the interference of S and sS. Since the source is very shallow, as determined by the P waves, a strict use of the standard techniques for determining S polarization angles would be misleading and erroneous due to this interference. A tack of directly modeling the SV and SH components was therefore taken.

The comparison between observed and synthetic was done by trial-and-error with the employment of a special metric to compare waveshapes and amplitudes in a more quantitative sense. Consider the scheme illustrated in Figure I.1.5. Define an 'effective' polarization angle by simply considering the inverse tangent of the magnitude of the SV/SH amplitude ratio, or

$$\gamma_i = \text{TAN}^{-1} ( A_{SV} / A_{SH} ) \quad (1)$$

where  $\gamma_i$  is the 'effective' polarization at the  $i^{\text{th}}$  station. This relation

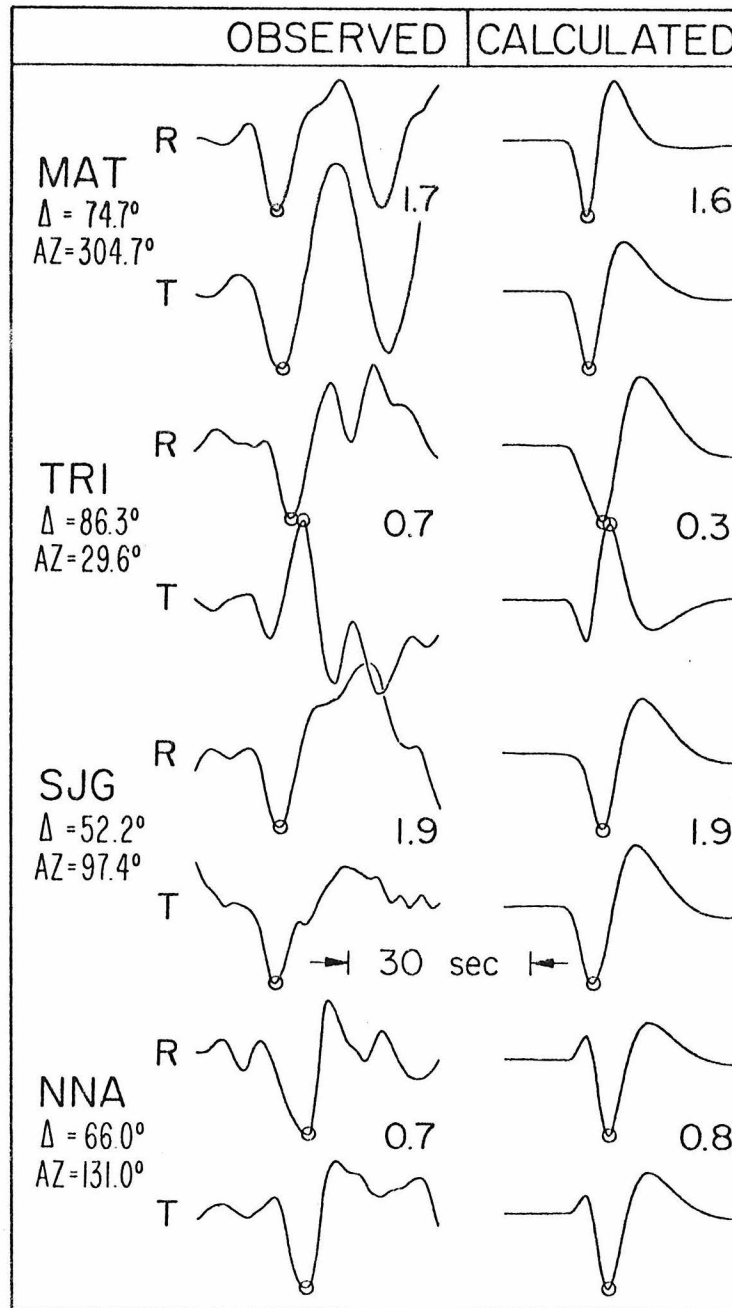


Figure I.1.4 Observed and synthetic SV and SH at four stations. The left-hand column contains the observed rotated S waves and the right, the corresponding synthetics for the final model. 'R' and 'T' stand for the radial and tangential components, respectively. The numbers in the right center of each pair corresponds to the SV/SH amplitude ratio at the points indicated by the small circles.

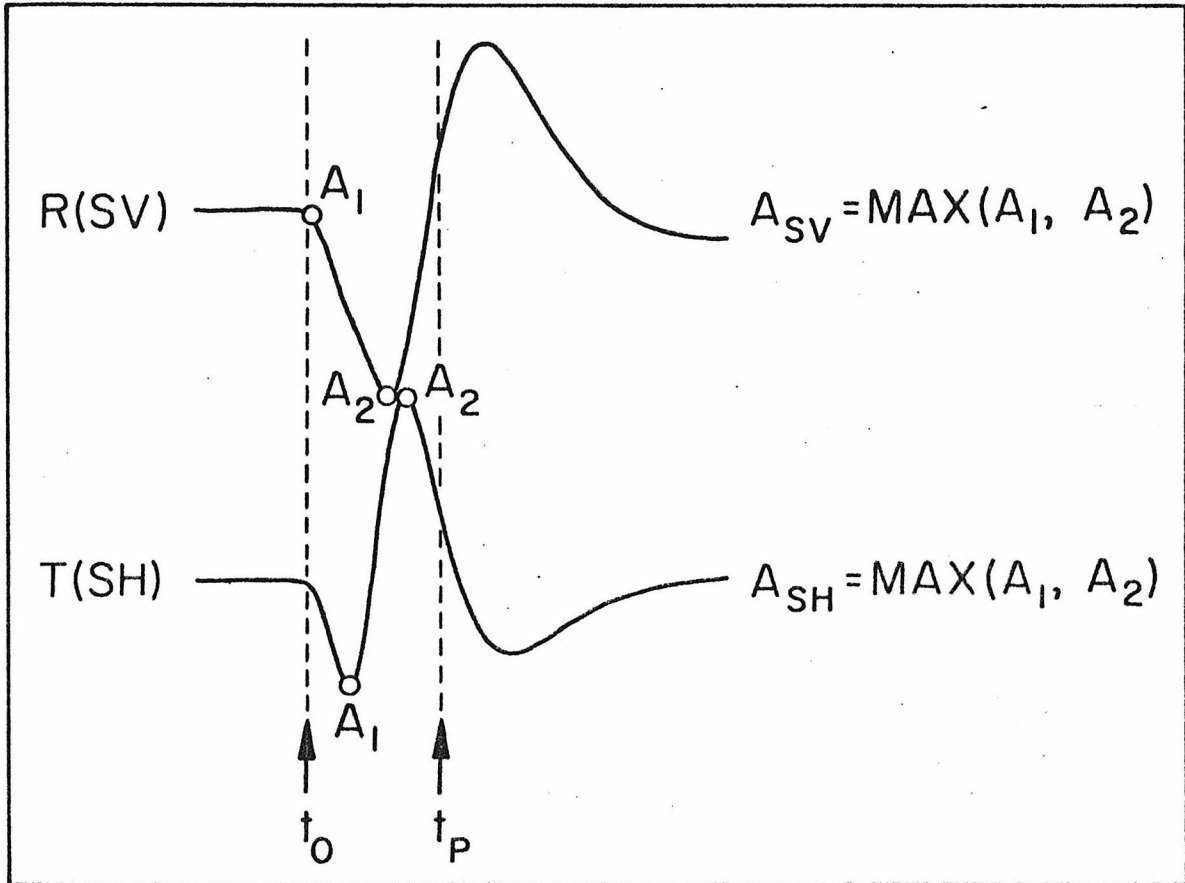


Figure I.1.5 Scheme for parameterizing SV - SH waveform pairs.

measures the effective strength of the two shear components. To measure waveshape and polarities define another angle,  $\omega_k$ , by

$$\omega_k = \text{TAN}^{-1}(A_1/A_2) \quad , \quad k = 1,2 \text{ (SV or SH)}. \quad (2)$$

These relations assume that the approximate time of sS is known so that an appropriate time interval can be considered and the arrivals identified. In relation (2), if the seismogram has only one peak within the time interval it is designated with  $A_2$  and  $A_1$  set to zero. This insures stability in  $\omega_k$  if the direct S wave goes through a node while sS stays relatively constant in amplitude. Using relations (1) and (2), further define a residual function or norm,  $\xi^2$ , by

$$\xi^2 = \sum_{i=1}^n \{ (\gamma_i - \bar{\gamma}_i)^2 + \sum_{k=1}^2 (\omega_k - \bar{\omega}_k)_i^2 \} \quad (3)$$

where,

$i$  = index of the  $i^{\text{th}}$  station

$k = 1, \text{ SV} ; 2, \text{ SH}$  at the  $i^{\text{th}}$  station

$\bar{\quad}$  = theoretical value of the particular angle.

Using the values found by the P wave modeling for depth, dip, and time function, the rake and strike were varied in  $10^\circ$  increments over several classes of models, e.g., right-lateral and left-lateral orientations. To fit the polarities and waveshapes it was apparent that a left-lateral model had to be used. Table I.1.3 illustrates the value of  $\xi$  versus various orientations around the best orientation of rake  $-70^\circ$  and strike  $180^\circ$ . These values indicate that trade-offs

TABLE I.1.3

THE RESIDUAL FUNCTION,  $\xi$ , VERSUS VARIOUS ORIENTATION  
ANGLES FOR THE OROVILLE S WAVE DATA (  $\delta = 65^\circ$  )

<u><math>\lambda</math></u> (°)	<u><math>\theta</math></u> (°)	<u><math>\xi</math></u>
-80	170	0.391
-80	180	0.416
-80	190	0.589
-70	170	0.386
-70	180	0.338
-70	190	0.508
-60	170	0.587
-60	180	0.506
-60	190	0.790

occur in  $\lambda$  and  $\theta$  which could possible allow the rake to be in the interval  $-70^\circ$  to  $-80^\circ$  and the strike within  $170^\circ$  to  $180^\circ$ . No weighting functions were applied to (3) and the statistics of such a parameterization were not investigated. However, high values of  $\sigma$ , e.g., 0.4, clearly represent bad fits as determined by simple visual correlation of the sizes and timing of observed peaks. It therefore serves as a good quantitative indicator to be used in conjunction with seismogram overlays. The right side of Figure I.1.4 shows the final S wave synthetics for the four stations used. The SV waves contain the phases S, pS, and sS. The SH waves contain only S and sS. Amplitudes are scaled by the receiver function for an upper crust of compressional and shear wave velocity 6.0 and 3.5 km/sec, respectively. Most seismograms show S and sS to be in phase except for TRI(SH) and NNA(SV and SH) where they are opposite polarity.

An independent check on the depth was done using the short period vertical P waves. Figure I.1.6 shows a histogram of the number of arrival time picks versus time, relative to the direct P wave, for the available teleseismic stations. Each arrival time was put into 0.1 sec boxes to each side of the time, the estimated reading error being  $\pm 0.1$  sec. This effectively spreads the arrival over 0.2 sec. Hence, the area of the histogram is twice the number of readings. A distinct bimodal distribution emerged from this process with peak times at about 1.6 and 2.5 sec. Because the long period P waves yielded a depth of approximately 5 km, these arrivals are interpreted to be the phases pP and sP. These times yield depths of 5.1 and 5.7 km from each respective phase. A maximum error of 0.4 sec, obtained from the widths of the distributions, yields an average depth of  $5.5 \pm 1.5$  km.

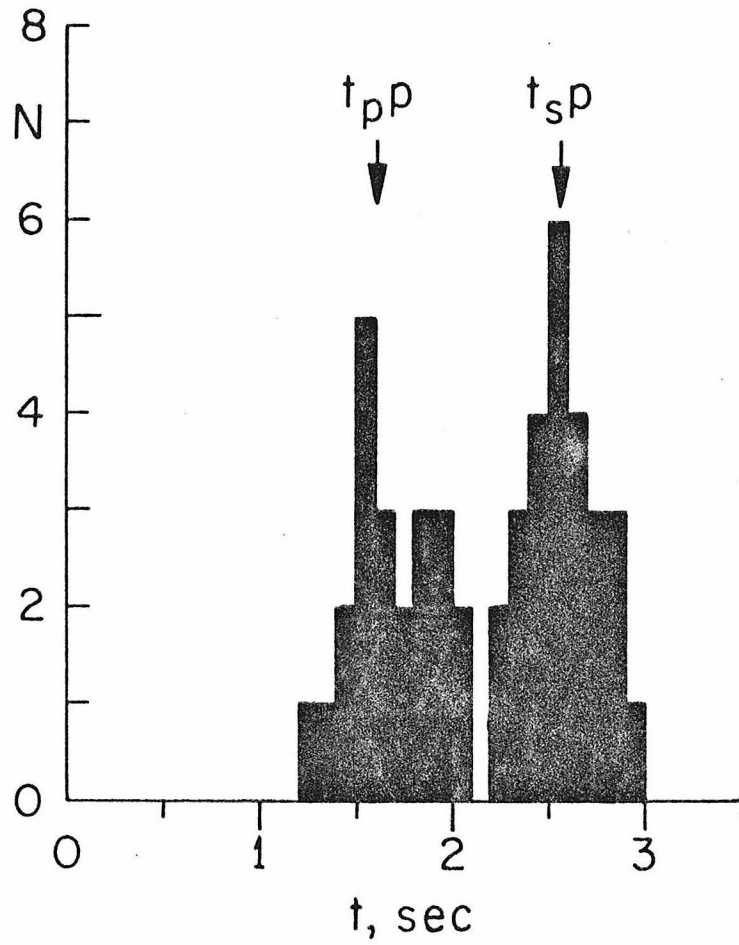


Figure I.1.6 Histogram of arrival time versus number of picks showing the bimodal distribution attributed to pP and sP.

The final P wave model comparisons are shown in Figure I.1.2. These synthetics contain 20 crustal rays with arrival times up to about 20 sec after the first P arrival. In general, the fits are quite satisfactory. The model predicts a dilatational direct P with an immediate compressional arrival composed of pP and sP. The small arrivals after these major phases are essentially interference effects produced by the addition of many small crustal reverberations adding in phase at these wavelengths. This particular effect can explain the start of the P coda for all the stations except MAT and SHK where the model predicts an unobserved arrival. This is not too disconcerting since these interference effects are dependent, to a large degree, on the exact nature of the source crust. This does imply, however, that, given the particular orientation and depth, the crustal structure at Oroville changes laterally, either in velocity/thickness or in the sharpness of layer boundaries. Scaling the synthetic waveforms directly to the observations gives a moment of  $5.7 \pm 2.0 \times 10^{24}$  dyne-dm (Table I.1.1). The error is one standard deviation in the amplitude scatter.

#### BODY WAVE DISCUSSION

The focal mechanism of a north-south striking, westward dipping, normal dip-slip fault agrees perfectly with the configuration of the aftershock zone (Bufe, et al., 1976; Ryall and VanWormer, 1975; Lahr et al., 1976). An estimate of 10 x 10 km for the fault plane area taken from the aftershock zone yields an average displacement of 17 cm on the fault. The shallow depth of 5.5 km also implies that rupture may have initiated near the center of the aftershock area and propagated

radially outwards. The time function duration of 3 sec and fault bounds assumed above yield a rupture velocity of less than 2 km/sec, assuming a simple propagating step dislocation model (Savage, 1966). These simple calculations indicate that the time function found here is sufficient to explain the entire faulting process as determined by the aftershock zone.

The origin time difference between the foreshock and mainshock, seen in this study, of 6.5 sec versus 8.1 sec has a very simple explanation in terms of the focal mechanism. For regional stations ( $\sim 150$  km) rays will be leaving the focal sphere toward the outer edge of the station distribution seen in Figure I.1.1. This means that, in general, direct P is near a node. The small direct P, arriving within the foreshock wavetrain, could easily be missed and the large surface reflections picked as the first arrival instead. This is not a terribly important point but it does illustrate the ambiguity of picking multiple source times from shallow earthquakes.

#### BODY WAVE SUMMARY

From an analysis of P and S waveforms the mechanism of the mainshock of the Oroville earthquake sequence is determined to be dip  $65^\circ$ W, north-south strike, and rake  $-70^\circ$  (left-lateral). The far-field time function is modeled successfully as a symmetric triangular pulse 3 sec in duration. Scaling the amplitudes of the theoretical to the observed yields a moment of  $5.7 \pm 2.0 \times 10^{24}$  dyne-cm. The duration of the time function is consistent with the faulting area determined by the aftershock zone. A hypocentral depth determination of  $5.5 \pm 1.5$  km is made

using both the long and short period P waves. A relative time of 6.5 sec is inferred for the mainshock-foreshock interval. This focal mechanism is consistent with the configuration of the aftershock zone.

### Surface Wave Data and Analysis

Vertical, long period seismograms from 25 WWSSN and Canadian Network stations were available to us for this study. The azimuthal coverage obtained with these data is shown in Figure I.1.7. Additionally, the horizontal component seismograms for 7 of the WWSSN stations were also obtained. The appropriate great circle Love wave paths for these stations are shown in Figure I.1.8. The Rayleigh and Love waves recorded on all these seismograms were digitized at 1.0 second intervals. The digitized records were analyzed in both the time and frequency domains in order to extract the source parameters.

Our method of determining the long-period source characteristics of this event is essentially the same as that described previously by Kanamori (1970) and Kanamori and Stewart (1976). The Rayleigh wave recordings were equalized to a standard distance of 90° and a standard magnification of (x 1500). Further the cosine filter

$$W(f) = \begin{cases} \frac{1}{1 - 4\left(\frac{f}{f_0}\right)^2} \frac{\sin 2\pi(f/f_0)}{2\pi(f/f_0)} & , 0 \leq f \leq f_0 \\ 0 & , f > f_0 \end{cases}$$

(where  $f$  = frequency and  $f_0$  = cut-off frequency) was applied to remove short-period contributions to the observations. (This filter was applied first with  $f_0 = 1/25 \text{ sec}^{-1}$  and then with  $f_0 = 1/40 \text{ sec}^{-1}$ ). The equalized

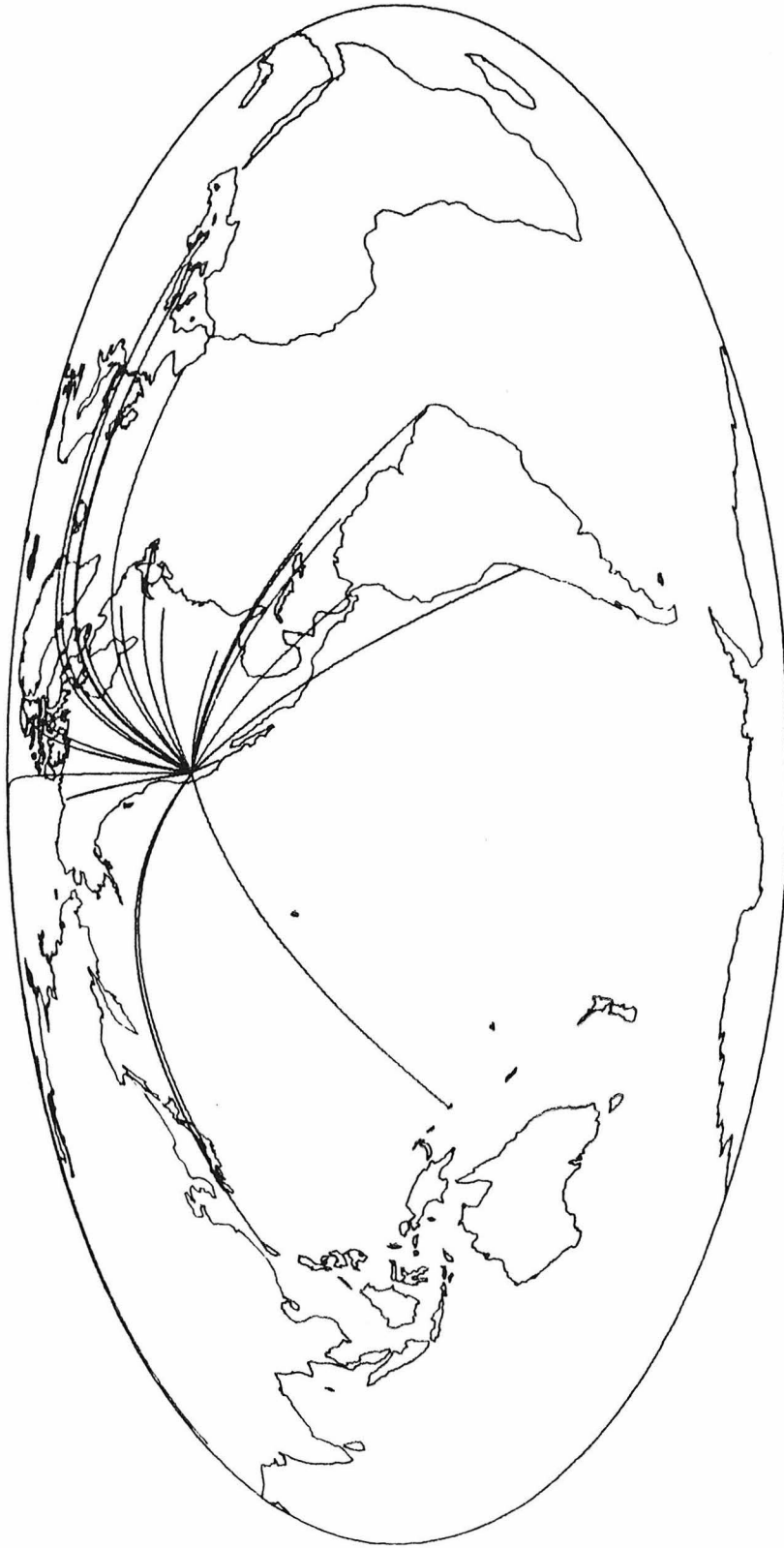


Figure I.1.7 Great circle Rayleigh wave paths used in this study.



Figure I.1.8 Great circle Love wave paths used in this study.

Rayleigh wave amplitudes thus obtained are plotted in Figure I.1.9 in the standard polar radiation pattern diagram. Because of the lack of observations to the south of the epicenter, we have not attempted to directly connect those points to the west of the epicenter to those to the southeast. The patterns are consistent with the fault geometry determined by the body wave study (strike =  $180^\circ$ , dip =  $65^\circ$ , slip =  $-70^\circ$ ) and with the configuration of the aftershock zone (Bufe et al., 1976 and Ryall and VanWormer, 1975; Lahr et al., (1976). The theoretical radiation pattern, for the Langston and Butler fault geometry, is computed by using the structure KHC2 (Chapter III) and is plotted with the observations in Figure I.1.9. The best fit to the data occurs when a seismic moment of  $1.9 \times 10^{25}$  dyne-cm is assumed. This value is significantly larger, by a factor of more than three, than the  $5.7 \times 10^{24}$  dyne-cm moment determined by the body waves. We considered it necessary, then, to check our moment computations with two other methods before any attempt was made to interpret this discrepancy in terms of the earthquake source.

Both the Love wave and the Rayleigh wave data were Fourier transformed in order to obtain the spectral densities at each observing station. Following the technique of Ben Menahem et al. (1970), we computed the seismic moment at each station from the observed spectral densities at periods of 50, 100, and 150 seconds. In this computation, the source depth was assumed to be 10 km and a continental structure was used. The average seismic moment thus obtained was  $1.85 \times 10^{25}$  dyne-cm, which agrees well with the equalized amplitude value.

The Love wave spectral densities yield a seismic moment of  $1.6 \times 10^{25}$  dyne-cm. Since Love waves are more strongly affected by structural

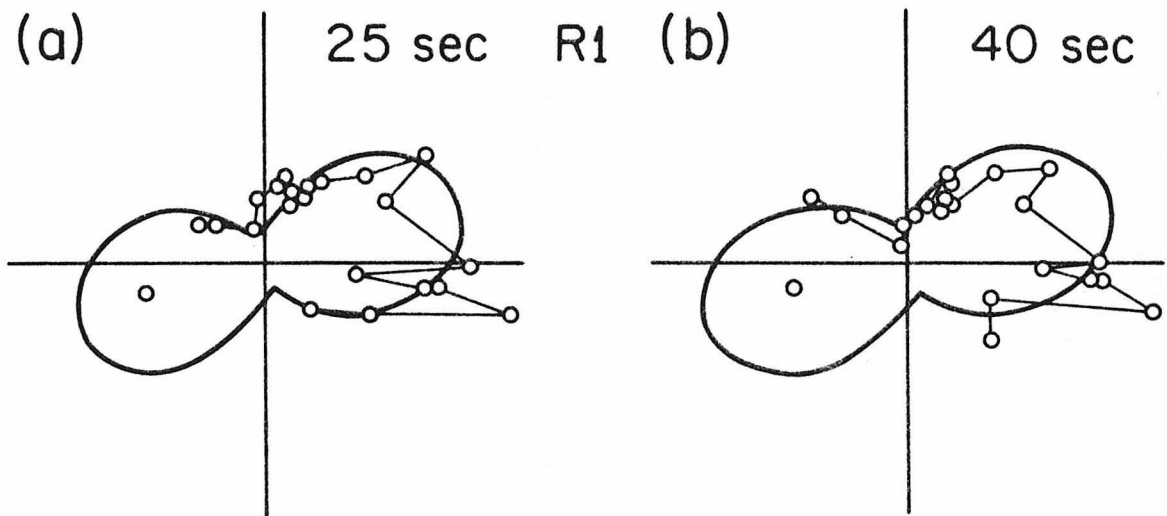


Figure I.1.9 Observed Rayleigh amplitudes (open circles) equalized to a distance of  $90^\circ$ . (1) High frequency cut-off at 25 seconds. (2) High frequency cut-off at 40 seconds. Solid curves are the theoretical radiation patterns for a seismic moment of  $1.9 \times 10^{25}$  dyne-cm.

heterogeneities than Rayleigh waves, this value is in good agreement with the Rayleigh wave values. In Table I.1.4 we give the actual 50 and 100 second period moment values, determined by the spectral densities, for the loop stations.

As a further check, synthetic Rayleigh waves were computed for each loop station using model KHC2 (Chapter III). This structure has a continental crust appropriate to southern California overlying an oceanic mantle. These synthetics were bandpass filtered with a long period cut-off at 150 seconds and with a short period cut-off at 40 seconds.

These bandpassed synthetics were compared with similarly bandpassed observed Rayleigh waves at these stations. Several of the synthetic Rayleigh waves from each loop are plotted with the corresponding observations in Figure I.1.10. The synthetic waveforms are normalized to the observed amplitudes by assuming the moment value noted with each waveform pair in this figure. Since model KHC2 has an oceanic-type phase velocity curve at long periods ( $T \geq 40$  sec), the agreement is very good for the entire wave train for such stations as MAT and HNR; for stations such as STJ or SHA the agreement is less good beyond the first two or three cycles. However, it is these first two or three cycles that are important for the moment computation.

The moment discrepancy cannot be explained by errors in  $Q$  in our computation. The value of  $Q_R$  used in the present study is approximately 150 over the period range from 30 to 100 sec. Tsai and Aki (1969) found that  $Q_R$  ranges from 120 to 250 in this period range. At a distance of  $60^\circ$  and at 1 minute period, a representative distance

TABLE I.1.4

Seismic moment values, from loop stations, as determined by the observed spectral densities at periods of 50, 100, and 150 seconds.

<u>STATION</u>	<u>PERIOD (sec)</u>	<u>Seismic Moment (<math>10^{25}</math> dyne-cm)</u>
MAT	150	1.76
	100	1.83
	50	2.51
SHK	150	3.81
	100	1.56
	350	1.57
HRN	150	1.42
	100	0.70
	50	1.12
TRN	150	2.47
	100	2.07
	50	2.72
SHA	150	
	100	3.33
	50	2.77
STJ	150	1.20
	100	0.74
	50	2.10
SJC	150	3.00
	100	2.04
	50	2.33
PTO	150	1.89
	100	1.04
	50	1.71
MNT	150	1.87
	100	0.93
	50	2.03
BHP	150	2.44
	100	2.30
	50	1.87
NAT	150	2.51
	100	1.31
	50	1.31

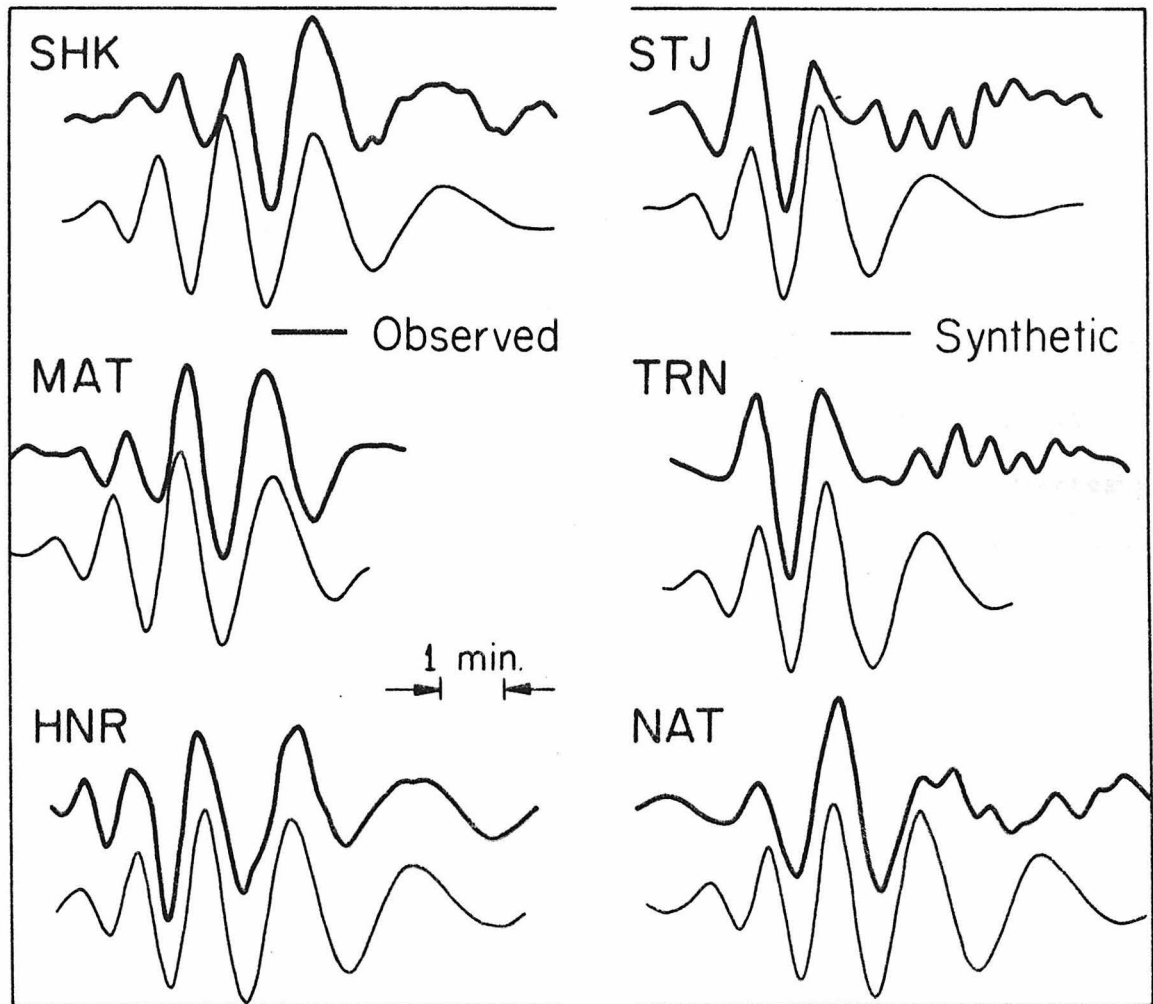


Figure I.1.10 Observed and synthetic Rayleigh waves, band passed at 150 seconds and 40 seconds, for several loop stations.

and period in this study, this uncertainty in  $Q$  affects the amplitude by about  $\pm 20\%$ . Thus the error in the moment resulting from the errors in  $Q$  is about  $\pm 20\%$ .

#### SURFACE WAVE DISCUSSION

With the long period seismic moment of the Oroville earthquake confirmed at  $1.9 \times 10^{25}$  dyne-cm, it is important to consider the resultant implications for the source function of this event. Figure I.1.11, adapted from Kanamori and Anderson (1975), is a plot of the log of the seismic moment versus  $M_s$ . From such a diagram, we can obtain the apparent stress of the earthquake source. The Oroville earthquake is plotted as the star symbol in the lower left. Its position indicates an apparent stress of only about 5 bars, very low for an intra-plate earthquake.

In Figure I.1.12, also adapted from Kanamori and Anderson (1975), we have plotted the log of the source dimension versus the log of seismic moment from which the stress drop may be determined. The Oroville earthquake again appears as a star symbol in the lower left. The stress drop is about 50 bars, roughly the lower bound of values typical of other intraplate events.

Kanamori and Anderson (1975) have shown that, in general, the apparent stress of an earthquake is roughly equal to  $1/2$  the observed stress drop. For the Oroville earthquake, however, this ratio is only about  $1/10$ . This implies a very low seismic efficiency. In light of the large long period moment, this low efficiency in turn implies that the excitation of seismic energy was "abnormally" biased toward long

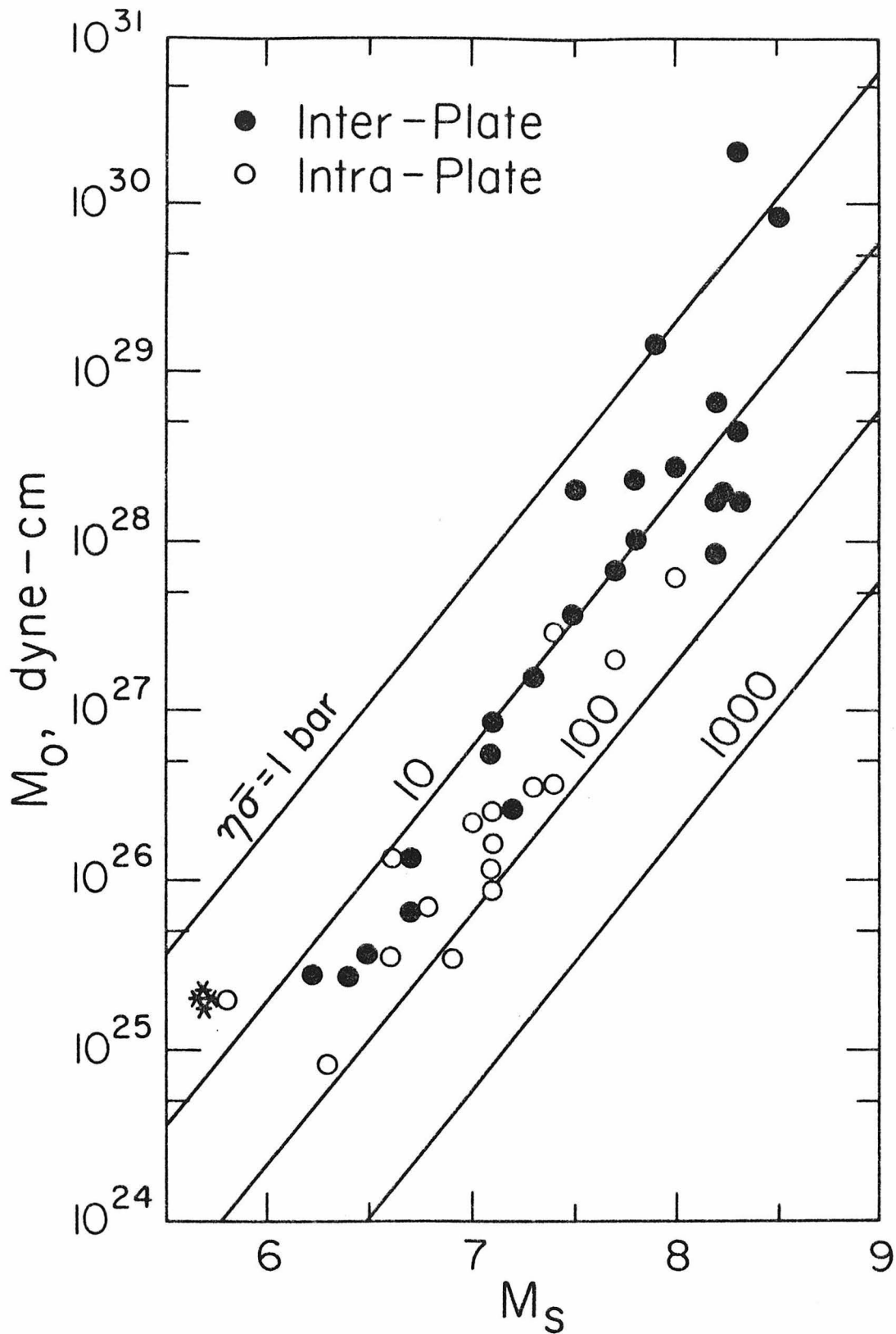


Figure I.1.11 Relation between  $M_s$  (20-second surface wave magnitude) and seismic moment. The straight lines are for constant apparent stress. The Oroville earthquake is the star symbol at lower left. (Adapted from Kanamori and Anderson, 1975.)

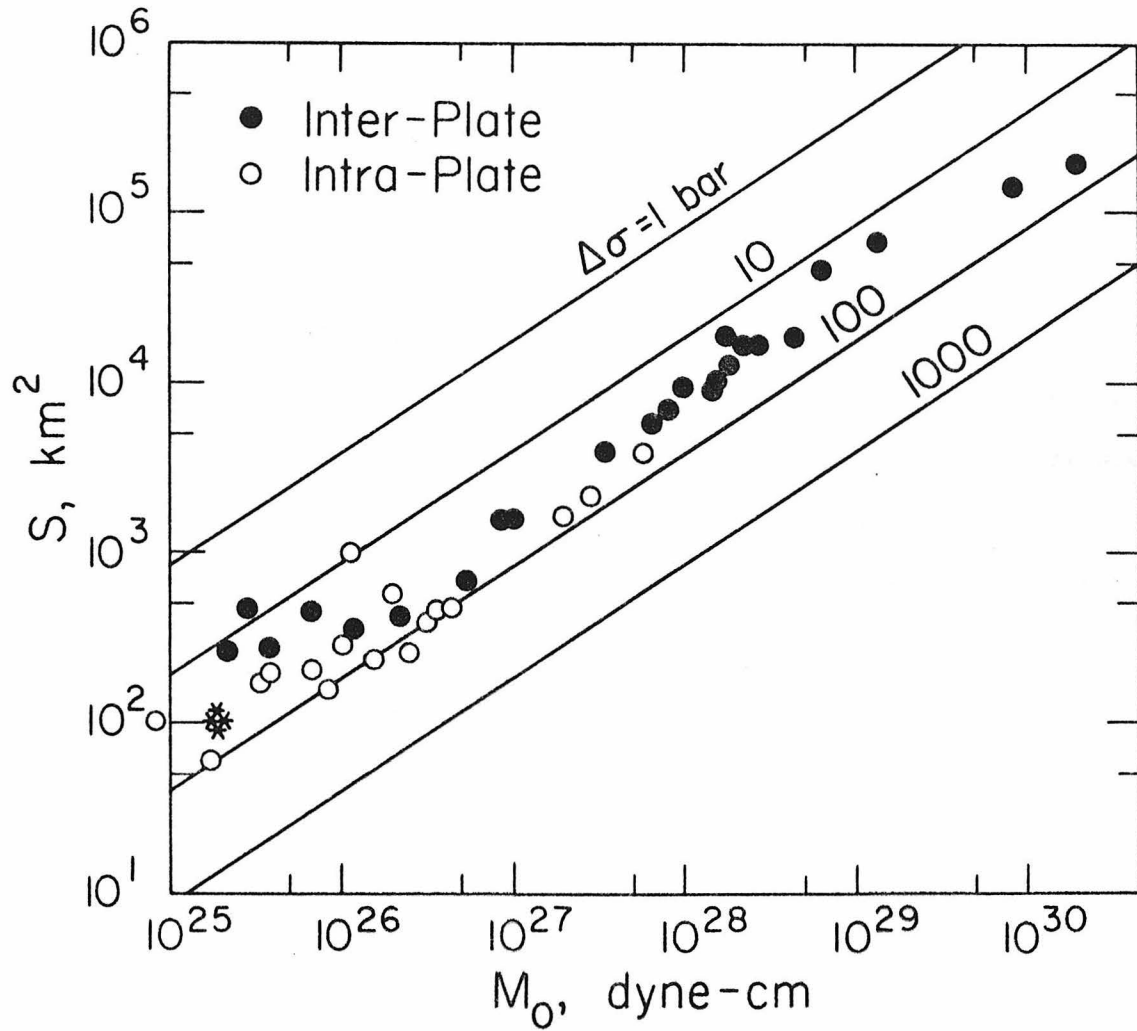


Figure I.1.12 Relation between fault area and seismic moment. The straight lines are for constant stress drop. The Oroville earthquake is the star symbol at lower left. (Adapted from Kanamori and Anderson, 1975.)

periods. Thus the discrepancy between the short period and long period moment determinations must involve an intrinsic difference in the earthquake source at longer periods.

If the rupture process of this event is bilateral, the body wave time function would suggest that most body-wave energy was radiated from the aftershock area defined by Bufe et al. (1976). Then two possibilities may be suggested to explain this discrepancy: (1) The long period source and the short period source have approximately the same spatial extent as defined by the aftershock area, but the deformation at the source had long period components which enhanced the excitation of surface waves. (2) The long period source involved a larger focal region than the aftershock area; the deformation outside the aftershock area was slow and did not excite short period body waves.

The far-field body wave time function is the derivative of the actual displacement time function at the source and, thus, a slow deformation may not be apparent in a body wave analysis. Such slow deformation could well be pre-seismic, post-seismic, or co-seismic with respect to the conventional P wave onset time of the Oroville earthquake. The present data are not sufficient to distinguish among these possibilities.

Recently, three deep aftershocks of the Oroville earthquake were recorded and located by investigators from the U.S.G.S. (Hill, personal communication). Two of these events occurred at a depth of 40 kilometers, the third at 20 kilometers. If the fault plane of the main Oroville earthquake is extended to these depths, all three aftershocks lie directly on that plane. This raises the intriguing possibility

that the high level of long period from the Oroville event stems from a slow deformation over a larger focal region extending to much greater depth than the faster, conventional rupture area. If this is the case, the second possibility suggested above may be favored.

#### SURFACE WAVE SUMMARY

A detailed analysis of the long period surface waves from the Oroville earthquake has confirmed the body wave source geometry. However, both time domain and frequency domain computations have yielded a seismic moment of  $1.9 \times 10^{25}$  dyne-cm for this event, approximately three times larger than the moment determined by body wave data. This larger moment implies a total static displacement of about 50 cm, assuming a fault dimension of  $100 \text{ km}^2$ . If a larger fault dimension is involved as suggested above, a smaller displacement would suffice to explain the surface-wave moment. The discrepancy between the short period moment value and that determined with long period data is likely to reflect an intrinsic difference between the source time history affecting different regions of the spectrum.

#### Ultra Long Period Body Wave Analysis

In the study of the Oroville earthquake, this part of the analysis was undertaken about two years after the completion of the teleseismic body wave and surface wave analyses. This further look at the Oroville source was motivated by a desire to better understand and to place some further constraints on the apparent moment anomaly between the body and surface waves. Since the initial analyses, two additional pieces of information were added to the picture. The body wave moment for the

Oroville event was determined using a  $t^* = 1$  to correct for the attenuation of P waves. HelMBERger and Hadley (in preparation) have obtained an accurate estimate of  $t^* = 1.3$  by modeling near field strong ground motion recordings of nuclear explosions at the Nevada Test Site and comparing amplitudes and waveshapes with teleseismic observations. Correcting for this difference in attenuation, a somewhat greater seismic moment of  $6.6 \pm 2 \times 10^{24}$  dyne-cm is obtained for the body waves. Secondly, Savage et al. (1977) have reported on a vertical geodetic survey in the region of the Oroville earthquake. The data are consistent with 0.36 meters of slip on a  $10 \times 12 \text{ km}^2$  rectangular fault outlined by the aftershock sequence. These values yield a seismic moment of  $1.4 \times 10^{25}$  dyne-cm which is in fair agreement with the surface wave moment. However, this geodetic moment includes contributions from aftershocks and depends upon the assumed area of the fault plane.

The Oroville earthquake was well recorded on the horizontal components of the ultra-long period Gilman seismometers, number designation 35A and 35B, at Pasadena. These seismograms offered the opportunity to study long period body phases from the Oroville event at a regional distance of 660 km. The Gilman instruments have a pendulum period of 60 seconds and a galvanometer period of 110 seconds; the peak response is at about 80 seconds. It was suggested in the surface wave analysis that the teleseismic body waves may have exhibited a smaller moment due to insensitivities to long period or slow components of the Oroville source. As the responses of these instruments are quite long period, the observed body phases will include any slow components of the Oroville source.

The east-west and north-south components of motion were digitized and rotated into tangential and radial components. The east-west component was fairly noise-free, but the north-south component exhibited 120 second noise with a signal to noise ratio of 2 with respect to the P body phases. The vertical instrument could not be used as it malfunctioned from the large amplitude high frequency arrivals from the earthquake. The horizontal components did not exhibit any apparent anomalous behavior. The radial and tangential components are shown in Figure I.1.13. The tangential component shows a very clean, large amplitude SH arrival. The low amplitude of the P energy on the tangential component indicates that the rotation was stable. The arrival is a sum of  $S_n$ , S, and multiple S reflections in the crust yielding a Love wave. As the instrument averages over these arrivals, we shall for convenience collectively call them simply SH. The radial component shows a small downward breaking  $P_n$  followed by  $P_g$ , which will be collectively termed "radial P", after which arrives a fairly simple Rayleigh wave. The impulse response of the Gilman instrument is shown at the right in Figure I.1.13.

The SH arrival was modeled by summing generalized rays from a point shear dislocation in a layer over a half space (see HelMBERGER, 1974; HelMBERGER and MALONE, 1975; HEATON and HelMBERGER, 1978; HEATON, 1978). The period of the SH arrival is about 37 seconds. For a distance of 660 km we are 5 to 6 wavelengths from the source and thus effectively in the far field. A simple 32 km thick crust overlying a mantle half-space was used in the calculation and is listed in Table I.1.5. Thirty-two generalized rays were summed to obtain the SH

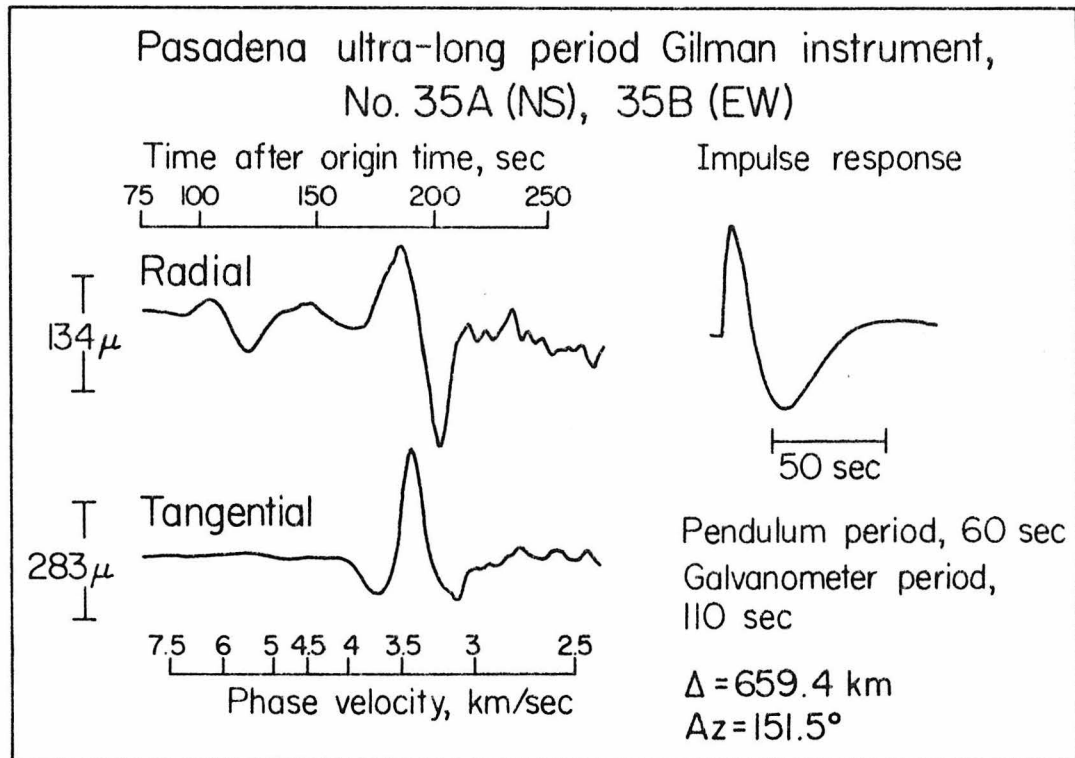


Figure I.1.13 Observed radial and tangential components of motion rotated from the Pasadena ultra-long period Gilman instruments, #35 (NS) and #35B (EW). The impulse response of the instruments is shown at the right.

TABLE I.1.5

VELOCITY MODEL FOR ULTRA-LONG PERIOD BODY WAVES

<u><math>\alpha</math>(km/sec)</u>	<u><math>\beta</math>(km/sec)</u>	<u><math>\rho</math> (g/cm<sup>3</sup>)</u>	<u>Th(km)</u>
6.2	3.5	2.7	32
8.2	4.5	3.4	--

impulse response containing  $S$ ,  $S_n$ , and the Love wave. A synthetic SH was then generated using the source parameters determined by the teleseismic body wave study and convolved with the three second far field time function and the Gilman instrument response. The fit between this synthetic and the observed SH arrival is shown in Figure I.1.14. The waveform and timing agreement is excellent. The seismic moment obtained by scaling the amplitude of the synthetic to the observed is  $8.2 \times 10^{24}$  dyne-cm, which is in agreement with the teleseismic body wave determination of  $6.6 \pm 2 \times 10^{24}$  dyne-cm.

In the body wave analysis of the Oroville earthquake the dip of the fault and the source depth were well constrained by the P-waves. Four S waves provided a lesser degree of control on the strike and rake. The actual strike noted in Figure I.1.14 and used in the body wave modeling is consistent with the strike determined from the aftershock zone,  $N3^\circ E \pm 3^\circ$  (Lahr et al., 1976). In modeling the Oroville teleseismic waves, rakes of  $-70^\circ$  and  $-80^\circ$  provided good fits to observed SV and SH, while rakes of  $-60^\circ$  and  $-90^\circ$  yielded poor fits to the data. To judge the sensitivity of the ultra-long period SH to changes of rake, a range of synthetics was generated varying the rake. These synthetics are shown in the right of Figure I.1.14. The fit of the waveforms to the observation are comparable between rakes of  $-90^\circ$  and  $-65^\circ$  but the fits are worse for  $-60^\circ$  and  $-55^\circ$ . A rake of  $-65^\circ$  provides a moment of  $1.2 \times 10^{25}$  dyne-cm which nears the Oroville surface wave determination of  $1.9 \times 10^{25}$  dyne-cm.

The radial P arrivals were also modeled by the generalized ray method (Helmberger, 1974; Heaton, 1978; Helmberger and Harkrider, 1978).

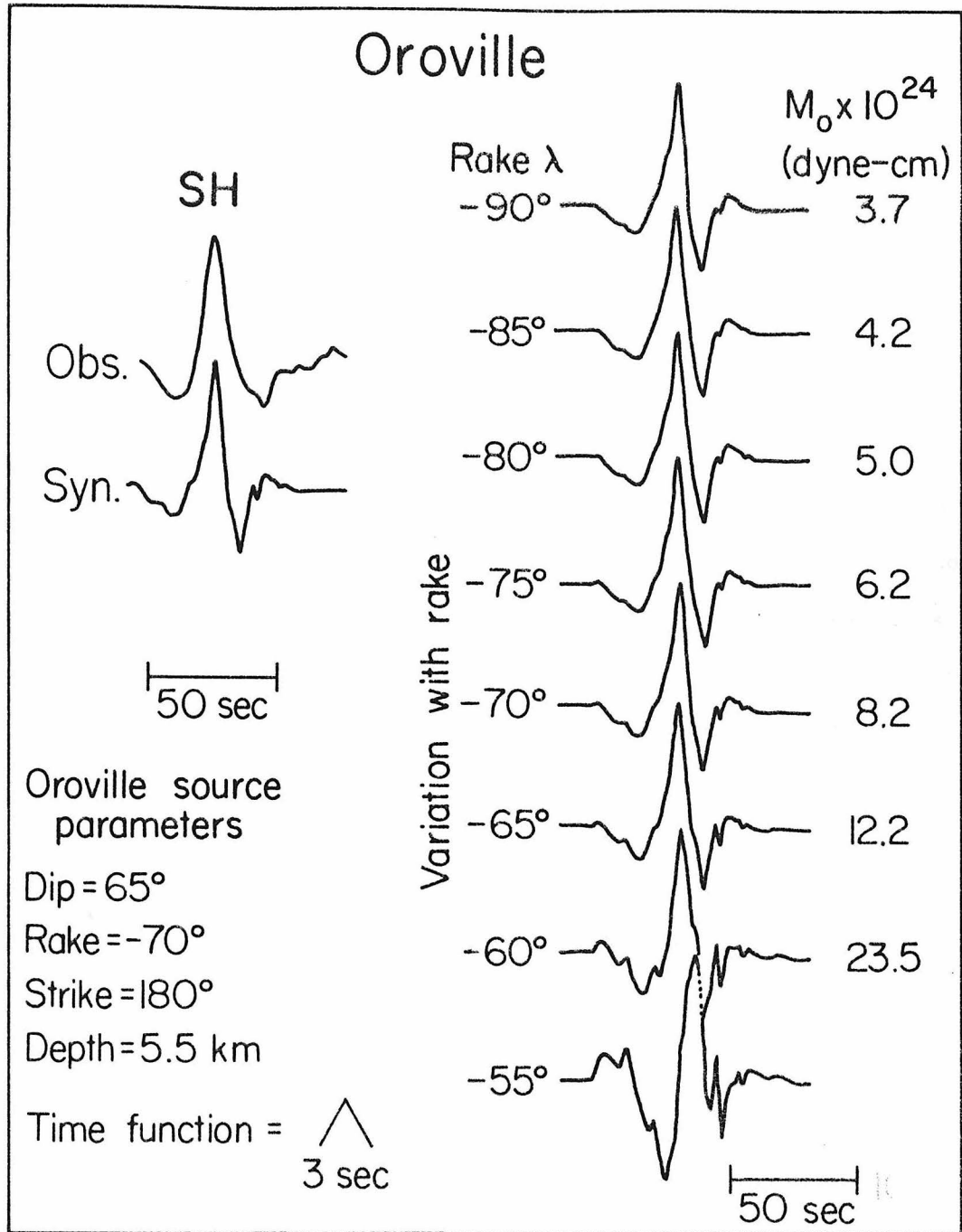


Figure I.1.14 At the left a comparison is shown between observed SH and a synthetic generated for the Oroville source parameters. The right column indicates the sensitivity of the SH synthetic to changes of the rake between -55° and -90°. The calculated seismic moment is noted to the right of each synthetic.

The same velocity model was used as in the SH case. All generalized rays up to three multiple crustal reflections, including all P-SV conversions, were included in the calculation. The comparison between the observed and synthetic radial P is shown in Figure I.1.15. The first motion and overall waveshape of the radial P fit well qualitatively, although the third swing is smaller on the synthetic than on the observed. The agreement begins to deviate significantly after about 60 seconds with the arrival of rays traveling primarily as SV. This was not unexpected as the SV are more sensitive to inaccuracies in the velocity model and more complicated in general than P or SH. The moment from the radial P using the Oroville teleseismic body wave source parameters is  $7.8 \times 10^{24}$  dyne-cm., which is in agreement with the SH determination. A study of the sensitivity of the radial P with changes of rake are also shown in Figure I.1.15. As with the SH, the waveforms are fairly insensitive to the rake between  $-90^\circ$  and  $-65^\circ$ , but rakes of  $-60^\circ$  and  $-55^\circ$  show substantially different waveshapes. If a rake of  $-65^\circ$  is chosen, the moment from the radial P is  $1 \times 10^{25}$  dyne-cm.

In the analysis of the Oroville ultra-long period body waves to this point, we have used the far field time function determined in the teleseismic body wave analysis: a three second symmetric triangle. Moments from the radial P and SH were in agreement with the body wave value, although using an allowable rake of  $-65^\circ$  would produce larger moments. In the previous discussion of the discrepancy between the body wave and surface wave moments for the Oroville earthquake, it was suggested that the teleseismic body wave may have been insensitive to slow deformations on the fault. To test the feasibility of this

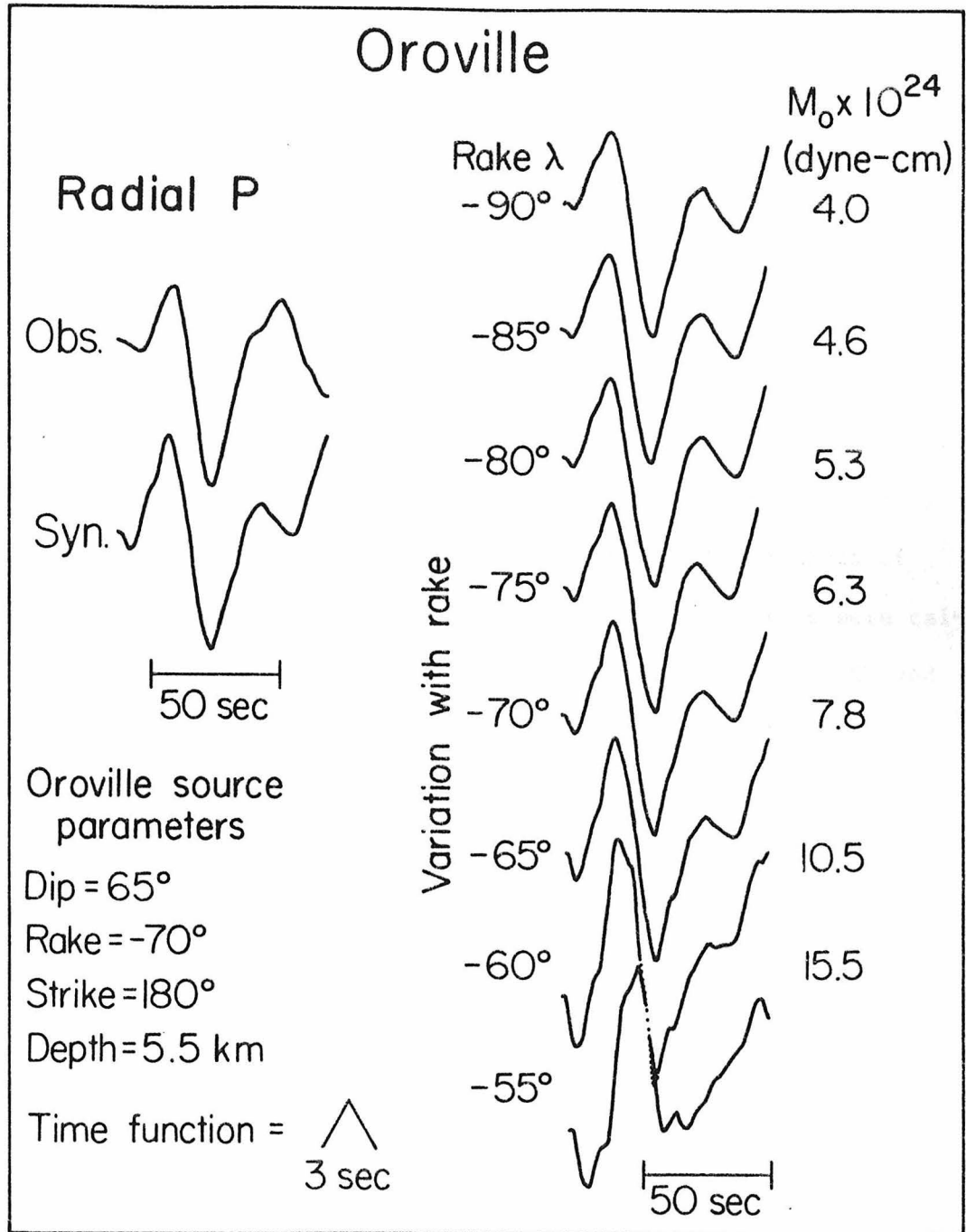


Figure I.1.15 At the left a comparison is shown between observed radial P and a synthetic generated for the Oroville source parameters. The right column indicates the sensitivity of the radial P synthetic to changes of the rake between -55° and -90°. The calculated seismic moment is noted to the right of each synthetic.

hypothesis, a range of SH and radial P synthetics were computed using longer duration source time functions. The time functions are illustrated in Figure I.1.16. The time function begins with the body wave three second symmetric triangle, but appended to it is an extended duration "tail". Synthetic SH and radial P generated for the Oroville source parameters and convolved with the extended duration time functions are also shown in Figure I.1.17. The longer time functions increase the apparent moment of Oroville and actually improve the fit of the synthetic to the observation in the SH case. A smoothing effect is observed on the radial P synthetics, but not much change in waveshape. The 15 second source time function yields SH and radial P moments of  $1.2 \times 10^{25}$  and  $9.6 \times 10^{24}$  dyne-cm, respectively. These values were calculated assuming a rake of  $-70^\circ$ . If we use a rake of  $-65^\circ$ , the SH and radial P yield moments of  $1.8 \times 10^{25}$  and  $1.3 \times 10^{25}$  dyne-cm, respectively. These values may be considered to be in fairly good agreement with the surface wave value of  $1.9 \times 10^{25}$  dyne-cm.

A comparison is shown in Figure I.1.17 between teleseismic P wave synthetics convolved with the three second symmetric triangle determined in the body wave analysis and convolved with a 15 second extended duration time function. The 15 second time function has twice the area of the 3 second triangle and thus has twice the effective moment. The synthetics agree extremely well in waveshape and amplitude. The principal difference in the waveforms is in the somewhat different character of the backswing ten seconds after the P onset. Details of this portion of the actual observations are, however, obscured by crust reverberations at the source and receiver. The amplitude of the second swing

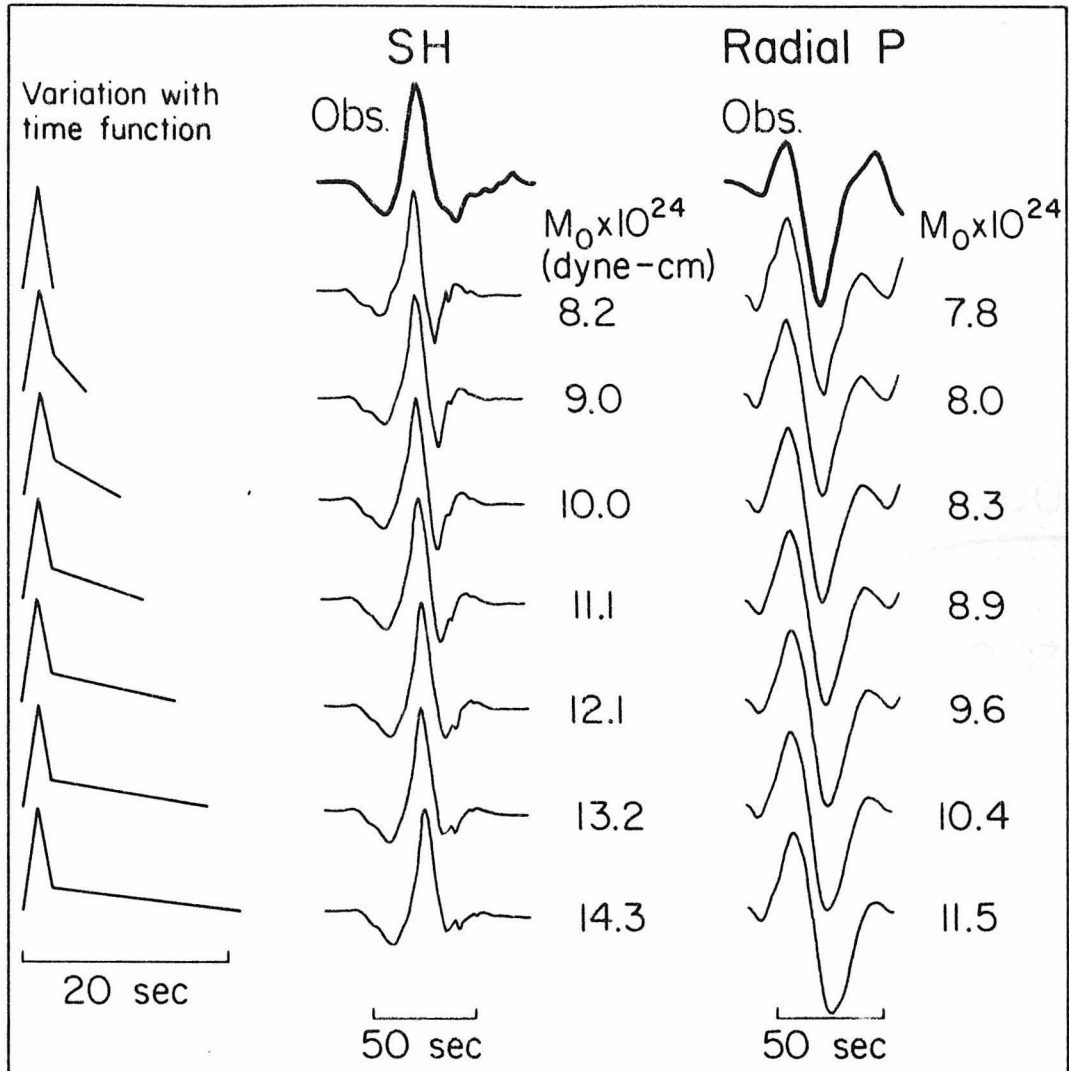


Figure I.1.16 The sensitivity of the SH and radial P synthetics to variations in the duration of the Oroville source time function is illustrated. The SH and radial P synthetics in the center and right columns, respectively, were generated for a rake of  $-70^\circ$  and convolved with the time function in the left column. The calculated seismic moment is noted at the right of each synthetic.

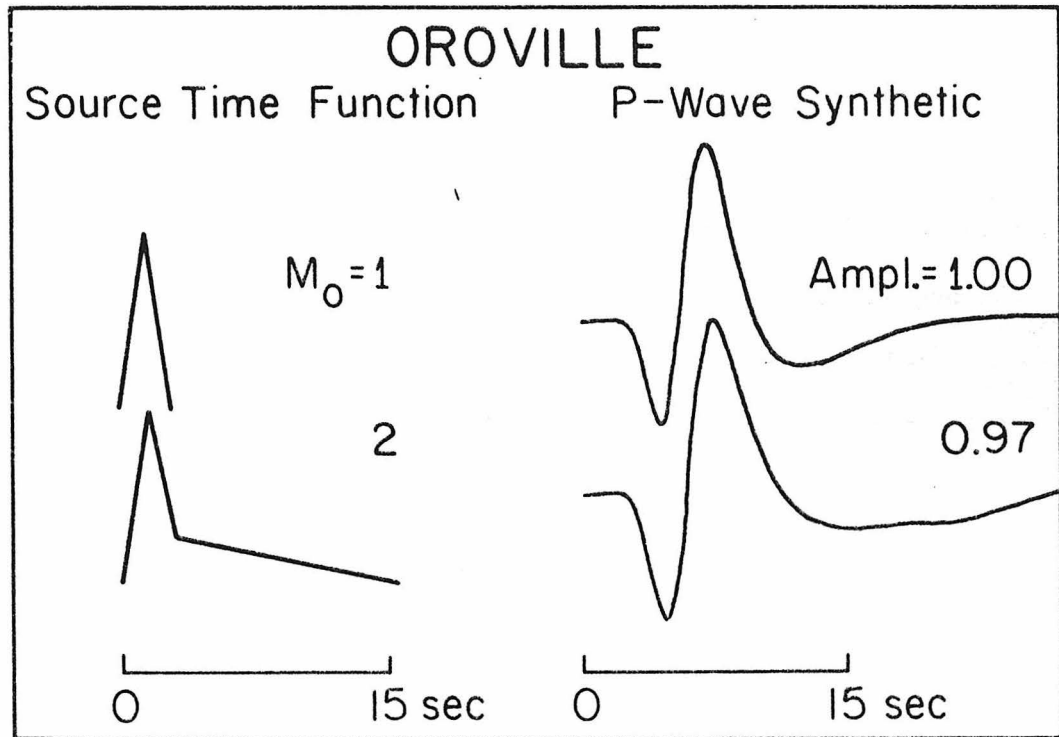


Figure I.1.17 The sensitivity of the Oroville teleseismic P wave synthetic to a variation in the source time function. The upper time function was used in the body wave analysis. The lower time function has twice the moment of the upper time function, yet yields a nearly identical synthetic.

is 15% greater for the 3 second time function than the 15 second time function, but this amplitude will trade off with minor changes of dip on the fault. The insensitivity of the synthetics to the 12 second "tail" on the three second triangle is in part due to the source mechanism of the Orville event. The surface reflections pP and sP are opposite in polarity and combine to be about the same amplitude as the direct P. Thus in summing these three rays a cancellation effect takes place which hides the excess moment.

The implication of Figure I.1.17 is fairly straightforward. The waveforms of the Oroville P waves are insensitive to extended duration components of the Oroville source time function. If the 15 second extended time function were used in the moment determination for Oroville, a seismic moment of  $1.3 \pm 0.4 \times 10^{25}$  dyne-cm. would result; a value in reasonable agreement with the surface wave moment. Naturally, the shape of the "tail" on the three second time function is unconstrained. The model illustrated in Figure I.1.16 was chosen for simplicity of parameterization and is not a unique example. Nevertheless, these results imply that due to considerable uncertainty in the Oroville far-field time function, the body wave moment could easily be a factor of two greater than the initial determination which assumed a three second time function.

#### ULTRA LONG PERIOD BODY WAVE SUMMARY

The analysis of the regional body waves on the Pasadena ultra-long period seismograph has shed some additional light on the discrepancy between teleseismic body wave and surface wave moments for the

Oroville earthquake. The radial P and SH arrivals on the seismograms are modeled quite well using a simple one layer crust over a mantle half-space. Synthetic radial P and SH generated for the Oroville teleseismic body wave source model yield seismic moments which are in good agreement with the teleseismic body wave determination. This result indicates that the ultra-long period body waves do not require an anomalously large moment for the Oroville earthquake that appears to be necessary from the surface wave analysis. However, uncertainties in the source parameters and time function of the earthquake exist which allow for a reasonable reconciliation of the various moment determinations.

The source depth, and fault dip and strike were well constrained by the body wave analysis and the aftershock data. A source rake between  $-70^\circ$  and  $-80^\circ$  (a small left lateral component) provided the best fit to teleseismic SH and SV data, but an additional uncertainty of  $5^\circ$  would easily be allowed. This  $5^\circ$  uncertainty can increase the apparent moment of the ultra-long period body waves by 50%.

The effect of extending the duration of the body wave source time function was considered. These extended duration sources increased the apparent moments of the radial P and SH and actually yield somewhat better fits to the SH arrival. The teleseismic P waveforms are shown to be insensitive to a 12 second "tail" appended to the three second triangle used in the body wave moment determination. However, recomputing the body wave moment for the extended source time function increases the determination by a factor of two.

Allowing for the uncertainty in the rake and including a twelve second tail on the three second triangular time function, we obtain

the following moment estimates for the Oroville earthquake: surface waves,  $1.9 \times 10^{25}$  dyne-cm; teleseismic body waves,  $1.3 \pm 0.4 \times 10^{25}$  dyne-cm; radial P,  $1.3 \times 10^{25}$  dyne-cm.; SH,  $1.8 \times 10^{25}$  dyne-cm. These moment determinations may be considered to agree adequately.

In conclusion, the ultra-long period body waves do not demand an anomalously large moment for the Oroville earthquake. However, an extended duration time function can reconcile the moment estimates from the various data sets, yielding moments fairly comparable to the surface wave determination. This extended duration time function is consistent with the hypothesis proposed in the surface wave discussion of slow deformations associated with the Oroville earthquake.

REFERENCES

- Ben Menahem, A., M. Rosenman, and D. G. Harkrider (1970). Fast evaluation of source parameters from isolated surface-wave signals, Bull. Seism. Soc. Am., 60, 1337.
- Bufe, C. G., F. W. Lester, K. M. Lahr, L. C. Seekins, T. C. Hanks (1976). Oroville earthquakes: normal faulting in the Sierra Nevada foothills, Science, 192, 72.
- Carpenter, E. W. (1966). Absorption of elastic waves - An operator for a constant Q mechanism, AWRE Report O-43/66, H. M. Stationery Office.
- Eaton, J. P. (1966). Crustal structure in northern and central California from seismic evidence, Calif. Div. Mines and Geol., Bull. 190, 419.
- Futterman, W. I. (1962). Dispersive body waves, J. Geophys. Res. 67, 5279.
- Heaton, T. H. (1978). Generalized Ray Models of Strong Ground Motion, Ph.D. Dissertation, Calif. Inst. of Tech., Pasadena, Ca.
- Heaton, T. H. and D. V. HelMBERGER (1978). Predictability of strong ground motion in the Imperial Valley: Modeling the M 4.9, November 4, 1976 Brawley earthquake, Bull. Seism. Soc. Am., 68, 31.
- HelMBERGER, D. V. (1974). Generalized ray theory for shear dislocations, Bull. Seism. Soc. Am., 64, 45.
- HelMBERGER, D. V., and G. R. Engen (1974). Upper mantle shear structure, J. Geophys. Res. 79, 4017.
- HelMBERGER, D. V. and S. D. Malone (1975). Modeling local earthquakes as shear dislocations in a layered half-space, J. Geophys. Res. 80, 4881.

- HelMBERGER, D. V. and D. G. Harkrider (1978). Modeling earthquakes with generalized ray theory.
- Kanamori, H., (1970). Synthesis of long period surface waves and its application to earthquake source studies - Kurile Island earthquake of October 13, 1963, J. Geophys. Res. 75, 5011.
- Kanamori, H., and G. S. Stewart (1976). Mode of the strain release along the Gibbs Fracture Zone, Mid-Atlantic Ridge, Phys. Earth Planet. Int., 11, 312.
- Lahr, K. M., J. C. Lahr, A. G. Lindh, C. G. Bufe, and F. W. Lester (1976). The August 1975 Oroville earthquakes, Bull Seism Soc Am., 66, 1085.
- Langston, C. A. (1976). A body wave inversion of the Koyna, India, earthquake of 10 December 1967 and some implications for body wave focal mechanisms, J. Geophys. Res., 81, 2517.
- Langston, C. A., and D. V. HelMBERGER (1975). A procedure for modeling shallow dislocation sources, Geophys. J. R. astr. Soc. 42, 117.
- Morrison, P., B. Stump, and R. Uhrhammer (1976). The Oroville earthquake sequence of August 1975, Bull. Seism. Soc. Am., 66, 1065.
- Ryall, A., and J. D. VanWormer (1975). Field study of the August 1975 Oroville earthquake sequence, Trans. Am. Geophys. Union 56, 1023.
- Savage, J. C. (1966). Radiation from a realistic model of faulting, Bull. Seism. Soc. Am., 56, 577.
- Savage, J. C., M. Lisowski, W. H. Prescott, and J. P. Church (1977). Geodetic measurements of deformation associated with the Oroville, California earthquake, J. Geophys. Res., 82, 1667.
- Tsai, Y. B., and K. Aki, (1969). Simultaneous determination of the seismic moment and attenuation of seismic surface waves, Bull. Seism. Soc. Am., 59, 275.

SECTION I.2 THE JULY 27, 1976 TANGSHAN, CHINA EARTHQUAKE - A COMPLEX  
SEQUENCE OF INTRAPLATE EVENTS

ABSTRACT

The Tangshan earthquake ( $M_s = 7.7$ ), of July 27, 1976 and its principal aftershock ( $M_s = 7.2$ ), which occurred fifteen hours following the main event, resulted in the loss of life of over 650,000 persons in north-east China. This is the second greatest earthquake disaster in recorded history, following the 1556 Shensi Province, Chinese earthquake in which at least 830,000 persons lost their lives. Detailed analyses of the teleseismic surface waves and body waves are made for the Tangshan event. The major conclusions are: (1) The Tangshan earthquake sequence is a complex one, including strike-slip, thrust, and normal-fault events. (2) The main shock, as determined from surface waves, occurred on a near vertical right-lateral strike-slip fault, striking  $N40^\circ E$ . (3) A seismic moment of  $1.8 \times 10^{27}$  dyne-cm is obtained. From the extent of the aftershock zone and relative location of the main shock epicenter, symmetric (1:1) bilateral faulting with a total length of 140 km may be inferred. If a fault width of 15 km is assumed, the average offset is estimated to be 2.7 meters with an average stress drop of about 30 bars. (4) The main shock was initiated by an event with a relatively slow onset and a seismic moment of  $4 \times 10^{26}$  dyne-cm. The preferred fault plane solution, determined from surface wave analyses, indicates a strike  $220^\circ$ , dip  $80^\circ$ , and rake  $-175^\circ$ . (5) Two thrust events follow the strike-slip event by 11 and 19 seconds respectively. They are located south to south-west of the initial event and have a total moment of  $8 \times 10^{25}$  dyne-cm. This

sequence is followed by several more events. (6) The principal after-shock was a normal-fault double event with the fault planes unconstrained by the P-wave first motions. Surface waves provide additional constraints to the mechanism to yield an oblique slip solution with strike N120°E, dip 45°SW, and rake -30°. A total moment of  $8 \times 10^{26}$  dyne-cm is obtained. (7) The triggering of lesser thrust and normal faults by a large strike-slip event in the Tangshan sequence has important consequences in the assessment of earthquake hazard in other complex strike-slip systems like the San Andreas.

#### INTRODUCTION

The Tangshan earthquake which occurred in north-east China on July 27, 1976 -- origin time  $19^{\text{h}}42^{\text{m}}54.6^{\text{s}}$  U.T.; location 39.6°N, 118.0°E (U.S.G.S.);  $M_s = 7.7$ ;  $m_b = 6.3$  (U.S.G.S.) -- stands in terms of loss of life as the greatest earthquake disaster of modern times. The Times (London) reported on January 6, 1977 an estimate from the People's Republic of China of over 650,000 killed. The city of Tangshan with a population of 1.6 million was virtually destroyed and extensive damage was suffered throughout the densely populated surrounding region. Indeed, Chairman Hua Kuo-Feng has said that the earthquake caused death and destruction on a scale "rarely seen in history" (The Times, January 6, 1977). Without diminishing the significance of these event in human terms, the Tangshan earthquake stands unique as the largest continental intraplate earthquake since the establishment of the World Wide Standardized Station Network (WWSSN). The availability of this data affords us a special opportunity to gain insight into the tectonic processes of this class of earthquake. This varied importance of the Tangshan earthquake sequence merits

a detailed seismological study of its faulting mechanism. Some local and regional studies of this event have been published in the Chinese literature: Qiu Qun, 1976; Zhu Chuan-zhen et al., 1977; Guo Shunmin et al., 1977; Ding Wenjing, 1978; Chen Pei-shan et al., 1978. This paper shall primarily be concerned with the following: (1) The analysis of available teleseismic data to obtain source parameters for the main event and principal aftershock. (2) The complexity of the earthquake sequence and its implications for intraplate earthquake processes. (3) Reasons for the enormously high casualties and destruction.

In this study long-period surface waves are analyzed to constrain the overall faulting parameters and seismic moments of the main shock and its principal aftershock. Teleseismic body waves are used to detail the faulting process. Japanese P-wave first motions (Katsumata, personal communication, 1976), are incorporated to provide additional regional control.

#### Seismological Data

The location of the main shock and the distribution of aftershocks are plotted in Figure I.2.1. The open and closed circles indicate aftershocks occurring before and after, respectively, the principal aftershock. The main aftershock, an  $M_s = 7.2$  event, occurred fifteen hours following the main shock. Locations are taken from the U.S.G.S.

P-wave first motion data for the main event are plotted in Figure I.2.2. The dashed line solution is chosen to best constrain the first motion data. The solid line solution represents the best solution to the surface-wave data. The surface-wave solution is more nearly consistent with the solution obtained by the local Chinese stations (Qiu Qun, 1976). First motion data for the principal aftershock are plotted

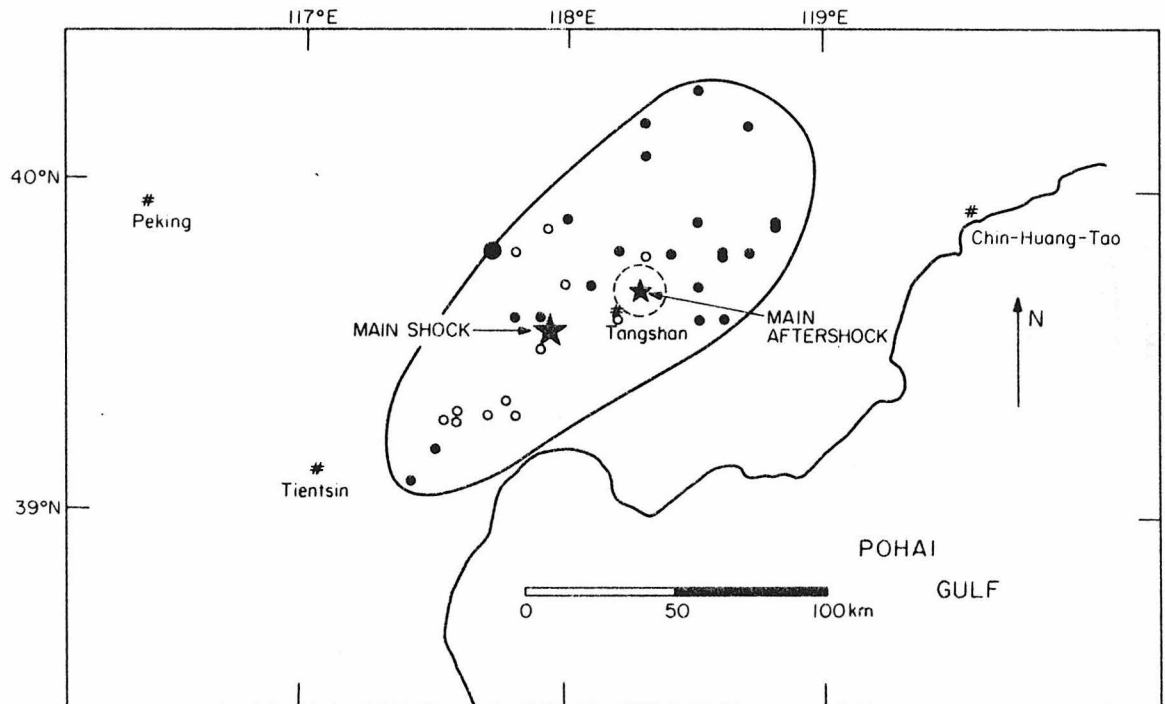


Figure I.2.1 A map of the main shock, main aftershock and other aftershock locations (U.S.G.S.). The open and closed circles are aftershocks which occurred before and after, respectively, the principal aftershock.

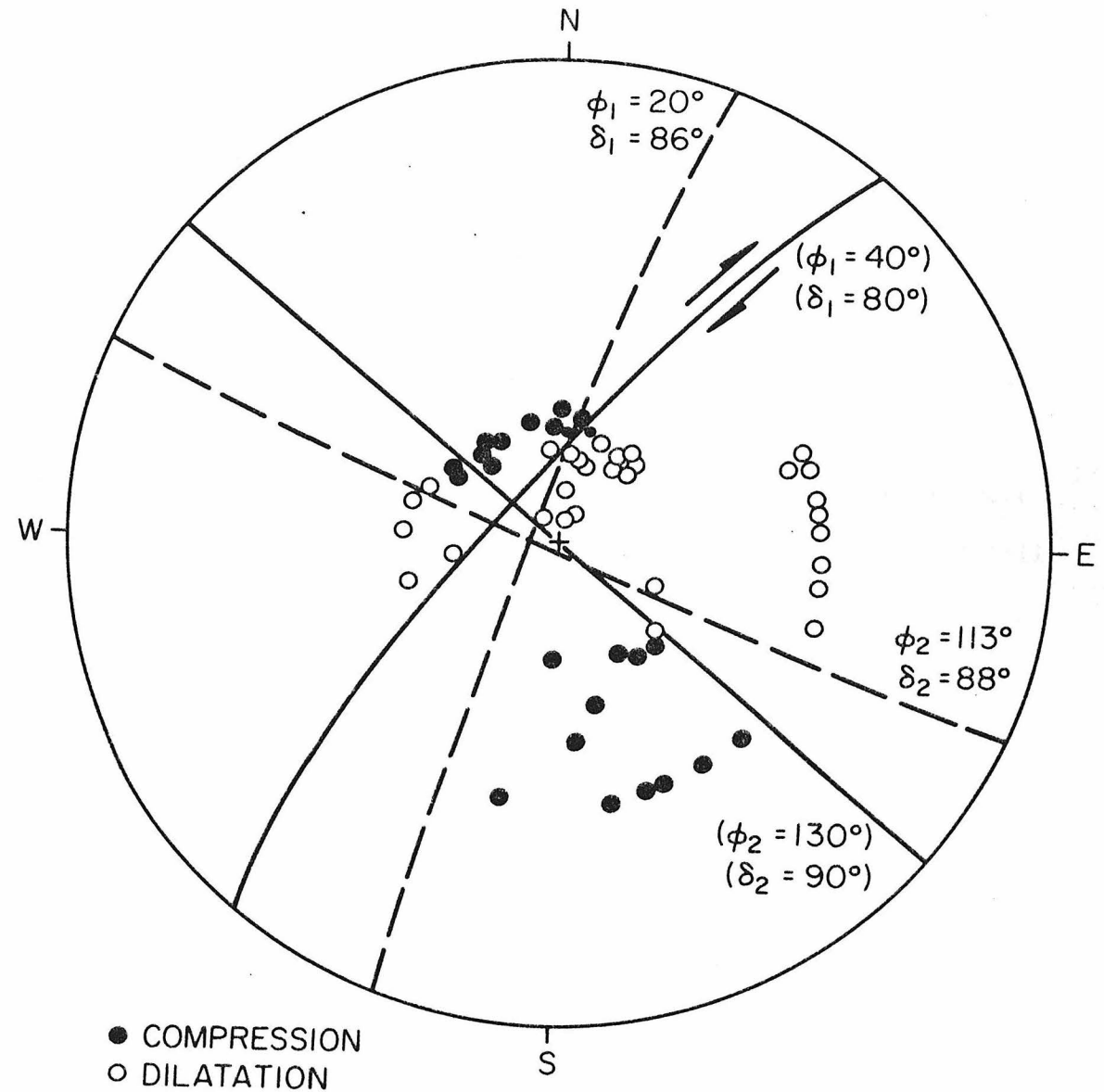


Figure I.2.2 The P-wave first motion data for the main shock of the Tangshan earthquake sequence. The dashed lines indicate the preferred first motion solution. The solid lines represent the best solution to the surface wave data. An equal area projection of the lower focal hemisphere is shown. The arrows indicate right-lateral strike-slip motion of the preferred fault plane of N40°E.

in Figure I.2.3. As all stations are dilatational, there is no constraint to the normal fault solution from the P-wave first motion data alone. The solution indicated is constrained by the surface-wave analysis.

Figure I.2.4 shows surface waves G3 (Love waves) and R3 (Rayleigh waves) for the main shock recorded by WSSN long-period seismographs and equalized to a propagation distance of  $360^\circ + 90^\circ$ . Surface waves G2 and R2 for the principal aftershock, equalized to a propagation distance of  $270^\circ$ , are shown in Figure I.2.5. The equalization procedure is described by Kanamori (1970). As short period ( $T \geq 40$  seconds) surface waves are severely affected by structural heterogeneities during propagation, these waves are removed by using a filter described in Kanamori and Stewart (1976) with a short period cut-off at 40 seconds and a long period roll-off at 300 seconds. The Love and Rayleigh waves for the main event indicate a four-lobed radiation pattern which is consistent with a shallow strike-slip mechanism. However, from the nodal directions, a faulting orientation with a strike of  $N40^\circ E$  is preferred, slightly rotated with respect to the preferred P-wave first motion solution. This will be discussed in the body wave analysis section. For the major aftershock the surface wave radiation is consistent with a dip-slip faulting solution: a four-lobed Love wave and two-lobed Rayleigh wave pattern (see Kanamori, 1970). A strike of  $N120^\circ E$  may be inferred from the nodal directions in the surface waves. The location and strike of this event with respect to a local northwest-southeast trending structural boundary observed on Tectonic Map of China (Geological Science Research Institute of China, 1975) are suggestive of a causal association.

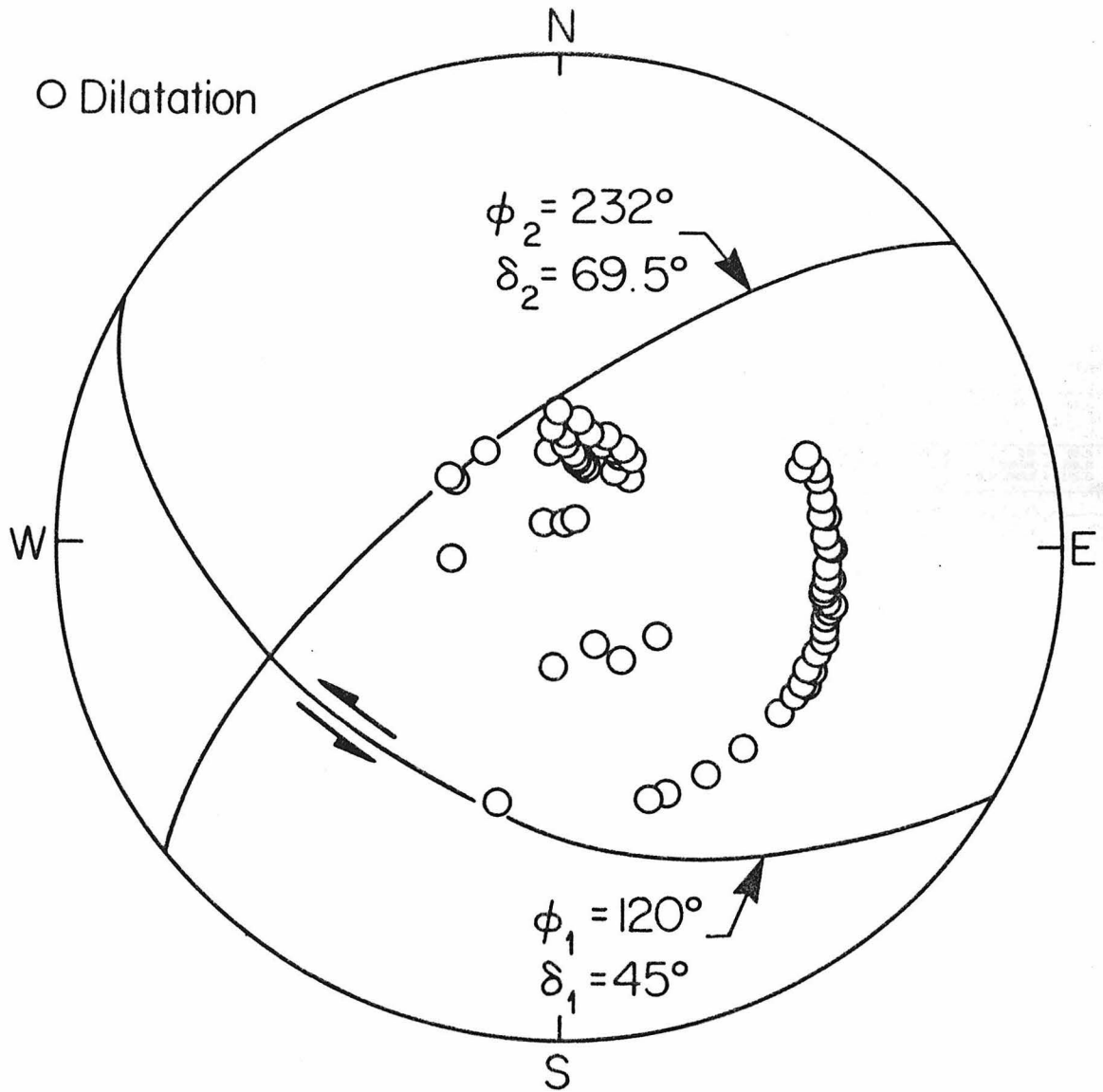


Figure I.2.3 The P-wave first motion data for the principal aftershock of Tangshan sequence. All stations registered a dilatational arrival. The solution shown, constrained by the surface wave data, indicates oblique normal faulting.

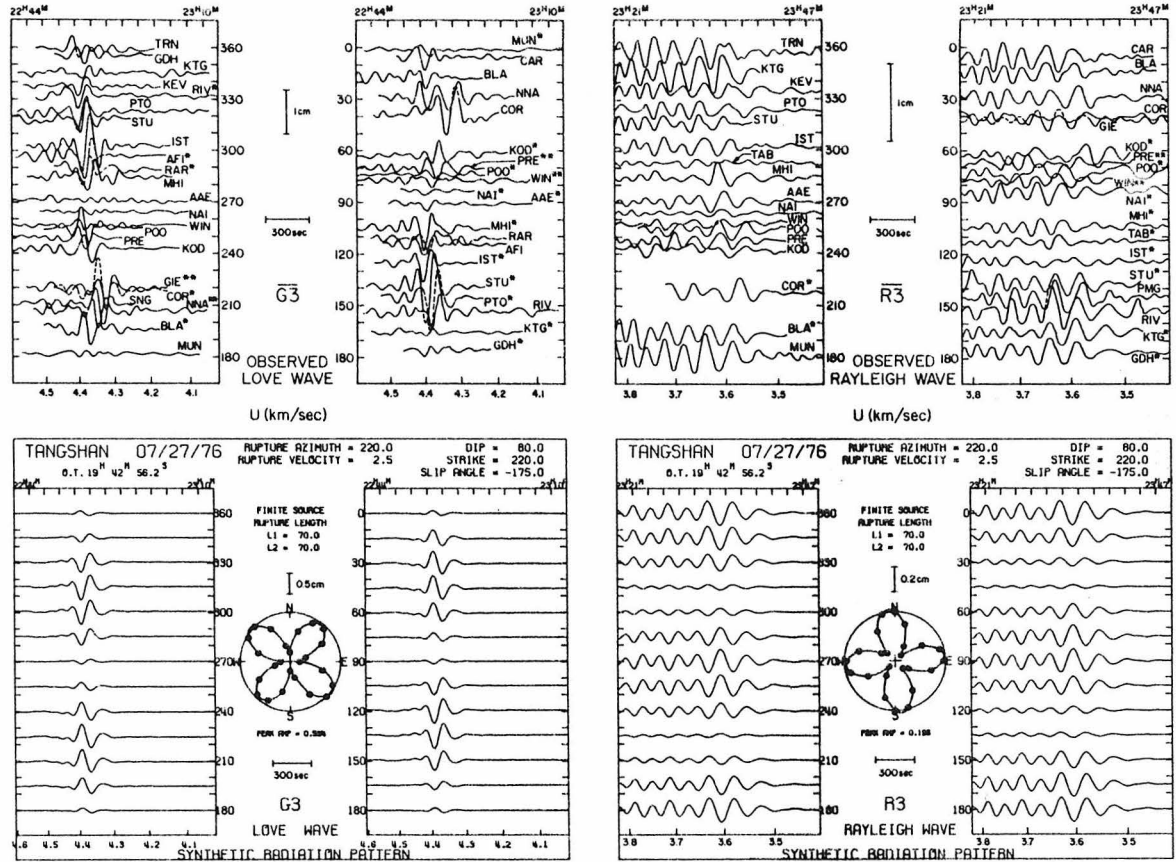


Figure I.2.4 Azimuthal plots of equalized seismograms for R3 and G3 and synthetic seismograms computed for the main shock of the Tangshan sequence. A source seismic moment  $10^{27}$  dyne-cm is used in the synthesis. In the observed patterns one asterisk indicates the R2 or G2 data were equalized to R3 or G3 distances. Two asterisks indicate the R4 or G4 were equalized to R3 or G3 distances. The amplitude scale is for the trace amplitude on the WWSSN long period instrument (15-100) with a magnification of 1500.

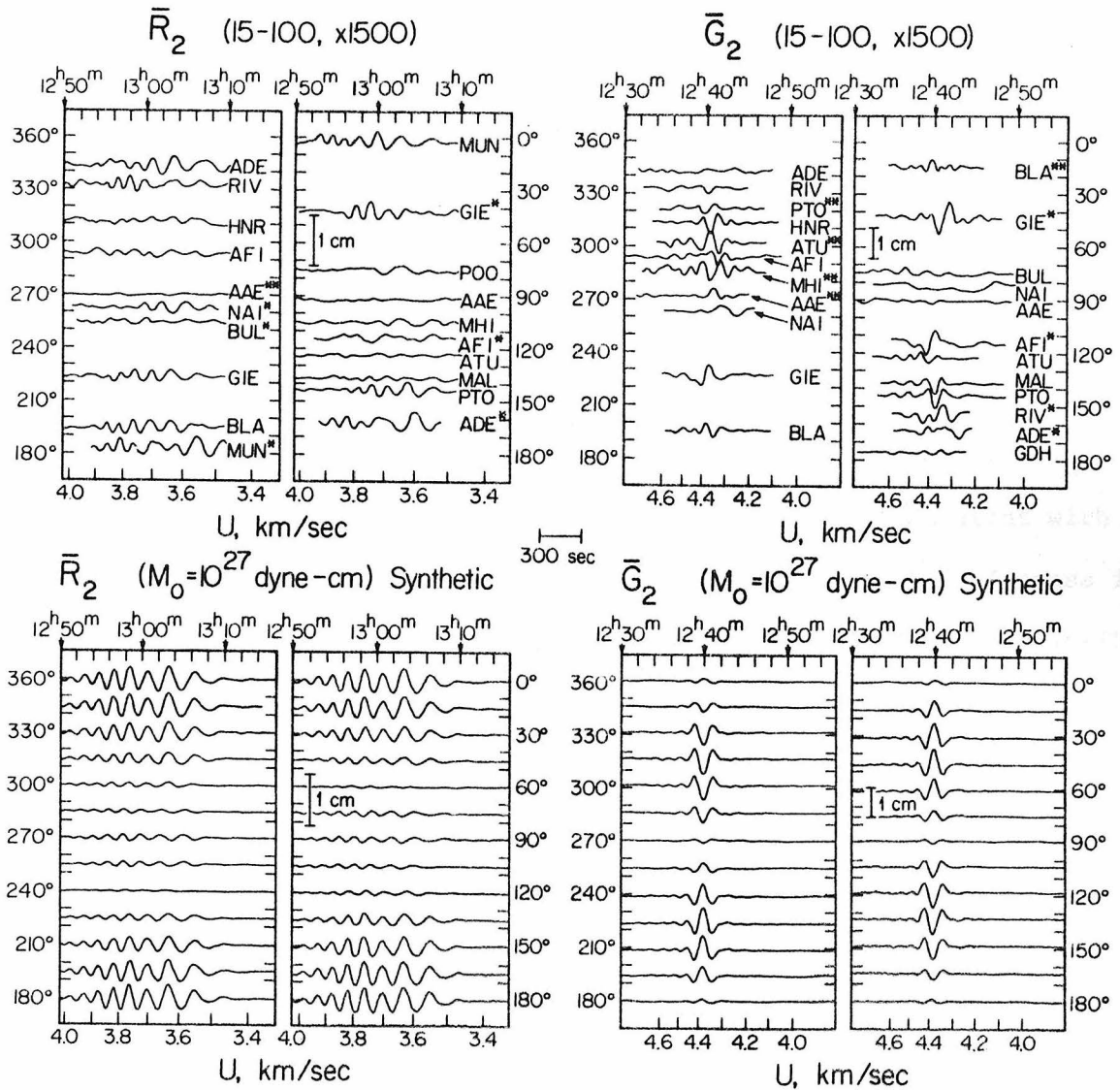


Figure I.2.5 Azimuthal plots of equalized seismograms for R2 and G2 and synthetic seismograms computed for the principal aftershock of the Tangshan sequence. A source seismic moment of  $10^{27}$  dyne-cm is used in the synthesis. In the observed patterns one asterisk indicates that R1 or G1 data were equalized to R2 or G2 distances. Two asterisks indicate that R3 or G3 were equalized to R2 or G2 distances. The amplitude scale is for the trace amplitude on the WWSSN long period instrument (15-100) with a magnification of 1500.

### Surface Wave Analysis

The general pattern of the surface wave radiation for the main event, as seen in Figure I.2.4, is consistent with the strike-slip solution determined from P-wave first motions, with the addition of a small rotation in strike. The geometry of the aftershock zone and the location of the epicenter suggest a northeast trending bilateral fault. Synthetic surface waves were computed for a double-couple at 16 km depth for a fault geometry with a strike  $220^\circ$ , dip  $80^\circ$ , and slip angle  $-175^\circ$  (sign conventions are given in Kanamori and Stewart, 1976). The method of synthesis, the velocity and Q structure are described in Kanamori (1970) and Kanamori and Cipar (1974). To be consistent with the aftershock distribution, a small correction for fault finiteness is included assuming a symmetric bilateral rupture 140 km in length striking  $220^\circ$  with a rupture velocity of 2.5 km/sec (Ben-Menahem, 1961). The filter used on the observed data is also applied to the synthetics to allow direct comparison. The computed synthetics are shown in Figure I.2.4 beneath the observations. In Figure I.2.6 the maximum trace amplitudes of the observed and synthetic records are compared. Using a seismic moment of  $1.8 \times 10^{27}$  dyne-cm, a quite satisfactory fit to the observation is obtained.

To model the surface waves for the principal aftershock, we assume a double-couple at a depth of 16 km, striking  $N120^\circ E$  with a  $45^\circ$  dip. The slip angle is varied to find the best fit to the observed amplitude ratio between the Rayleigh and Love waves. A slip angle  $\gamma = -30^\circ$  provides a satisfactory match. Although the effect is minor and probably not observable in the data, source finiteness is included for the sake of complete-

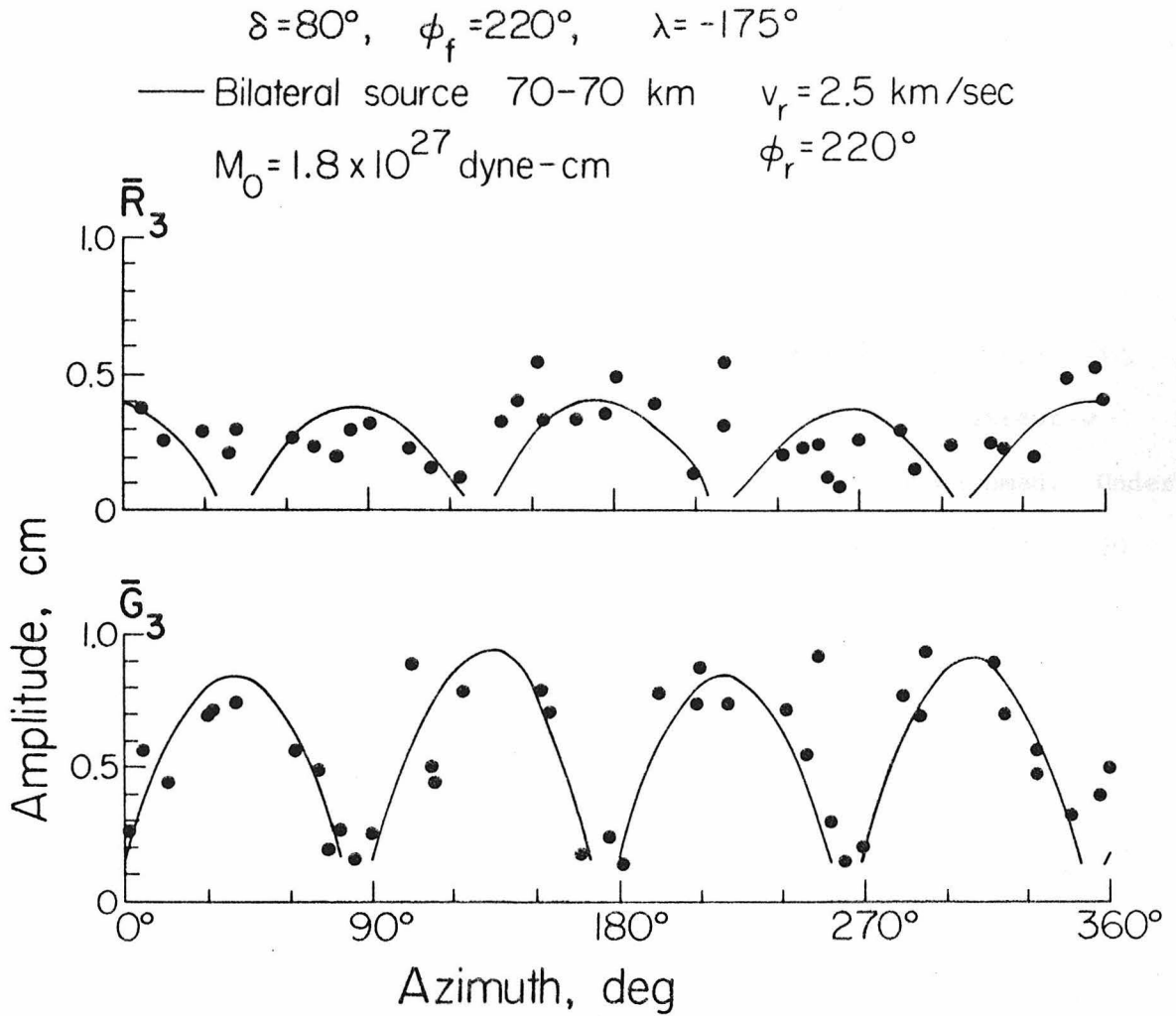


Figure I.2.6 Equalized station peak-to-peak amplitudes for observed R3 and G3 data from the main event in the Tangshan sequence. The data (solid circles) are plotted as a function of azimuth. The curve represents the fault model used in this study.

ness to fit the relation of the principal aftershock's epicenter to the overall width of the Tangshan aftershock zone. A bilateral fault (35 km: 15 km) striking at  $120^\circ$  with a rupture velocity of 2.5 km/sec is assumed. Synthetic Rayleigh and Love waves are shown beneath the observations in Figure I.2.5. The maximum trace amplitude of the observations are compared in Figure I.2.7 to the synthetics. Assuming a seismic moment of  $8 \times 10^{26}$  dyne-cm, a reasonably good fit is obtained.

Although details of the extent of faulting have not been released by the Chinese government, rough estimates of the average dislocation  $\bar{D}$  and stress drop  $\Delta\sigma$  may be made. A fault length  $L = 140$  km for the main event can be assumed from the aftershock zone. The vertical extent  $w$  is unknown, but for illustrative purposes  $w = 15$  km may be assumed. Under these assumptions we have  $\bar{D} = M_0 / \mu L w = 2.7$  meters and  $\Delta\sigma = 2\mu\bar{D} / \pi w = 30$  bars, where a rigidity  $\mu = 3.5 \times 10^{11}$  dyne/cm<sup>2</sup> is used and the fault is assumed to have broken at the free surface.

### Body Wave Analysis

The analyses of long-period surface waves for the main event and the principal aftershock yield gross fault parameters, but provide no resolution of details concerning the nature and complexity of the faulting process. To obtain this information, an analysis is made of the teleseismic body waves for these events. Figure I.2.8 shows P-wave observations for the main shock. The waveforms are quite complex, but a qualitative description can be made. At the distance range of most of these stations, the only later phase which might interfere with the P-wave train is PcP. However, for a vertical strike-slip fault PcP is

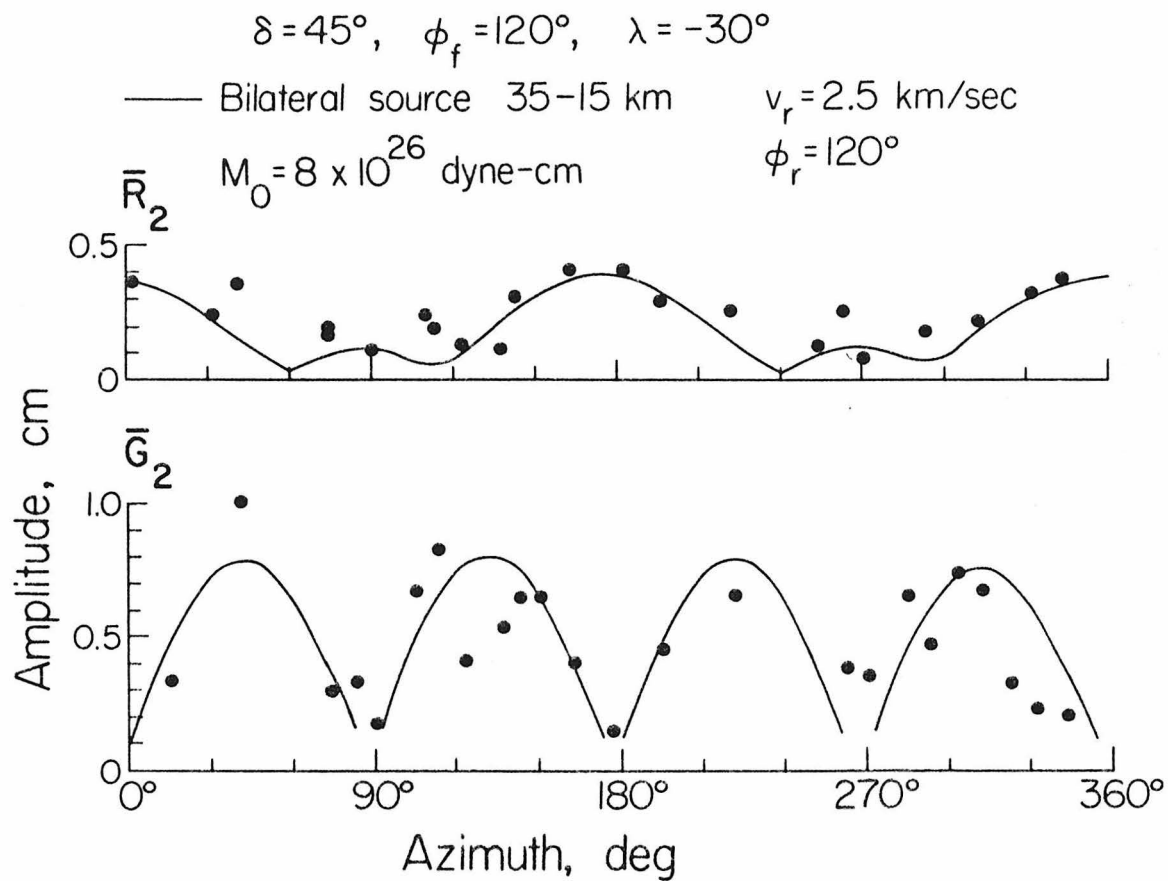


Figure I.2.7 Equalized station peak-to-peak amplitudes for observed R2 and G2 data for the principal aftershock of the Tangshan sequence. The data (solid circles) are plotted as a function of azimuth. The curve represents the fault model used in this study.

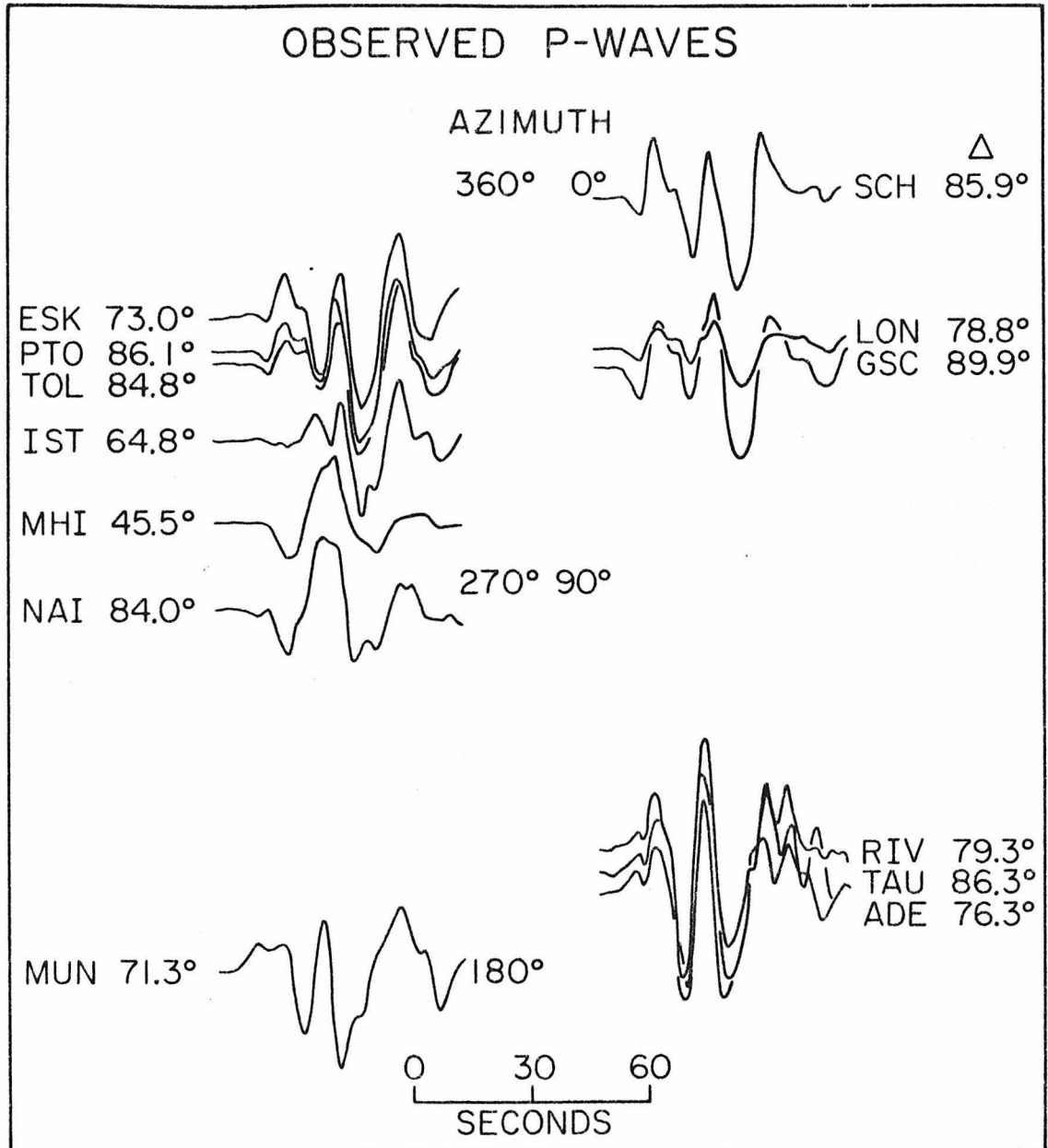


Figure I.2.8 Observed long-period P-waves for the main shock of the Tangshan sequence. The data are plotted as a function of azimuth. The distance in degrees is indicated beside the station name. The amplitudes are corrected for geometric spreading.

always nodal, so that the observed complexity may be ascribed to the source. The initial motion is emergent in nature and reflects the strike-slip solution of the P-wave first motion data. The difference between the teleseismic and local first motion solutions is probably not significant, as strike-slip mechanisms can be quite sensitive to local non-planar structure (see Langston, 1977). A later arrival of much larger amplitude is consistently observed (most dramatically at stations RIV, TAU and ADE). There are two significant peculiarities associated with this arrival: its amplitude does not change sign in the four-lobed manner of vertical strike-slip radiation, and the relative timing of the phase varies with azimuth. These observations suggest that part of the faulting in the main Tangshan sequence was not of a strike-slip nature and occurred away from the main shock epicenter.

A more quantitative description of the source is obtained by attempting to match the observed records by synthetic waveforms. This technique has been successfully applied to other complex events (Burdick and Mellman, 1976; Kanamori and Stewart, 1978; Rial, 1978). To fit the first portion of the records, synthetics were generated for a point double couple with the mechanism of the P-wave first motion solution at a depth of 10 km in a homogeneous half-space. The surface reflections pP and sP were included in the synthetics. The faulting solution obtained by first motions provided a qualitatively good match to the observations. However, stations situated near the nodes (see IST) show significant complexities within the first few seconds that are not observed for stations away from the nodes. This is consistent with the hypothesis suggested above of some lateral heterogeneity within the source region. A triangular source time

function with a rise time of 5.5 sec and fall-off time of 3.25 sec was used to provide an adequate fit to the pulse shape for the non-nodal stations. The seismic moment of this first event is estimated from the average of stations SCH, LON, GSC, RIV, TAU, ADE, and MUN to be  $4 \times 10^{26}$  dyne-cm with 25% uncertainty. This solution is fixed and the next arrivals are modeled. Kanamori and Stewart (1978) successfully fit P-wave seismograms of the 1976 Guatemalan earthquake, a major strike-slip event, by several sources lagged in time and all having identical mechanisms. An attempt to fit the later portion of the P-waves of the Tangshan event with a strike-slip solution was fruitless. The azimuthal variation of the relative timing between the first event and the later arrivals can be accounted for by locating the source of these phases roughly 45 km south to south-southwest of the epicenter of the main event. By body wave inversion (see Burdick and Mellman, 1976; Langston, 1976), and trial and error, a satisfactory fit to the observation was achieved by including two thrust events following the initial strike slip event. The location of these events with respect to the main event is uncertain to approximately 15 km distance and  $30^\circ$  azimuth. The first thrust event occurred roughly 11 seconds after the initial strike-slip source and had a relative seismic moment 5% of the initial event. The second thrust source was three times larger and followed the first thrust event by 8 seconds, or 19 seconds from the initial onset of the earthquake. The resolution of the thrust solutions is poor, but a mechanism with a north-northwest strike and a steep dip to the west helped to fit the somewhat different character of the waveforms in the western azimuths. The sum of the moments of these two events,  $8 \times 10^{25}$  dyne-cm, is a factor of five smaller than the initial strike-slip solution, but the arrivals

from these events dominate the P wave train. This happens because teleseismic P-waves for strike-slip events have take-off angles near the nodes of the radiation pattern, whereas for thrust events the P waves leave near the maximum of the radiation pattern.

Figure I.2.9 shows synthetics and observations for two representative, non-nodal stations. The fits are satisfactory considering the complications in the problem. Further resolution is not worth pursuing for several reasons. Details of the local crustal structure, particularly the sediment cover, are not documented. The surface wave analysis has shown that the overall faulting was basically strike-slip, but due to radiation pattern effects small, presumably triggered, thrust events mask the strike slip radiation. Finally, there is some evidence from first-motions and nodal stations that lateral heterogeneity may affect the waveforms. Figure I.2.10 shows short and long period vertical component records for Goldstone, California (GSC). The arrival times of the three modeled events are indicated on the short period record. The emergent nature of the initial strike-slip solution is clearly seen. The long-period record shows a number of arrivals several minutes after the initial rupture. Presumably a number of these later events are strike-slip, such that the total moment sum of the body waves approaches that of the surface waves, which are sufficiently long period (100-200 seconds) to average over the source complexity. Multiple event rupture in strike-slip earthquakes has been previously observed for the 1967 Caracas earthquake (Rial, 1978) and the 1976 Guatemalan earthquake (Kanamori and Stewart, 1978).

Figure I.2.11 shows several P-waves for the principal aftershock.

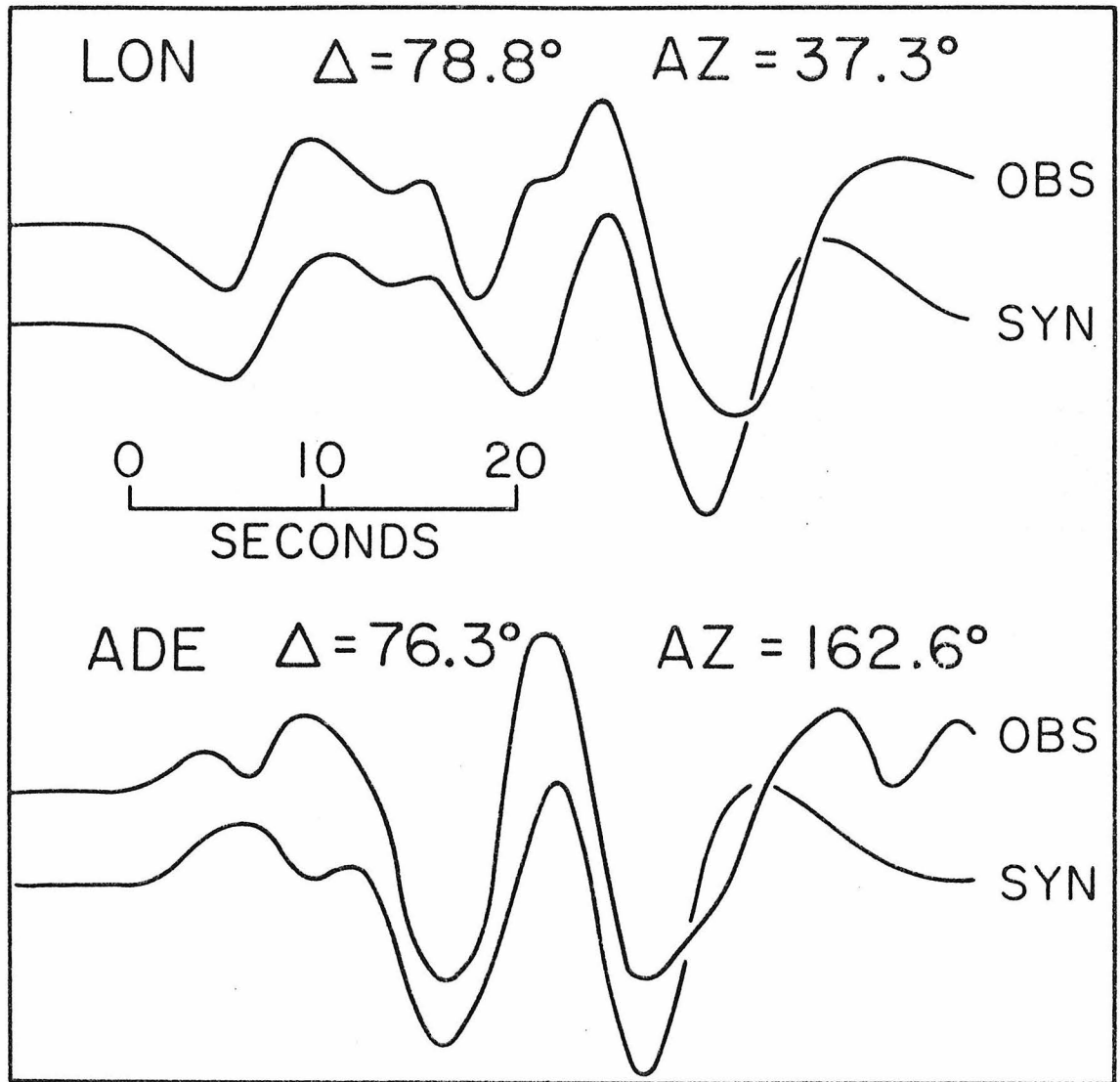


Figure I.2.9 Observed and synthetic long-period P-waves for stations LON and ADE for the main shock of the Tangshan sequence.

GSC Mag = 100K  $\Delta = 89.9^\circ$   
 AZ =  $42.0^\circ$   
 P1 P2 P3 (a)

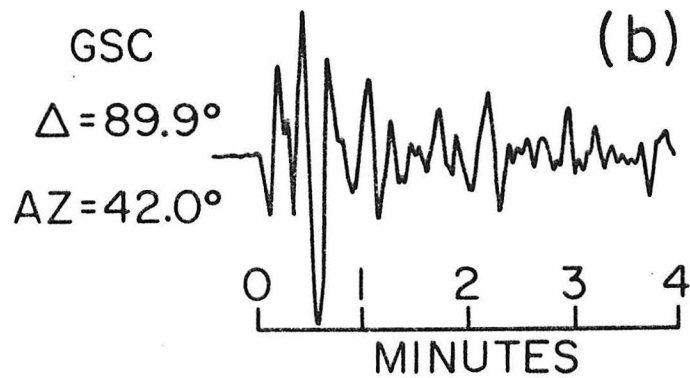
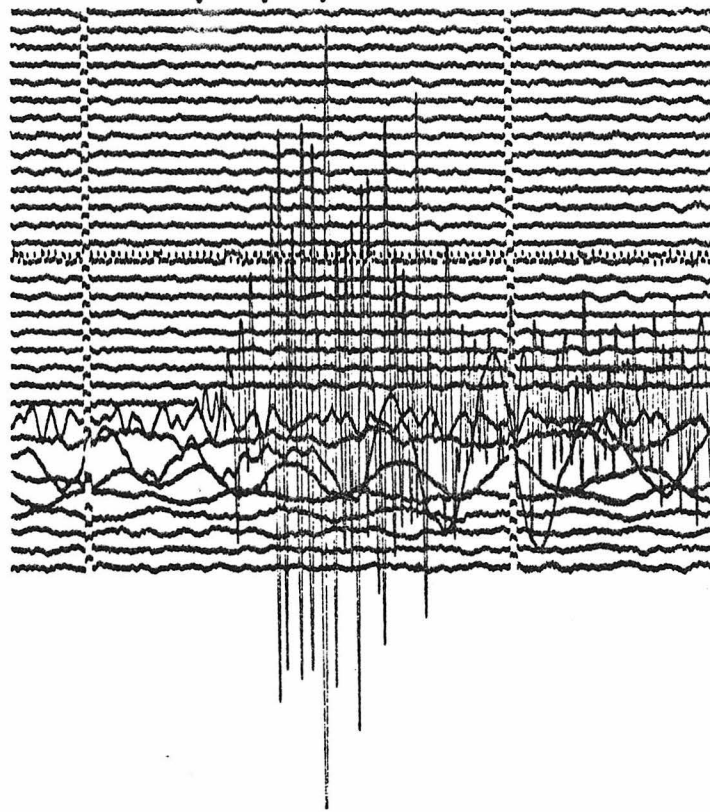


Figure I.2.10 Observed P-waves from the short-period (a) and long-period (b) vertical component seismograms for station GSC at Goldstone, California. The arrows on the short-period record indicate the approximate arrival times of the initial strike-slip shock and the two thrust co-shocks from the main event.

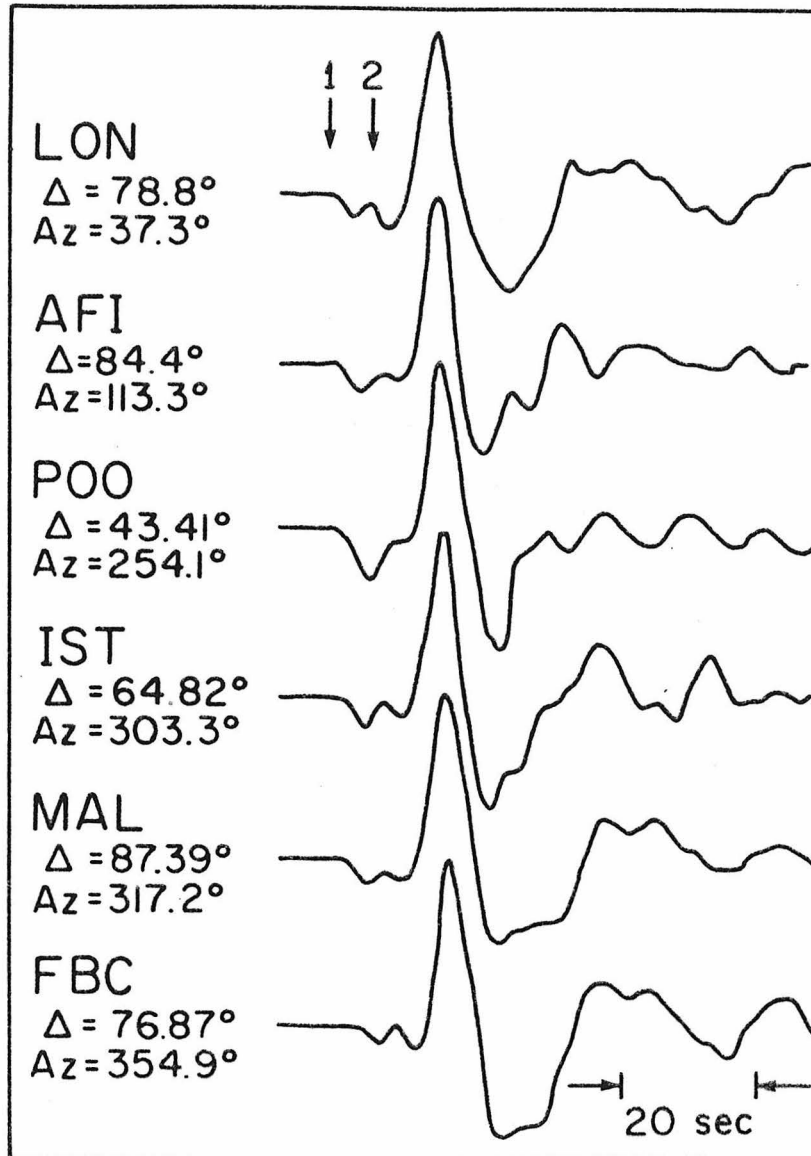


Figure I.2.11 Observed long-period P-waves from the principal aftershock of the Tangshan sequence. The arrows indicate the two shocks of this double event.

The waveforms indicate that the earthquake was a normal faulting double event (see Figure 4 in Langston and HelMBERGER, 1975). Synthetics were generated for the aftershock to attempt to resolve more information of the faulting. The strike and slip angle are not resolvable, but the amplitude ratio of pP to direct P suggests a dip near  $45^\circ$  and a depth of approximately 7 km. These constraints assume that the dip of the two mechanisms is similar. There is some azimuthal variation in the amplitude relationship of the two events, but uncertainties in the radiation pattern and in the effect of crustal structure preclude any judgment as to possible differences between the source mechanisms.

#### DISCUSSION

Incorporating the aftershock data and the surface and body wave analyses, a faulting scenario of the Tangshan sequence is illustrated in Figure I.2.12. The initial rupture begins rather slowly and has a near vertical strike-slip mechanism, striking  $N40^\circ E$ . The rupture propagates in a bilateral fashion northeast and southwest. After roughly ten seconds the readjustment of the local stress system triggers thrusting 45 km south of the epicenter. These events, though small with respect to the overall radiation, are roughly of magnitude  $M_w = 6 \frac{1}{2}$  (Kanamori, 1977). Fifteen hours after the main event sequence a large oblique normal event occurs on a northwest-southeast trending structural boundary. In a simplified view, the system is one of block translation-- motion of the southeastern block produces compression at the southern boundary and extension at the northern boundary.

As the Tangshan event is the largest continental intraplate earth-

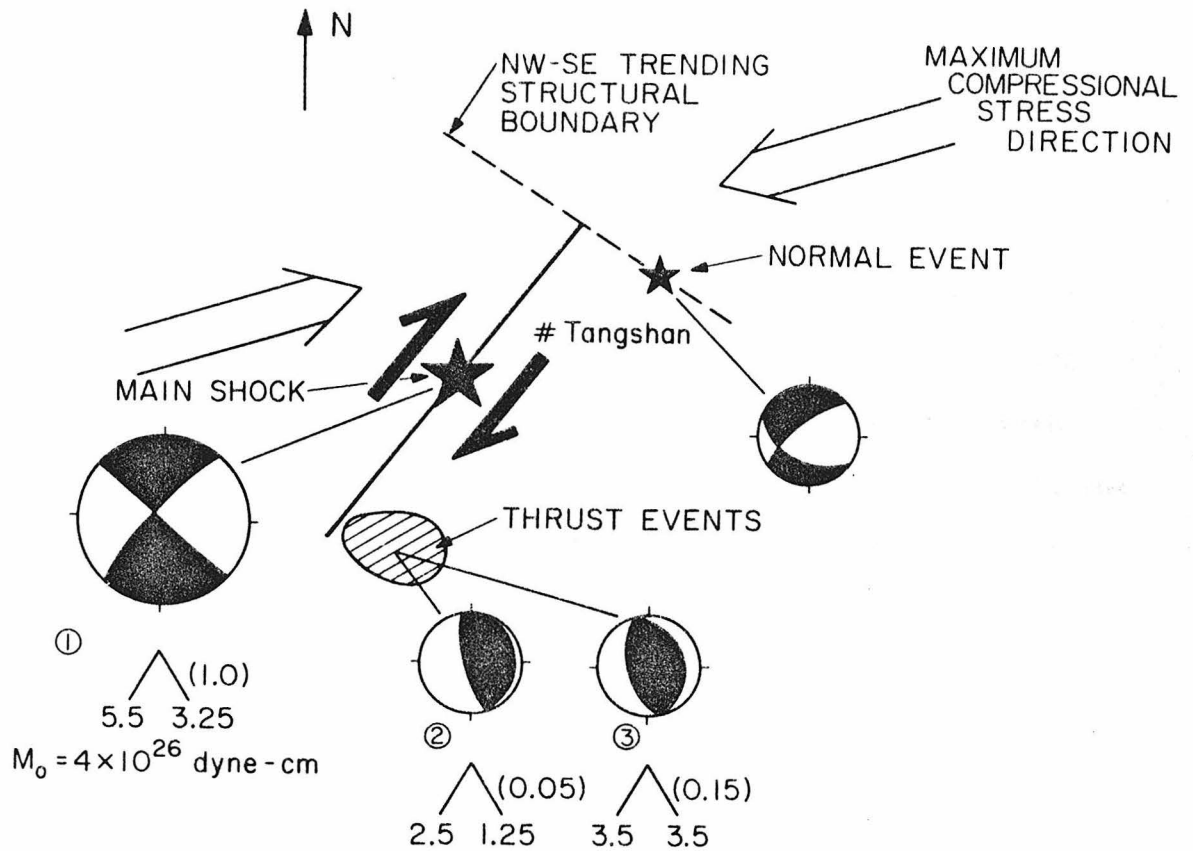


Figure I.2.12 Seismotectonic illustration of the Tangshan earthquake sequence. Rise times and fall-off times for the triangular source time functions used in the body-wave synthetics of the initial strike-slip shock and thrust co-shocks are indicated. The relative moments are shown in parentheses. No body-wave moment or time function was determined for the normal aftershock.

quake since the establishment of the WSSN, it is pedagogically useful to make a comparison with the 1976 Guatemalan earthquake -- the largest continental strike-slip interplate event -- which was studied in detail by Kanamori and Stewart, 1978. The Tangshan event is smaller both in fault length and moment. Assuming shallow faulting ( $w \sim 15$  km) for both events, the average dislocation and stress drop for both events are similar:  $\bar{D} \sim 2$  meters and  $\Delta\sigma \sim 30$  bars. Both events had associated normal faulting. The normal aftershocks of the Guatemala earthquake were minor in size, whereas the large normal aftershock of the Tangshan earthquake was nearly half the size of the main shock. No thrusting was observed to be associated with the Guatemalan earthquake. Both events consist of a number of smaller independent events. Overall, the Tangshan intraplate earthquake sequence with its variety and size of co-shocks and aftershocks is considerably more complicated in nature than the Guatemalan interplate earthquake.

The enormous loss of life and destruction caused by the Tangshan event importunes an understanding of seismological causative factors. Although the nature of the construction practices in the epicentral region are of primary importance and cannot be discussed within the scope of this paper, three seismological factors are considered to have significantly increased the damage potential. The first relates to the overall nature and complexity of the earthquake. Vertical strike-slip earthquakes radiate most of their energy horizontally into the local source region. Small thrust co-shocks enlarged the region of high local intensities. The principal aftershock fifteen hours following the main event was exceptionally large and probably destroyed most structures

which were weakened but survived the main shock.

A second seismological factor contributing to the destructiveness of the Tangshan sequence is the effect of the local geology on seismic energy release. The epicentral region of the Tangshan event is an area of sedimentary cover. The thickness of these sediments is not known; however, studies have shown that even moderate thicknesses of sediments effectively amplify seismic intensities relative to nearby bedrock (Gutenberg, 1956, 1957; Borchardt, 1970). Sedimentary basin structures can also trap and focus the seismic energy (Hong and HelMBERGER, 1978). The effects of sedimentary cover, though man-made land fill, were dramatically observed in the 1906 San Francisco earthquake. In the "Report of the State Earthquake Investigation Commission" on the 1906 event H. O. Wood (1908) concluded in his discussion of the damage in San Francisco that "...the amount of damage produced by the earthquake...depended chiefly upon the geological character of the ground. Where the surface was solid rock, the shock produced little damage; whereas upon made land great violence was manifested..."

A third seismological consideration is with respect to the characteristic fall-off of intensity of shaking with distance in the region. This characteristic fall-off varies significantly, specifically exemplified in the United States. In the older eastern United States small earthquakes are felt over a much larger area than the tectonic, younger west. Consequently, earthquakes of a given magnitude tend to be more damaging in the east than the west. The reasons for this phenomenon are not clearly understood, but are probably related to the attenuative properties of the crust and mantle. It is likely that the intensity fall-off character-

istics of northeast China are more akin to those of the stable continental eastern United States than the basin and range, tectonic environment of the west. Thus, the region of severe damage for the Tangshan event was probably much larger than would have been true for a similar event on the San Andreas system in California.

#### CONCLUSION

The Tangshan earthquake and its principal aftershock represent a complex intraplate event sequence with strike-slip, normal, and thrust faulting. The main shock was a bilateral strike-slip event, striking north  $40^\circ$  east. Associated thrusting events occurred south of the main shock epicenter concurrently with the main rupture. The principal aftershock was an oblique normal double event, striking approximately perpendicular to the main shock. The seismic moment of the main event was  $1.8 \times 10^{27}$  dyne-cm; the moment for the principal aftershock was  $8 \times 10^{26}$  dyne-cm. The complexity of the sequence contrasts the intraplate Tangshan event with the large interplate Guatemala earthquake.

REFERENCES

- Ben Menahem, A. (1961). Radiation of seismic surface waves from finite moving sources, Bull. Seismol. Soc. Am., 51, 401-435.
- Borcherdt, R. D. (1970). Effects of local geology on ground motion near San Francisco Bay, Bull. Seismol. Soc. Am., 60, 29-61.
- Burdick, L. J. and G. R. Mellman (1976). Inversion of the body waves from the Borrego Mountain earthquake to the source mechanism, Bull. Seismol. Soc. Am., 66, 1485-1499.
- Chen Pei-shan et al., (1978). The Stress Field of the Peking - Tientsin - Tangshan - Zhangjiakon Area Before and After the Tangshan Earthquake of July 28, 1976. Acta Geophysica Sinica, Vol. 21, No. 1, p. 57.
- Ding Wenjing (1978). Distribution Characteristics and Migration Regularity of Strong Aftershock of Tangshan Earthquake. Scientia Geologica Sinica, 1978, No. 1, p. 72.
- Geological Science Research Institute of China (1975), Tectonic Map of China, printed by Map Publication Service, China (available from New China Book Store, Peking, China).
- Guo Shunmin, et al., (1977). Discussion of the Regional Structural Background and the Seismogenic Model of the Tangshan Earthquake. Scientia Geologica Sinica, 1977, No. 4, p. 321
- Gutenberg, B. (1956). Effects of ground on shaking in earthquakes, Transactions, A.G.U., 37, 757-760.
- Gutenberg, B. (1957). Effects of ground on earthquake motion, Bull Seismol. Soc. Am., 47, 221-250.
- Hong, T.-L. and D. V. Helmberger (1978). Glorified optics and wave propagation in non-planar structure, Bull. Seismol. Soc. Am., in press.

- Kanamori, H. (1970). Synthesis of long-period surface waves and its application to earthquake source studies, Kurile Islands earthquake of October 13, 1963, J. Geophys. Res., 75, 5011-5027.
- Kanamori, H. and J. J. Cipar (1974). Focal process of the Great Chilean earthquake May 22, 1960, Phys. Earth Planet. Int., 9, 128-136.
- Kanamori, H. and G. S. Stewart (1976). Mode of the strain release along the Gibbs fracture zone. Mid-Atlantic Ridge, Phys. Earth Planet. Int., 11, 312-332.
- Kanamori, G. and G. S. Stewart (1978). Seismological aspects of the Guatemala earthquake of February 4, 1976. J. Geophys. Res., 83, 3427-3434.
- Kanamori, H. (1977). The energy release in great earthquakes, J. Geophys. Res., 82, 2981-2987.
- Langston, C.A. (1976). A body wave inversion of the Koyna, India, earthquake of December 10, 1967, and some implications for body wave focal mechanisms, J. Geophys. Res., 81, 2517-2529..
- Langston, C. A. (1977). The effect of planar dipping structure on source and receiver for constant ray parameter, Bull. Seismol. Soc. Am., 67, 1029-2050.
- Langston, C. A. and D. V. Helmberger (1975). A procedure for modelling shallow dislocations, Geophys. J. R. astr. Soc., 42, 117-130.
- Qiu Qun (1976). On the Background and Seismic Activity of the M=7.8 Tangshan Earthquake, Hopei Province, of July 28, 1976. Acta Geophysica Sinica, Vol. 19, no. 4, p. 269.
- Rial, J. A. (1978). The Caracas, Venezuela earthquake of July 1967: A multiple source event, J. Geophys. Res., in press.
- The Times (London), January 6, 1977, page 1.

- Wood, H. O. (1908). Distribution of Apparent Intensity in San Francisco, The California Earthquake of April 18, 1906, Report of the State Earthquake Investigation Commission, Carnegie Inst. of Wash., Publ. 87, Washington, D.C. 220-245.
- Zhu Chuan-zhen et al., (1977). Source Parameters for Small Earthquakes Before and After the M=7.8 Tangshan Earthquake. Acta Geophysica Sinica, Vol. 20, No. 4, p. 269.

SECTION I.3 BODY WAVE ANALYSIS OF THE APRIL 26, 1973 HAWAIIAN EARTHQUAKEABSTRACT

Long period P and S waves from WWSS and Canadian networks are analyzed to determine source parameters for the April 26, 1973 Hawaiian earthquake. The earthquake is found to be a double event with both events exhibiting similar fault plane solutions: left lateral motion on an east-west striking plane dipping  $55^\circ$  south, or right lateral motion on a near vertical north-south striking plane. The second source initiated 3 seconds after and 15 km NE of the first. Source depths of 42 and 32 km, and symmetric triangular source time functions 3.3 and 2.5 seconds in duration, respectively, are obtained from the waveform analysis of the two events. Amplitude distortion of surface reflected phases is noted and can be attributed to the dipping surface of the island of Hawaii. Several lines of evidence indicate lateral heterogeneity in the source region. No common focal mechanism was found that was able to simultaneously fit P and SH waveforms. Shear wave travel times and P and SH amplitudes show anomalous values in the eastern azimuth. The focal mechanism determined from the local array data appears to be significantly inconsistent with the SH data.

INTRODUCTION

The April 26, 1973 Hawaiian earthquake generated a number of high quality observations of shear phases at seismic recording stations throughout the world. As good local control of the epicenter was provided by the seismic array of the Hawaii Volcano observatory on the island of Hawaii, the event offered an opportunity to measure accurate

shear travel times from the middle of the Pacific plate. In this section an analysis is made of the teleseismic body waves to determine focal parameters and a source time function for the Hawaiian earthquake. In the next chapter S-wave travel times from the event are measured by a waveform correlation technique comparing synthetic and observed S waves. The source mechanism obtained herein is also used in Chapter II to study waveforms and travel times of the shear phase SS generated by the Hawaiian earthquake. The results of the source analysis and S and SS studies are, however, somewhat confounded by several lines of evidence suggesting lateral heterogeneity in the velocity structure of the Hawaii source region.

#### DATA ANALYSIS

The 1973 Hawaiian event was an intermediate size -  $m_b = 6.0$ ,  $M_s = 6.2$  (N.E.I.S.) - subcrustal earthquake occurring beneath the northeast coast of the island of Hawaii near the City of Hilo. The origin time and location are reported by Unger and Ward (1979), using local control from the 29 stations seismograph array on the island of Hawaii: origin time 20<sup>h</sup> 26<sup>n</sup> 30.8<sup>s</sup> GMT; location 19.90° N., 155.13° W.; depth 48 km. Unger and Ward also note, "Damage from the earthquake, which was estimated by county officials to be \$5.6 million, was considerable along the northeast coast of the island, where 11 people were injured; most of the structural damage occurred in the city of Hilo. Maximum intensity was reported to be about VIII (Modified Mercalli scale) in the epicentral region and at least VI over virtually all of the island..." A strong ground motion accelerograph located at Kilauea, Hawaii about 50 km from the epicenter recorded maximum horizontal accelerations of 0.17g. and maximum vertical accelerations of 0.07g.

The location of the 1973 Hawaiian earthquake and the extent of its aftershocks are shown in Figure I.3.1. Also indicated in Figure I.3.1 is the approximate location of a large second shock following the main shock by roughly 3 seconds. The location of the initial shock and aftershocks are taken from Unger and Ward (1979) and are controlled by a local array of 29 stations on the island of Hawaii. The location of the large secondary co-shock is approximate and is deduced from the analysis of body waveforms.

Long period P and SH data were collected from WSSN and Canadian Network stations. P-waves at 33 stations and S-waves at 29 stations were twice digitized and averaged to minimize digitization errors. S-waves were rotated into radial (SV) and transverse (SH) components. Only the SH data were used in the analysis. A selection of the P and SH waveforms are shown in Figure I.3.3, I.3.5, and I.3.6. The P-wave data are typically of high quality. The SH data vary in quality. Data in the eastern azimuths to North and South America are of high quality and relatively low noise. Back azimuths at stations in North America and Japan crucial to the accurate determination of SH nodal planes are such that S-waves are nearly naturally rotated into SH. This greatly minimizes noise from rotation errors and interference with SV coupled PL waves. The SH data to the southwest were found to be relatively poorer in quality. The waveforms of S and sS in these azimuths were considerably more complicated in nature. Some of these complications may more than likely be circumstantially ascribed to near source lateral heterogeneity, as rays traveling to the southwest pass or reflect beneath the island of Hawaii.

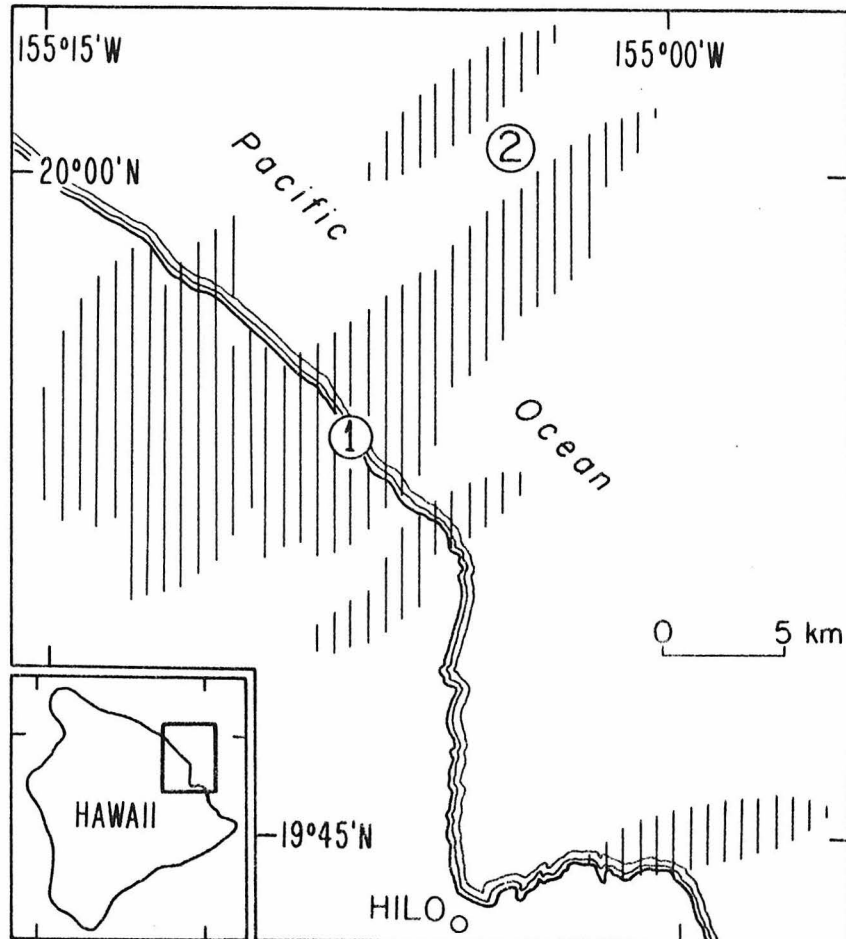


Figure I.3.1 A map showing the location of the April 26, 1973 Hawaiian earthquake and the extent of its aftershocks. The location of a second shock is deduced from the body wave analysis. (adapted from Unger and Ward, 1979).

P-wave first motion data are plotted in Figure I.3.2 on an equal area projection of the lower focal hemisphere. Although the azimuthal coverage is fairly good, the solution is unconstrained. Solution constraints are provided by the SH data. A secondary arrival consistently having the same direction of motion as the first motion is observed on the P-wave records for all the stations in the data set. This arrival is noted in Figure I.3.3 and is seen on other P-wave observations in Figure I.3.6. The relative timing between the initial and second P-wave arrivals varies in a systematic azimuthal fashion from 2.5 seconds for stations in the United States to about 5 seconds for stations in the Philippine Islands. The relative amplitude of the primary and secondary arrivals also varies. The timing and waveform characteristics of the second arrival strongly suggested that the 1973 Hawaiian earthquake was actually a double event with both sources having similar mechanisms and the second source situated northeast of the first.

First motions of SH are shown in Figure I.3.2 for an equal area lower hemisphere projection following the convention of Langston and HelMBERGER (1975), where positive is clockwise about the source. The SH first motions provide a better constraint of the source mechanism than do the P data. S-wave observations are shown in Figure I.3.5. Stations BLA and BAG in Figure I.3.5 indicate different SH first motions for the two sources.

Three source mechanisms are noted on the first motion diagrams in Figure I.3.2. Solutions 1S and 2 are determined from the analysis of the SH waveforms and represent a best fit to the SH data for the two sources. These focal solutions are listed in Table I.3.1. The SH

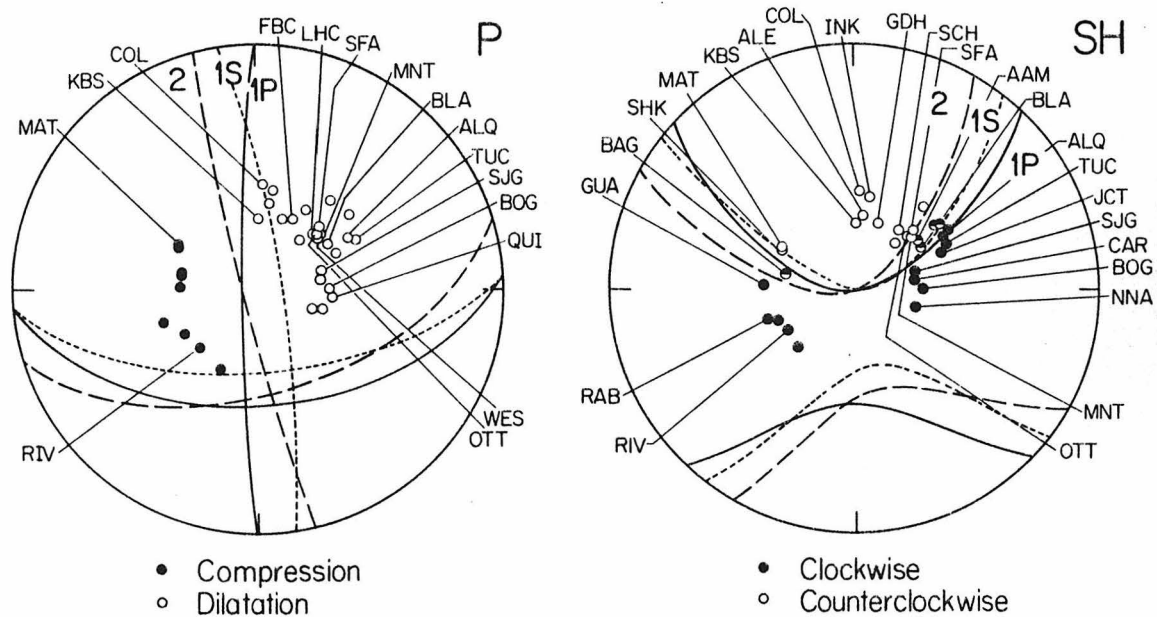


Figure I.3.2 Equal area projection of the lower half of the focal sphere showing P and SH first motions. Selected stations referred in the study are denoted. Fault plane solutions of the double event obtained from the body wave analysis are shown. Two solutions are indicated for the first event best fitting the P waves (1P) and SH (1S). The composite symbol on the SH focal sphere indicates different first motions for the first and second sources.

TABLE I.3.1HAWAII SOURCE PARAMETERS  
FROM INVERSION OF SH WAVEFORMS

## Source 1S

dip $\delta$	81°
rake $\gamma$	152°
strike $\theta$	-9°

## Source 2

dip $\delta$	95°
rake $\gamma$	145°
strike $\theta$	-14°

solution for the first source, 1S, does not fit the P-wave first motion for station KBS. The P-wave first motions allow a wide range of focal mechanisms, but it was noted in a systematic study of the P and SH waveforms that no solution for the first source could be found which simultaneously fit both the P and SH data. The P-wave solution for the first source, 1P, in Figure I.3.2 provided a good fit to the P-waveforms when used in conjunction with the SH determined second source and is listed in Table I.3.2.

In modeling the Hawaiian earthquake, synthetic seismograms were generated for a point shear dislocation in a layered elastic medium following the method of Langston and Helmberger (1975) and fit to the observed P and SH waveforms by trial and error and body wave inversion (see Burdick and Mellman, 1976; Langston, 1976). The effect of body wave attenuation was accounted for by convolving the synthetic seismograms with a Futterman (1962) attenuation operator with  $t^* = 1$  for P waves and  $t^* = 4$  for the SH waves. The crust-mantle model assumed for the Hawaii source region was adapted from Crosson (1976) and Hill (1969) and is listed in Table I.3.3. The shear velocity was initially assumed at Poisson's ratio, but a check of the relative timing of pP, sP, and sS suggested a ratio of VP to VS of 1.84.

To determine time functions for the two sources, the instrument response was deconvolved from the P-wave observations. Symmetric triangular time functions were fit to the pulse shapes. Station MAT in Figure I.3.6 was particularly suited for this measure. The first source was well fit with a symmetric triangle  $3.3 \pm 0.3$  seconds in duration. The second source was less constrained, but could be matched with a symmetric triangle  $2.5 \pm 0.8$  seconds in duration.

TABLE I.3.2

## HAWAII SOURCE PARAMETERS

## FITTING P-WAVEFORMS

## Source 1P

dip $\delta$	94°
rake $\gamma$	141°
strike $\theta$	0°

## Source 2

dip $\delta$	94°
rake $\gamma$	145°
strike $\theta$	-14°

TABLE I.3.3

## VELOCITY MODEL

<u><math>\alpha</math> (km/sec)</u>	<u><math>\beta</math> (km/sec)</u>	<u><math>\rho</math> (gm/cm<sup>3</sup>)</u>	<u>depth(km)</u>
1.50	0.00	1.03	0.4
5.30	2.80	2.60	5.5
7.00	3.70	3.00	12.0
8.30	4.50	3.40	22.0
8.47	4.52	3.45	30.0
8.55	4.65	3.50	

A depth of  $48 \pm 7$  km, for the first shock, was reported by Unger and Ward (1979). A depth was determined from the teleseismic observations from the relative arrival times of the surface reflected phases to the direct arrivals. In modeling the P-wave observations an immediate difficulty presented itself in matching the surface reflected phases pP and sP. This problem is illustrated with four P-wave observations in Figure I.3.3 for the source mechanism in Table I.3.3. The waveforms of the direct P-waves are well fit, as are the arrival times and directions of motion of pP and sP, assuming source depths of 42 km and 32 km for the two sources. However, the amplitude of sP at stations in the eastern azimuths is much larger on the synthetics than is observed. A systematic check of source mechanisms fitting the direct arrivals revealed this to be a consistent problem. This problem is effectively resolved in noting that the 1973 earthquake occurred beneath the largest mountain on earth and that the free surface of the island and crust-water interface are not flat, but rather have substantial gradients. The topography and bathymetry in the vicinity of the sP reflection points dip northeast between  $3^\circ$  and  $20^\circ$ . The effect of planar dipping structure is discussed by Langston (1977), and is illustrated in Figure I.3.4. Basically, the effect of the dipping surface is to change the point on the focal sphere from which sP is radiated. Including a  $5^\circ$  dipping island surface moves the sP radiation at QUI toward a sP nodal line, reducing the amplitude of sP relative to the direct P-waves. Uncertainties in the correction for dip effectively compromise the use of the surface reflected phases in the determination of the source mechanisms of the two events. Timing information from the surface reflected phases is relatively preserved, however. A source depth of 42 km for the first event and 32 km

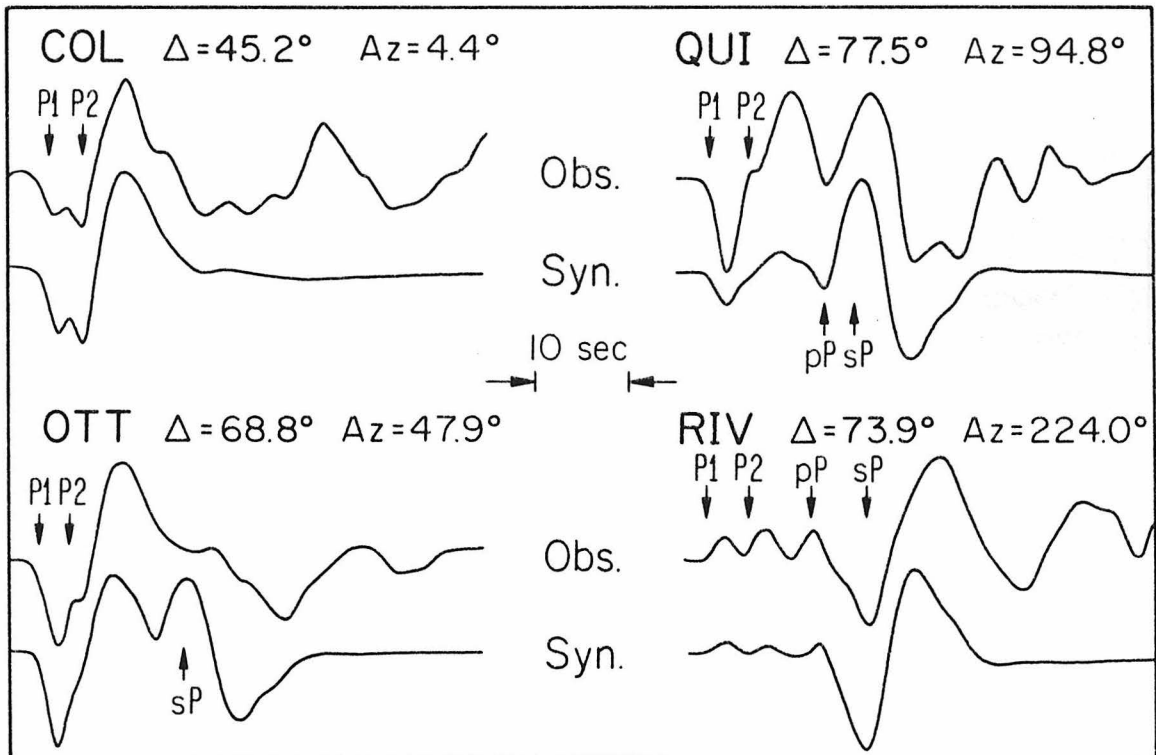


Figure I.3.3 A comparison is shown of four P wave observations and synthetics computed from the source model in Table I.3.2. The direct P arrivals from the two sources, P1 and P2, are indicated. The waveforms of the direct P waves are well fit, but the amplitudes of the surface reflections are poorly matched.

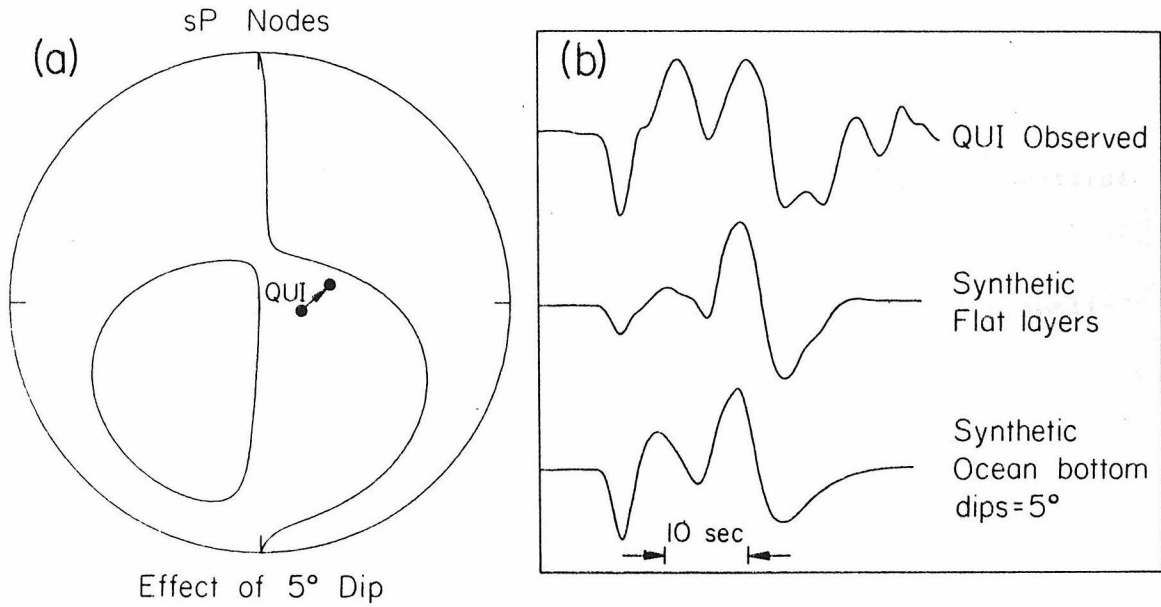


Figure I.3.4 The nodal lines of sP for the fault plane solution 1P in Figure I.3.2 are shown in (a). A 5° dipping free surface moves the apparent location of QUI on the focal sphere. The dipping surface decreases the amplitude of sP relative to direct P for the synthetic in (b).

for the second provides the best qualitative fit to the pP, sP, and sS arrivals. The shallower depth of the second source allowed the arrivals of the surface reflections from the two events to overlap, producing a better fit to the observations. However, uncertainties in the crust-mantle model, sources, and effect of dipping structure suggest this point is perhaps not resolvable. The depth of 42 km for the first source is within the error bounds of the local determination. Unger and Ward (1979) used a mantle velocity of 8.2 km/sec in determining the location of the event. If we adjust our velocity model to this lower value, the pP-P times yield a depth of 45 km for the first event.

Without the additional control of the pP and sP relative amplitudes, the direct P-waves cannot by themselves constrain either source, but do provide relative control between the two sources. The timing variation between the direct P arrivals of the two sources was fit if the second source initiated 3 seconds after and was located 15 km northeast of the first source. This assumes a 10 km depth difference between the sources. If the two sources are placed at the same depth, the time lag between the sources is 4 seconds.

Fixing the source depths, source time functions, and relative locations, the SH waveforms in the eastern azimuth plus BAG, SHK, and MAT in the west - see Figure I.3.2 - were inverted to determine the best fault plane solution for each source for the SH data. Only the direct SH ray for each source was modeled. The solutions obtained from the inversion of the SH data for the two sources are shown in Figure I.3.2 - mechanisms 1S and 2 - and are listed in Table I.3.2.

Comparisons between the observations and synthetics are shown in Figure I.3.5. The overall waveform comparison is quite satisfactory. As was noted earlier, however, this SH solution violates the P-wave first motion at KBS - see Figure I.3.2. Figure I.3.6 shows the fit of the SH solutions to selected P-wave data. The agreement is good except at COL. In Figure I.3.3 the P waveform of COL was well matched using the fault plane solutions 1P and 2 shown in Figure I.3.2 and listed in Table I.3.3. This P-wave solution, however, does not adequately fit the SH data. Several inversion runs were tried using a joint P and SH data set, but the fit to COL could not be improved without substantially degrading the fit to the SH data - particularly the crucial SH observation at BLA.

The solutions 1S and 1P in Figure I.3.2 are not so dissimilar as to cause much concern, but some thought is in order as to the nature of the apparent incompatibility of the P and SH data. Three possibilities present themselves. (1) Too much confidence is placed upon the SH data near the SH nodes. (2) The assumed P and S velocity at the source is incorrect; therefore distorting the focal sphere. (3) The velocity structure at the source is somewhat laterally heterogeneous. As noted earlier, in answer to (1), the S wave data detailing the SH nodal lines are high quality, low noise and within  $10^\circ$  of being naturally rotated into SH. (2) Changing the source velocities by 4% shifts all stations radially inward or outward on the focal sphere by less than  $1.5^\circ$ . This effect is small and does not significantly change the relative relationship of the P and SH data. Given the location of the Hawaiian earthquake source beneath the largest volcano on earth, the third possibility seemed probable.

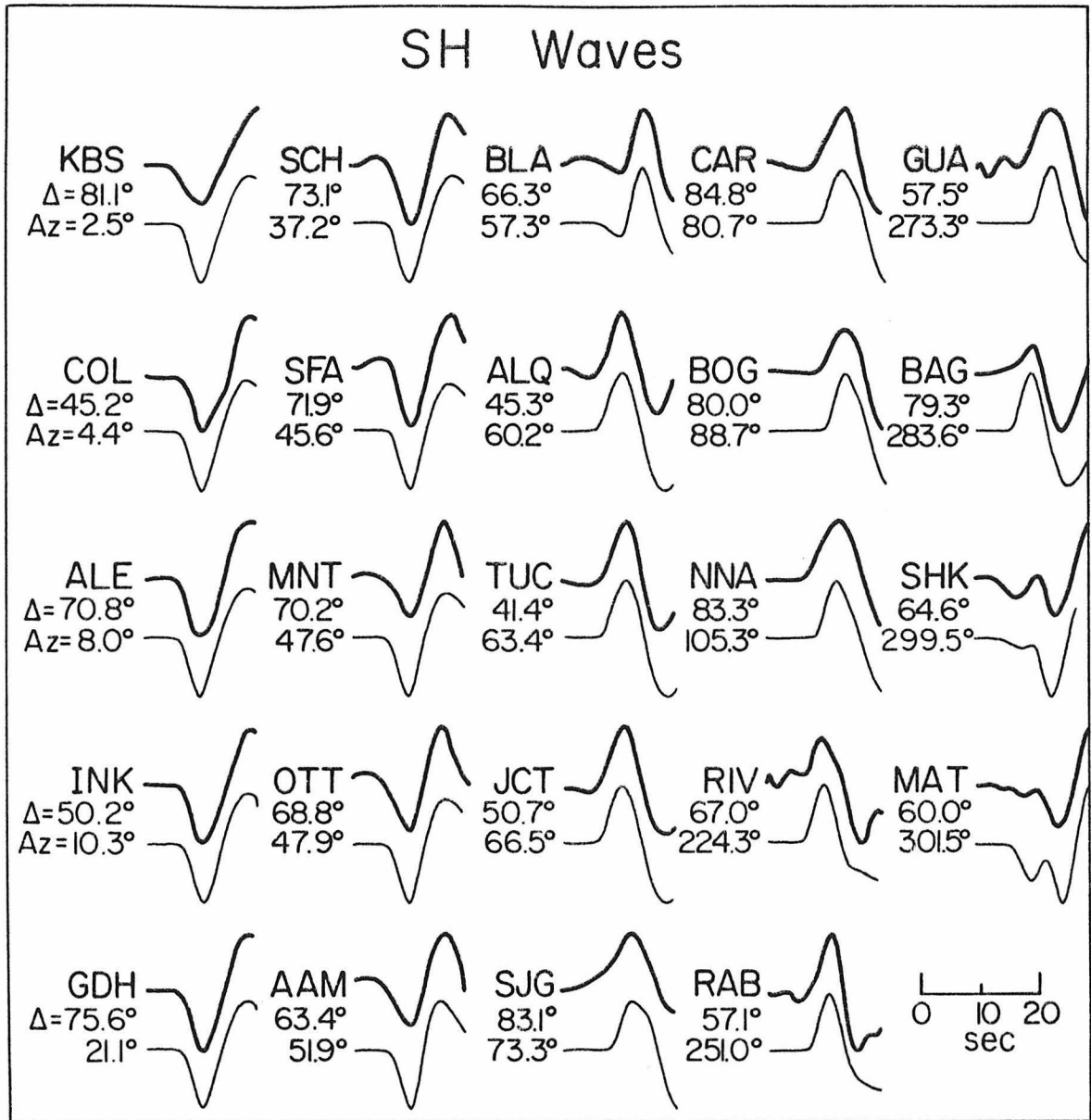


Figure I.3.5 Observed SH waves and synthetics computed for the source model in Table I.3.1. Each seismogram pair consists of the observed on top and the synthetic directly below for each station.

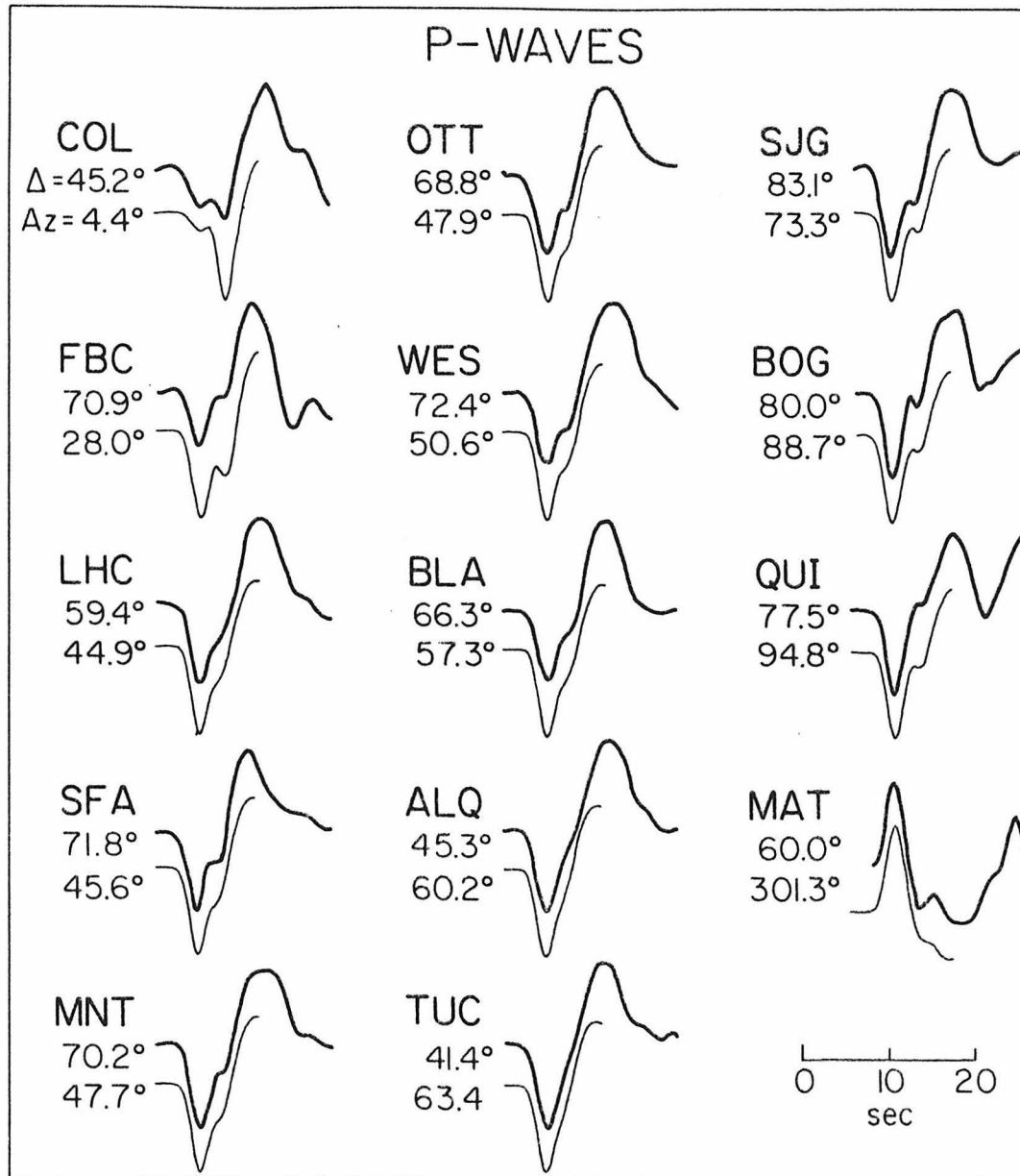


Figure I.3.6 Observed P waves and synthetics computed for the source model in Table I.3.1. Each seismogram pair consists of the observed on top and the synthetic directly below for each station.

At this point in the analysis of the event shear wave travel times from the earthquake were measured. Precise timing was accomplished by a waveform correlation technique comparing the observed SH with synthetics generated for the well-constrained SH source model. The study is discussed in the next chapter, but one result is helpful at this point. Much lower scatter was exhibited in the travel times of rays leaving the source to the northeast between  $0^\circ$  and  $60^\circ$  azimuth compared to rays at other azimuths. The change in the character of the travel times suggest a varying velocity structure in the earthquake source region.

A similar change in character may be noted for the amplitudes of the P and SH data at about a  $50^\circ$  azimuth. Table I.3.4 list P-wave moments calculated for the first source using the P-wave source model 1P. The moment of the second source is approximately one-third of the first, although trade-offs in uncertainties of the durations of the sources can change this estimate by 50%. Table I.3.5 lists the SH wave moments determined for the first source from the SH source model 1S. The P-wave moments for azimuths between  $0^\circ$  and  $50^\circ$  average at  $3.5 \times 10^{25}$  dyne-cm. Past  $50^\circ$  the apparent P amplitudes grow significantly to values for South American stations a factor of 5 to 7 greater than the stations in the northeast. The average moment of the SH waves between  $0^\circ$  and  $50^\circ$  is  $5.3 \times 10^{25}$  dyne-cm. The amplification observed at BKS, BLA, and DUG may be ascribed to instabilities in the measurement for nodal stations, but the amplitudes of non-nodal stations at azimuths greater than  $60^\circ$  average a factor of two greater than the amplitude data to the northeast.

TABLE I.3.4

P-WAVE MOMENTS FOR SOURCE 1P

<u>STATION</u>	<u>AZ</u> <u>(deg.)</u>	<u><math>\Delta</math></u> <u>(deg.)</u>	<u><math>M_0 \times 10^{25}</math></u> <u>(dyne-cm)</u>
COL	4.5	45.24	3.71
MBC	9.4	59.24	2.70
INK	10.3	50.24	1.86
GDH	21.1	75.59	3.82
FBC	28.0	70.89	3.72
FCC	32.5	58.25	2.87
COR	39.9	36.10	5.14
LHC	44.9	59.42	2.98
SFA	45.6	71.88	4.21
OTT	48.0	68.78	4.02
WES	50.6	72.40	4.57
BKS	50.9	33.68	5.25
BLA	57.2	66.30	6.11
ALQ	60.2	45.30	5.37
TUC	63.5	41.42	6.21
SJG	73.5	83.08	6.79
CAR	80.7	84.82	9.51
BOG	88.6	80.05	11.93
QUI	94.7	77.50	26.01
NNA	105.2	83.28	20.54
SHK	299.5	64.63	5.77
MAT	301.3	59.94	5.00

TABLE I.3.4

SH - WAVE MOMENTS FOR SOURCE 1S

<u>STATION</u>	<u>AZ</u> (deg.)	<u><math>\Delta</math></u> (deg.)	<u><math>M_0 \times 10^{25}</math></u> (dyne-cm)
KBS	2.5	81.11	3.76
COL	4.5	45.24	5.44
ALE	8.0	70.76	5.20
MBC	9.4	59.24	6.72
INK	10.3	50.24	5.68
KTG	14.3	84.17	4.64
RES	15.0	68.23	5.52
GDH	21.1	75.59	4.96
PHC	24.0	37.73	6.32
FSJ	26.9	41.71	5.04
FBC	28.0	70.89	5.04
FCC	32.5	58.25	6.96
VIC	34.5	38.28	3.20
FFC	35.6	59.94	6.16
PNT	35.7	40.79	4.48
SCH	37.2	73.04	3.12
COR	39.9	36.10	6.24
STJ	41.7	83.55	3.92
LHC	44.9	59.42	7.44
SFA	45.6	71.88	4.80
OTT	48.0	68.78	4.24
BKS	50.9	33.68	19.20
DUG	51.3	41.36	23.76
BLA	57.2	66.30	23.76
ALQ	60.2	45.30	12.95
OXF	61.1	59.31	8.24
TUC	63.5	41.42	9.68
JCT	66.5	50.73	10.96
SJG	73.5	83.08	11.76

TABLE I.3.4

(Continued)

<u>STATION</u>	<u>AZ</u> <u>(deg.)</u>	<u>Δ</u> <u>(deg.)</u>	<u>Mo x 10<sup>25</sup></u> <u>(dyne-cm)</u>
CAR	80.7	84.82	19.04
LPS	83.7	62.97	8.48
bog	88.6	80.05	11.60
QUI	94.7	77.50	16.40
GIE	99.7	66.68	10.00
NNA	105.2	83.28	7.04
ARE	107.5	89.73	8.32
GUA	273.6	57.53	7.68
BAG	283.6	79.33	3.60
SHK	299.5	64.63	8.32
MAT	301.3	59.94	14.32

Thus shear wave travel times, and P and SH amplitudes exhibit a change in character at an azimuth of about  $50^\circ$  to  $60^\circ$ . As the SH data detailing the location of the SH nodal lines also lie in this azimuth, one may presume that the lateral heterogeneity affecting the amplitude and travel time data will produce distortional effects in the SH radiation from the source. The inability to find a fault plane solution adequately fitting both the P and SH waveforms represents a further manifestation of the lateral heterogeneity in the source region of the 1973 Hawaiian earthquake.

#### DISCUSSION

Although difficulties with lateral heterogeneity and the dipping surface of the island have impaired our ability to finely tune the source parameters, the overall source mechanism of the April 26, 1973 Hawaiian earthquake is fairly well-constrained by the P and SH waveforms and first motions. The earthquake was found to be a double event, with both events having similar strike-slip mechanisms: left lateral motion on an east-west striking plane dipping southward  $55^\circ$ ; right lateral motion on a near vertical north-south striking plane with a slip angle plunging  $35^\circ$  south. The approximate location of the second source relative to the first event is shown in Figure I.3.1, and fits fairly well with an observed trend of aftershocks northeast of the main shock. However, the azimuth of the second source does not lie on strike with either nodal plane of events, indicating the two sources did not occur on a common fault. Rather, en echelon faulting may be ascribed to the double Hawaii event. En echelon faulting in a multiple

event has been previously observed by Rial (1978) for the Caracas, Venezuela earthquake of July, 1967. The east-west trend of aftershocks about the first source suggests the east-west nodal plane was the active fault plane.

Amplitude distortion effects observed for the surface reflected phases were found to be attributable to the dipping surface of the overlying island. The best waveform fit to surface reflected phases suggested source depths of 42 km and 32 km for the first and second sources, respectively. The depth of the first source is within the error bounds of the locally determined depth of  $48 \pm 7$  km (Unger and Ward, 1979). As a slower mantle velocity was used in the local determination, about 5 km should be added to the teleseismic source depths for comparison. The source depth of the second event is less constrained and could lie at the depth of the first event.

Unger and Ward (1979) report a fault plane solution for the main shock determined from P-wave first motions from the local network and world-wide stations: nodal planes oriented  $N33^{\circ}E$  dipping  $77^{\circ}W$  and  $N70^{\circ}$  dipping  $61^{\circ}S$ . The solution is primarily constrained by the local network and violates some teleseismic P-wave first motions. This local solution is similar to the solution presented in Figure I.3.2, but with a clockwise rotation of  $33^{\circ}$ . This discrepancy is considerably greater than the difference between solution 1P and 1S in Figure I.3.2. The teleseismic SH data are clearly incompatible with the local data. Two explanations may be invoked to explain the discrepancy. The local solution was found using a simple one layer crust over the mantle. Lateral heterogeneity and dipping internal structure

beneath the island will distort the apparent location on the focal sphere of the locally determined P-nodal line. Further, the local stations constraining the N33°E nodal plane lie on the flanks of the active volcanoes Mauna Loa and Kilauea opposite to the 1973 earthquake, such that the upward traveling P-waves will interact with the cores of the volcanoes. This view of the discrepancy between the teleseismically determined fault plane solution and locally constrained solution of the 1973 Hawaiian earthquake is suggestive that the focal mechanisms of mantle earthquakes beneath Hawaii determined by the local array may be substantially biased due to uncertainties in the velocity structure, and the accuracies of the determinations may be poorer than previously suspected. An alternative view of the discrepancy is that the P first motions recorded by the local array represented a foreshock a second or so before the main shock. A magnitude 4.5 foreshock would effectively mask the local data and yet go undetected teleseismically. A reexamination of the local seismograms of the event could substantiate this possibility.

The orientation of the axis of maximum principle stress for the two events trends approximately N45°E and is inclined about 25°, the axis of least principle stress trends S45°E and is also inclined at 25°. These directions do not agree with the hypothesis of the origin of the Hawaiian chain as a propagating tensional fracture (Green, 1971; Turcotte and Oxburgh, 1973), nor with the stress directions in the Pacific plate proposed by Jackson and Shaw (1975). The orientation of the maximum principle stress is qualitatively consistent with

gravitational loading effects from the island of Hawaii upon the lithosphere.

The only surface geologic or tectonic feature which suggest possible association with the earthquake is the east rift zone of the dormant volcano, Mauna Kea (Fiske and Jackson, 1972). This zone strikes east-west in the vicinity of the epicenter of the event. However, studies of the active rift zone of Kilauea indicate these features are limited to the crust (Fiske and Jackson, 1972).

The Hawaiian earthquake radiated a strong downward S pulse which was observed on the high gain long period seismograph at Kipapa, Oahu, three degrees distant as multiple ScS reflections up to ScS<sub>6</sub> (Best et al., 1974). These near vertical incidence phases provided an accurate estimate of the total crust-mantle travel time and average attenuation beneath the Hawaiian ridge. The relative strength of downward S for the focal mechanism presented here is about 60% of the maximum for the focal sphere.

Several lines of evidence have indicated lateral heterogeneity in the source region of the 1973 Hawaiian earthquake. No common source model was found to satisfy all the details of the P and SH waveforms. The P and SH amplitude data indicate that the eastern stations show significant amplification relative to stations in the northeast azimuth. Shear wave travel times from the Hawaiian event - determined in the next chapter - to stations in the northeast average at about 1 second slow relative to the Jeffreys-Bullen baseline. Stations in the east (azimuth >60°) average about 8 seconds slower than JB. Thus, the lateral heterogeneity manifests itself as a region of low shear

velocity, yet it amplifies P and SH which travel through the region. The qualitative nature of the evidence, however, does not appear to warrant a more specific interpretation of the lateral heterogeneity.

REFERENCES

- Best, W. J., L. R. Johnson, T. V. McEvelly (1974). ScS and the mantle beneath Hawaii, EOS Transactions, 56, 1147.
- Burdick, L. J. and G. R. Mellman (1976). Inversion of the body waves from the Borrego Mountain earthquake to the source mechanism, Bull. Seism. Soc. Am., 66, 1485.
- Crosson, R. S. (1976). Velocity structure below the island of Hawaii from earthquake modeling, EOS Transactions, 57, 961.
- Fiske, R. S. and E. D. Jackson (1972). Orientation and growth of Hawaiian volcanic rifts: the effects of regional structure and gravitational stress, Proc. Roy. Soc. London A, 329, 299.
- Futterman, W. I. (1962). Dispersive body waves, J. Geophys. Res., 67, 5279.
- Green, D. H. (1971). Composition of basaltic magmas as indicators on conditions of origin: application to oceanic volcanism, Phil. Trans. Roy. Soc. London A, 268, 707.
- Hil, D. P. (1969). Crustal structure of the island of Hawaii from seismic refraction measurements, Bull. Seism. Soc. Am., 59, 101.
- Jackson, E. D. and H. R. Shaw (1975). Stress fields in the central portion of the Pacific plate: delineated in time by linear volcanic chains, J. Geophys. Res., 80, 1861.
- Langston, C. A. (1976). A body wave inversion of the Koyna, India, earthquake of December 10, 1967, and some implications for body wave focal mechanisms, J. Geophys. Res. 81, 2517.

- Langston, C. A. (1977). The effect of planar dipping structure on source and receiver for constant ray parameter, Bull. Seism. Soc. Am., 67, 1029.
- Langston, C. A. and D. V. Helmberger (1975). A procedure for modeling shallow dislocations, Geophys. J. R. Astr. Soc., 42, 117.
- Rial, J. A. (1978). The Caracas, Venezuela earthquake of July 1967: multiple-source event, J. Geophys. Res., 83, 5405.
- Turcotte, D. L. and E. R. Oxburgh (1973). Mid-plate tectonics, Nature, 224, 337.
- Unger, J. D. and P. L. Ward (1979). A large, deep Hawaiian earthquake -- The Honoumuli, Hawaii event of April 26, 1973, submitted to Bull. Seism. Soc. Am.

CHAPTER II  
TRAVEL TIMES OF SHEAR PHASES USING  
WAVEFORM CORRELATION

SECTION II.1 SHEAR WAVE TRAVEL-TIMES FROM TWO WELL-CONSTRAINED EARTHQUAKESABSTRACT

A waveform correlation technique (Hart, 1975) for determining precise teleseismic shear wave travel times is applied to two large earthquakes with well-constrained source mechanisms, the 1968 Borrego Mountain, California earthquake and the 1973 Hawaii earthquake. A total of 87 SH travel-times in the distance range of  $30^{\circ}$  -  $92^{\circ}$  were obtained through analysis of WWSSN and Canadian Network seismograms from these two events. Major features of the travel time data include a trend toward faster travel times at a distance of about  $40^{\circ}$  (previously noted by Ibrahim and Nuttli, 1967, and Hart, 1975); another somewhat less pronounced trend toward faster times at about  $75^{\circ}$ ; a plus six second baseline shift, with respect to the Jeffreys-Bullen Table, for the Borrego Mountain data; and large azimuthally-dependent scatter for the Hawaiian data, probably reflecting dramatic lateral variations in the near source region. When azimuthal variations in the Hawaii data are removed, the travel times from both events show low scatter.

INTRODUCTION

The difficulty in determining the precise arrival times of teleseismic shear waves is a well-known problem in observational seismology. This difficulty arises largely from the fact that shear waves are secondary arrivals on the seismogram and the onset of the S-wave pulse is often obscured by precursory arrivals. This difficulty is further compounded by the relatively low Q of most long range S waves. The high frequencies

are thus preferentially removed from the pulse and the resulting arrival has a somewhat emergent onset. One promising approach was utilized by Hart (1975) to overcome these difficulties. This technique uses a waveform correlation between the observed shear wave and a synthetic shear wave to obtain a reliable onset time of the observation. The success of the waveform correlation method is directly dependent upon the accuracy with which the source time function is known for the event in question. At the time of the earlier study the seismic sources which best satisfied this requirement were nuclear explosions. Using a source derived in P wave studies (HelMBERGER and HARKRIDER, 1972), and assuming the observed shear waves were generated as pS, Hart (1975) picked S arrivals from five large nuclear explosions. However, the utility of explosion sources for shear wave travel time studies is limited. Even the largest of the nuclear explosions produce only relatively low amplitude shear waves, making phase identification difficult. As the shear energy is theoretically pure SV, converted P precursors and  $P_L$  coupling contribute significantly to the noise. The considerable SH energy observed from large explosions, and not predicted by the HelMBERGER-HARKRIDER model, may well be a further source of error.

In this section a waveform correlation approach is adopted to pick SH shear wave arrival times from two large earthquakes, the 1968 Borrego Mountain and 1973 Hawaiian earthquakes. The source time functions for both events have previously been carefully determined by body waveform analysis (BURDICK and MELLMAN, 1976; Chapter I.3) and origin times and locations are well constrained due to local control. The degree to which local control constrains the origin time and hypocentral locations of these events is important, especially if one wishes to compare baseline

shifts. In the case of the Borrego Mountain earthquake, there is excellent control from the Caltech network. Allen and Nordquist (1972) estimated the epicenter location error to be within 3 km. Their depth estimate of 11.1 km was confirmed by Burdick and Mellman (1976). With those limits, the effect of origin time and hypocenter errors on seismic travel-times are bound by the instrument timing accuracy. In 1968, that accuracy was 0.4 to 0.5 seconds or better. Local control for the 1973 Hawaiian event is also good although not to the degree of the first event. The problem with the Hawaiian earthquake is that the epicenter lies just off the coast and thus slightly outside of the local seismic network. Since the depth determined by the teleseismic waveform analysis agrees well with the local determination the overall accuracy to which we can estimate origin effects on these travel-times is 1 to 2 seconds. These errors,  $\leq 0.5$  seconds for Borrego and  $\leq 2.0$  seconds for Hawaii, can be considered as potential error limits on the travel-time baseline for those events. The large SH shear wave energy generated by these events allows travel times to be reliably determined to distances of  $90^\circ$ . To avoid waveform complications from upper mantle triplications, the minimum distance used was  $30^\circ$ .

#### TRAVEL-TIMES

The first event used in this study was the Borrego Mountain, California earthquake. This event was a magnitude 6.4 strike-slip earthquake which occurred on April 9, 1968 at 02:28:59.1 GMT (Allen and Nordquist, 1972). The actual source mechanism of this earthquake was determined through a detailed inversion of teleseismic P and S waveforms by Burdick

and Mellman (1976). The Burdick and Mellman mechanism demonstrated that this earthquake was actually a multiple event consisting of a main shock and two aftershocks. The source parameters describing these three events are given in Table II.1.1. Using the Burdick and Mellman mechanism it is a straightforward task to compute synthetic seismograms of the long-period S wave arrivals. Since the Borrego Mountain earthquake was a shallow event, the observed S pulse is actually a combination of both S and sS and the synthetics were constructed to include both rays. Figure II.1.1 shows a comparison between the observed S waves and synthetics for several stations. To include attenuation, the synthetics were convolved with a Futterman (1962) Q operator with  $t^* = 5.2$ , the value used by Burdick and Mellman (1976). Since the effect of errors in  $t^*$  becomes more pronounced later in the waveform, to determine the onset time of the observations, only the first swing of the S-wave pulse is used in the correlation procedure. This effectively reduces errors in the waveform correlation method when the true attenuation is uncertain (section II.3). It is possible not only to determine the best correlation and hence the best estimate of arrival time but also the total range of acceptable correlation. Thus, accurate estimates of error limits for the travel-times were obtained. The Borrego Mountain data set yielded 42 high quality SH arrivals on WWSSN and Canadian network stations in the distance range of  $30^\circ$  to  $92^\circ$ . The travel-times corresponding to these arrivals, corrected to the free surface and including elevation and ellipticity corrections, are listed in Table II.1.2. In Figure II.1.2 we have plotted 40 of these travel-times as residuals with respect to

Table II.1.1

Source Parameters for the Borrego Mountain  
and Hawaii Earthquakes

Borrego Mountain

April 9, 1968; Lat. = 33.190° N, Long. = 116.128° W

Main shock: 02:28:59.1 GMT

Strike = -45°, Dip = 81°, Rake = 178°, Depth = 8 km

Moment =  $11.2 \times 10^{25}$  dyne-cm

1st aftershock: 02:29:08.0 GMT

Strike = 128°, Dip = 77°, Rake = 12°, Depth = 7km

Moment =  $2.46 \times 10^{25}$  dyne-cm

2nd aftershock: 02:29:14.4 GMT

Strike = -91°, Dip = 28°, Rake = 98°, Depth = 11 km

Moment =  $0.78 \times 10^{25}$  dyne-cm

Hawaii

April 26, 1973; Lat. = 19.903° N, Long. = 155.130° W

Main shock: 20:26:30.8 GMT

Strike = -9°, Dip = 81°, Rake = 152°, Depth = 42 km

Moment =  $3.8 \times 10^{25}$  dyne-cm

1st aftershock: 20:26:34.0 GMT

Strike = -14°, Dip = 94°, Rake = 145°, Depth = 32 km

Moment =  $1.2 \times 10^{25}$  dyne-cm

Table II.1,2

SH Travel Times and Amplitudes  
 from Borrego Mountain  
 (Hypocenter corrected to surface)

Sta	$\Delta$ (deg)	Azimuth (deg)	T Obs. (m:s)	Error (sec)	T-T <sub>JB</sub> (sec)
SCB	30.52	59.0	11:21.8	+ .5 - .6	3.4
GEO	31.91	68.4	11:44.9	+ .4 - .5	4.7
SCP	31.30	64.8	11:33.5	+ .75 - .25	2.8
OGD	33.76	64.4	12:15.1	+ .5 - .5	6.0
OTT	33.23	56.5	12:04.8	+ .5 - .8	4.0
MNT	34.71	56.6	12:28.0	+ .5 - .8	4.3
WES	36.22	62.1	12:55.2	+ .7 - .5	8.1
SFA	36.79	54.1	13:00.2	+1.0 -1.0	4.4
COL	37.13	338.2	13:07.0	+ .4 - .4	6.0
KIP	38.79	263.9	13:35.9	+ .9 - .5	9.2
SCH	40.49	42.5	13:55.8	+ .5 - .5	4.0
BHP	41.44	117.2	14:09.8	+ .5 - .5	4.4
MAL	41.78	58.3	14:15.8	+1.2 - .8	4.9

Table II.1.2 (Cont'd.)

Sta	$\Delta$ (deg)	Azimuth (deg)	T Obs. (m:s)	Error (sec)	T-T <sub>JB</sub> (sec)
FBC	42.33	29.2	14:20.0	+1.0 -1.0	0.9
RES	42.86	8.1	14:30.9	+1.0 -1.0	4.1
BEC	42.90	76.4	14:31.7	+1.0 - .5	4.3
MBC	43.16	358.9	14:35.3	+ .5 - .6	4.1
QUI	48.53	125.4	15:56.4	+ .5 - .5	8.3
STJ	49.06	53.3	16:03.4	+ .3 - .3	7.9
GDH	49.71	24.5	16:11.8	+ .3 - .3	7.2
NNA	58.49	133.4	18:09.7	+ .5 - .8	6.7
NOR	58.76	9.8	18:11.8	+ .25 - .4	5.2
KTG	60.49	22.7	18:34.7	+ .7 - .25	5.8
AKU	63.42	27.3	12:15.2	+ .5 - .5	9.2
KBS	64.24	9.7	19:22.4	+ .25 - .3	6.2
ARE	65.22	132.1	19:35.1	+ .5 - .25	6.9
AFI	70.77	238.1	20:40.5	+1.0 - .5	5.9

Table II.1.2 (Cont'd.)

Sta	$\Delta$ (deg)	Azimuth (deg)	T Obs. (m:s)	Error (sec)	T-T <sub>JB</sub> (sec)
ANT	71.40	136.2	20:49.2	+ .5 - .5	7.3
VAL	73.39	38.4	21:38.4	+ .5 - .6	4.2
KEV	73.90	12.6	21:13.9	+ .5 - .6	3.6
KRK	74.47	11.6	21:21.0	+ .5 - .7	4.3
ESK	74.91	33.0	21:26.3	+ .6 - .25	5.0
KON	77.26	25.0	21:54.5	+ .25 - .25	7.2
UME	77.35	18.3	21:53.2	+ .25 - .5	4.9
PEL	78.63	142.4	22:34.7	+ .25 - .7	5.2
PTO	80.42	46.9	22:06.8	+ .5 - .7	4.8
NUR	81.25	18.5	22:34.7	+ .25 - .7	5.2
LOR	83.48	36.4	22:58.8	+ .25 - .5	6.6
STU	85.00	32.8	23:15.1	+ .6 - .5	7.8
NAT	85.35	99.1	3:20.6	+ .7 - .25	9.9
MAL	85.69	48.5	23:18.9	+ .7 - .5	4.9

Table II.1.2 (Cont'd)

Sta.	$\Delta$ (deg)	Azimuth (deg)	T Obs. (m:s)	Error (sec)	T-T <sub>JB</sub> (sec)
SHK	86.72	309.6	23:27.9	+ .5 - .5	4.0
LPA	86.97	135.6	23:30.0	+ .4 - .4	3.7
TRI	89.36	36.2	23:55.0	+ .7 - .5	6.4
AQU	91.72	34.9	24:18.1	+1.1 - .5	8.3

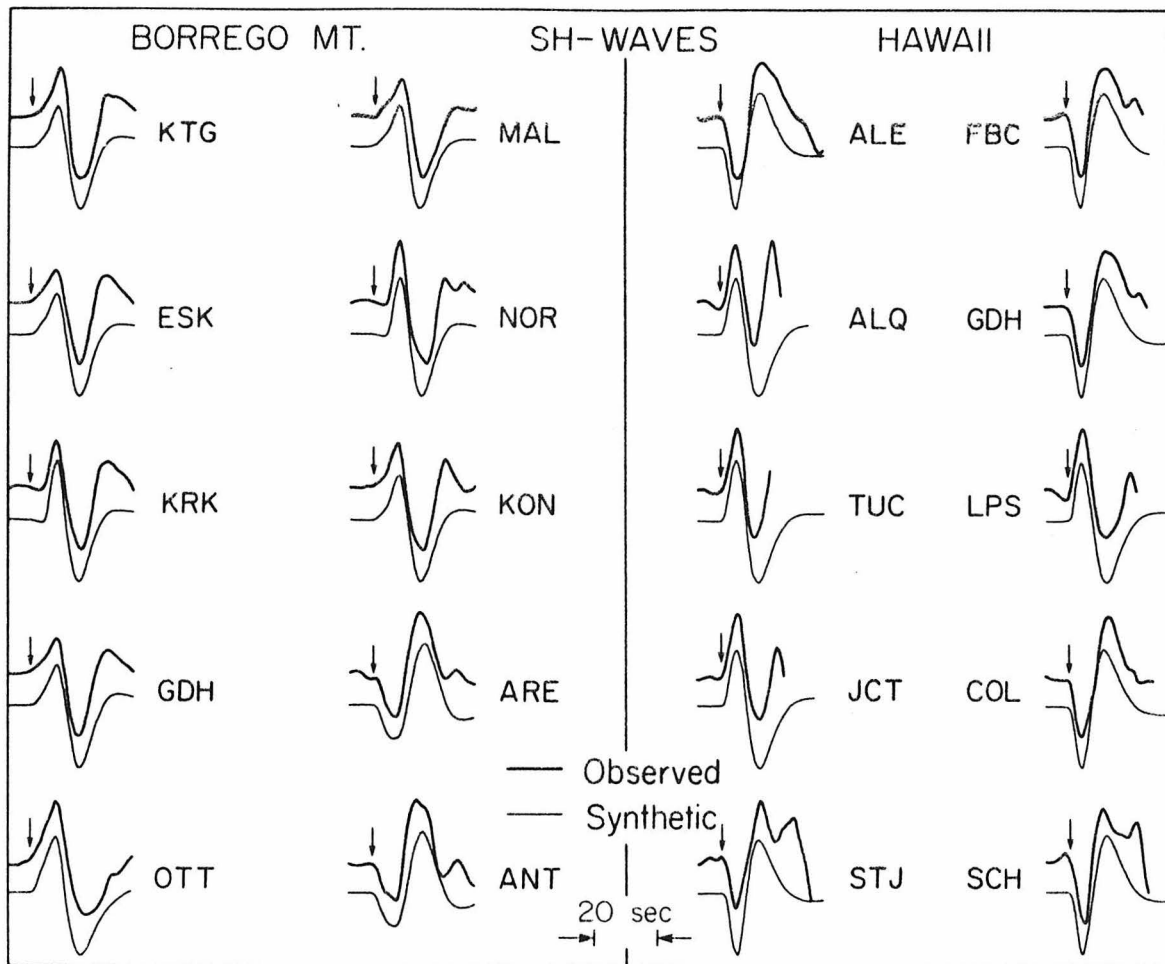


Figure II.1.1 Observed and synthetic SH arrivals for 10 seismograms of the Borrego Mountain earthquake and 10 seismograms of the Hawaii earthquake. The Borrego Mountain synthetics include both the direct S ray and the sS arrival; the Hawaii synthetics, due to the large hypocentral depth of that event, include only the direct S ray. The synthetics include attenuation effects. The seismogram pairs are plotted with the synthetic trace beneath the observed trace. The predicted arrival time (best correlation time) of the SH energy is indicated by a small arrow above each observed seismogram.

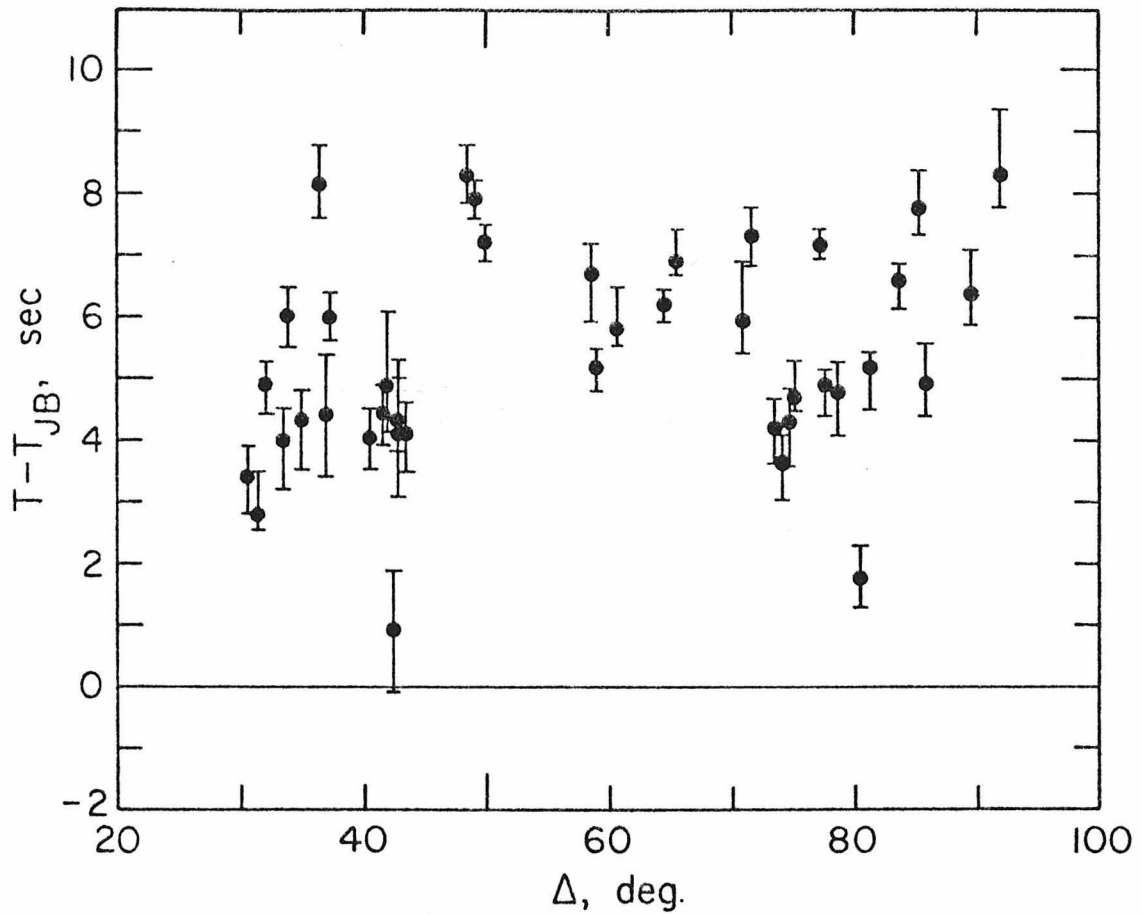


Figure II.1.2 SH travel time residuals with respect to the Jeffreys-Bullen Tables (1940) for the Borrego Mountain data set. The solid circle indicates the best correlation time. The error bars indicate the total range of acceptable correlation as well as estimates of reading and timing accuracies for each record.

the Jeffreys-Bullen (1940) Tables. The two stations deleted, KIP and AKU, are tectonic island stations whose travel-times are substantially late relative to other stations at the same distance range. An additional correction of + 0.4 seconds was given to stations with 30 - 90 instruments, (i.e., pendulum period of 30 seconds and galvanometer period of 90 seconds), MNT, FBC, SCH, OTT, and RES. This correction equalizes the apparent onset time of a 30-90 instrument to that of a 15-100 instrument. The overall data set exhibits a + 6 second baseline shift relative to the J-B times. The structure between 35° and 50° appears consistent with earlier studies (Ibrahim and Nuttli, 1967; Hart, 1975). However, the residuals show a definite trough at about 75° which has not been previously observed. The positive gradient in the S residuals past 80° is in agreement with observations by Hales and Roberts (1970).

The analysis of travel-times from the Hawaiian earthquake is more complex. This event occurred on April 26, 1973 at 20:26:30.8 GMT north-east of the city of Hilo at a depth of 42 km. The source mechanism of this earthquake (chapter I.3) is one of a double event with both shocks having similar mechanisms. Source parameters are given in Table II.1.1. Synthetic shear waves were computed including only the direct S wave from each shock as sS comes in much later at these depths. To be consistent with the initial source study (chapter I.3), an attenuation operator with  $t^* = 4.0$  was used in the calculations. Figure II.1.1 also illustrates several observed and synthetic S waves for this event.

In Table II.1.3 we have tabulated the corrected travel times for 45 observed SH arrivals, spanning a distance range of 34° to 90°. These travel times, plotted in Figure II.1.3 as residuals with respect to J-B

Table II.1.3

## Travel Times and Amplitudes

from Hawaii

(Hypocenter corrected to 33 km depth)

Sta.	$\Delta$ (deg)	Azimuth (deg)	T Obs. (m:s)	Error (sec)	T-T <sub>JB</sub> (sec)
BKS	33.68	50.9	12:03.6	+ .7 - .7	3.9
COR	36.9	39.9	12:45.1	+ .25 - .7	8.0
PHC	37.73	24.0	13:10.3	+ .5 - .5	8.2
VIC	38.28	34.5	13:17.8	+ .5 - .25	7.3
PNT	40.79	35.7	13:54.0	+ .6 -1.4	5.8
DUG	41.36	51.3	14:01.5	+1.0 -1.0	4.9
TUC	41.42	63.5	14:06.1	+ .5 - .5	8.6
FSJ	41.71	26.9	14:08.6	+1.0 -1.0	6.8
COL	45.24	4.5	14:54.0	+ .3 - .3	0.9
ALQ	45.30	60.2	15:02.6	+ .5 - .5	8.6
INK	50.24	10.3	16:04.1	+ .3 - .25	0.5
JCT	50.73	66.5	16:15.1	+ .5 - .5	4.7
FFC	52.94	35.6	16:41.5	+ .5 - .5	0.8

Table II.1.3 (Cont'd)

Sta.	$\Delta$ (deg)	Azimuth (deg)	T Obs. (m:s)	Error (sec)	T-T <sub>JB</sub> (sec)
DAL	53.25	63.4	16:50.1	+ .5 - .4	5.2
GUA	57.53	273.6	17:46.8	+ .5 - .5	4.8
FCC	58.25	32.5	17:50.8	+ .7 - .7	-0.7
MBC	59.24	9.4	18:06.2	+ .7 - .7	1.8
OXF	59.31	61.1	18:10.5	+ .5 - .7	5.2
LHC	59.42	44.9	18:06.7	+ .5 - .5	0.0
MAT	59.94	301.3	18:19.0	+ .4 - .4	5.6
SHA	60.74	65.3	18:31.9	+ .25 - .5	8.2
LPS	62.97	83.7	18:59.1	+ .2 - .3	8.7
AAM	63.34	51.9	18:56.5	+ .3 - .4	0.0
SHK	64.63	299.5	19:17.1	+ .7 - .7	4.7
BLA	66.30	57.2	19:34.1	+ .5 - .5	1.3
GIE	66.68	99.7	19:47.7	+1.0 -1.0	10.3
RES	68.23	15.0	18:56.6	+1.8 - .25	1.5
OTT	68.78	48.0	20:03.6	+ .8 - .6	1.0

Table II.1.3 (Cont'd)

Sta.	$\Delta$ (deg)	Azimuth (deg)	T Obs. (m:s)	Error (sec)	T-T <sub>JB</sub> (sec)
MNT	70.23	47.6	20:19.8	+ .8 - .6	0.1
ALE	70.76	8.0	20:27.2	+ .5 - .5	1.1
FBC	70.89	28.0	20:24.6	+ .3 - .3	-2.7
SFA	71.88	45.6	20:39.3	+ .3 - .3	0.5
WES	72.40	50.6	20:46.3	+ .6 - .6	1.5
SCH	73.04	37.2	20:51.0	+ .4 - .3	-1.0
GDH	75.59	21.1	22:23.6	+ .25 - .25	3.1
QUI	77.50	94.7	21:49.3	+ .5 - .1	8.0
BAG	79.33	283.6	22:05.0	+ .3 - .7	4.2
BOG	80.05	88.6	22:14.8	+ .4 - .2	6.5
KBS	81.11	2.5	22:26.8	+ .7 - .5	7.5
SJG	83.08	73.3	22:39.4	+ .5 - .5	0.0
NNA	83.28	105.2	22:45.5	+ .5 - .4	4.1
STJ	83.55	41.7	22:43.6	+ .75 - .75	-0.5
KTG	84.17	14.3	22:55.1	+ .7 - .4	4.8

Table II.1.3 (Cont'd)

Sta.	$\Delta$ (deg)	Azimuth (deg)	T Obs. (m:s)	Error (sec)	$T-T_{JB}$ (sec)
CAR	84.82	80.7	23:00.1	+ .5 - .4	3.4
ARE	89.73	107.5	23:48:3	+ .3 - .3	5.1

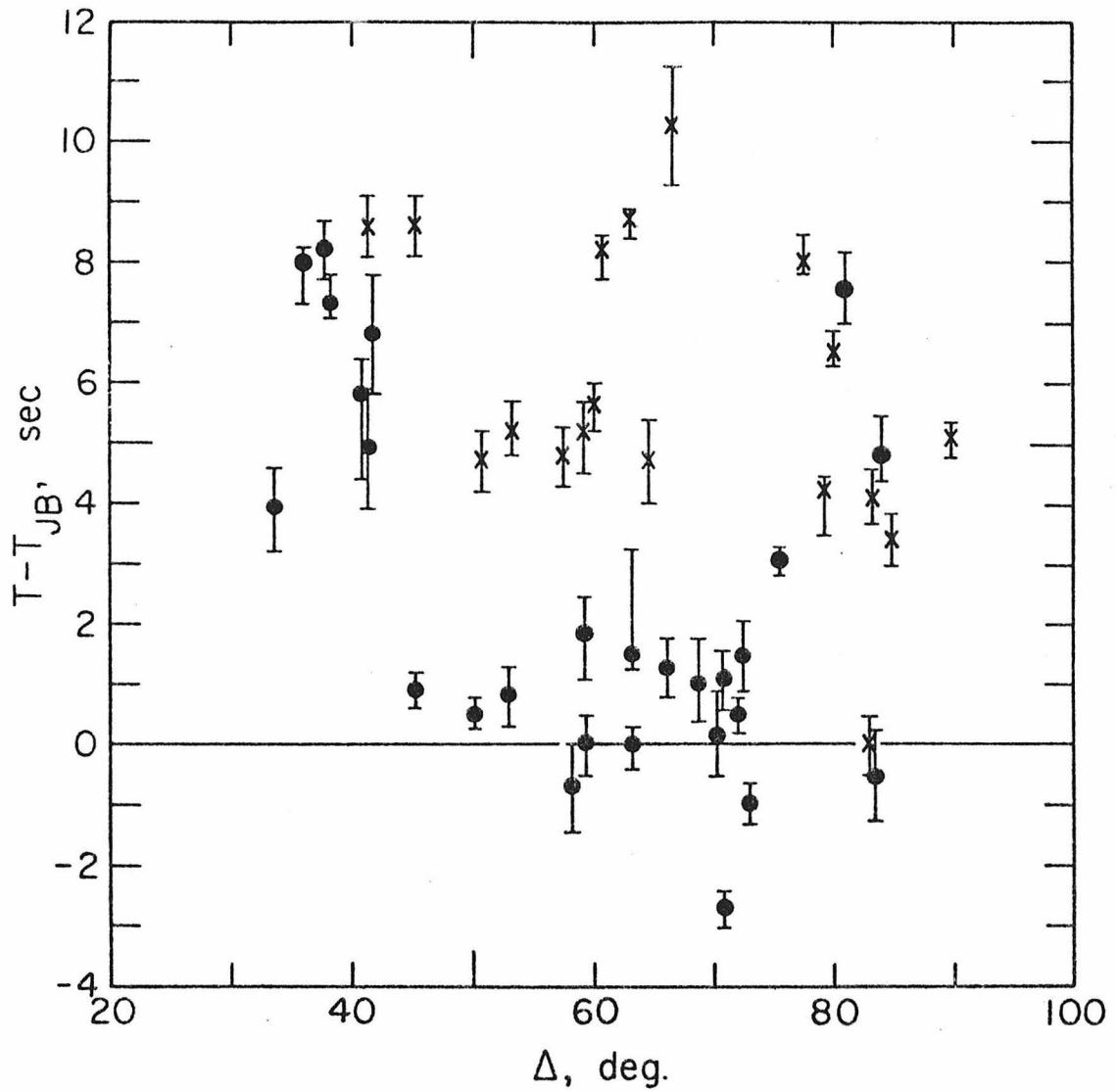


Figure II.1.3 SH travel time residuals with respect to the J-B Tables (1940) for the Hawaii data set. Those times plotted as solid circles correspond to stations whose azimuth from the source fall within the range of  $0^\circ$  to  $60^\circ$ . All others are plotted as crosses.

33 km depth times, show large scatter. Much of the scatter, however, appears to be due to a rather pronounced laterally heterogeneous velocity structure at the source. In the waveform analysis of the earthquake source in chapter I.3 it was noted that shear waves passing under the island of Hawaii to stations in New Zealand, Australia and New Guinea were far more complicated than comparable stations at other azimuths. Continuing on this tack Figure II.1.4 plots the location of the epicenter with respect to the Island of Hawaii and the azimuthal window of station coverage. Travel time residuals at stations at azimuths within the shaded wedge are plotted as circles in Figure II.1.3, those outside this wedge as crosses. In Figure II.1.5, these residuals are plotted as a function of azimuth from the epicenter for those stations with azimuths between  $0^\circ$  and  $107.5^\circ$  and distances between  $42^\circ$  and  $80^\circ$  to further clarify this point. The much lower scatter exhibited in the travel times of rays leaving the island to the northeast compared to rays at other azimuths strongly suggests a sharply varying velocity structure on the edges of the island of Hawaii. This change can not be presumed to reflect differences in tectonic settings of the stations. From Figure II.1.4 it is seen that roughly half of the stations leaving with azimuths greater than  $60^\circ$  are mid-continental North American. There is no obvious reason, for example, to expect travel-times to OXF or SHA to be markedly different than AAM or BLA. If only the stations within the shaded wedge in Figure II.1.4 are considered for the moment, it is seen that shear travel-times for distances greater than  $45^\circ$  have a baseline quite close to J-B and show no strong trend. The residuals for distances less than  $45^\circ$ , which represent stations on the west coast

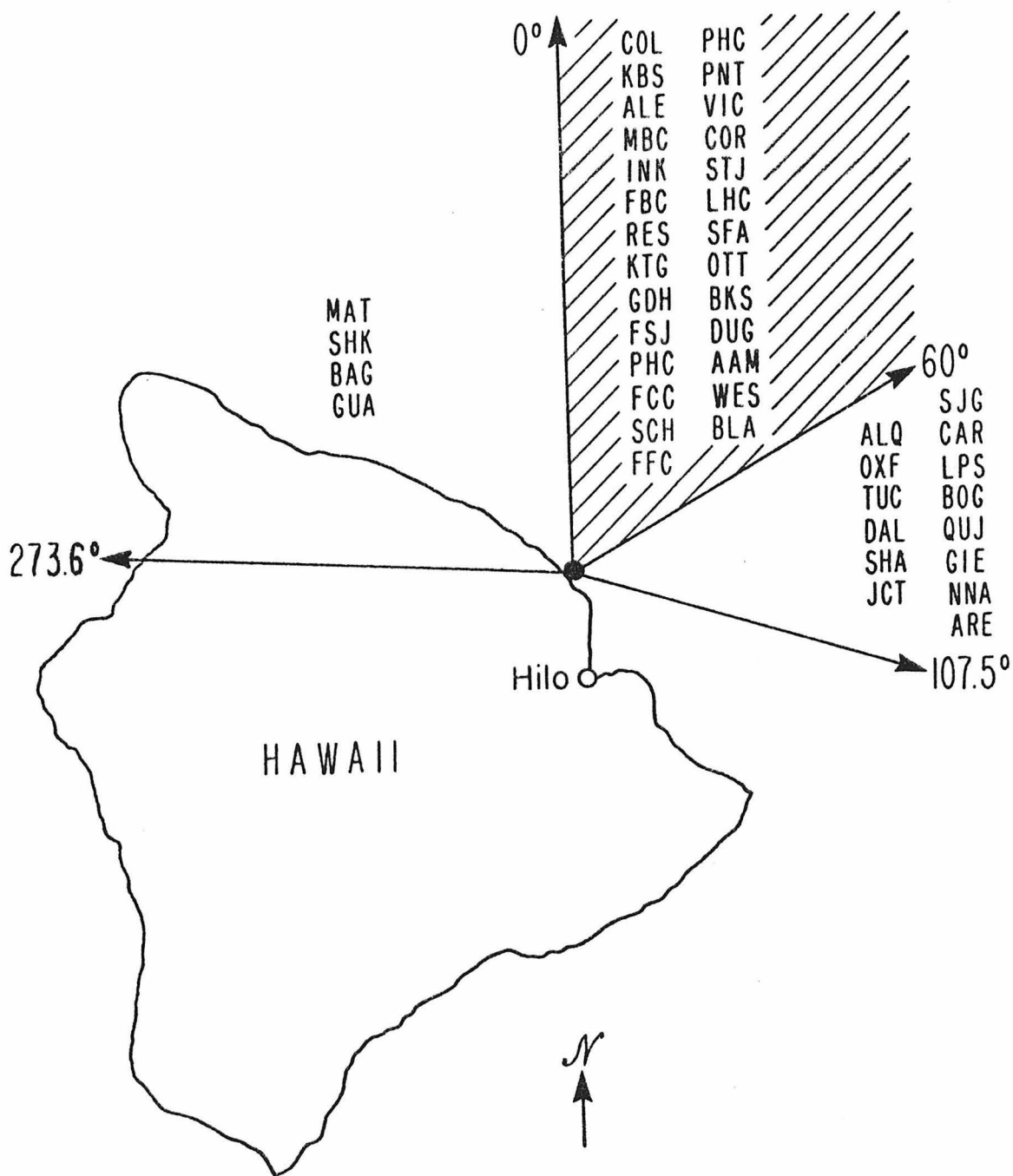


Figure II.1.4 Distribution, in azimuth, of WSSN and Canadian Network stations used in the analysis of the Hawaiian earthquake. Stations outside the shaded regions show anomalous travel times and amplitudes.

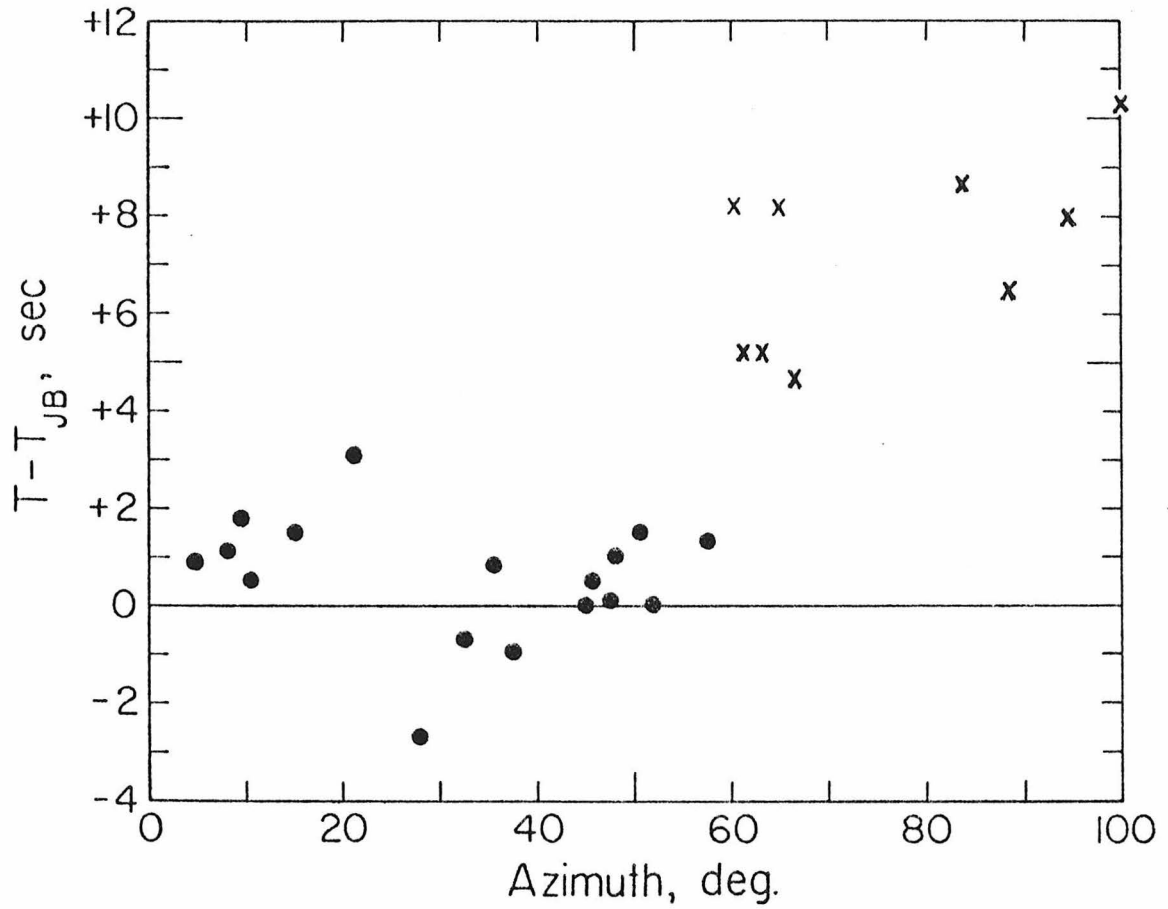


Figure II.1.5 SH travel time residuals from Hawaii, with respect to the J-B tables (1940) as a function of azimuth from the epicenter for stations in the distance range  $42^\circ$  to  $80^\circ$  and azimuths between  $0^\circ$  and  $107.5^\circ$ .

of North America, are much greater.

### DISCUSSION

The Borrego Mountain data set has no apparent internal azimuthal variations, but exhibits a six second baseline shift relative to J-B. P wave residuals for stations of the Caltech Seismic Network in the vicinity of the Borrego Mountain epicenter tend to cluster at about  $+ 0.6 \pm 0.5$  second relative to J-B (Raikes, personal communication). The origin time of the earthquake determined by the ISC is  $1.1 \pm 0.2$  seconds later than the well constrained Caltech determination. The ratio of S wave station anomaly to P wave anomaly has been found by many workers to be on the order of  $4 \pm 1$  (Doyle and Hales, 1967; Hales and Roberts, 1970; Followill and Nuttli, 1970). Therefore about  $4 \pm 1$  seconds of the Borrego S wave baseline may be consistent with observed station anomalies. Extremely slow S-wave station anomalies have been reported by Sengupta (1975) for WWSSN along the east African rift zone--AAE (+5.9 sec.), NAI (+ 5.7 sec.). These stations also show S to P station anomaly ratios of about 6. The Borrego Mountain epicenter is located within the proximity of the landward extension of the Gulf of California ridge system. Duschenes and Soloman (1977) measured shear wave travel-time residuals from mid-ocean ridge crest earthquakes and found S delays of 8 to 10 seconds relative to J-B. As the origin times of these events are determined by P waves and thus implicitly contain P delay information, the true S delays from these events are even greater. Thus, the slow Borrego S times are qualitatively consistent with the view of the Salton Trough as a continental continuation of the active

spreading center in the Gulf of California (e.g. Biehler et al., 1964).

The shear travel-times from the Hawaiian earthquake are primarily characterized by the azimuthal nature of their scatter. In the determination of the seismic moment of the earthquake in chapter I.3 a similar pattern of scatter was observed in the amplitudes of SH. Figure II.1.6 plots the ratio of the observed amplitude to the synthetic amplitude for the Hawaii S waves. Restricting the data to stations which fall within the shaded wedge in Figure II.1.3, it is shown in Figure II.1.7 that the amplitude scatter is considerably reduced. Thus both shear wave travel-times and amplitudes show effects which point to lateral heterogeneity in the source region of the Hawaiian earthquake. As the hypocenter of the event lies at a depth of 42 km beneath the northeast edge of the island of Hawaii—approximately 45 km from the center of island — the suggestion of a laterally varying velocity structure in this region can not be considered surprising. The qualitative nature of the azimuthal variations of shear travel times and amplitudes, however, does not lend itself to a more specific interpretation of the lateral heterogeneity.

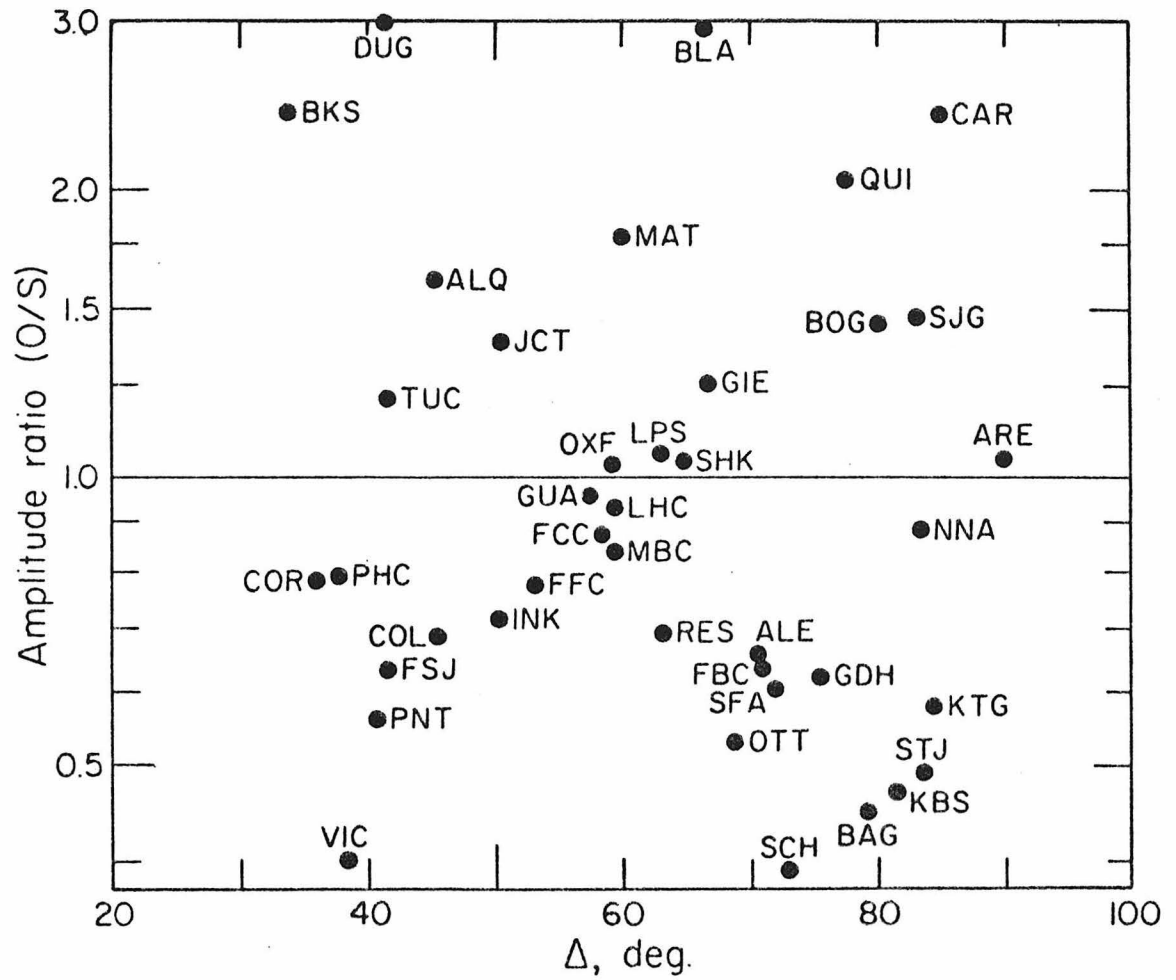


Figure II.1.6 SH amplitude ratios as a function of distance for the complete Hawaiian earthquake data set assuming a moment of  $8.0 \times 10^{25}$  dyne-cm.

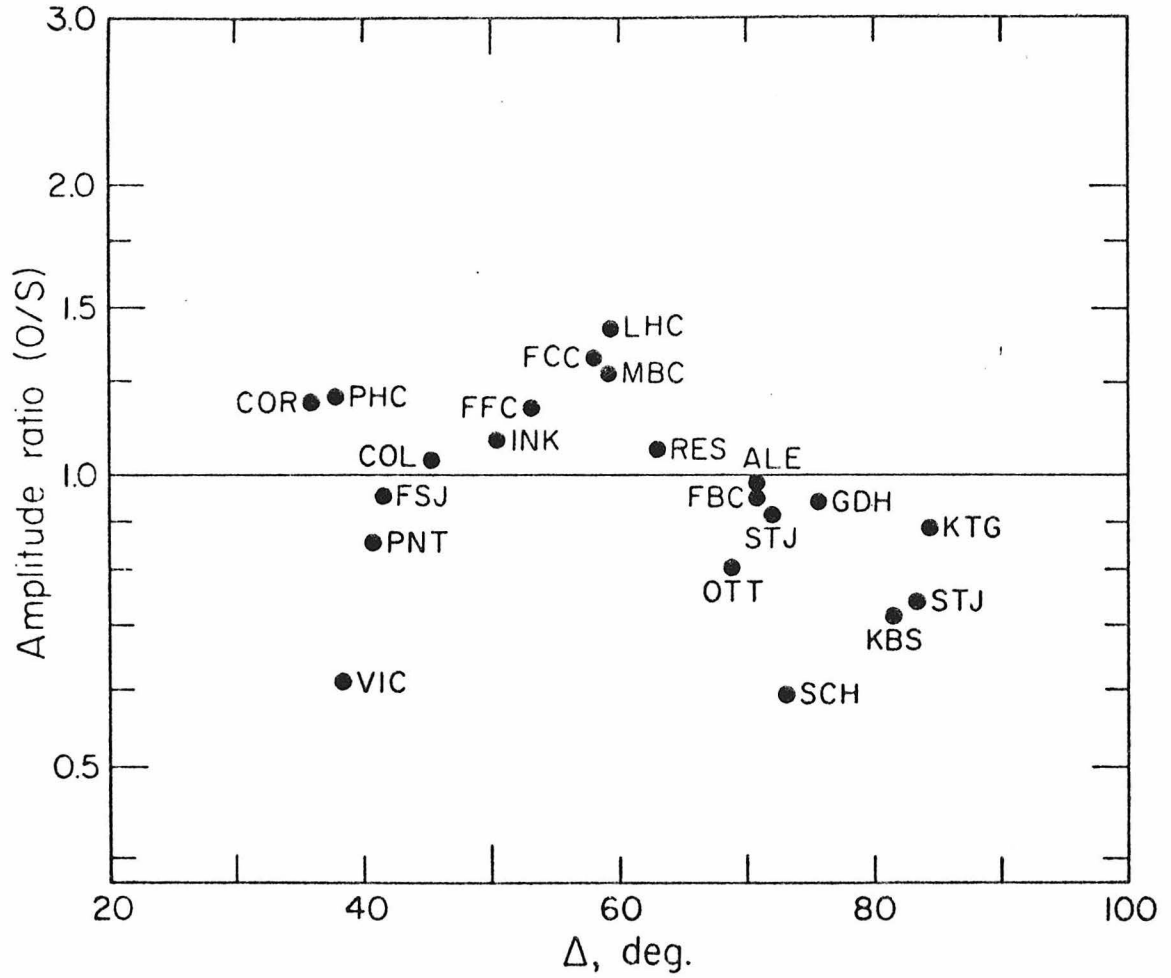


Figure II.1.7 SH amplitude ratios as a function of distance for the reduced Hawaiian earthquake data set (i.e., only those stations at azimuths between  $0^\circ$  and  $60^\circ$ ), assuming a moment of  $5.3 \times 10^{25}$  dyne-cm.

REFERENCES

- Allen, C. R. and J. M. Nordquist (1972). Foreshock, main shock and larger aftershocks of the Borrego Mountain earthquake, U.S. Geol. Survey Prof. Paper 787, 16.
- Biehler, S., R.L. Kovach and C. R. Allen (1964). Geophysical framework of northern end of Gulf of California structural province, Am. Assoc. Petroleum Geologists Mem. 3, 126.
- Burdick, L. J. and G. R. Mellman (1976). Inversion of the body waves from the Borrego Mountain earthquake to the source mechanism, Bull. Seism. Soc. Am., 66, 1485.
- Doyle, H. A. and A. L. Hales (1967). An analysis of the travel times of S waves to North American stations in the distance range of 28° to 82°, Bull. Seism. Soc. Am., 57, 761.
- Duschenes, J. D. and S. C. Solomon (1977). Shear wave travel-time residuals from oceanic earthquakes and the evolution of the oceanic lithosphere, J. Geophys. Res., 82, 1985.
- Followill, F. E. and O. W. Nuttli (1970). Shear body wave travel times and velocity distribution in the lower mantle (abstract), Geol. Soc. Am., 66th Annual Mtg., 2, 92.
- Futterman, W. I. (1962). Dispersive body waves, J. Geophys. Res., 67, 5279.
- Hales, A. L. and J. L. Roberts (1970). Shear velocities in the lower mantle and the radius of the core, Bull. Seism. Soc. Am., 60, 1427.
- Hart, R. S. (1975). Shear velocity in the lower mantle from explosion data, J. Geophys. Res., 80, 4897.

- Helmberger, D. V. and D. G. Harkrider (1972). Seismic source descriptions of underground explosions and a depth discriminate, Geophys. J. R. astr. Soc., 31, 45.
- Ibrahim, A. K. and O. W. Nuttli (1967). Travel-time curves and upper mantle structure from long period S waves, Bull. Seism. Soc. Am., 57, 1063.
- Jeffreys, H. and K. E. Bullen (1940). Seismological Tables, Brit. Assoc. Adv. of Sci., Gray-Milne Trust, London, 55 pp.
- Sengupta, M. K. (1975). The structure of the earth's mantle from body wave observations (Ph.D. dissertation), Massachusetts Institute of Technology, Cambridge, Mass., 579 pp.

SECTION II.2 SHEAR WAVE-TRAVEL TIMES FROM SSABSTRACT

The seismic shear phase SS is considered as a tool in the reconnaissance of the earth. The Hilbert transform is empirically verified as a reasonable mimic of the distortion incurred at the internal caustic in the propagation of SS. Travel times are obtained by a waveform correlation technique for 26 well recorded SHSH waves from the 1968 Borrego Mountain earthquake. Significant variation is found in the travel time residuals for paths reflected under the Canadian shield. A correlation of the variation with tectonic sub-province is suggested. The data are sufficiently precise to indicate lateral heterogeneity of several percent in the upper mantle velocities within the Canadian shield.

INTRODUCTION

The relatively fixed distribution of sources and receivers used in the study of the earth's interior is a fundamental impediment to progress in seismology today. Sources in new locations are impractical, since, to be utilitarian, they must be nuclear explosions. Ocean bottom seismometers are an alternative to the fixed, land based receivers. However, until employment of sufficient numbers is accomplished and enough large events are recorded, their contribution will be small.

The study of the shear phase ScS has opened a novel approach to bridging the impediment: ScS<sub>n</sub> in its traverse from source to core to free surface to core to receiver samples an intermediary portion of the earth. Multiple ScS travel times (Okal and Anderson, 1975; Sipkin and Jordan 1975, 1976; Butler 1977; Okal, 1978) and attenuation data

(Jordan and Sipkin, 1977) have provided much information on the lateral variation of the earth's properties and fuel for mantle dynamical theory (Jordan, 1975a,b).

The purpose of this paper is to document preliminary results in the development of the seismic shear phase SS as an earth reconnaissance tool. SS is a shear wave which reflects once off the earth's free surface at the midpoint of its propagation. However, due to distortion effects in its propagation, analysis of SS is not as straightforward as ScS.

The development of SS as a useful seismological tool is a natural progression from our increasing experience with waveform modeling of body waves. This experience is manifested in two ways: (1) our understanding of and ability to model earthquake sources, and (2) the capability of using these now known sources to study propagation problems in the earth.

In recent years a technique has been developed using generalized ray theory to determine detailed fault parameters for shallow events based on waveforms of teleseismic body phases. The method uses a modified ray theory which includes crustal phases at the source-P, pP, sP, etc.-as well as crustal interactions at the receiver. Long-period waveforms are then synthesized and compared with the observed in the time domain using a correlation operator. Fault orientation such as strike, dip, and rake, as well as focal depth and source time duration are estimated based on the fit to the data, which generally includes waveforms as a function of azimuth and takeoff angle. The technique has been successfully applied to about two dozen events. Recent litera-

ture includes: 1967 Koyna, India earthquake (Langston, 1976); Borrego Mountain (Burdick and Mellman, 1976); Oroville earthquake (Langston and Butler, 1976); Puget Sound earthquake of 1965 (Langston and Blum, 1977) Truckee earthquake (Burdick, 1977); San Fernando earthquake (Langston, 1978); 1976 Tangshan China earthquake sequence (Butler et al., 1978); 1966 El Golfo earthquake (Ebel et al., 1978); 1969 New Hebrides earthquake sequence (Ebel, 1978); 1967 Caracas earthquake (Rial, 1978); 1973 Hawaiian earthquake (Chapter I.3)

This paper shall be concerned with an application of two of the above mentioned source studies to the problem of obtaining SS travel times.

#### REVIEW OF SS

SS is a shear wave which reflects once off the earth's free surface at the midpoint of its propagation. The nature of the propagation, however, is such that the wave interacts with an internal caustic and is phase shifted. At sufficiently high frequencies Jeffreys and Lapwood (1957) have shown that the distortion incurred is manifested as a constant  $\pi/2$  phase shift in each frequency.

The behavior of the high frequency asymptote has been treated by a body of acoustic literature (Arons and Tennie, 1950; Tolstoy, 1968; Blatstein 1977; Sachs and Silbiger, 1971). Hill (1974) has shown for an analytic velocity model that to maintain causality, the phase shift at low frequencies must go to zero. Helmberger (1973) attempted to model PP using a coarsely layered, but more realistic earth model by the generalized ray method.

In an observational vein, Choy and Richards (1975) demonstrated qualitatively that the pulse distortion of SS was well approximated by a constant  $\pi/2$  phase shift. Applying a frequency independent  $\pi/2$  phase shift is equivalent to the Hilbert transformation of a function to its allied function. It was found that the comparison of the waveforms of SS and Hilbert transformed S for several events was quite favorable. Some research has been conducted using the phase SS to extract travel times (Brune, 1964), torsional overtone dispersion (Brune and Gilbert, 1974), and shear attenuation (Brune, 1977). However, as these studies neglected distortional propagation effects due to the caustic, their results may have to be reevaluated.

The effect of Hilbert transformation is illustrated in Figure II.2.1, with a delta function. It is easily seen that obtaining a geometric ray arrival time for a phase distorted in this manner would be quite difficult by conventional visual picking methods. As an additional check to the justification of using a Hilbert transform to mimic the effect of the caustic, several S and SS waves were sought for the following fortuitous geometry. Stations were chosen for events for which S and SS leave the source at the same ray parameter and azimuth; that is, the station recording SS is twice the distance of the station recording S. In this way the S wave is nearly the input to SS before the distortion at the caustic. Three of these event-station-pairs are shown in Figure II.2.2. The middle trace for each event was produced by performing a Hilbert transformation upon the S wave (top trace), as suggested by Choy and Richards (1975). As SS suffers twice the attenuation of S, a Futterman Q operator with  $t^*=4$  was also applied to the middle trace. The fit

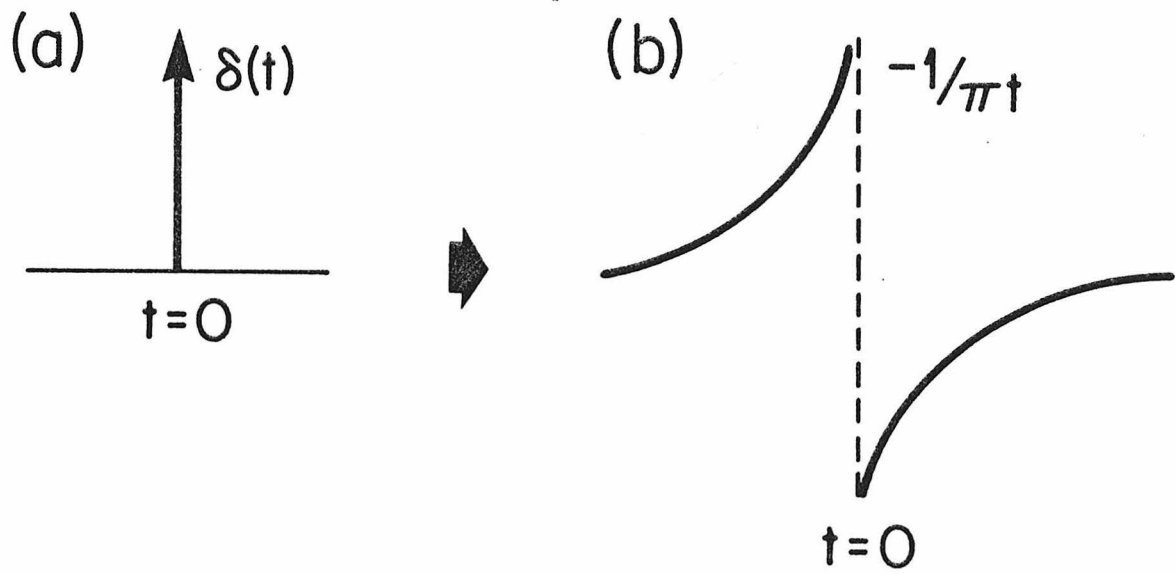


Figure II.2.1 a) Delta function arriving at time  $t=0$   
b) The Hilbert transform of  $\delta(t)$ ,  $(-1/\pi t)$ . Note that the energy arrives before the ray arrival time. (adapted from Choy and Richards, 1975).

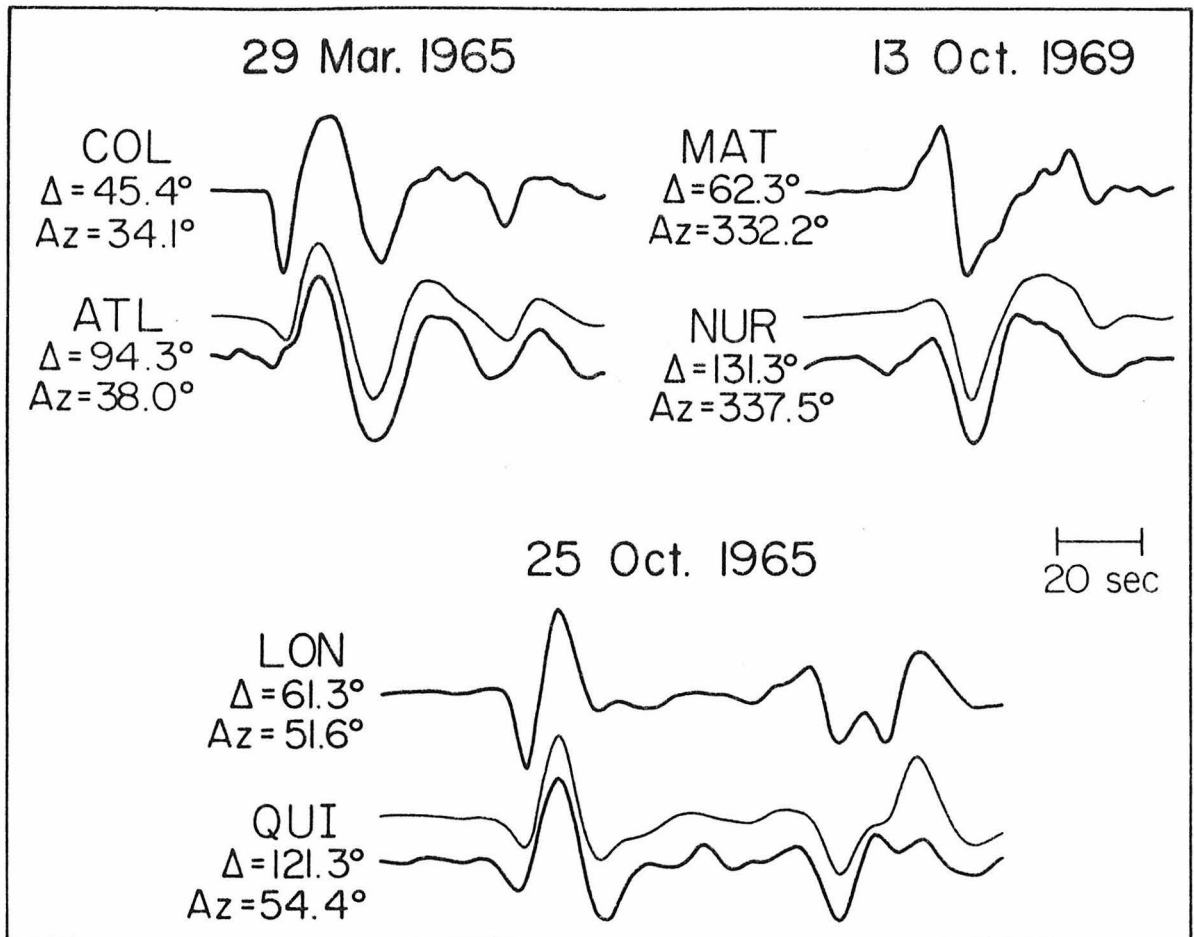


Figure II.2.2 Recordings of S and SS for three earthquakes where the station recording SS (lower trace) is roughly twice the distance from the source and at nearly the same azimuth as the station recording direct S (upper trace). The center trace for each event illustrates the effect of applying a Hilbert transform to the S wave (upper trace) to imitate the effect of the SS caustic.

between the synthetically produced SS and the observed is quite good - an important point since the phase distortion at the caustic is theoretically asymptotic to a constant  $\pi/2$  only at high frequencies.

#### TRAVEL-TIMES

As we have seen from Figures II.2.1 and II.2.2, it is difficult, if not impossible, to pick the conventional geometric arrival time of a distorted phase such as SS by visual onset methods. To overcome this difficulty, a waveform correlation method was utilized to determine travel times of SS.

All SS waves recorded by stations of the WWSSN for the 1968 Borrego Mountain earthquake and 1973 Hawaiian earthquake were collected, digitized, and rotated into SH and SV components of motion. The source time functions for these two events are well-constrained by the waveform source studies of, respectively, Burdick and Mellman (1976) and Chapter I.3. Synthetic SS waves are then generated using these mechanisms in the following manner. The ray parameter of SS for a particular station is the same as the ray parameter of S for a virtual station at half the distance to the source. Synthetic S waves are computed using the appropriate ray parameter and azimuth. The effect of the caustic of SS is mimicked by Hilbert transformation of the S wave to its allied function. The arrival time on the original S wave synthetic is used as the reference visual onset time. To include attenuation, the synthetics were convolved with a Futterman (1962) Q operator. Values of  $t_{\beta}^*$  between 8 and 10 were chosen to include nearly the range of uncertainty associated with the phase. Since the effect of errors in  $t^*$  become

more pronounced later in the waveform, only the initial major swing of the SS wave is used in the correlation procedure. A visual inspection of the overall likeness of the synthetic and observed waveforms is made in judging the quality of each observation. In the actual timing determination, it is possible not only to define the best correlation and hence the best estimate of the travel time, but also the total range of acceptable correlation. Thus, the precision of the travel time may be accurately estimated. The overall intent of the timing procedure is to produce as nearly as possible an onset time for SS that can be easily compared to previous S studies based on conventional visual timing methods.

The application of this waveform correlation method has been applied to S waves by Hart and Butler (1978) to the same earthquakes used in this study. The Borrego Mountain, California earthquake was a magnitude 6.4 strike-slip event which occurred on April 9, 1968 at 02:28:59.1 GMT (Allen and Nordquist, 1972). The error of the epicentral location is estimated to be within 3 km (Allen and Nordquist). The depth estimate of 11 km was confirmed by Burdick and Mellman (1976).

Within these limits the affect of origin time and hypocentral errors on seismic travel-times are bound by instrument timing accuracy. In 1968, the accuracy was 0.4 to 0.5 seconds or better. Burdick and Mellman (1976) demonstrated that the Borrego earthquake was actually a multiple event consisting of a main shock and two aftershocks. The source parameters describing these three events are given in Table II.

2.1. As the Borrego event was shallow, the observed shear waves are actually the combination of S and sS, and thus the SS synthetics were constructed to include both the direct ray and the near source, surface

TABLE II.2.1

SOURCE PARAMETERS FOR THE BORREGO MOUNTAIN  
AND HAWAII EARTHQUAKES

Borrego Mountain

April 9, 1968; Lat. = 33.190° N, Long. = 116.128° W

Main shock: 02:28:59.1 GMT

Strike = -45°, Dip = 81°, Rake = 178°, Depth = 8 km

Moment =  $11.2 \times 10^{25}$  dyne-cm

1st aftershock: 02:29:08.0 GMT

Strike = 128°, Dip = 77°, Rake = 12°, Depth = 7 km

Moment =  $2.46 \times 10^{25}$  dyne-cm

2nd aftershock: 02:29:14.4 GMT

Strike = -91°, Dip = 28°, Rake = 98°, Depth = 11 km

Moment =  $0.78 \times 10^{25}$  dyne-cm

Hawaii

April 26, 1973; Lat. = 19.903° N. Long. = 155.130° W

Main shock: 20:26:30.8 GMT

Strike = -9°, Dip = 81°, Rake = 152°, Depth = 42 km

Moment =  $3.8 \times 10^{25}$  dyne-cm

1st aftershock: 20:26:34.0 GMT

Strike = -14°, Dip = 94°, Rake = 145°, Depth = 32 km

Moment =  $1.2 \times 10^{25}$  dyne-cm

reflection.

The Hawaiian earthquake occurred on April 26, 1973 at 20:26:30.8 GMT northeast of the city of Hilo at a depth of 42 km. The local control for this event is good, though not to the degree of the Borrego Mountain earthquake. The problem with the Hawaiian earthquake is that the epicenter lies just off the coast and thus slightly outside the local seismic network. The source mechanism of this event (Chapter I.3) is one of a double event with both shocks having similar mechanisms. The source parameters are given in Table II.2.1. As the depth of the event as determined by the teleseismic waveform analysis agrees well with the local determination, the overall accuracy to which travel times may be trusted is to within two seconds. As the near source, surface reflected shear energy arrives nearly 15 seconds after the direct arrivals for these depths, only the direct ray is included in the synthetics.

The Borrego Mountain data set yielded 26 high quality transverse SS or SHSH, observations; the Hawaiian data set yielded 12 SHSH observations. These high quality observations were then carefully redigitized twice and averaged together to minimize errors. The lesser number of high quality Hawaiian observations is due to an azimuthal near source travel time anomaly - reported in the previous section - presumably indicating near source, laterally varying structure. This anomaly lends greater uncertainty to any SS time for the Hawaiian event. The S waveform observations, however, are well matched by synthetics generated for the source model. The 12 SS observations from the Hawaiian earthquake were modelled primarily as an additional test to see how well synthetic SS can match observed waveforms. In a treatment of SVSV for

both events, it was found that none of the synthetics satisfactorily matched the observations. SV is notoriously known to exhibit greater complexity than SHSH. These complexities may be attributed in part to P-SV conversions at the source, midpoint reflection, and receiver and in part to interference with SV coupled PL waves.

The comparison between SS observations and synthetics is illustrated in Figures II.2.3 and II.2.4 for the Borrego Mountain earthquake, and Figure II.2.5 for the Hawaiian earthquake. The upper trace for each station shows the synthetic S wave generated for the appropriate source time function. An SS wave is produced by Hilbert transformation of the S wave to yield the middle traces. The match between the synthetic and observed SS is quite good in all cases, affording us a large measure of confidence in the method. The quality of the fits also indicates considerable potential in using SS for additional constraints in waveform studies of earthquake source mechanisms. As SS observations are available for twice the range of S waves, SS may be very useful in source studies hindered by azimuthal gaps in station coverage due to the oceans.

In anticipation of questions to be raised in the discussion section, tests were conducted to determine the importance of midpoint reflection and receiver structure. To accomplish this several crust-to-mantle transition models were tried by computing the transfer function for the layered stack by Haskell propagator matrices (Haskell, 1953; Harkrider, 1964, Fuchs, 1966). These transfer functions were then convolved with the synthetic SS. The effect of a 6.5 km/sec, 33 km thick crust over an 8.0 km/sec mantle is small due to the low amplitude and time separation of the precursors and reverberations. Large mid-crustal discontinuities can pro-

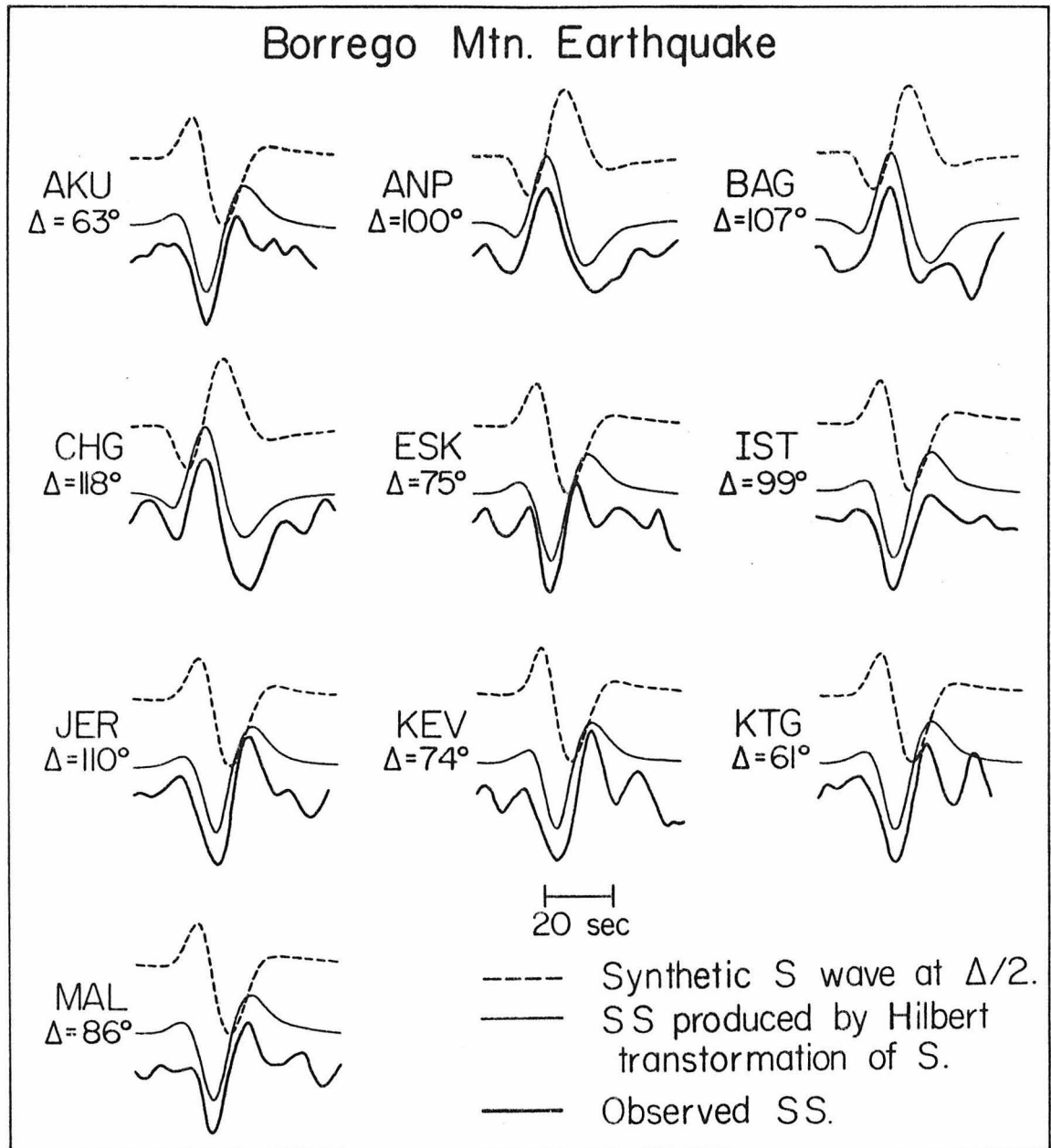


Figure II.2.3 A comparison between observed SS from the Borrego Mountain earthquake and synthetic SS. The synthetics were generated using the source time function of Burdick and Mellman (1976) and corrected for the SS caustic by Hilbert transformation.

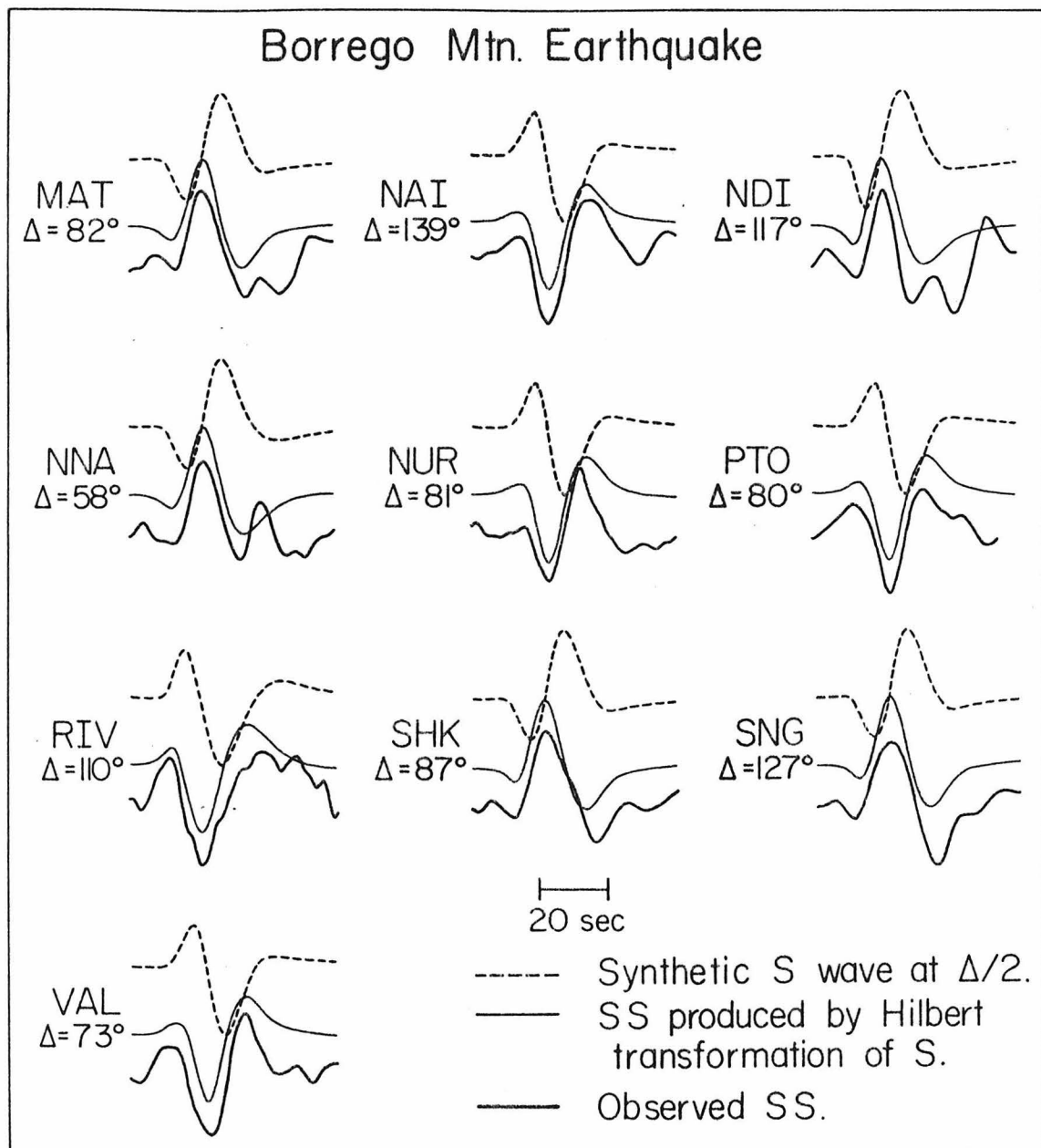


Figure II.2.4 A comparison between observed SS from the Borrego Mountain earthquake and synthetic SS. The synthetics were generated using the source time function of Burdick and Mellman (1976) and corrected for the SS caustic by Hilbert transformation.

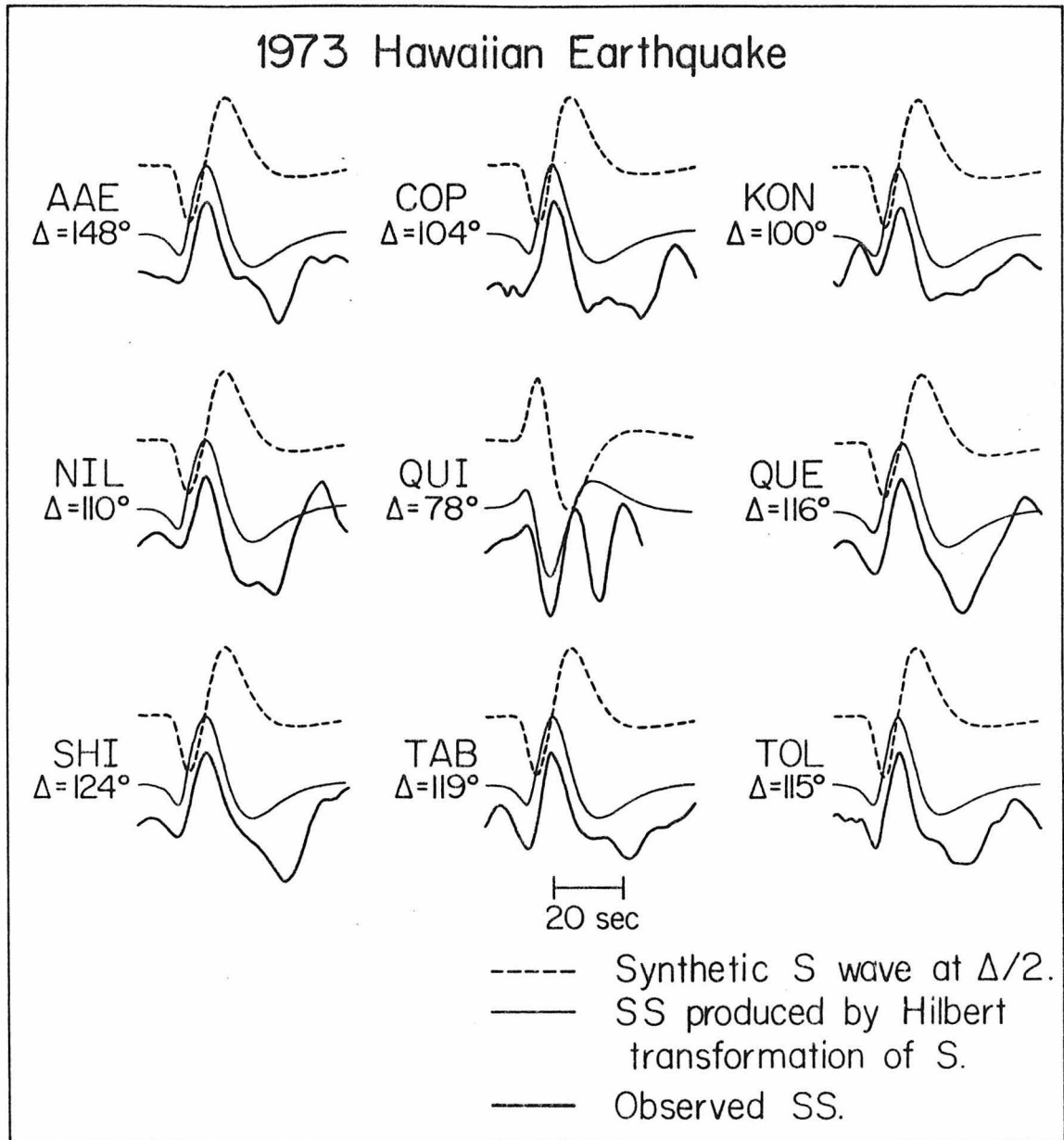


Figure II.2.5 A comparison between observed SS from the 1973 Hawaiian earthquake and synthetic SS. The synthetic SS phases were generated using the source time function determined in chapter I.3 and corrected for the caustic by Hilbert transformation.

uce distortion effects. However, crustal sections for the midpoint reflections of SS used in this study are not known in sufficient detail to justify any corrections of this nature. The only exception to this is for the SS recorded at JER from the Borrego Mountain earthquake. The midpoint reflection for this path lies in the middle of the Greenland icecap, whose thickness is nearly 3 km. In generating the synthetic SS for JER the crust-ice reflection and ice reverberations are included.

Tables II.2.2 and II.2.3 list SS travel times for the Borrego Mountain and Hawaiian earthquakes, respectively. The distance and azimuth of the station, coordinates of the midpoint reflection, and the precision of each measurement are included. The times have been corrected for surface elevation of the receiver and midpoint reflection, and the ellipticity at the source, midpoint reflection, and receiver. The Borrego data have been corrected to a surface focus; the Hawaiian data to 33 km depth. No station corrections have been applied to the data. As discussed above, the Borrego Mountain times are accurate to within 0.5 seconds. In Figure II.2.6 the Borrego data are plotted in an azimuthal equal-distance projection centered at the epicenter. In the previous section we found a large azimuthal source anomaly associated with the Hawaiian S data, presumably due to lateral heterogeneity. As the interpretation of SS travel times from Hawaii suffer the same complications, only the Borrego data will be discussed.

Differential SS-S times are shown in Table II.2.4 for stations whose S times were previously measured in Chapter II.1. These differential times are plotted in Figure II.2.7 in an azimuthal equal-area projection centered on the Borrego epicenter. The lower center JB residual is a

TABLE II.2.2

SS TRAVEL TIME RESIDUALS  
FROM BORREGO MOUNTAIN

STATION	DELTA	AZIMUTH	REFLECTION POINT		T-T <sub>JB</sub> (SEC.)	ERROR (SEC.)
			LAT.	LONG.		
AKU	63.42	27.3	58.95°N	88.41°W	+5.0	+0.8 -0.8
ANP	100.14	309.0	49.16°N	178.66°E	+5.1	+1.5 -0.8
BAG	106.79	303.1	44.02°N	175.09°E	+3.1	+1.0 -0.6
CHG	118.39	321.7	57.77°N	160.53°E	+7.5	+1.4 -1.4
ESK	74.91	33.0	59.51°N	75.62°W	-4.3	+0.9 -1.6
JER	109.96	25.8	68.71°N	38.69°E	+8.8	+1.1 -1.3
IST	99.45	26.0	68.14°N	32.85°E	+4.9	+0.8 -0.6
KEV	73.91	12.6	68.16°N	95.61°W	+1.1	+1.9 -1.9
KTG	60.50	22.7	59.53°N	93.70°W	+1.7	+0.9 -0.6
MAL	85.70	48.5	51.21°N	62.06°W	+0.3	+0.9 -0.9
MAT	81.92	308.4	49.01°N	166.94°W	+4.8	+0.8 -0.9
NAI	139.33	44.3	48.96°N	19.66°W	+10.6	+0.9 -0.8
NDI	117.19	346.8	78.80°N	149.22°E	+4.9	+1.0 -.05
NNA	58.49	133.4	11.26°N	94.92°W	+11.2	+0.5 -0.7
NUR	81.26	18.5	68.77°N	81.56°W	+1.4	+0.8 -0.7
PTO	80.43	46.9	52.00°N	66.44°W	-3.1	+1.1 -0.5
RIV	109.57	241.9	0.48°S	162.24°W	+8.5	+1.0 -1.0
SHK	86.73	309.5	49.86°N	171.08°W	+6.8	+0.9 -0.8
SNG	126.81	312.1	48.49°N	158.07°E	+10.3	+1.0 -1.0
VAL	73.40	38.4	56.23°N	74.46°W	-7.6	+1.8 -1.8

TABLE II.2.3

## SS TRAVEL TIME RESIDUALS

FROM HAWAII

<u>STATION</u>	<u>DELTA</u>	<u>AZIMUTH</u>	<u>REFLECTION POINT</u>		<u>T-T<sub>JB</sub></u>	<u>ERROR</u>
			<u>LAT.</u>	<u>LONG.</u>	<u>(SEC.)</u>	<u>(SEC.)</u>
AAE	148.16	333.3	64.47°N	110.55°E	+4.6	+1.0 -0.8
COP	103.99	7.2	70.85°N	137.71°W	+4.4	+0.9 -1.3
KON	99.77	7.8	68.73°N	138.61°W	+6.7	+0.8 -0.9
NIL	109.56	318.6	50.71°N	146.70°E	+6.1	+1.6 -1.1
QUE	115.82	319.9	52.33°N	142.08°E	+4.5	+1.1 -1.1
QUI	77.50	94.8	12.48°N	115.44°W	+10.6	+0.5 -1.1
SHI	124.02	330.8	62.31°N	137.63°E	+3.9	+1.0 -1.0
TAB	118.92	340.7	69.66°N	150.37°E	+8.4	+0.9 -0.9
TOL	114.70	24.2	64.00°N	100.80°W	+0.8	+0.8 -0.8

TABLE II.2.4

SS-S DIFFERENTIAL TRAVEL TIME RESIDUAL  
FROM BORREGO MOUNTAIN

STATION	S WAVE*		SS WAVE		SS-S	
	T-T <sub>JB</sub>	ERROR	T-T <sub>JB</sub>	ERROR	T-T <sub>JB</sub>	ERROR
AKU	+9.2	+0.5 -0.5	+5.0	+0.8 -0.8	-4.2	+1.3 -1.3
ESK	+5.0	+0.6 -0.3	-4.3	+0.9 -1.6	-9.3	+1.3 -2.6
KEV	+3.6	+0.5 -0.6	+1.1	+1.9 -1.9	-2.5	+2.5 -2.4
KTG	+5.8	+0.7 -0.3	+1.7	+0.9 -0.6	-4.1	+1.2 -1.3
MAL	+4.9	+0.7 -0.5	+0.3	+0.9 -0.9	-4.6	+1.4 -1.6
NNA	+6.7	+0.5 -0.8	+11.2	+0.5 -0.5	+4.5	+1.3 -1.0
NUR	+5.2	+0.3 -0.7	+1.4	+0.8 -0.7	-3.8	+1.5 -1.0
PTO	+4.8	+0.5 -0.7	-3.1	+1.1 -0.5	-7.9	+1.8 -1.0
SHK	+4.0	+0.5 -0.5	-6.8	+0.9 -0.8	-2.8	+1.4 -1.3
VAL	+4.2	+0.5 -0.6	-7.6	+1.8 -1.8	-11.8	+2.4 -2.3
QUI**	+8.0	+0.5 -0.3	+10.6	+0.5 -1.1	+2.6	+0.8 -1.6

\*Chapter II.1

\*\*from 1973 Hawaiian earthquake

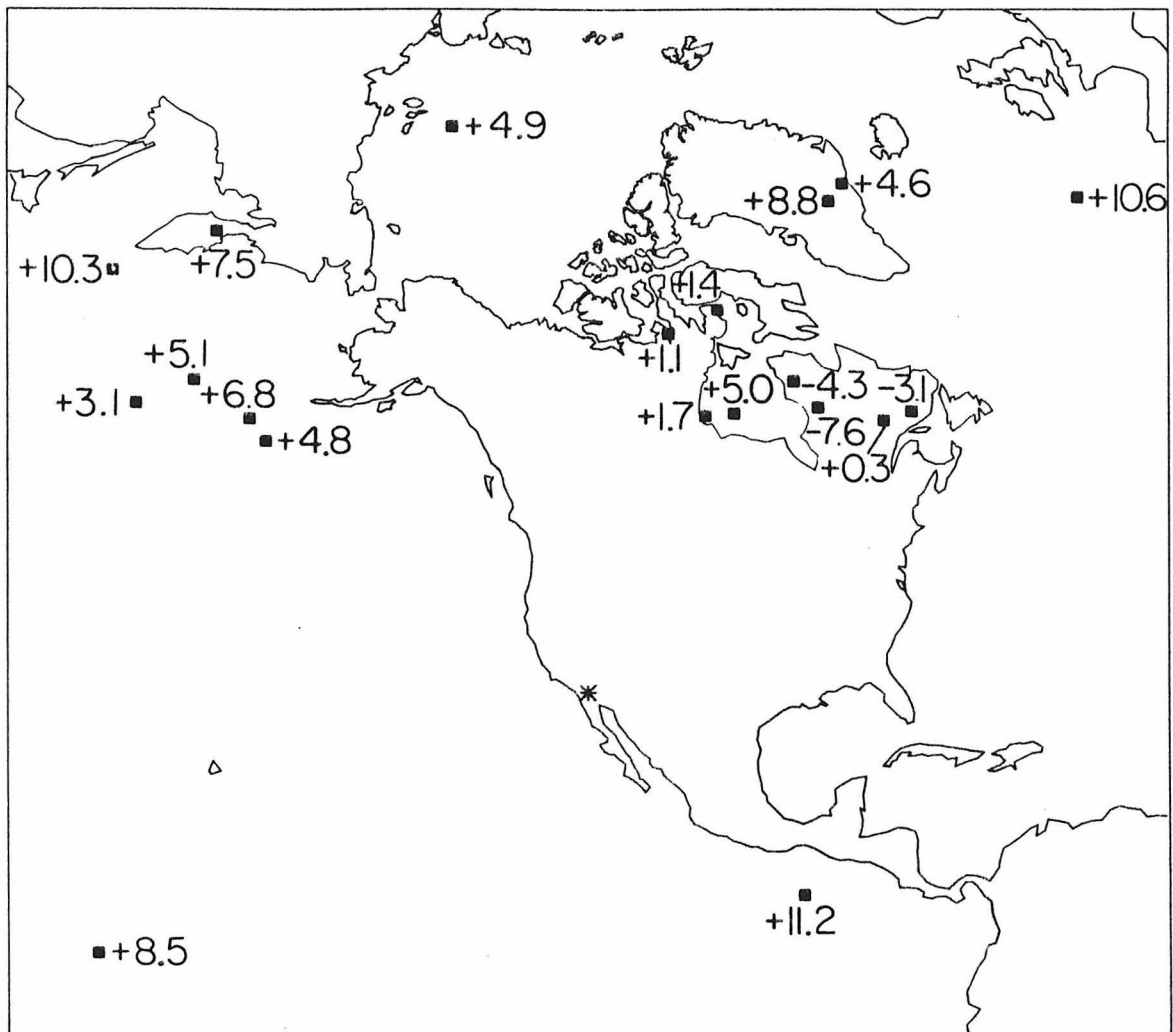


Figure II.2.6 Travel time residuals with respect to the Jeffreys-Bullen times (positive = late) of SS from the 1968 Borrego Mountain earthquake (asterisk). The square indicates the mid-point of the propagation path where the phase reflects off the earth's free surface.

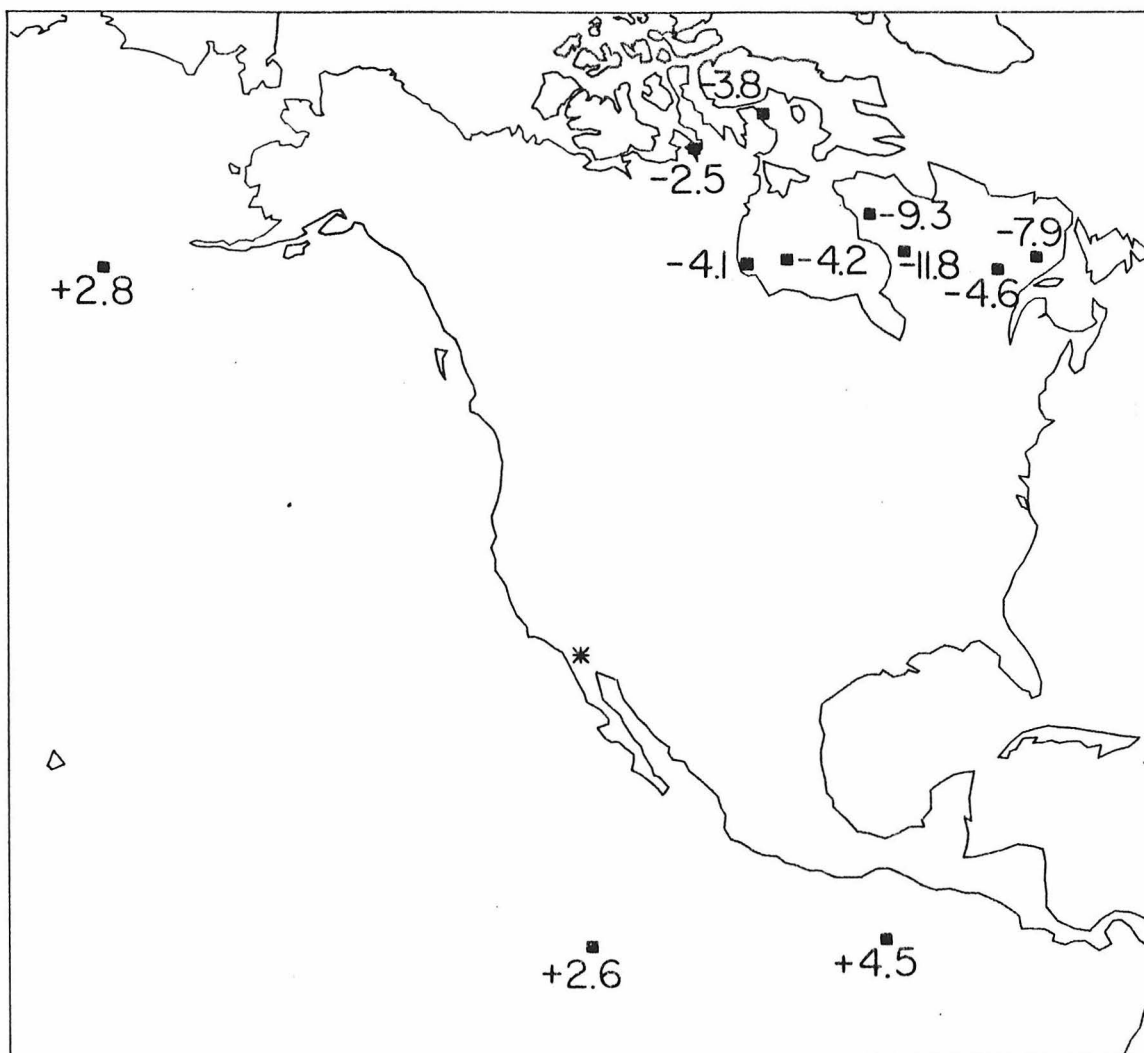


Figure II.2.7 Differential travel time residuals (with respect to the Jeffreys-Bullen times; positive = late) for SS-S from the 1968 Borrego Mountain earthquake (asterisk). The squares indicate the mid-points of the propagation paths where the phase reflects off the earth's free surface. The +2.6 second differential travel time residual on the lower center is from the 1973 Hawaiian earthquake.

differential time from the Hawaiian earthquake for station QUI.

No station corrections were applied to the absolute SS times. This choice was made for a number of reasons. S station anomalies determined by different studies are at times significantly inconsistent (Doyle and Hales, 1967; Hales and Roberts, 1970; Sengupta, 1975). The quality of the corrections themselves is not homogeneous. Many are based on relatively few measurements. The standard deviations of the corrections often do not preclude a no correction value. No azimuthal dependence was included in the above S studies whereas P corrections (Bolt and Nuttli, 1966) and S-P corrections (Uhrhammer, 1977) have been shown to exhibit significant azimuthal variations. A comparison was made between the SS-S differential times and absolute SS times, with and without station corrections. Station corrections were found to degrade more often than improve agreement. Although a blanket application of station corrections to the absolute SS travel times does not seem to be desired, a knowledge of possible corrections is useful in judging individual SS travel time anomalies. For this reason a list of station corrections from Sengupta (1975) is included in Table II.2. 5.

#### DISCUSSION

The Borrego data in Figure II.2.6 show remarkable range in the JB residuals - from 7.6 seconds fast in the Canadian shield to 11.2 seconds slow in the Guatemalan Basin. In this figure it is more important to consider the variation of the residuals in a relative sense as opposed to each individual measurement. In the previous section we found that the baseline of the S wave travel times for Borrego was 6 seconds late

TABLE II.2.5

## STATION ANOMALY FOR S TRAVEL TIMES

(SEN GUPTA, 1975)

<u>STA</u>	<u>VALUE*</u>	<u>S.D.</u>	<u>N</u>
AAE	+5.88	2.82	4
ANP	-0.66	4.09	12
BAC	0.37	2.47	13
CHG	-1.07	2.07	13
COP	-3.06	3.11	8
ESK	-1.71	2.06	13
JER	-2.63	4.00	7
IST	-4.04	3.99	3
KEV	-3.90	1.65	7
KON	-2.29	1.12	8
KTG	-0.63	1.86	4
MAL	-0.93	1.93	5
NAI	5.67	3.21	7
NDI	-3.47	1.99	15
NIL	-1.80	0.42	2
NNA	3.20	4.33	4
NUR	-4.36	1.26	8
PTO	0.17	2.84	10
QUE	-1.30	2.37	10
QUI	1.00	0.00	1
RIU	1.94	1.76	12
SHI	-3.24	0.92	9
SHK	0.34	2.57	4
TAB	-0.79	2.36	6
TOL	4.43	0.81	5
VAL	-1.37	1.12	7

\*negative is fast

with respect to JB. Thus, even though the Borrego times are accurate in an absolute sense to within 0.5 seconds, the source region has associated with it a 6 second slow, travel time anomaly. As there is no apparent azimuthal trend in the anomaly, an approximate source correction of six seconds will be automatically applied in the discussion of these points. The differential times presented in Figure II.2.7 are naturally free of this anomalous effect in the source region, and also anomalies at the receivers. All travel times are discussed relative to the Jeffreys-Bullen tables (1940). Source corrected absolute times were compared to differential times at common stations. The average agreement of the two timing methods was within 1.2 seconds. Table II.2.6 lists a brief description of the reflection points for the data in Figures II.2.6 and II.2.7.

Two-way SS reflections in the north Pacific and southwest of Hawaii scatter at roughly  $\pm 2.7$  sec around JB values. The reflection in the north Atlantic is 4.6 seconds slower than JB, but a correction for the receiver, NAI, may be in order. Station NAI - Nairobi, Kenya - lies along the East African rift zone and shows a + 5.7 station anomaly in Table II.2.5 (from Sengupta, 1975). This correction brings the value, -1.1 seconds, in agreement with the Pacific data. The reflection at the Siberian continental shelf in the Arctic ocean for a receiver at NDI on the Indian shield is 1.1 second fast. A station correction of -3.5 seconds decreases this value to +2.4 seconds slow relative to JB. The two reflections at the Kurile-Kamchatka subduction zone are + 1.5 and + 4.6 seconds slow.

TABLE II.2.6

## DESCRIPTION REFLECTION POINTS

FOR FIGURES II.2.6, II.2.7

<u>STATION</u>	<u>SS T-T<sub>JB</sub> (SEC.)</u>	<u>SS-S T-T<sub>JB</sub> (SEC.)</u>	<u>REFLECTION POINT</u>
AKU	+5.0	-4.2	Hudson Bay, Phanerozoic
ANP	+5.1		north Pacific, ~ 70 m.y.
BAG	+3.1		north Pacific, ~ 70 m.y.
CHG	+7.5		Kamchatka, subduction zone
ESK	-4.3	-9.3	Canadian shield, Superior province
JER	+8.8		Greenland shield
IST	+4.9		Greenland shield
KEV	+1.1		Canadian shield, Churchill province
KTG	+1.7	-4.1	Hudson Bay, Phanerozoic
MAL	+0.3	-4.6	Canadian shield, Grenville province
MAT	+4.8		north Pacific, ~ 70 m.y.
QUI		+2.5	east Pacific, 10-36 m.y.
NAI	+10.6		north Atlantic, 53-65 m.y.
NDI	+4.9		Siberian continental shelf
NNA	+11.2	+4.5	Guatemala basin, ~ 40 m.y.
NUR	+1.4	-3.8	Canadian shield, Churchill province
PTO	-3.1	-7.9	Canadian shield, Grenville province
RIV	+8.5		central Pacific, ~ 100 m.y.
SHK	+6.8		north Pacific, ~ 70 m.y.
SNG	+10.3		Kurile islands, subduction zone
VAL	-7.6	-11.8	Canadian shield, Superior province

The source corrected residuals of SS recorded at JER(-2.8 sec) and IST (-1.4) which reflect at Greenland are comparable to the oceanic values. Although the geology of Greenland beneath the ice cap is not known, the exposed edges are Precambrian shield. The SS residuals reflecting beneath the Canadian shield are contrastingly quite fast. The differential SS-S times in Figure II.2.7 range from 2.5 to 11.8 seconds faster than JB. The extremely slow times for the Greenland shield cannot be explained by a receiver anomaly, as the station corrections for JER and IST from Sengupta (1975) in Table II.2.5 are fast with respect to the average earth.

The source corrected absolute SS times for oceanic reflections - whether or not station corrections are applied - average at the JB baseline. The three differential SS-S times in Figure II.2.7 reflecting beneath the Pacific average 3.3 sec slower than JB. The reflections in the Pacific do not substantially correlate with the age of the oceanic lithosphere. The data in north Pacific, ~70 m.y., range between -3.3 to +2.8 sec. The datum in the 100 m.y. central Pacific is 2.5 sec slower than JB. The slowest time, + 4.5 seconds, lies on 40 m.y. old crust, while the +2.6 second residual reflects beneath 10-25 m.y. old lithosphere.

The largest shear anomaly in the data set is not an SS time, but rather is the six second slow anomaly of the Borrego source (Chapter II.1). This is equivalent to a +12 second SS residual and is significantly slower than any of the SS differential or source corrected absolute times. The Borrego epicenter is located at the western edge of the Salton trough in southern California. This is a region of high heat

flow, geothermal activity, gravity variations and extensional tectonics, and is viewed as a continental continuation of the active spreading center in the Gulf of California. Duschenes and Solomon (1977) have measured shear wave residuals from ridge crest and intraplate oceanic earthquakes. When plotted as a function of age these (one-way) residuals show a  $6 \pm 1$  sec decrease from ridge crest to lithosphere 100 m.y. old. As the origin times of these events are determined by P waves and thus implicitly contain P delay information, the true S decrease with age may be a second or so greater. The Borrego earthquake shear anomaly is approximately  $6 \pm 1.5$  seconds slower than one way SS residuals for reflections beneath the ~70 m.y. old north Pacific, and is consistent with the oceanic S delay versus age variation of Duschenes and Solomon (1977) between the ridgecrest and 70 m.y. old lithosphere. This agreement indicates that the average shear velocity beneath the Salton trough in southern California is comparable to average shear velocities at mid-ocean ridge spreading centers.

A useful framework in which to view these SS data is within the context of ScS travel-times (Okal and Anderson, 1975; Sipkin and Jordan, 1975, 1976; Okal, 1978). However, some care must be taken to properly compare SS times with ScS times. SS samples more of the upper mantle in its propagation and reflection than ScS, which travels nearly vertically. For example, the propagation path of SS in the upper 225 km of

of the earth is approximately 25% longer than a vertical path. Thus SS travel time anomalies need to be reduced by a rough factor of 0.8 for comparison with ScS data.

The method of timing the SS phases in this study is different from the method employed in the ScS studies. SS times were picked by a waveform correlation between the observations and synthetic seismograms. Synthetic shear waves were generated for the earthquake source time function at the appropriate ray parameter and azimuth, and corrected for attenuation. The reference arrival time is determined from the synthetic. The synthetics are then Hilbert transformed to mimic the distortional effects at the caustic and compared to the observations. In the correlation between the observations and synthetics to pick the best arrival time, only the initial portion of the waveforms is used to minimize effects due to uncertainties in the attenuation.

The ScS times of Okal and Anderson (1975), Sipkin and Jordan (1975, 1976), and Okal (1978) are differential measurements between multiple ScS and either ScS or S. The timing method is by cross-correlation of the phase pairs. Butler (1977) has pointed out that cross-correlation timing between seismic phases which have suffered different amounts of attenuation is biased systematically late with respect to a method based upon the visual onsets of the waveforms. The approximate amount of bias is calculated by Butler (1977) comparing onset timing to cross-correlation timing using synthetic seismograms generated for a range of relative attenuations. These results are applicable in the comparison of ScS times determined by cross-correlation and SS times which were determined by waveform correlation referenced

to the onset time of the synthetic. Basically the ScS times are about 1 to 4 seconds slower than corresponding SS times; the amount of the effect being dependent upon the attenuation of ScS. Estimates of  $Q_{\beta}$  for ScS range between  $Q_{\beta} = 600$  (Anderson and Kovach, 1964; Kovach and Anderson, 1964) for South American data to  $Q_{\beta} = 156 \pm 13$  (Jordan and Sipkin, 1977) for multiple ScS reflections in the western Pacific. Regional differences in attenuation will vary this correction between SS and ScS times.

The average two-way ScS residual for "average ocean" (70-90 m.y.) is +1.6 seconds (Okal, 1978) to +2.4 seconds (Sipkin and Jordan, 1976). The SS data in the 70 m.y. north Pacific fall +3 seconds around the JB baseline. The SS-S differential times for reflections beneath the Canadian shield average 6 seconds faster than JB, and compare well with the -4 second average ScS residual for shields (Sipkin and Jordan, 1976). The SS residuals for reflections beneath the Greenland ice cap, +2.8 sec and -1.4 sec, are comparable to the oceanic values. As the exposed edges of Greenland are Precambrian shield, these slow times represent a significant exception to shield versus ocean differences proffered by Sipkin and Jordan (1976).

Although with such a sparse sampling one cannot rule out coincidence, there appear to be some systematics in the Canadian shield values. The Canadian shield is not a single structural entity; rather, it comprises seven tectonic provinces of Precambrian age, each with its own stratigraphic and structural history (Stockwell, 1964). Hudson Bay is of Phanerozoic age. Figure II.2.8 plots the differential SS-S times in relation to these tectonic provinces; the precision of the residuals

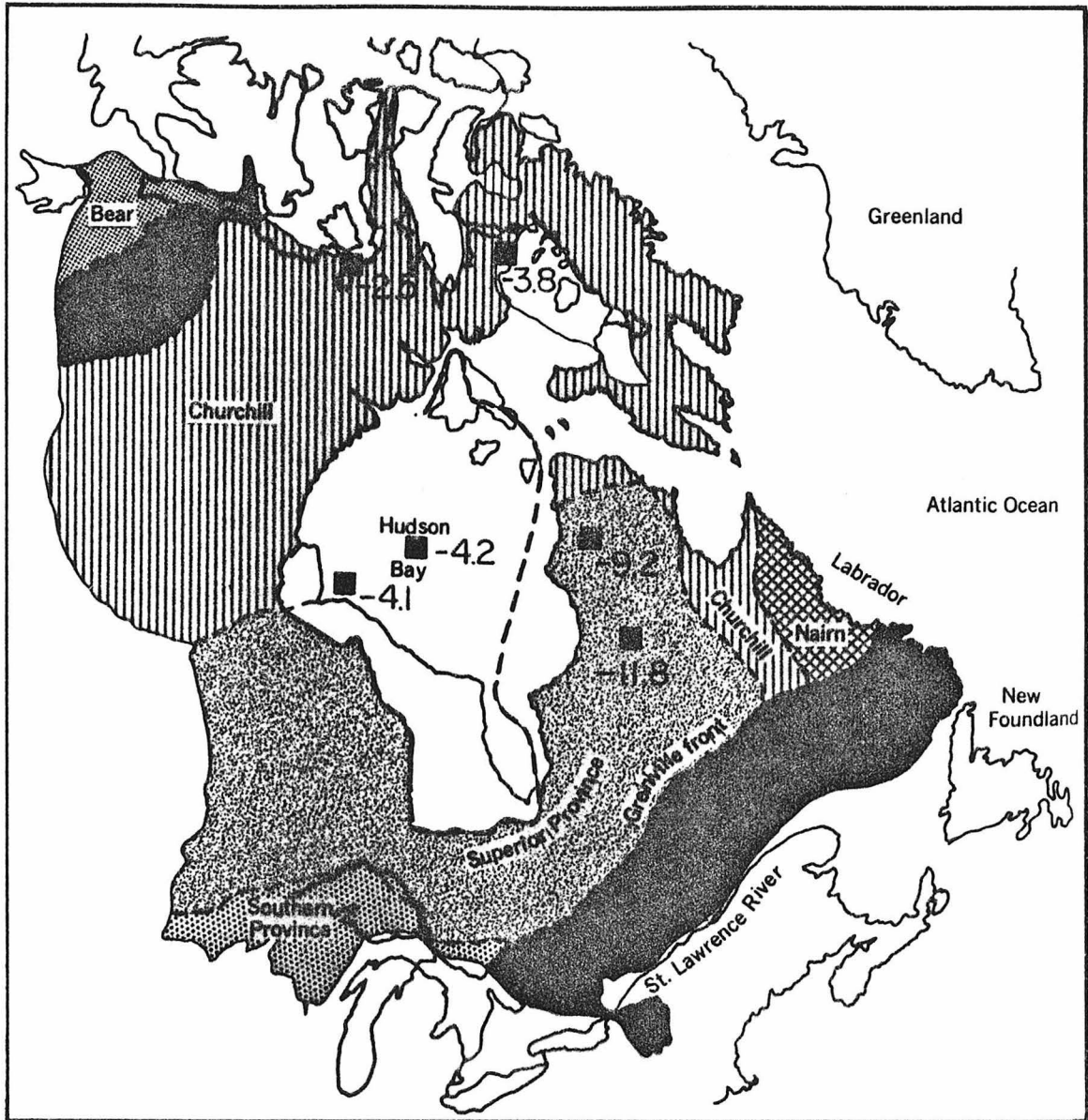


Figure II.2.8 Differential travel time residuals (with respect to Jeffreys-Bullen times; negative = early) for SS-S from the 1968 Borrego Mountain earthquake. The squares mark the midpoint reflection of SS in relation to structural provinces within the Canadian shield.

is noted in Table II.2.4. The data naturally fall such that each of the four provinces sampled is characterized by a self-consistent, yet distinct, travel time anomaly. This variation does not correlate with age: Superior ~2500 m.y.; Churchill ~1700 m.y.; Grenville ~950 m.y.; Hudson Bay <600 m.y. (Stockwell, 1964). Correlations with other geophysical parameters were also unsatisfactory - including heat flow, gravity, magnetism, and postglacial uplift.

The extremal difference in the travel time residuals to be explained - including error - is 4.5 seconds between the Churchill province (KEV) and the Superior province (VAL). For a vertical incidence this value corrects to 3.6 seconds. A number of studies (see Berry, 1973; Hashizume, 1976) have been concerned with the determination of regionalized crust and upper lid velocity sections. Hashizume (1976) using surface waves states "The Superior province, the Churchill province and the Hudson Platform are formed of a quite uniform crustal structure when they are measured in the scale of earth structure and regionalization assumed. The regional variations of shear velocities of the granitic and basaltic layers (middle and lower crust) of the above regions are small, less than 0.015 km/sec, whereas the regional variations of the upper-mantle velocities are a little larger. The Grenville province may have a higher velocity structure..." Berry and Fuchs (1973) report a seismic refraction survey in the northeast Canadian shield. The average thickness of the Superior crust is 34 km compared to 39 for Grenville. The upper crust in the Grenville is about 0.15 km/sec faster than the Superior (Berry and Fuchs, 1973). Using data from the Project Early Rise experiment, Mereau and Hunter (1968) determined crustal thicknesses of 30 to 35 km for the Superior province north of Lake Superior,

thickening rapidly to values from 40 to 50 km north of the Superior-Churchill geological boundary. Berry (1973) reports studies indicating an average crustal thickness of 35 km for the Hudson platform.

Part of the effect in our extremal difference between Superior and Churchill residuals can be accounted from varying the crustal thickness. Assuming a thickness contrast of 15 km and shear velocity contrast at the Moho of 1.1 km/sec, perhaps 2.0 seconds may be explained of the 3.6 second extremal difference. If we restrict variations to 225 km depth, the remaining 1.6 seconds difference suggests a 2% velocity variation in the uppermost mantle beneath the Canadian shield. This 2% variation would seem to be a minimum, as this assumes an optimal case. Crustal thickness variation cannot affect differences among the Superior, Grenville and Hudson values.

The variations must also be considerably larger if the Greenland values are fit into the framework. Even applying generous source (6 seconds) and receiver (Table II.2.5) corrections, the JER residual remains of the order 1 second slow with respect to JB. A surface wave dispersion study of Greenland (Gregersen, 1970) indicates that the crust is comparable in thickness and seismic velocities to the Canadian shield.

In conclusion, the correlation between travel-time anomaly and tectonic province in the Canadian shield is uncertain until such time as additional data of corroborative nature can be obtained. However, the data are sufficiently precise to indicate lateral variations of several per cent in upper mantle velocities within stable, structural entities.

REFERENCES

- Allen, C. R. and J. M. Nordquist (1972). Foreshock, main shock and larger after shocks of the Borrego Mountain earthquake, U.S. Geol. Surv., Prof. Pap. 787, 16.
- Anderson, D. L. and R. L. Kovach (1964). Attenuation in the mantle and rigidity in the earth's core from multiply reflected core phases, Natl. Acad. Sci., Proc. 51, 168.
- Arons, A. B. and D. R. Tennie (1950). Phase distortion of acoustic pulses obliquely reflected from a medium of higher sound velocity, J. Acoust. Soc. Am. 22, 231.
- Berry, M. J. (1973). Structure of the crust and upper mantle in Canada, Tectonophysics 20, 183.
- Berry, M. J. and K. Fuchs (1973). Crustal structure of the Superior and Grenville provinces of the northeast Canadian shield, Seismol. Soc. Am., Bull. 63, 1393.
- Blatstein, I. M. (1971). Calculations of underwater explosion pulses at caustics, J. Acoust. Soc. Am. 49, 1568.
- Bolt, B. A. and O. W. Nuttli (1966). P wave residuals as a function of azimuth, 1, Observations, J. Geophys. Res. 71, 5977.
- Brune, J. N (1964). Travel times, body waves, and normal modes of the Earth, Seismol. Soc. Am., Bull. 54, 2099.
- Brune, J. N. (1977). Q of Shear waves estimated from S-SS spectral ratios, Geophys. Res. Lett. 4, 179.
- Brune, J. N. and F. Gilbert (1974). Torsional Overtone dispersion from correlations of S waves and SS waves, Seismol. Soc. A., Bull. 64, 313.

- Burdick, L. J. (1977). Broad band seismic studies of body waves  
(Ph.D. dissertation), Calif. Inst. Tech., Pasadena, Ca., 151 pp.
- Burdick, L. J. and G. R. Mellman (1976). Inversion of the body waves  
from the Borrego Mountain earthquake to the source mechanism,  
Bull. Seism. Soc. Am. 66, 1485.
- Butler, R. (1977). A source of bias in multiple ScS differential  
times determined by waveform correlation, Geophys. Res. Lett. 4,  
593.
- Butler, R., G. S. Stewart, and H. Kanamori (1978). The July 27, 1976,  
Tangshan, China earthquake - a complex sequence of intraplate  
events, Bull. Seism. Soc. Am. 69, 207.
- Choy, G. L. and P. G. Richards (1975). Pulse distortion and Hilbert  
transformation in multiply reflected and refracted body waves,  
Bull. Seism. Soc. Am. 65, 55.
- Duschenes, J. D. and S. C. Solomon (1977). Shear wave travel time  
residuals from oceanic earthquakes and the evolution of oceanic  
lithosphere, J. Geophys. Res., 82, 1985.
- Doyle, H. A. and A. L. Hales (1967). An analysis of the travel times of  
S waves to North American stations in the distance range 28° to 82°,  
Bull Seism. Soc. Am., 57, 761.
- Ebel, J. E. (1977). Comparison of waveforms from a foreshock-mainshock-  
aftershock sequence in the New Hebrides Islands, EOS Transactions 58,  
1194.
- Ebel, J. E., L. J. Burdick, and G. S. Stewart (1978). The source mecha-  
nism of the August 7, 1966 El Golfo earthquake, Bull. Seism. Soc.  
Am. 68, 1281.

- Fuchs, K. (1966). The transfer for P waves for a system consisting of a point source in a layered medium, Bull. Seism. Soc. Am. 56, 75.
- Futterman, W. I. (1962). Dispersive body waves J. Geophys. Res. 67, 5279.
- Gregerson, S. (1970). Surface wave dispersion and crust structure in Greenland, Geophys. J. R. Astr. Soc., 22, 29.
- Hales, A. H. and J. L. Roberts (1970). Shear velocities in the lower mantle and the radius of the core, Bull. Seism. Soc. Am. 60, 1427.
- Harkrider, D. G. (1964). Surface waves in multilayered elastic media, I. Rayleigh and Love waves from buried sources in a multilayered elastic half-space, Bull. Seism. Soc. Am. 54, 627.
- Hart, R. S. and R. Butler (1978). Shear wave travel times and amplitudes for two well-constrained earthquakes, Bull. Seism. Soc. Am. 68, 973.
- Hashizume, H. (1976). Surface-wave study of the Canadian Shield, Phys. Earth. Planet. Int. 11, 333.
- Haskell, N. A. (1953). The dispersion of surface waves on multilayered media, Bull. Seism. Soc. Am. 43, 17.
- HelMBERGER, D. V. (1973). Numerical seismograms of long period body waves from seventeen to forty degrees, Bull. Seism. Soc. Am. 63, 633.
- Hill, D. P. (1974). Phase shift and pulse distortion in body waves due to internal caustics, Bull. Seism. Soc. Am. 64, 1733.
- Jeffreys, H. and K. E. Bullen (1940). Seismological Tables, Brit. Assoc. Adv. of Sci., Gray-Milne Trust, London 55 pp.

- Jeffreys, H. and E. R. Lapwood (1957). The flection of a pulse within a sphere, Proc. Roy. Soc. (London) Ser. A 241, 455.
- Jordan, T. H. (1975a). Lateral heterogeneity and mantle dynamics, Nature 257, 745.
- Jordan, T. H. (1957b). The continental tectosphere, Rev. Geophys. Space Phys. 13, 1.
- Jordan, T. H. and S. A. Sipkin (1977). Estimation of the attenuation operator for multiple ScS waves, Geophys. Res. Lett. 4, 167.
- Kovach, R. L. and D. L. Anderson (1964). Attenuation of shear waves in the upper and lower mantle, Bull. Seism. Soc. Am. 54, 1855.
- Langston, C. A. (1976). A body wave inversion of the Koyna, India, earthquake of December 10, 1967, and some implications for body wave focal mechanisms, J. Geophys. Res. 81, 2517.
- Langston, C. A. (1978). The February 9, 1971 San Fernando earthquake, a study of source finiteness in teleseismic body waves Bull. Seism. Soc. Am. 68, 1.
- Langston, C. A. and D. E. Blum (1977). The April 29, 1975 Puget Sound earthquake and the crustal and upper mantle structure of western Washington, Bull. Seism. Soc. Am. 67, 693.
- Langston, C. A. and R. Butler (1976). Focal mechanism of the August 1, 1975 Oroville earthquake, Bull. Seism. Soc. Am. 66, 111.
- Mereau, R. F. and J. A. Hunter (1968). Crust and upper-mantle structure under the Canadian shield from Project Early Rise data, Bull. Seism. Soc. Am. 59, 147.
- Okal, E. (1978). Seismic investigations of upper-mantle lateral heterogeneity, II (Ph.D. dissertation), Calif. Inst. Tech., Pasadena, Ca., 249 pp.

- Okal, E. A. and D. L. Anderson (1975). A study of lateral heterogeneities in the upper-mantle by multiple ScS travel-time residuals, Geophys. Res. Lett. 2, 313.
- Rial, J. A. (1978). The Caracas, Venezuela earthquake of July 1967. A multiple source event (in preparation).
- Sachs, D. A. and S. Silbiger (1971). Focusing and refraction of harmonic sound and transient pulses in stratified media, J. Acoust. Soc. Am. 49, 824.
- Sengupta, M. K. (1975). The structure of the earth's mantle from body wave observations (Ph.D. dissertation), Massachusetts Institute of Technology, Cambridge, Ma., 579 pp.
- Sipkin, S. A. and T. H. Jordan (1975). Lateral heterogeneity of the upper mantle determined from the travel times of ScS, J. Geophys. Res. 80, 1474.
- Sipkin, S. A. and T. H. Jordan (1976). Lateral heterogeneity of the upper mantle determined from the travel times of multiple ScS. J. Geophys. Res. 81, 6307.
- Sipkin, S. A., J. A. Orcutt, and T. H. Jordan (1978). An examination of ScS travel times with a causal Q reflectivity algorithm for SH polarized waves, EOS Transactions 59, 324.
- Stockwell, C. H. (1964). Fourth report on structural provinces, orogenies, and time classification of the Canadian Precambrian Shield, Geol. Surv. Canada, Dept. of Mines and Technical Surveys, Paper 64-17 (Part II).
- Tolstoy, I. (1968). Phase changes and pulse deformation in acoustics, J. Acoust. Soc. Am. 44, 675.
- Uhrhammer, R. A. (1977). Shear wave velocity structure in the earth from differential shear wave measurements, Ph.D. Thesis, University of California, Berkeley.

### SECTION II.3 A SOURCE OF BIAS IN MULTIPLE ScS TRAVEL-TIMES

#### ABSTRACT

Differential travel times determined by waveform correlation techniques between seismic phase pairs suffer an inherent systematic bias with respect to conventional visual timing methods if the phase pairs have different attenuation histories. Synthetic shear waves are generated with attenuation histories appropriate for multiple ScS waves. The bias between the  $\text{ScS}_2$ -ScS differential time determined by visual onset and a differential time picked by waveform cross-correlation ranges between 2.2 and 3.8 seconds late, for an assumed average  $Q_\beta$  of the mantle of 312 and 156, respectively. Corrections are calculated for the various  $\text{ScS}_n$ - $\text{ScS}_{n-1}$  phase pairs for a range of ScS  $t^*$  values.

#### INTRODUCTION

The determination of multiple ScS travel times has been the subject of recent investigations (Okal and Anderson, 1975; Sipkin and Jordan, 1976) to infer lateral heterogeneities in the upper mantle. Differential times are measured between phase pairs  $\text{ScS}_n$ - $\text{ScS}_{n-1}$  or  $\text{ScS}_n$ -S to eliminate source and receiver effects. As the SH polarized components of these phases suffer little waveform distortion on reflection and in propagation, it has been the technique to obtain these differential times by waveform cross-correlation. However, this method overlooks an important consideration. If the seismic phase pairs experience different amounts of attenuation, the waveforms will no longer be identical as the attenuation operator does not act merely to reduce amplitude.

We can illustrate rather quickly the gross effect of the omission of attenuation from waveform cross-correlation considerations. Figure II.3.1 shows the impulse response of an attenuation operator for which  $Q$  is constant in the seismic frequency band (Futterman, 1962; Carpenter, 1966; Strick, 1970; Liu et al., 1976; Minster, 1978 a,b). It has been shown that for reasonable attenuations, the attenuation operator is a function only of  $t^*$  the ratio of travel time and the path average  $Q$  (Carpenter, 1966; Minster, 1978b). Let us define the arrival time  $\tau_a$ , as the time when the operator reaches 1/100 of its peak value, or 40 db. This corresponds very closely to the visual onset of the pulse, i.e., the conventional seismological arrival time. Consider the cross-correlation of two waves,  $\tilde{A}$  and  $\tilde{B}$ , which differ only in their attenuation histories. If  $\tilde{A}$  is delta function and  $\tilde{B} = \tilde{A} * \tilde{Q}$ , a delta function convolved with the  $Q$  operator, the cross-correlation of  $\tilde{A}$  and  $\tilde{B}$  will yield its maximum at  $\tau_p$ , the peak time of the attenuation operator. Consequently, the relative timing between  $\tilde{A}$  and  $\tilde{B}$  measured by cross-correlation will be overestimated by an amount  $\tau_p - \tau_a$  seconds greater than a conventional timing measurement of visual onsets.

#### DETERMINATION OF THE EFFECT FOR ScS

In a similar manner, differential travel times of multiple ScS determined by cross-correlation techniques will be systematically overestimated. This is illustrated in Figure II.3.2. The upper trace shows a synthetic ScS waveform, produced by convolving a 3-second symmetric triangular source time function with a WWSSN 15-100 instrument and an attenuation operator with  $t^* = 4$ .

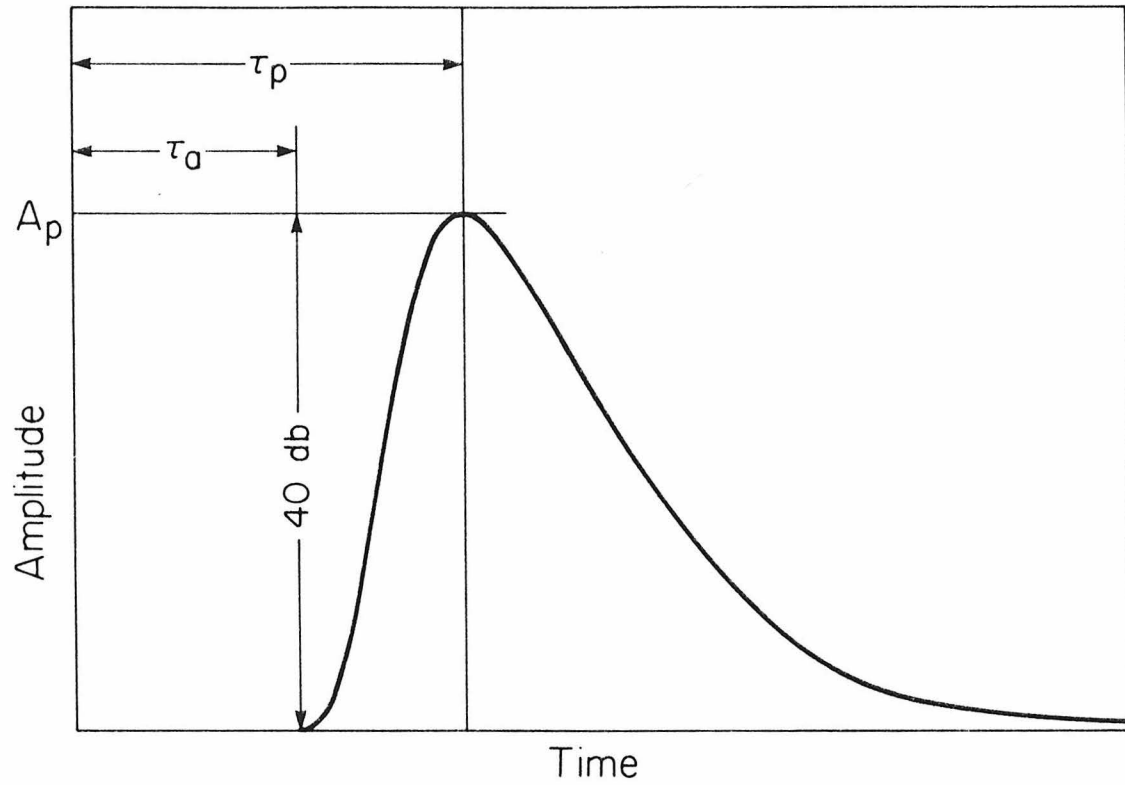


Figure II.3.1 Impulse response of an attenuation operator for which  $Q$  is constant in the seismic frequency band.  $\tau_a$  is the "arrival" time,  $\tau_p$  the peak time,  $A_p$  the peak amplitude. (adapted from Minster, 1978b)

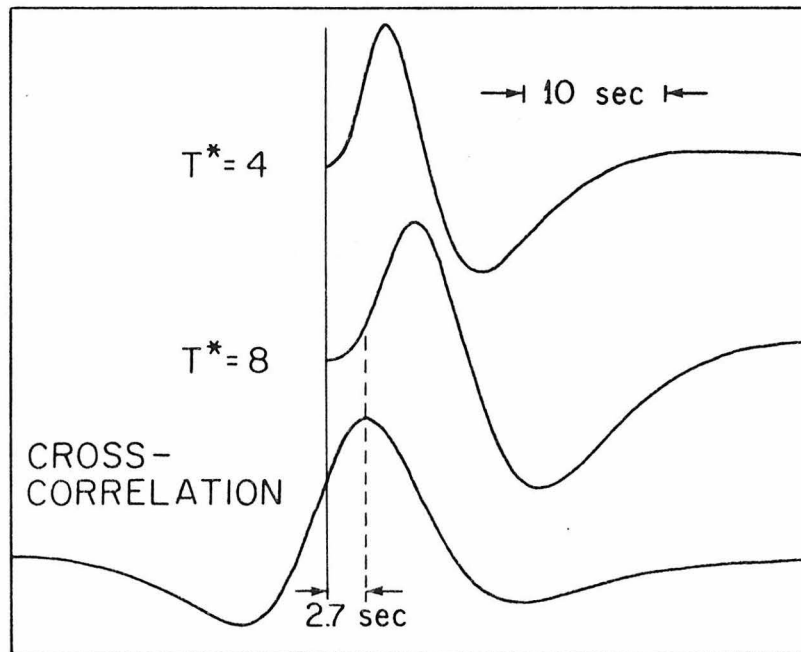


Figure II.3.2 Bias in cross-correlation time pick when the correlated waves suffer different attenuations.

The middle trace plots a synthetic  $ScS_2$  waveform aligned with the upper trace at the visual arrival time. As the travel time of  $ScS_2$  is approximately twice that of  $ScS$ ,  $t^* = 8$  was used in the attenuation operator. The source time function was chosen to be representative of deep focus earthquakes (Burdick and Helmberger, 1974; Mikumo, 1971). It is readily apparent for the time scale on which these are plotted that a simple waveform correlation approach will produce inaccurate relative timing between the phases. The lower trace plots the cross-correlation of  $ScS$  to  $ScS_2$ . The maximum of the cross-correlation picks an  $ScS_2$  arrival time that is 2.7 seconds later than the visual  $ScS_2$  arrival time. If we accept the classical visual onset time as the standard or true arrival time of seismic pulse, then cross-correlation timing is biased late with respect to this reference. This result is only weakly dependent on the assumed source time function: an impulse source yields a bias of 2.6 seconds; a 6-second symmetric triangular source yields a bias of 2.8 seconds. Correlations other than cross-correlation also have biases. Relative timing from first peaks, first zero crossings, and second peaks yield biases of 2.2, 3.0 and 4.2 seconds respectively.

Differential travel times of multiple  $ScS$  measured by waveform correlation have been reported by Okal and Anderson (1975) and Sipkin and Jordan (1976). As these differential times are freely compared to Jeffreys-Bullen times, it is implied that the waveform correlation times are equivalent to conventional travel times. This is clearly not the case. This timing difference is greater than the reported precision of multiple  $ScS$  times: 0.5 seconds (Okal and Anderson, 1975) and 1.0

second (Sipkin and Jordan, 1976). Figure II.3.3 summarizes the effect on the various  $ScS_n - ScS_{n-1}$  pairs assuming a 3-second symmetric triangular source time function. The net bias in differential travel time is plotted versus the  $t^*$  value of  $ScS_n$ . The  $t^*$  of  $ScS_n$  is assumed to be  $n$  times the  $t^*$  of  $ScS$ . For a vertical  $ScS$  travel time of approximately 936 seconds a range of  $t^*$  from 3 to 6 is equivalent to a range of average mantle  $Q_\beta$  of 312 to 156. Thus, depending upon the assumed average  $Q_\beta$  of the mantle or the  $t^*$  of  $ScS$ , the differential travel time  $ScS_2 - ScS$  picked by cross-correlation will be 2.2 to 3.8 seconds later than the true or conventional differential time.

The quantitative bias in  $ScS_n - S$  differential times is somewhat more difficult to plot as the  $t^*$  of  $ScS_n$  is not a multiple of the  $t^*$  of  $S$ . As only a minor number of these observations have been reported (Okal and Anderson, 1975), the exact biases for these phase pairs are not included, but a qualitative estimate may be made from Figure II.3.3. The bias in differential times between  $ScS$  and  $S$  from cross-correlation is 0.7 seconds for  $t^*_{ScS} = 4$  and  $t^*_S = 3$ , or  $t^*_{ScS} = 5$  and  $t^*_S = 4$ .

### IMPLICATIONS

The differential multiple  $ScS$  times of Okal and Anderson (1975) and Sipkin and Jordan (1976) measured by waveform correlation are systematically biased late with respect to conventional travel times. The amount of bias is a function of the differential attenuation between the correlated phase pairs. The timing precision of 0.5 seconds (Okal and Anderson, 1975) or 1.0 second (Sipkin and Jordan, 1976) is relevant only to the correlated differential time, not the conventional differential time. A correction to the correlated time to obtain the conventional time may

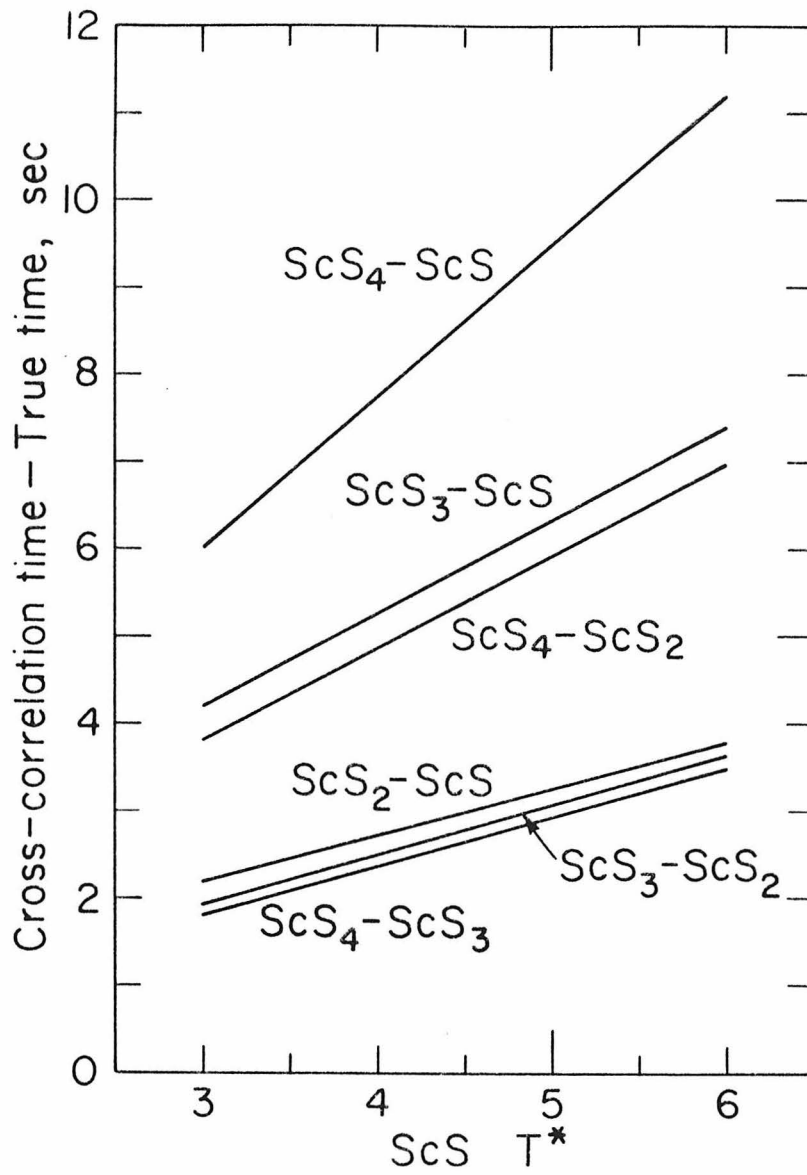


Figure II.3.3 Bias in differential travel times for ScS<sub>n</sub>-ScS<sub>n-1</sub> pairs as a function of the  $t^*$  of ScS.

be estimated from Figure II.3.3, but unless the differential attenuation is known, this correction may be inaccurate by several seconds. Part of the regional variation of multiple ScS times probably reflects a regional variation in attenuation, and hence a variation of the bias in the differential times.

Sipkin and Jordan (1976) estimated a vertical ScS travel time of  $937.3 \pm 1.0$  seconds for the spherically average earth by averaging JB residuals from different tectonic provinces weighted in proportion to surface area and adding the average residual to the Jeffreys-Buellen time of 935.7 seconds. This time, however, is not the true time but an average correlated time. Jordan and Sipkin (1977) determined an apparent  $Q$  for ScS in western Pacific of  $156 \pm 13$ . The average whole mantle  $Q_{\beta}$  for  $Q$  model SL1 (Anderson and Hart, 1977) is 286. Using these  $Q$  values and Figure II.3.3, we may assume a gross correction of -2.3 to -3.8 seconds to the correlated time to obtain the true time. This corrected true time contains a further source of uncertainty. As mentioned above, there probably exists a regional variation in the correlation bias. Thus the Sipkin and Jordan (1976) ScS time is an average of correlation times having a heterogeneous distribution of biases. The rough correction of the correlation bias to the Sipkin and Jordan (1976) time suggests a vertical ScS time 0.7 to 2.2 seconds faster than JB.

We have seen that differential timing between seismic phases suffering different attenuation will inherit a systematic bias when the timing is measured by waveform correlation. If the differential attenuation is known, a correction may be estimated from Figure II.3.3. A more appropriate procedure would be to first correct the waveforms for

the differential attenuation and then cross-correlate to pick the timing. For example, to obtain the differential time between phase pairs  $\underset{\sim}{A}$  and  $\underset{\sim}{B}$  with  $t_{\underset{\sim}{B}}^* > t_{\underset{\sim}{A}}^*$ , we use the differential attenuation

$$t_{\underset{\sim}{\Delta}}^* = t_{\underset{\sim}{B}}^* - t_{\underset{\sim}{A}}^*$$

We correct phase A to have a common attenuation with  $\underset{\sim}{B}$  by convolving  $\underset{\sim}{A}$  with an attenuation operator  $Q(t_{\underset{\sim}{\Delta}}^*)$ . Waveform cross-correlation will now produce a true differential time. If  $t_{\underset{\sim}{\Delta}}^*$  is not known, uncertainties of a second or more will be inherent.

For high quality data, there is a possibility for simultaneous determination of the differential time and  $t_{\underset{\sim}{\Delta}}^*$ . For the phase pairs  $\underset{\sim}{A}$  and  $\underset{\sim}{B}$  above we compute the normalized cross-correlation of B and  $\underset{\sim}{A} * Q(t_{\underset{\sim}{\Delta}}^*)$  for a range of  $t_{\underset{\sim}{\Delta}}^*$ . The maximum normalized cross-correlation will occur, for data without noise, at the true differential time and  $t_{\underset{\sim}{\Delta}}^*$ . An assessment of the resolution of the true differential time and  $t_{\underset{\sim}{\Delta}}^*$  from this technique in the presence of noise is difficult. Nevertheless, in view of the importance of accurately determining multiple ScS times with the additional benefit of estimating the differential attenuation, an investigation of this procedure would seem worthwhile.

REFERENCES

- Anderson, D. L. and R. S. Hart (1977). The Q of the Earth, J. Geophys. Res., 83, No. 5869-5882.
- Burdick, L. J. and D. V. Helmberger (1974). Time Functions Appropriate for Deep Earthquakes, Bull. Seism. Soc. Am., 64, 1419-1428.
- Carpenter, E. W. (1966). Absorption of Elastic Waves - an Operator for a Constant Q Mechanism, AWRE Report No. 0-43/66, H. M. Stationery Office.
- Futterman, W. I. (1962). Dispersive Body Waves, J. Geophys. Res., 67, 5279-5291.
- Jordan, T. H. and S. A. Sipkin (1977). Estimation of the Attenuation Operator for Multiple ScS Waves, Geophys. Res. Lett., 4, 167-170.
- Liu, H.-P., D. L. Anderson, and H. Kanamori (1976). Velocity Dispersion Due to Anelasticity, Geophys. J. R. astr. Soc., 47, 41-58.
- Mikumo, T. (1971). Source Processes of Deep and Intermediate Earthquakes as Inferred from Long Period P and S Waveforms, J. Phys. Earth, 19, 303-320.
- Minster, J. B. (1978). Transient and Impulse Response of a One-Dimensional Linearly Attenuating Medium, Part I: Analytic Results, Geophys. J. R. astr. Soc., 52, 479-501.
- Minster, J. B. (1978). Transient and Impulse Response of a One-Dimensional Linearly Attenuating Medium, Part II: A Parametric Study, Geophys. J. R. astr. Soc., 52, 503-524.
- Okal, E. A. and D. L. Anderson (1975). A Study of Lateral Heterogeneities in the Upper Mantle by Multiple ScS Travel-Time Residuals, Geophys. Res. Lett., 2, 313-316.

Sipkin, S. A. and T. H. Jordan (1976). Lateral Heterogeneity of the Upper Mantle Determined from the Travel Times of Multiple ScS, J. Geophys. Res., 81 6307-6320.

Strick, E. (1970). A Predicted Pedestal Effect for Pulse Propagation in Constant-Q Solids, Geophysics, 34, 387-403.

CHAPTER III  
LONG PERIOD GROUND MOTION FROM  
A GREAT EARTHQUAKE

ABSTRACT

Direct body waves and fundamental surface waves are calculated for a credible, hypothetical great earthquake on the San Andreas fault. The prototype event assumed is the Fort Tejon earthquake of January 9, 1857. Amplitudes and durations of long period ground motion ( $T > 1$  second) are found for a receiver in downtown Los Angeles. Calculations are carried out for various epicenters, dislocation profiles, and time functions. Ground motion from Love radiation is found to be most important, with peak-to-peak amplitudes up to 14 cm and durations up to 5 minutes. This duration is a factor of 3 longer than previous design earthquakes have assumed. Although the present result reveals several important features of long-period ground motion resulting from a great earthquake, more details of rupture propagation need to be known before a more definitive prediction can be made. The present result should be considered tentative.

INTRODUCTION

Shaking or strong ground motion due to the release of elastic energy from the faulting process is the primary cause of damage from most earthquakes. The study of strong ground motion has naturally been the concern of many seismologists and earthquake engineers. Stricter building codes in areas of earthquake risk, and building designs more resistant to earthquake shaking have been consequences of this research. The data on which most of these studies are based are strong motion accelerograms recorded in the epicentral area of earthquakes. However, only three records exist for magnitude 7 events and no magnitude 8 events have been recorded

(Jennings et al., 1968). To fill this gap, various scaling arguments have been made to infer the nature of ground motion for a great earthquake from an understanding of smaller events (Jennings et al., 1968; Hanks, 1976). These arguments might be qualitatively useful in the absence of empirical data, but leave much to be desired in terms of credible, quantitative estimates of ground shaking from a great earthquake.

This chapter will approach the problem of ground motions from a large earthquake from a direct modelling procedure. In recent years seismologists have seen a large measure of success in modelling earthquake sources by simple dislocations in an elastic medium. Hermann and Nuttli (1975) applied dislocation theory to understand multiple-mode surface wave contributions to ground motions for moderate-sized earthquakes for a continental path. The applicability of simple dislocation theory methods for modelling ground motion as a function of the earthquake size and the period range of ground shaking will be considered. Justifying this technique, we model the long period ground motions from a hypothetical earthquake on the San Andreas fault patterned on the Fort Tejon earthquake of January 9, 1857. These long period ground motions ( $T > 1$  second) have little effect on ordinary structures. However, high-rise buildings, oil tanks, suspension bridges, reservoirs, and off-shore oil drilling platforms have natural resonances which lie in the long period ranges.

The basic procedure is as follows. The segment of the San Andreas fault system which broke during the 1857 event is subdivided into many small subsegments. The ground motion response of each subsegment is computed for direct body waves and fundamental surface waves for a

receiver located in downtown Los Angeles. The responses of the sub-segments are time-lagged and summed to simulate rupture propagation for several different epicenters. Smooth and non-smooth rupture processes are considered. Uncertainties in the complexity of the rupture, velocity structure, and the effects of lateral heterogeneities preclude definitive results. However, tentative conclusions of the nature of long-period ground motion from a great earthquake may be reached for such gross parameters as overall amplitudes and durations.

#### THE MODEL

In principle, if the geometric shape and size of the fault plane,  $S$ , the slip,  $\vec{D}(\vec{r}, t)$ , on the fault plane as a function of position  $\vec{r}$  and time  $t$ , and the structure of the propagation medium are known, one can accurately compute the ground motion. However, in actual problems the slip  $\vec{D}(\vec{r}, t)$  can be a very complex function and the structure is not known in detail. Even if the structure is reasonably well known, it is usually laterally heterogeneous and the computation of the response is exceedingly difficult. Various seismological studies during the past decade have, however, shown that under certain circumstances the ground displacement caused by an earthquake can be predicted by a simple model. At periods  $T \geq 1$  second, it has been shown that for many small to moderate size earthquakes (source dimension  $L \leq 30$  km), a relatively smooth simple dislocation model and a very simple structure can explain both near-field ground motion and teleseismic data very well. Near-field studies include: 1966 Parkfield earthquake (Aki, 1968; Haskell, 1969), 1943 Tottori earthquake (Kanamori, 1972), 1971 San Fernando earthquake (Mikumo, 1973a; Trifunac, 1974), 1969 Gifu earthquake (Mikumo, 1973b),

1968 Saitama earthquake (Abe, 1974), 1968 Borrego Mountain earthquake (Heaton and Helmberger, 1977), 1973 Morgan Hill earthquake (Helmberger and Malone, 1975), and the 1976 Brawley earthquake (Heaton and Helmberger 1978). Teleseismic studies include: 1967 Koyna earthquake (Langston, 1976). 1975 Oroville earthquake (Langston and Butler, 1977), 1968 Borrego Mountain earthquake (Burdick and Mellman, 1976), 1966 El Golfo earthquake (Ebel et al., 1978), and the 1971 San Fernando earthquake (Langston, 1978).

As a specific example, the Helmberger and Malone (1975) study of the Morgan Hill earthquake modelled observed seismograms in the distance range 10 to 100 km by the generalized ray technique using a simple source time function and a layered structure. The close agreement between their synthetic seismograms and the observed suggests that a simple source imbedded in a credible crustal model may explain many of the complexities in local field seismograms. However, even for these well studied earthquakes listed above, very short period ( $T < 1$  sec) waves are difficult to explain.

When the source dimension becomes very large ( $L \geq 150$  km), the source process cannot be modelled by a simple smooth dislocation source even for the period range  $T \geq 1$  second. It is known that many large earthquakes are complex multiple shocks; e.g., the 1976 Guatemalan earthquake (Kanamori and Stewart, 1978). However, at very long periods ( $T > 100$  seconds) even such a large complex event can be modelled by a simple propagating dislocation source. Observed waveforms of long period Rayleigh and Love waves can usually be explained very well by using a smooth propagating dislocation source and a laterally homogeneous gross earth model; e.g., Kanamori (1970); Kanamori and Cipar (1974), Kanamori and Stewart (1978),

Stewart and Cohn (1978), Stewart (1978), and Butler et al. (1979).

The situation described above may be summarized schematically by Figure III.1. The applicability and limitations in using a relatively smooth source in modelling a given earthquake is a function of the source dimension of the event and the period range of interest. The dividing line is only qualitative.

Considering now a large earthquake on the San Andreas fault with a source dimension of 100 km or greater, it is clear from Figure III.1 that for periods shorter than one second a very complex source must be used. As a good model is not available for such a complex source, it would be difficult to make a meaningful numerical model of the ground shaking. In the period range 1 to 10 seconds the proximity of the dividing line is such that a more or less smooth source may be used to model the ground motion if some complexity is added. These periods, though not the high-frequency strong ground motion experienced in earthquakes, are nevertheless of engineering significance to large structures which have natural periods within this range.

The Fort Tejon earthquake of January 9, 1857 may be considered a prototype of a future great earthquake on the San Andreas fault. Felt from Sacramento to Yuma, this remarkable event is associated with the most recent movement of the Carrizo Plain and "great bend" sections of the San Andreas fault system. Compilations by Wood (1955), Agnew (unpublished manuscript, 1972), and Agnew and Sieh (1978) of contemporary accounts suggest that the earthquake was characterized by short period strong ground motion in the meizo-seismal area and longer period effects felt over a much larger region. Seiching of rivers and bodies of water

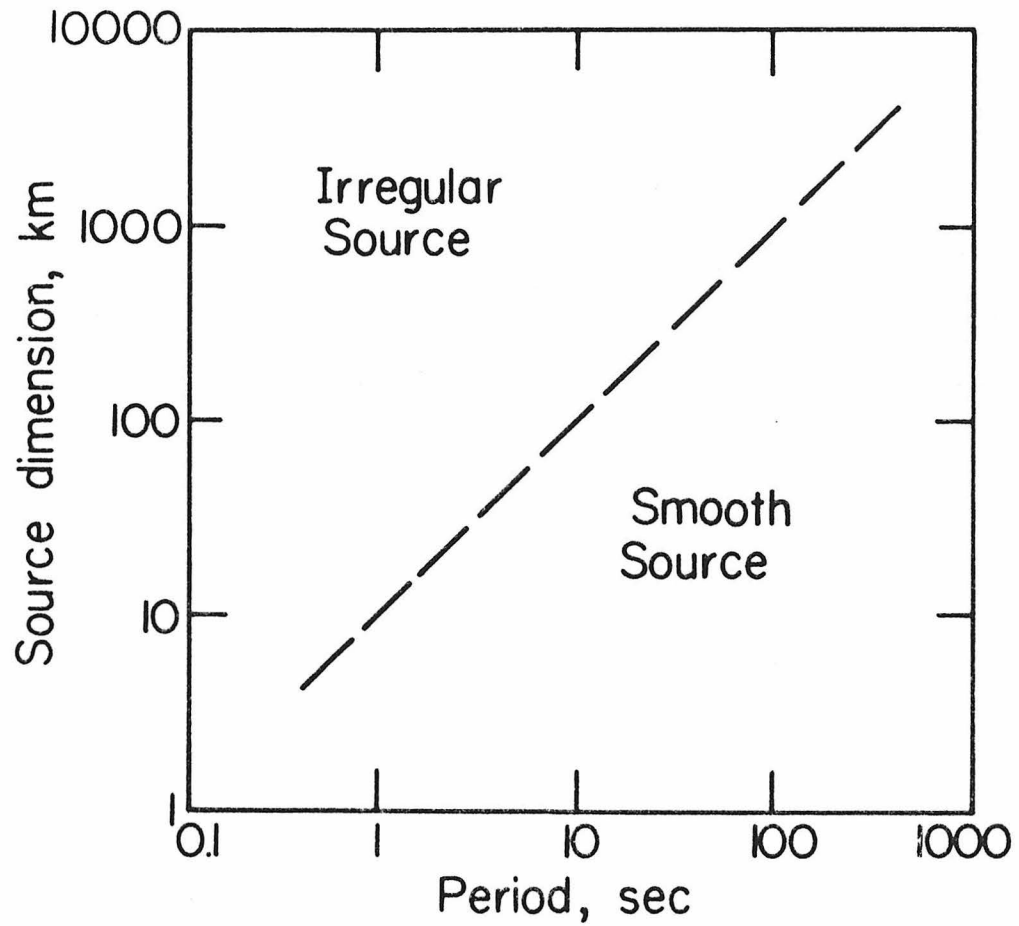


Figure III.1 The approximate applicability of a relatively smooth source is shown as a function of source dimension and period range of interest.

were reported as far north as Sacramento. Fissures in the earth, presumably due to lurching in soft ground, were reported near Ventura, North Long Beach, Fountain Valley, and San Bernardino. Faulting on the San Andreas was mentioned extending southeast from Lake Elizabeth and as far north as Parkfield. Although faulting accounts in the historical record are consistent with right-lateral strike slip motion, no good accounts are given as to the amount of offset.

Additional constraints on the faulting associated with the Fort Tejon earthquake may be inferred from recent geomorphological studies along the San Andreas. Wallace (1968) measured stream offsets in the Carrizo Plain. The data are scattered, but a clustering of values of 10 meters is indicated. In a detailed geomorphic study of the San Andreas from Parkfield to San Bernardino, Sieh (1978) concurs with Wallace's 10 meters in the Carrizo Plain, but reports evidence that the displacement may have been only half of that southeast of Tejon pass. Trenching across the San Andreas at Palette Creek (Sieh, 1978) indicates that fault movements associated with the Fort Tejon earthquake extended at least to this location. There is some question as to the southern terminus of the faulting, but the absence of contemporary accounts of faulting at San Bernardino would suggest that the rupture ceased north of this city.

The limits and the geometry of the assumed Fort Tejon fault model are shown in Figure III.2: a right lateral pure strike slip fault extending 375 km from Parkfield to near San Bernardino. The depth of faulting is assumed to be 15 km uniformly over the length of the fault. This value is consistent with the maximum depth of earthquakes in south-

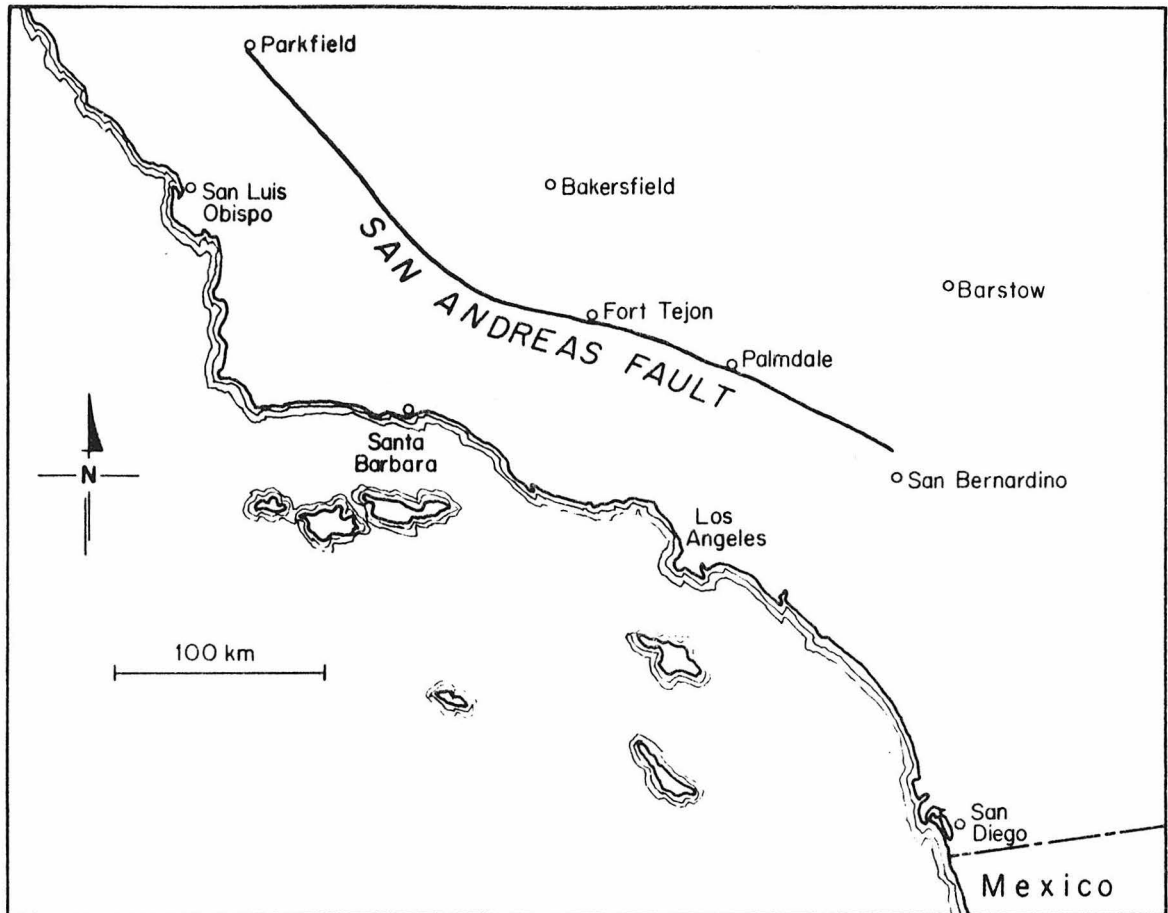


Figure III.2 The segment of the San Andreas fault used in the modelling.

ern California and is presumably a depth where fault creep or some other process substitutes for brittle fracture. This depth is also consistent with models for geodetic data from the 1906 San Francisco earthquake on the northern segment of the San Andreas. From the geomorphic work (Wallace, 1968; Sieh, 1978) on stream offsets in the Carrizo Plain, a potential displacement of 10 meters must be considered credible. Given these assumptions the seismic moment,  $M_0$ , defined as

$$M_0 = \mu DS \quad (1)$$

( $\mu$  = rigidity; D = displacement; S = fault area) for the hypothetical event would be about  $1.5 \times 10^{28}$  dyne-cm.

For a laterally heterogeneous crustal structure a meaningful numerical calculation of ground motion would be difficult, if not impossible. Seismic refraction surveys in southern California (Kanamori and Hadley, 1975) indicate that the region has a remarkably homogeneous crust. The crustal model obtained by Kanamori and Hadley (1975) is used with excellent success in locating local earthquakes in southern California by SCARLET (Southern California Array for Research on Local Earthquakes and Teleseisms). This study adopts a seismic model designated KHC2, incorporating the Kanamori and Hadley crustal model slightly modified to include a 1 km layer of sediment (see Table III.1). Shear velocities are assumed from Poisson's ratio. For the purpose of

TABLE III.1

KHC2 CRUST  
(adapted from Kanamori and Hadley, 1975)

Compressional Velocity (km/sec)	Shear Velocity (km/sec)	Density ( $\rho/\text{cm}^3$ )	Thickness (km)
2.5	1.4	2.5	1.0
5.5	3.1	2.6	3.0
6.3	3.6	2.7	23.4
6.8	3.9	2.9	5.0

calculating surface-wave excitation functions, this crustal model overlies a gross earth mantle, model C2 of Anderson and Hart (1976).

Several important parameters--the epicenter, fault rupture velocity, and the dislocation particle velocity--must be assumed. The epicenter of the 1857 Fort Tejon earthquake is unknown. This study will consider three extreme cases: (1) an epicenter at Parkfield with rupture propagating toward Los Angeles; (2) an epicenter at the San Bernardino with the rupture propagating northward; (3) an epicenter at the point on the fault closest to Los Angeles, near Palmdale, and rupturing in a bi-lateral fashion. An average velocity of 2.5 km/sec and an average dislocation particle velocity of 1 m/sec are chosen in the present study. These values are consistent with determinations for other crustal earthquakes (e.g., Geller, 1976).

Figure II.1 suggests that some degree of complexity must be included in the Fort Tejon source model. The manner in which we have chosen to include complexity is somewhat ad hoc, but has a basis within a conceptualization of the earthquake source. For earthquakes of small source dimension we have seen that they may be characterized by a rather simple smooth source model for periods  $T \geq 1$  second. In modelling these small events with a dislocation source, it is sufficient to use only a single set of parameters--displacement, particle velocity, and rupture velocity--for the entire fault surface. For earthquakes of large source dimension this treatment is inadequate. Two large strike-slip earthquakes, the 1967 Caracas earthquake (Rial, 1978) and the 1976 Guatemalan earthquake (Kanamori and Stewart, 1978), were found to be multiple shocks--a propagating sequence of smaller quasi-independent events filling the fault sur-

face. Kanamori and Stewart (1978) envisaged these complex multiple shocks in terms of a heterogeneous distribution of stress along the fault plane. This heterogeneity may be caused by asperities, differences in strength, differences in pore pressure, differences in slip characteristics (stable sliding versus stick-slip), or combinations of these factors.

In concordance with these concepts, complexity is added to the Fort Tejon source model in the following manner. The assumed dislocation parameters--displacement  $D = 10$  meters, particle velocity  $\dot{D} = 1$  m/sec, and rupture velocity  $V_R = 2.5$  km/sec--are viewed as average values for the fault. Piecewise along the fault the parameters  $D$ ,  $\dot{D}$ , and  $V_R$  vary about these average values. Over a local section of the fault we expect some coherence in the parameters. Following Haskell (1966) and Aki (1967) we introduce a correlation length  $k_L^{-1}$ . Consider the displacement  $D(x)$  to be

$$D(x) = D_0 + d(x) \quad (2)$$

Where  $D_0$  is the average offset over the fault and  $d(x)$  is the random variation about this average. If we assume that the autocorrelation of  $d(x)$

$$A(\xi) = \int_{-\infty}^{\infty} d(x) d(x + \xi) dx \quad (3)$$

has the functional form

$$A(\xi) \sim e^{-k_L |\xi|} \quad (4)$$

then the variation  $d(x)$  will maintain a coherence over a length  $k_L^{-1}$ .

The amplitude spectrum of  $d(x)$ ,  $|\hat{d}(k)|$ , is related to  $A(\xi)$  by

$$|\hat{d}(k)|^2 = \int_{-\infty}^{\infty} A(\xi) e^{-ik\xi} d\xi \quad (5)$$

Integrating, we have

$$|\hat{d}(k)| \sim \left( \frac{k_L}{k_L^2 + k^2} \right)^{1/2} \quad (6)$$

Now, choosing a phase spectrum, we may transform  $\hat{d}(k)$  back to obtain  $d(x)$  with the desired coherence property.

In practice for a discretized fault, we have in the Fourier domain

$$\hat{d}(k_n) = \left( \frac{k_L}{k_L^2 + k_n^2} \right)^{1/2} e^{i\psi_n} \quad (7)$$

where  $\psi_n$  is a randomly generated phase. The variation  $d(x)$  is then recovered by a Fast Fourier Transform and scaled to the desired range of variation.

The same treatment is followed for the particle velocity,  $\dot{D}$ , and rupture velocity,  $V_R$ .

In the computation of Fort Tejon body wave radiation we assumed two basic models. The first model simulates smooth rupture and, thus,  $D$ ,  $\dot{D}$ , and  $V_R$  are held constant over the fault. Secondly, several random

models were run with the displacement,  $D$ , ranging from 0 to 20 meters with a correlation length of 10 km. The rise time ( $\tau = D/\dot{D}$ ) and rupture velocity were held constant at, respectively, 10 sec and 2.5 km/sec.

The surface wave computations included a smooth model with  $D$ ,  $\dot{D}$ , and  $V_R$  held constant and three different random models (see Table III.2). The short correlation length of random model 2 produces the effect of an uncorrelated or totally random variation.

All calculations in this paper are for the fault geometry assumed in Figure III.2 and a receiver at downtown Los Angeles.

#### BODY WAVES

In computing the near-field body wave displacements, we employed the De Hoop-Haskell method (De Hoop, 1958; Haskell, 1969). The fault assumed in Figure III.2 was subdivided into one hundred and fifty 2.5 km segments. We numerically double-integrated the expressions (3.1)-(4.3) in Haskell (1969) over each fault segment placed in an infinite homogeneous medium with a P wave velocity of 6.3 km/sec and S wave velocity of 3.6 km/sec. The effect of the free surface was accounted for by doubling the amplitude in the whole space calculation.

As mentioned earlier, for these body wave calculations the rise time of the slip dislocation for each fault segment was 10 seconds and a velocity of rupture of 2.5 km/sec was assumed. Thus, upon calculation of the displacement time history in Los Angeles from each fault segment, we may sum the displacements from each of the segments shifting the time to account for the propagation of the rupture from the chosen epicenter.

Several of the models computed are shown in Figure III.3. A quanti-

TABLE III.2

## Surface-wave fault models

Model Type	Correlation length (km)	Displacement (meters)	Particle velocity (m/sec)	Rupture velocity (km/sec)
SMOOTH	---	10.0	1.0	2.5
Random #1	10.0	10.0 $\pm$ 2.5	1.0 $\pm$ .5	2.5 $\pm$ .5
Random #2	0.1	10.0 $\pm$ 2.5	1.0 $\pm$ .5	2.5 $\pm$ .5
Random #3	10.0	10.0 $\pm$ 2.5	1.0 $\pm$ 1.0	2.5 $\pm$ .5

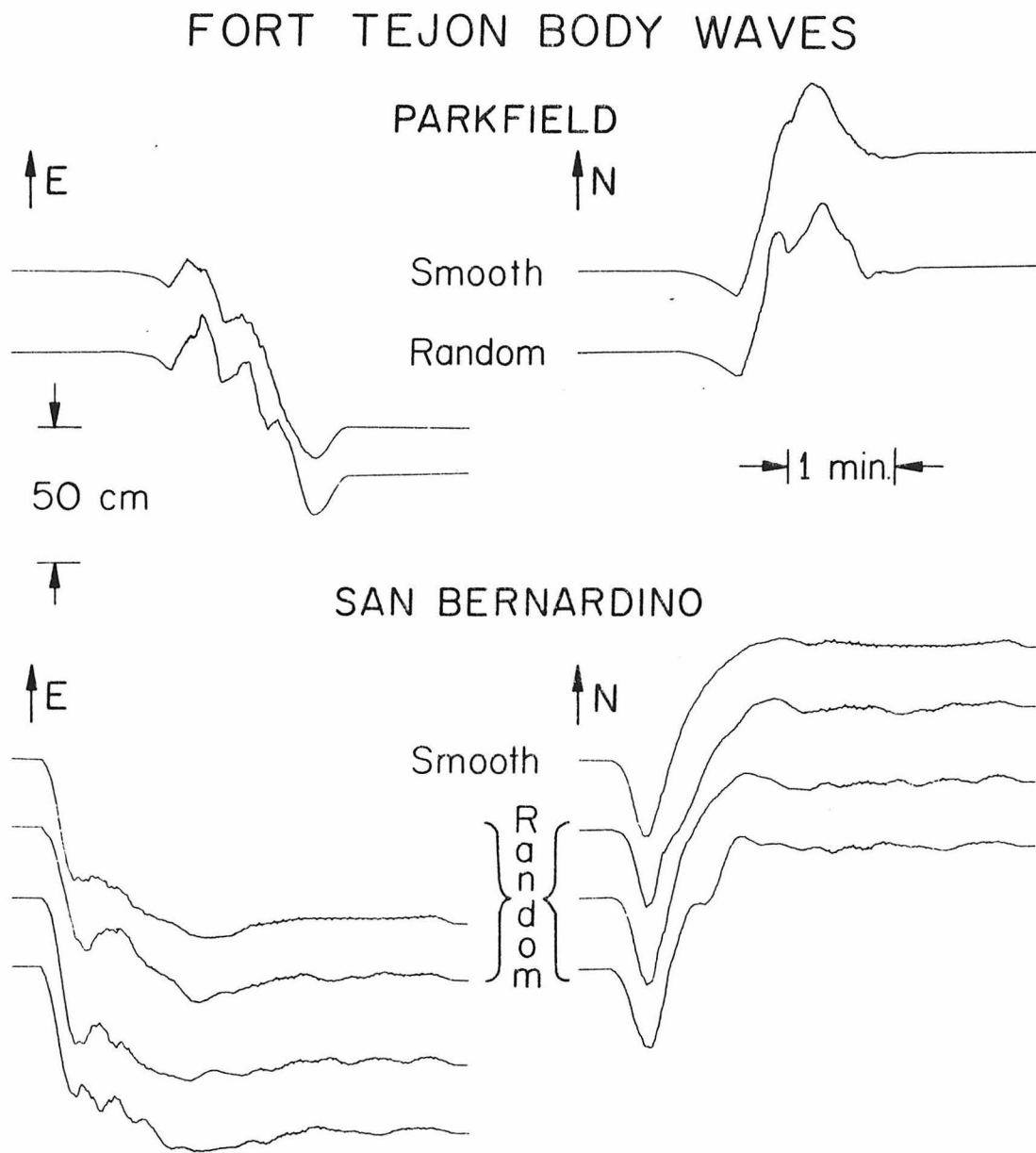


Figure III.3 Body wave displacements (direct ray only) for a receiver in downtown Los Angeles.

tative measurement of the amplitudes and duration of ground motion for these synthetics in several period windows will be provided in the discussion section. It is useful at this time, however, to qualitatively describe these results. The upper part of Figure III.3 shows horizontal body waves computed for a smooth and random model with an epicenter at Parkfield, the rupture propagating toward Los Angeles. The lower part of the figure plots body waves from an epicenter at the San Bernardino end of the fault. The gross features exhibited by the smooth and random models are quite similar. The ground motions calculated for these two extreme epicenters are quite different. These differences are largely the result of two processes: the direction of rupture propagation and the change in the source radiation felt at Los Angeles as the geometry between fault and receiver change during the rupture propagation. The section of the fault from Parkfield to the Carrizo Plain contributes to only a minor part of the near field displacements, as Los Angeles is nearly on the strike of the fault. Thus, the motion from a Parkfield epicenter builds to a static value more slowly than for a San Bernardino epicenter. For the San Bernardino traces we see on the eastern components of motion a displacement of roughly 45 cm in 20 seconds. Static offsets of 55 cm and 42 cm are observed for the smooth model on the east-west and north-south components, respectively. The random faults reach slightly different values owing to the distribution of the random displacements on the fault; i.e., the southern two-thirds of the fault largely control the static displacements. The sharp change in the direction of motion on the north-south component of the San Bernardino synthetics is a result of change in sign of the source radiation felt by the receiver as the double-couple propagates northward.

As the De Hoop-Haskell method calculates only the direct body waves, the synthetics do not include the considerable influence of Moho refractions and reflections, and crustal reverberations. These other body wave arrivals are ignored in this present study to better enable an understanding of the effects of source complexity. The body wave results presented may be viewed as lower bound estimates of the ground motion from the body waves.

### SURFACE WAVES

The excitation of surface waves in a layered medium from a simple dislocation source has been completely formulated. One can use either the propagator matrices method developed by Harkrider (1964) and Ben-Menahem and Harkrider (1964) or by the asymptotic expressions for free oscillations used by Kanamori and Stewart (1976). The latter course is followed in this paper. This technique is briefly outlined below; for more details the reader may refer to Appendix 1 of Kanamori and Stewart (1976).

The transverse component for Love waves excited by a point double-couple with a step time function can be given by

$$U_{\phi}(\Delta, t) = \frac{1}{2\pi} \int_{-\infty}^{+\infty} C_L(\sigma) \exp(i\sigma t) d\sigma \quad (8a)$$

$$C_L(\sigma) = \frac{1}{\sqrt{\sin \Delta}} \exp\left(-\frac{\pi}{4} i\right) \exp\left(-i \frac{\sigma a \Delta}{c}\right) \left[ P_L P_L^{(1)} + i q_L Q_L^{(1)} \right], \sigma \geq 0 \quad (8b)$$

$$C_L(\sigma) = C_L^*(-\sigma), \quad \sigma < 0 \quad (8c)$$

where  $\Delta$  is the distance in radians,  $t$  is the time,  $\sigma$  is the angular frequency,  $a$  the earth's radius, and  $c$  is the phase velocity. In the above,  $p_L$  and  $q_L$  are constants determined by the fault geometry and the azimuth of the receiver, and  $P_L^{(1)}$  and  $Q_L^{(1)}$  are the excitation functions which can be computed by normal mode theory, given an earth model and source depth. Similarly, the vertical component of Rayleigh waves can be given by

$$U_r(\Delta, t) = \frac{1}{2\pi} \int_{-\infty}^{\infty} C_R(\sigma) \exp(i\sigma t) d\sigma \quad (9a)$$

$$C_R(\sigma) = \frac{1}{\sqrt{\sin \Delta}} \exp\left(\frac{\pi}{4} i\right) \exp\left(-\frac{\sigma a \Delta}{c}\right) \left[ s_R s_R^{(1)} + p_R p_R^{(1)} + i q_R q_R^{(1)} \right], \sigma \geq 0 \quad (9b)$$

$$C_R(\sigma) = C_R^* (-\sigma), \quad (9c)$$

where the  $s_R$ ,  $p_R$ ,  $q_R$ ,  $s_R^{(1)}$ ,  $p_R^{(1)}$ , and  $q_R^{(1)}$  are analogous to the  $p_L$ ,  $q_L$ ,  $P_L^{(1)}$ , and  $Q_L^{(1)}$  defined for the Love Waves. The radial component of the Rayleigh waves is much smaller than the Love waves for a vertical strike-slip source and is not included in the computation of horizontal surface waves.

In the modelling of the surface wave we used earth model KHC2 (see Table II.1). The excitation functions  $P_R^{(1)}$ ,  $Q_R^{(1)}$ ,  $S_R^{(1)}$ ,  $P_L^{(1)}$ , and  $Q_L^{(1)}$  were calculated over a range of normal modes for periods from 1 second to 500 seconds for five discrete depths: 2, 5, 8, 12, and 15 km. A study was made of the relative excitation of overtone modes to the fundamental. For periods greater than about 15 seconds, the overtones

may be neglected. For periods less than 15 seconds the overtones have significant contribution to the body waves. For the surface wave calculations, only the fundamental modes are used. The excitation functions for the different depths were averaged to yield an effective vertical line source. Equations (8a) and (9a) were interpolated between the smoothly varying excitation functions to obtain the response at appropriate periods and then transformed to the time domain by Fast Fourier Transform. As for the body waves, the fault geometry in Figure III.2 was assumed. The fault was subdivided into 150 sections of 2.5 km each. The  $p_R$ ,  $q_R$ ,  $s_R$ ,  $p_L$ , and  $q_L$  were then calculated for each segment using downtown Los Angeles as the receiver site. Attenuation was incorporated in the calculation by multiplying the integrals of equations (8a) and (9a) by

$$\exp \left( - \frac{\sigma d}{2QU} \right) \quad (10)$$

where  $d$  is the distance in kilometers to Los Angeles,  $U$  the group velocity, and  $Q$  the quality factor. A constant  $Q$  of 300 was used in this study. The source finiteness of each segment is accounted for by the inclusion in the integrals (8a) and (9a) of the factor

$$\frac{\sin(\sigma t_c / 2)}{\sigma t_c / 2} \quad (11)$$

where  $t_c$  is the rupture-time constant given by

$$t_c = \frac{L_s}{c} \left( \frac{c}{V_R} - \cos \theta \right) \quad (12)$$

with  $L_s$  the fault segment length,  $c$  the phase velocity,  $V_R$  the rupture velocity, and  $\theta$  the azimuth of receiver measured from the rupture direction. By appropriately time-shifting and summing the effects of each segment for a chosen epicenter we produce a propagating rupture.

The dislocation time function was assumed to be a linear ramp function of rise time  $\tau$ , where  $\tau = D/\dot{D}$ . The excitation functions are calculated for a step time function. The correction for a finite rise time may be made with a further factor in equations (8a) and (9a) of

$$\frac{\sin\left(\frac{\sigma\tau}{2}\right)}{\frac{\sigma\tau}{2}} \quad (13)$$

Synthetic Rayleigh waves are shown in Figure III.4 for the Fort Tejon models listed in Table II.2. Epicenters are chosen at Parkfield, Palmdale, and San Bernardino. Similarly, Figures III.5 and III.6 show respectively, the north-south and east-west components of the Love waves. Two components are necessary to describe the Love waves as there is no true transverse component of motion due to the changing geometry between the source and receiver as the earthquake propagates. As with the body waves, we consider at this time a qualitative review of the surface wave synthetics and defer a more quantitative discussion to the next section.

Neither the Rayleigh nor the Love waves exhibit the customary well-dispersed waveforms observed at teleseismic distances for other earthquakes. The surface wave radiation pattern for both Rayleigh and Love waves for a vertical strike-slip double-couple is four-lobed. Thus, as the source propagates along the fault, the radiation felt by the receiver varies rapidly between loops and nodes. Hence even for the so-called smooth

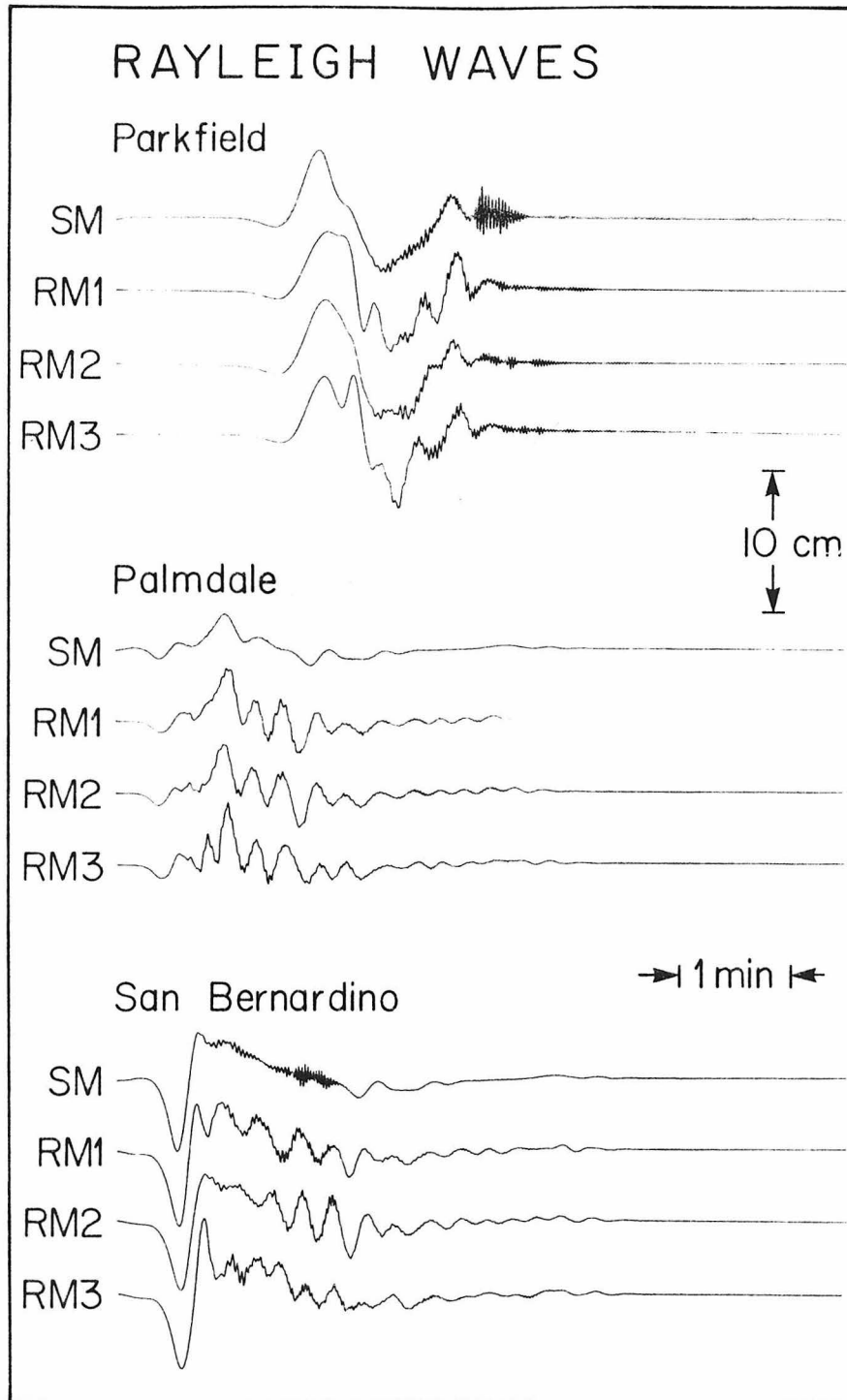


Figure III.4 Synthetic Rayleigh waves calculated for a receiver in downtown Los Angeles for the Fort Tejon models listed in Table III.2. Epicenters are chosen at Parkfield, Palmdale, and San Bernardino (SM-smooth model; RM-random model).

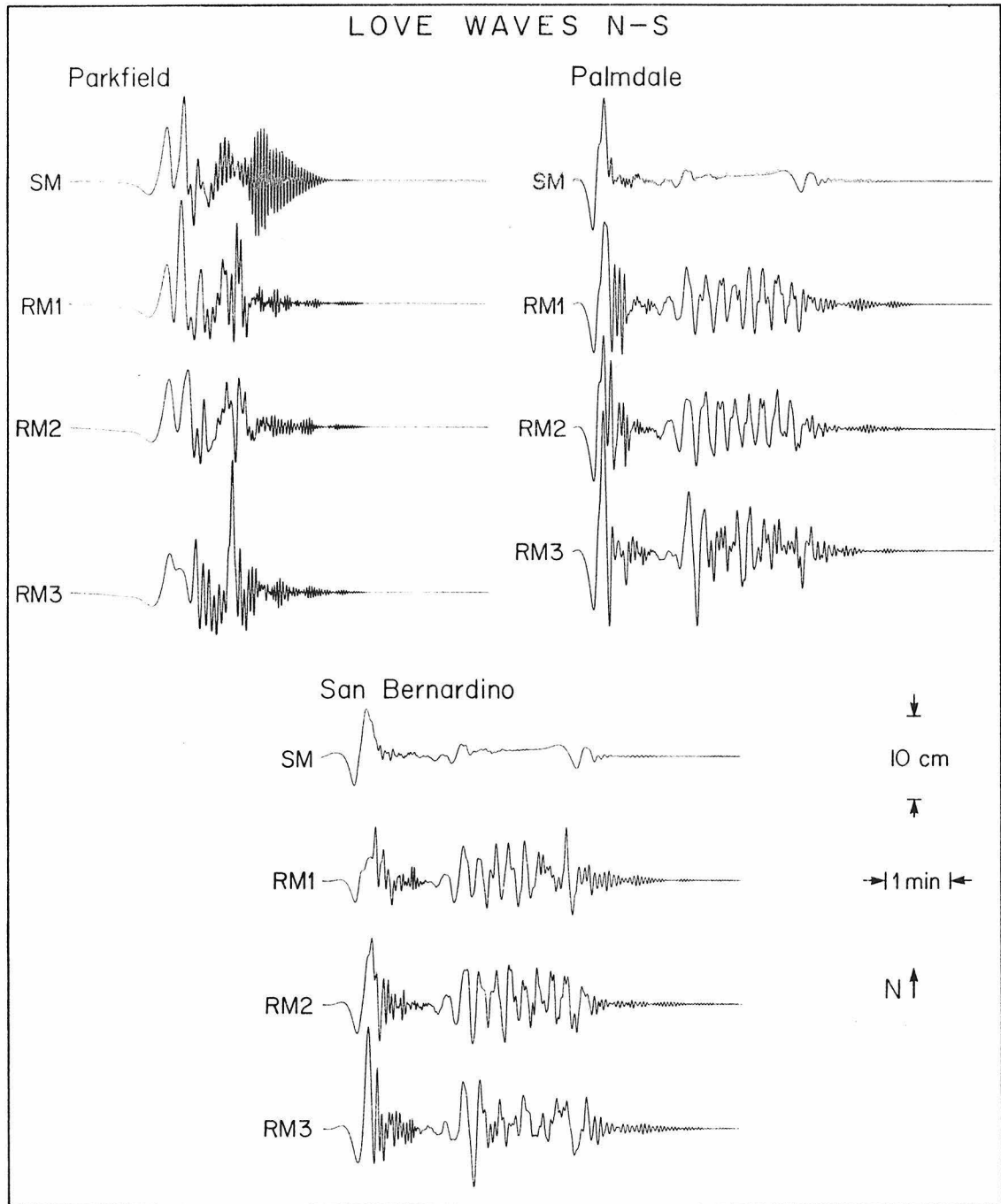


Figure III.5 Synthetic Love waves, north-south component, calculated for a receiver in downtown Los Angeles for the Fort Tejon models listed in Table III.2

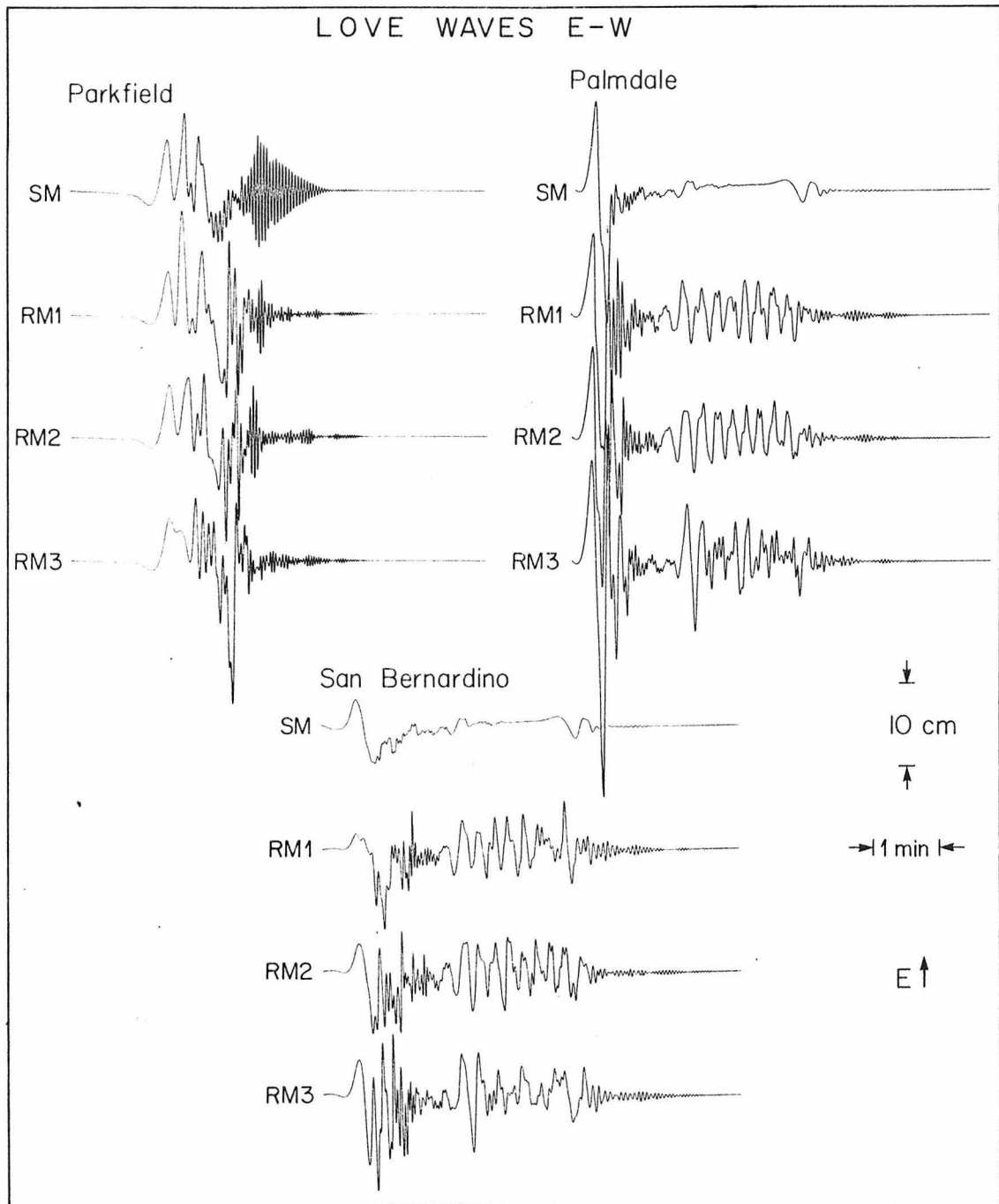


Figure III.6 Synthetic Love waves, east-west component, calculated for a receiver in downtown Los Angeles for the Fort Tejon models listed in Table III.2

model, the synthetics have a complicated waveform.

Comparing the gross features of the Rayleigh and Love waves, we see that though the very long period components ( $T > 10$  seconds) of both types are of the roughly comparable order of 10 cm, the Love waves exhibit an order of magnitude more energy in the seismic bands in which we are concerned, periods between 1 and 10 seconds. At very long periods a gross Love to Rayleigh wave amplitude ratio of 2 may be expected for a vertical pure strike-slip fault. For shallow faults, however, another factor plays a more important role for the period range of interest. If we look at the shape of Rayleigh wave excitation functions appropriate for our Fort Tejon model, we find that there is a sign change, or rather a node, between the free surface and 15 km depth for periods between 1 and 10 seconds. The Love to Rayleigh ratio for this depth range is significantly amplified. This effect for the vertical pure strike-slip fault has previously been documented by Harkrider (1970), who noted that the nodal period in seconds of the Rayleigh to Love spectral ratio is roughly equal to the source depth in kilometers for this type of earthquake.

The Rayleigh wave synthetics for the smooth and random models are quite similar. This result is not unexpected in view of the above discussion. The very long period components which make up the Rayleigh waves simply average over the heterogeneities in our model. The Love wave synthetics for random models show considerably more structure than their corresponding smooth model. The energy between the periods 1 and 10 seconds have wavelengths which are much more sensitive to the heterogeneities. The effect is not so much a boost of the maximum amplitude but rather is an increase in the duration of large amplitude motion.

Comparing the synthetics of the three different random models, we note that they are quite similar. This result suggests that though the addition of randomness is quite important in the determination of amplitudes and durations of ground motion, the synthetics are not sensitive to the specific parameters of the random variation along the fault.

In terms of the amplitude of ground motions from the surface waves the location of the epicenter in the Fort Tejon models is not crucial. However, the location of the epicenter is important for estimating durations of ground motion. An epicenter at Parkfield probably represents the lower bound on duration, as the source moves closer to Los Angeles as it ruptures. The synthetics for the Palmdale and San Bernardino epicenters, which are quite similar, represent the reverse situation and may be considered rough upper bounds on the duration of surface wave ground motion.

#### DISCUSSION

To place the results of the Fort Tejon synthetics in some perspective, we may compare them to a design earthquake. The upper traces in Figures III.7a and III.7b show a Fort Tejon surface wave synthetic and design earthquake A-1 (Jennings *et al.*, 1968). Earthquake A-1 was generated by a random process with a prescribed acceleration power spectral density, multiplied by envelope functions chosen to model the changing intensity of accelerations at the beginning and end of real accelerograms. The accelerations associated with earthquake A-1 were scaled such that the average value of the spectral intensity is 150% as strong as the average spectrum intensity recorded on two accelerograms of the magnitude 7 El Centro earthquake of 1940. Earthquake A-1 "is designed to

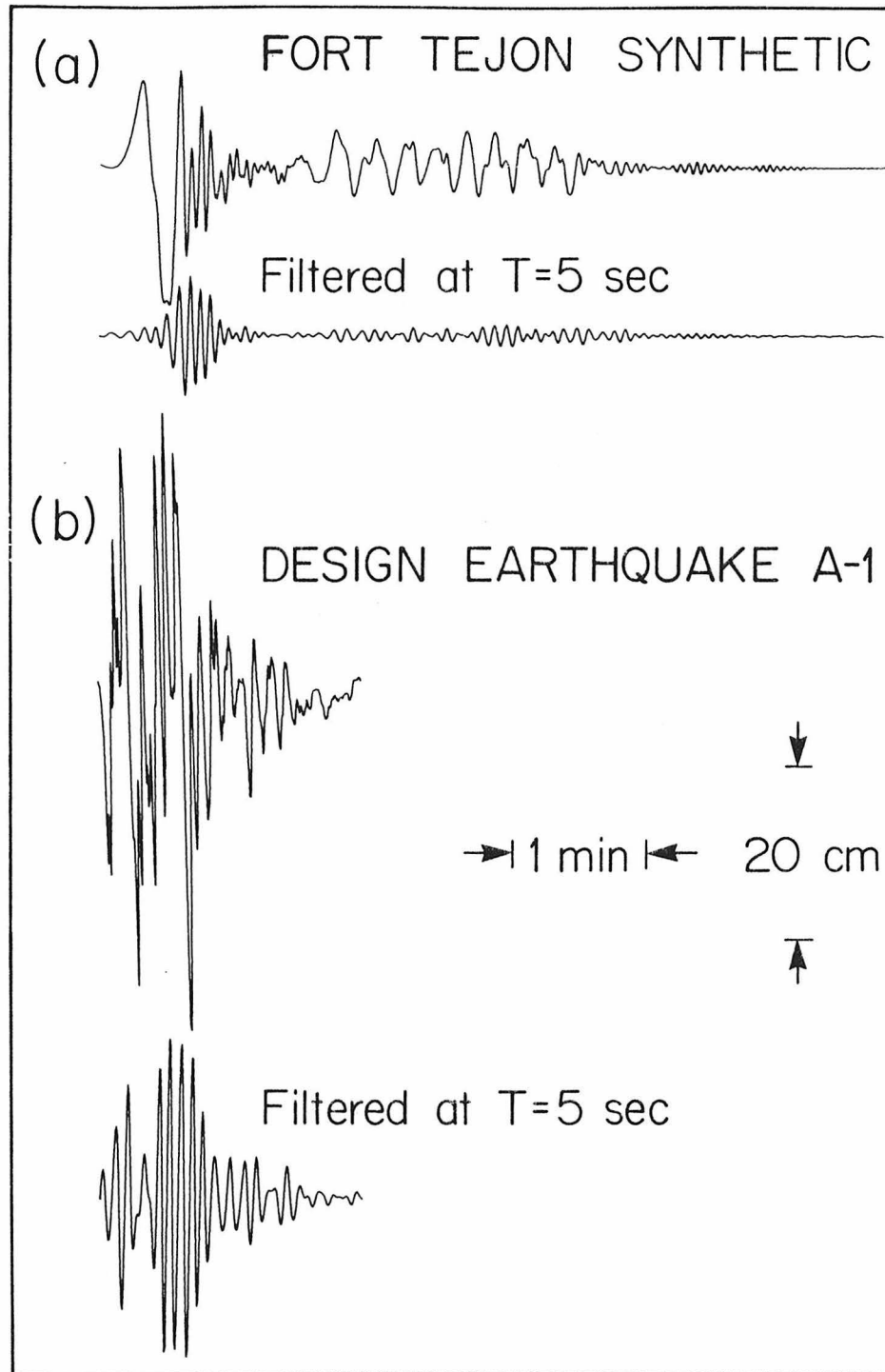


Figure III.7 Comparison of Fort Tejon synthetic with design earthquake A-1 (Jennings *et al.*, 1968). The filtered traces were obtained using a gaussian filter peaked at 5 seconds.

represent an upper bound for the ground motions expected in the vicinity of a causative fault during an earthquake having a Richter magnitude of 8 or greater". In comparison, the amplitude of ground motion of the design earthquake is roughly twice that of the Fort Tejon synthetics. However, the duration of ground motion for the Fort Tejon synthetics is considerably longer than the upper bound of 120 seconds set for the design earthquake.

To quantify the results we narrow band-pass filtered the Fort Tejon body and surface wave synthetics using a Gaussian filter. Three periods of interest were chosen for the filtering: 3, 5, and 7 seconds. Figure III.7 illustrates the effect of the 5 second filter on a synthetic and the design earthquake. We may characterize each of the filtered synthetics by two gross measures: the maximum peak-to-peak amplitude and the "scaled duration" of the ground motion. We define the scaled duration to be the length of time for which the amplitude of the ground motion is greater than 10% of the maximum amplitude.

Figures III.8, III.9, and III.10 plot the maximum amplitude versus the scaled duration for the synthetics and the design earthquake for filters at 3, 5 and 7 second periods respectively. The points are grouped only to indicate wave type and epicenter, and not to imply a range limitation. There were no systematic differences between the Palmdale and San Bernardino epicenters for the Love waves and for the body waves; among the three epicenters for the Rayleigh waves; between the north-south and east-west components of the Love waves; or among the three different random models. Therefore, no distinct categories are made from these groups.

Let us first consider the ground motion at a period of 5 seconds

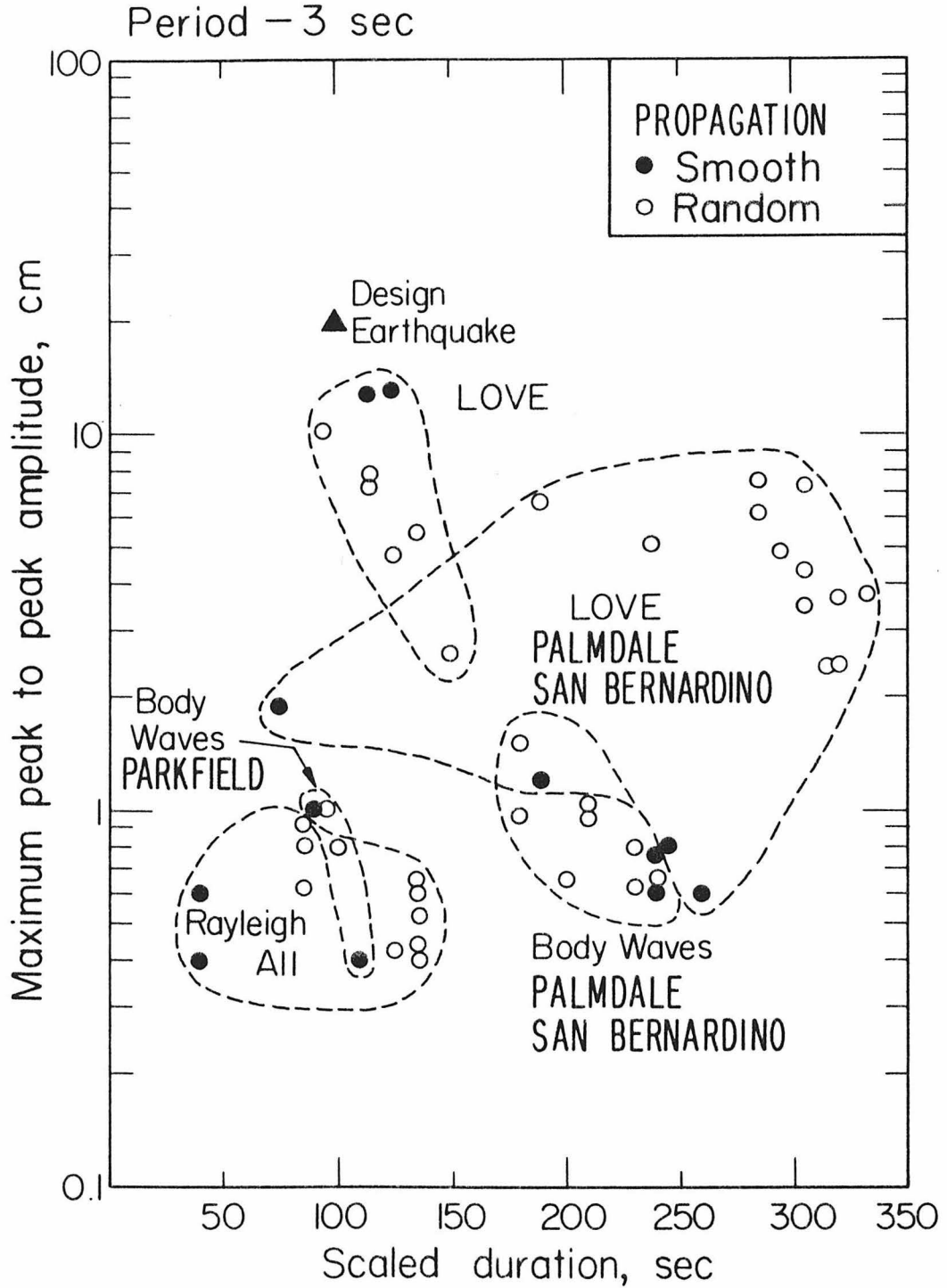


Figure III.8 Maximum amplitude versus scaled duration for the synthetics in Figures III.3-III.6 filtered at 3 seconds. Smooth and random propagation models are designated. The dashed lines qualitatively group the data.

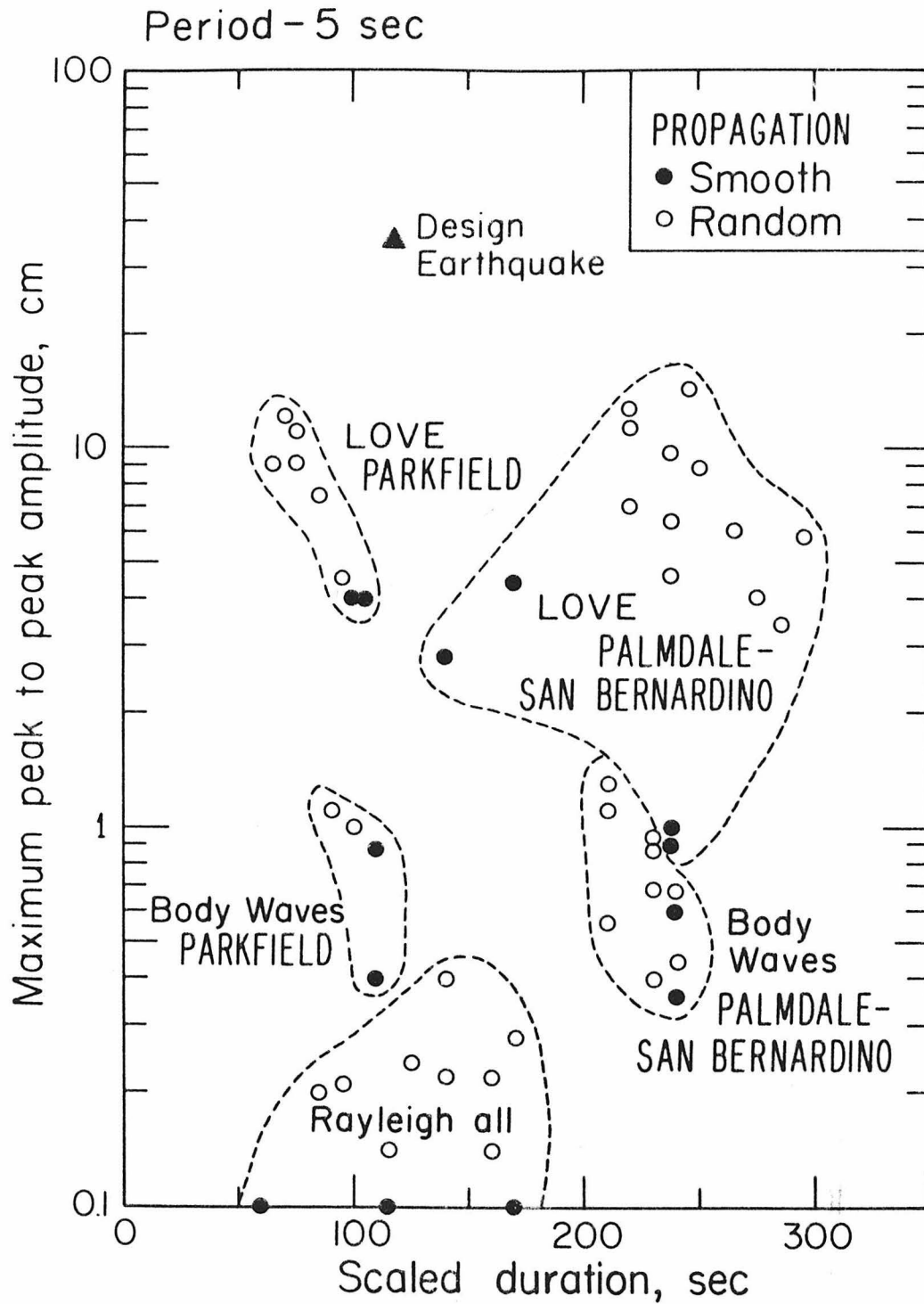


Figure III.9 Maximum amplitude versus scaled duration for the synthetics in Figures III.3-III.6 filtered at 5 seconds. Smooth and random propagation models are designated. The dashed lines qualitatively group the data.

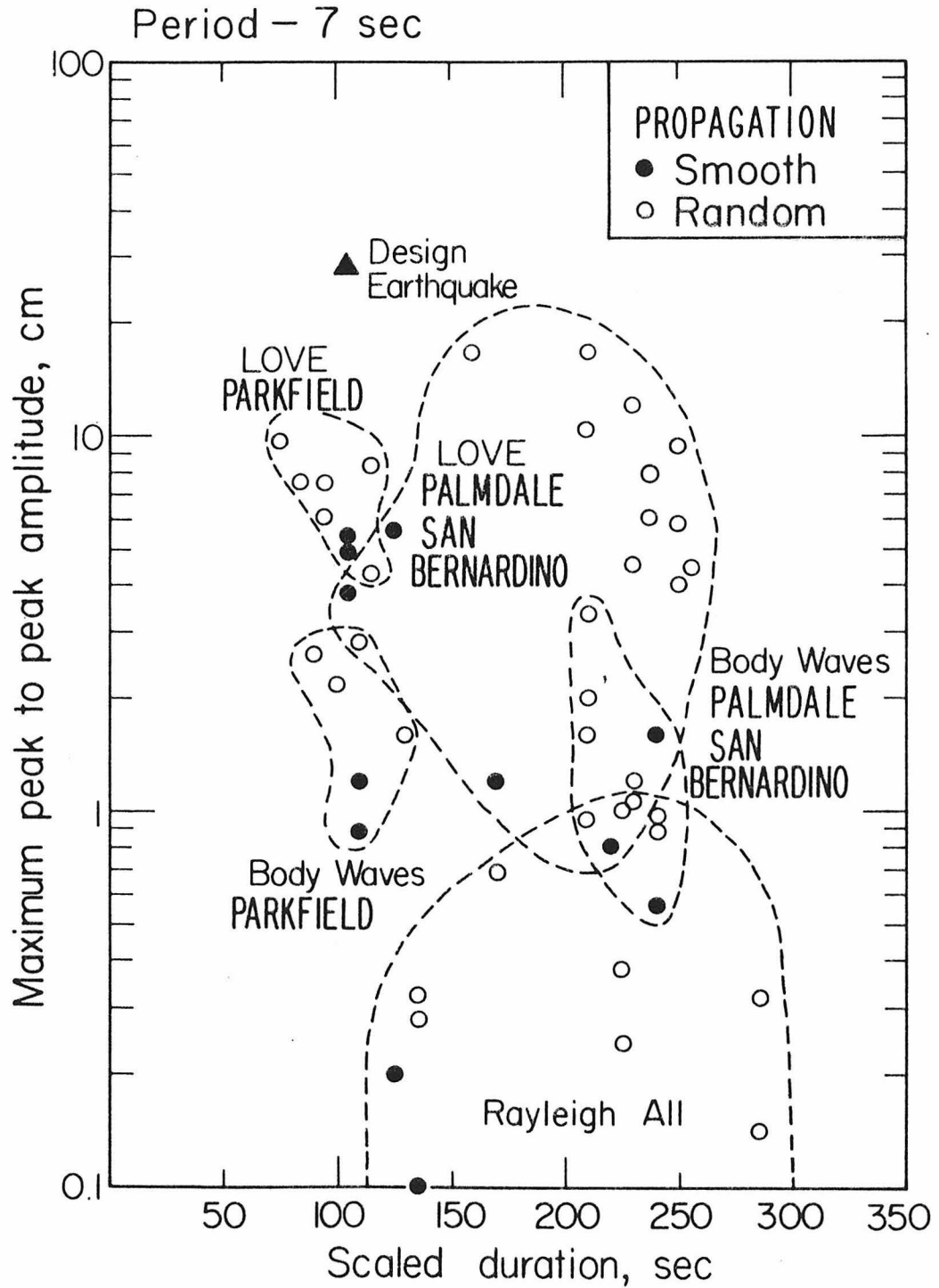


Figure III.10 Maximum amplitude versus scaled duration for the synthetics in Figures III.3-III.6 filtered at 7 seconds. Smooth and random propagation models are designated. The dashed lines qualitatively group the data.

(Figure III.9). The Love wave radiation is by far the most important seismic energy radiated at 5 seconds, being an order of magnitude larger in amplitude than either the body waves or Rayleigh waves. The maximum amplitudes for the Love waves are similar for epicenters at either end of the fault -- roughly 4 to 15 cm for most synthetics. The random models have considerably larger amplitudes associated with them. The location of the epicenter plays an important role in the scaled duration of ground motion. An epicenter at Parkfield has a scaled duration of some 80 seconds, while Palmdale or San Bernardino epicenters may have scaled durations of up to 300 seconds. The design earthquake A-1 is plotted as the triangle in the upper part of the figure. Though the amplitudes of earthquake A-1 are large, the scaled duration may be more than a factor of three shorter than the Love wave synthetics.

The results for filtered periods at 3 and 7 seconds (Figures III.8 and III.10) are similar to those found at 5 seconds. Love waves still play the most important role both in terms of maximum amplitude and scaled duration. The design earthquake significantly underestimates scaled durations at both 3 and 7 seconds filtered periods. For 3 second Love waves scaled durations of up to 5-1/2 minutes are credible.

Before summarizing the results, it is important to attempt to qualitatively estimate what effects possible misassumptions and obvious shortcomings have on this study. The body wave calculations in this paper included only direct P and S waves and ignored crustal and Moho refractions and reflections. Only the fundamental mode was used in the surface wave calculations. Thus we have underestimated the amount of radiated seismic energy. A laterally homogeneous structure was assumed in the calculations.

Crustal heterogeneities could act as scatterers and diminish maximum amplitudes, although the scaled durations would probably increase. A low velocity zone in the Southern Californian crust would tend to trap energy near the surface and increase surface wave amplitudes, though this would be period dependent. The local effect of the Los Angeles basin is unknown. Finally, randomness was added to our models in an ad hoc manner. Although the synthetics were not sensitive to the parameters chosen for the random models, we cannot rule out finding somewhat different results if randomness was added in a different manner.

Finally, some prepublication results of Kanamori (1979) lend support to the results presented here. In this study Kanamori models a Fort Tejon size earthquake on the San Andreas fault by dividing the fault into a number of discreet, smaller sub-events. The ground motion for these smaller sub-events is empirically modelled using displacement records from intermediate size California earthquakes. The rupture process of a large Fort Tejon size event is simulated by time lagging and adding the scaled ground motions for these discreet sub-events. The ground motions obtained by this more empirical method are somewhat larger than obtained in the study presented here, but the overall agreement is quite satisfactory.

#### SUMMARY

Tentative results have been presented toward an understanding of long period ground motion in Los Angeles from a great earthquake on the San Andreas fault. In the period band three-to-seven seconds ground motion from Love radiation is found to be most important, with peak-to-peak amplitudes up to 14 cm and scaled durations up to 5 minutes. Although

the amplitudes obtained for the ground motion are smaller than previous design earthquakes, the durations are longer by 2+ minutes. The inclusion of some complexity in the earthquake source is found to significantly enhance the amplitudes and durations of the long period ground motion for the models assumed. The amplitudes are not particularly sensitive to the epicenter, whereas durations for a San Bernardino epicenter are significantly longer than Parkfield epicenters. As only the direct body waves and fundamental surface waves were used in the analysis, the amplitudes of the ground motion should be considered lower bounds for the models presented. Uncertainties in details of the rupture process and the local crustal structure preclude more definitive conclusions at this time.

REFERENCES

- Abe, K. (1974). Seismic displacement and ground motion near a fault: The Saitama earthquake of September 21, 1931, J. Geophys. Res. 79, 4393-4399.
- Agnew, D. C. and K. E. Sieh (1978). A documentary study of the felt effect of the great California earthquake of 1857, Bull. Seism. Soc. Am., 68, 1717.
- Aki, K. (1967). Scaling law of seismic spectrum, J. Geophys. Res. 72, 1217-1231.
- Aki, K. (1968). Seismic displacements near a fault, J. Geophys. Res. 73, 5359-5376.
- Anderson, D. L. and R. S. Hart (1976). An earth model based on free oscillations and body waves, J. Geophys. Res. 81, 1461-1475.
- Ben-Menahem, A. and D. G. Harkrider (1964). Radiation patterns of seismic surface waves from buried dipolar point sources in a flat stratified earth, J. Geophys. Res. 69, 2605-2620.
- Burdick, L. J. and G. R. Mellman (1976). Inversion of the body waves from the Borrego Mountain earthquake to the source mechanism, Bull. Seism. Soc. Am. 66, 1485-1499.
- Butler, R., G. S. Stewart, and H. Kanamori (1979). The July 27, 1976 Tangshan, China earthquake - A complex sequence of intraplate events, Bull. Seism. Soc. Am. 69, 207-220.
- De Hoop, A. T. (1958). Representation theorems for the displacement in an elastic solid and their application to elastodynamic diffraction theory, Thesis, Technische Hogeschool, Delft.

- Ebel, J. E., L. J. Burdick and G. S. Stewart (1978). The source mechanism of the August 7, 1966 El Golfo earthquake, Bull. Seism. Soc. Am., 68, 1281-1292.
- Geller, R. J. (1976). Scaling relations for earthquake source parameters and magnitudes, Bull. Seism. Soc. Am. 66, 1501-1523.
- Hanks, T. C. (1976). Observations and estimation of long-period strong ground motion in the Los Angeles basin, Earthquake Eng. Struct. Dynam. 4, 473-488.
- Harkrider, D. G. (1964). Surface waves in multilayered elastic media, I. Rayleigh and Love waves from buried sources in a multilayered elastic half-space, Bull. Seism. Soc. Am. 54, 627.
- Haskell, N. (1964). Total energy and energy spectral density of elastic wave radiation from propagating faults, Bull. Seism. Soc. Am. 54, 1811-1841.
- Haskell, N. (1966). Total energy and energy spectral density of elastic wave radiation from propagating faults, 2, Bull. Seism. Soc. Am. 56, 125-140.
- Haskell, N. (1969). Elastic displacements in the near-field of a propagating fault, Bull. Seism. Soc. Am. 59, 865-908.
- Heaton, T. H. and D. V. Helmberger (1977). A study of the strong ground motion of the Borrego Mountain, California earthquake, Bull. Seism. Soc. Am. 67, 315-330.
- Heaton, T. H. and D. V. Helmberger (1978). Predictability of strong ground motion in the Imperial Valley: Modelling the M 4.9, November 4, 1976 Brawley earthquake, Bull. Seism. Soc. Am. 68, 31-48.
- Helmberger, D. V. and S. D. Malone (1975). Modelling local earthquakes as shear dislocations in a layered half-space, J. Geophys. Res. 80, 4881-4888.

- Hermann, R. B. and O. W. Nuttli (1975). Ground-motion modelling at regional distances for earthquakes in a continental interior, I. theory and observations, Earthquake Eng. Struct. Dynam. 4, 49-58
- Jennings, P. C., G. W. Housner and N.C. Tsai (1968). Simulated earthquake motions, National Science Foundation report, Earthquake Engineering Res. Lab., Calif. Inst. of Tech., Pasadena, April.
- Kanamori, H. (1970). Synthesis of long-period surface waves and its application to earthquake source studies, Kurile Islands earthquake of October 13, 1963, J. Geophys. Res. 75, 5011-5027.
- Kanamori, H. (1972). Determination of effective tectonic stress associated with earthquake faulting. The Tottori earthquake of 1943, Phys. Earth Planet. Int. 5. 426-434.
- Kanamori, H. (1977). The energy release in great earthquakes, J. Geophys. Res. 82, 2981-2987.
- Kanamori, H. (1979). Semi-empirical approach to prediction of long-period ground motion (pre-publication results).
- Kanamori, H. and J. J. Cipar (1974). Focal process of the Great Chilean earthquake May 22, 1960, Phys. Earth Planet. Int. 9, 128-136.
- Kanamori, H. and D. Hadley (1975). Crustal structure and temporal velocity change in Southern California, Pageoph. 113, 275-280.
- Kanamori, H. and G. S. Stewart (1976). Mode of the strain release along the Gibbs fracture zone, Mid-Atlantic Ridge, Phys. Earth Planet. Int. 11, 312-332.
- Kanamori, H. and G. S. Stewart (1978). Seismological aspects of the Guatemala earthquake of February 4, 1976, J. Geophys. Res., 83, 3427-3434.

- Langston, C. A. (1976). A body wave inversion of the Koyna, India earthquake of December 10, 1967, and some implications for body wave focal mechanisms, J. Geophys. Res. 81, 2517-2529.
- Langston, C. A. (1978). The February 9, 1971 San Fernando earthquake, a study of source finiteness in teleseismic body waves, Bull. Seism. Soc. Am. 68, 1.
- Langston, C. A. (1978). The February 9, 1971 San Fernando earthquake, a study of source finiteness in teleseismic body waves, Bull. Seism. Soc. Am. 68, 1.
- Mikumo, T. (1973). Faulting mechanism of the Gifu earthquake of September 9, 1969, and some related problems, J. Phys. Earth. 21, 191-212.
- Mikumo, T. (1973). Faulting process of the San Fernando earthquake of February 9, 1971 inferred from static and dynamic near-field displacements, Bull. Seism. Soc. Am. 63, 249-269.
- Rial, J. A. (1978). The Caracas, Venezuela earthquake of July 1967: A multiple source event, J. Geophys. Res., (in press).
- Sieh, K. (1978). Slip along the San Andreas fault associated with the great 1857 earthquake, Bull. Seism. Soc. Am. 68, 1421.
- Stewart, G. S. (1978). Implications for plate-tectonics of the August 19, 1977 Indonesian decoupling normal-fault earthquake, EOS Transactions (abstract), 59, 326.
- Stewart, G. W. and S. N. Cohn (1978). The August 16, 1976 Mindanao, Philippine earthquake ( $M_s = 7.8$ ) - Evidence for a subduction zone south of Mindanao, (submitted for publication).
- Trifunac, M. D. (1974). A three-dimensional dislocation model for the

San Fernando, California earthquake of February 9, 1971, Bull. Seism. Soc. Am. 64, 149-172.

Wallace, R. E. (1968). Notes on stream channels offset by the San Andreas fault, southern coast ranges, California, in Proc. of Conf. on Geologic Problems of the San Andreas Fault System, W. R. Dickinson and A. Grantz, Editors, Stanford Univ. Publ., Geol. Sci., Univ. Ser. 11, 6-21.

Wood, H. O. (1908). Distribution of Apparent Intensity in San Francisco, in The California Earthquake of April 18, 1906, Report of the State Earthquake Investigation Commission, Carnegie Inst. of Wash., Publ. 87, Washington, D.C., 220-245.

Wood, H. O. (1955). The 1857 earthquake in California, Bull. Seism. Soc. Am. 45, 47-67.

**CHAPTER IV**

**AN AMPLITUDE STUDY OF RUSSIAN NUCLEAR  
EVENTS FOR WSSN STATIONS IN THE UNITED STATES**

ABSTRACT

Short period P wave amplitude data from nuclear explosions in the Soviet Union recorded by WWSSN stations in the United States are presented. Thirty-four events in five test sites are analyzed. The consistency and similarity of the initial P waveforms allow a stable amplitude measure. A well-defined amplitude pattern is obtained for each source region. The test sites at northern and southern Novaya Zemlya show a relative amplitude trend of a factor of three across the United States in their respective amplitude patterns. This is in contrast to two sites at Semipalatinsk which are in good relative agreement. A pattern of lateral variation of amplitude in the United States is obtained for a northern azimuth of approach. Stations situated on sediments are corrected for amplification effects. Stations in the western U.S. do not have systematically lower amplitudes than eastern U.S. stations, in contrast to previous studies. Lowest amplitudes are found in Golden, Colorado (Gol) and Albuquerque, New Mexico (ALQ), a factor of four lower than high amplitude stations. Preliminary amplitude data are presented from earthquakes in the Kuriles and South America. Events are chosen for consistency of waveforms across the U.S. to minimize earthquake source and directivity effects. These earthquake data indicate that amplitude variations in the United States are azimuthally dependent.

INTRODUCTION

Since the establishment of the World Wide Standard Seismograph Network (WWSSN) and during the deployment of the Long Range Seismic

Measurement (LRSM) stations in the early 1960's a number of studies have undertaken the measurement of the variation of teleseismic body wave amplitudes in the conterminous United States. Cleary (1967) measured first peak amplitudes of P waves from short period LRSM recordings of 22 earthquakes, each having common first motions across the United States, and noted that the signal strength tended to be lower in the west than elsewhere, although exceptions did occur. Evernden and Clark (1970) and Booth, Marshall, and Young (1974) determined magnitude anomalies for stations of the LRSM and found short period (1 sec) magnitudes in the western United States - WUS, approximately west of the eastern front of the Rocky Mountains - are about 0.5 magnitude units (a factor of 3) smaller than the eastern United States - EUS, east of the Rocky Mountains. Long period magnitude (16 sec) anomalies for the LRSM show large amplitudes along the Gulf coast but no other distinct pattern (Booth et al., 1974). Solomon and Toksoz (1970) used a spectral ratio technique on long period WWSSN recordings of P and S waves from two deep focus South American earthquakes to determine apparent attenuation variation across the United States, and concluded that attenuation was higher between the Rockies and Sierra Nevada - Cascades, and the northeastern United States. Der, Masse, and Gurski (1975) using short period LRSM stations measured maximum amplitudes of P and S waves and the dominant period of S waves for 3 deep focus South American and two deep focus Kurile earthquakes and concluded that the data indicated higher attenuation in WUS than EUS. In a study using four deep focus South American earthquakes recorded by the WWSSN in the the United States, Burdick (1978) utilized

the ratios of short period to long period amplitudes of P and S waves to minimize the effect of source radiation in determining amplitude variations at the receiver. No lateral amplitude variation across the United States was seen in this data set.

The purpose of this chapter is to report on the variation of P wave amplitudes in the United States from nuclear explosions in the Soviet Union. Amplitude data from 34 nuclear explosions at 5 test sites are presented in 24 WWSSN stations in the conterminous United States plus BEC, Bermuda. The results are interpreted in terms of source, path and receiver effects. Source effects are deduced by intercomparing amplitude patterns among the different sites. Data which have been diffracted at the core mantle boundary are presented, but will be discussed and interpreted in a forthcoming paper. The apparent amplitude variation in the United States for a northern azimuth of approach is determined from an average of all non-diffracted data. The effect of signal amplification for a receiver situated on low velocity sediments is considered. A qualitative measure is made of the importance of scattering in the amplitude variation utilizing the horizontal components of the P waves. An explanation of the amplitude variation in terms of attenuation differences is considered. Finally, to provide an indication of the azimuthally varying characteristics of the amplitude pattern, preliminary results are presented in a study of amplitude patterns in the United States using earthquakes in the Kuriles and South America.

#### Nature of the Study

The overall geometry of the stations of the WWSSN in the United States and the source regions of the nuclear explosions in the Soviet

Union are shown in Figure IV.1. The Russian events used in this study - listed in Table IV.1. - have been naturally divided into several groups based on test sites. All events between 1965 and early 1976 having a yield of 70 kt. or greater, are analyzed in the collection of data. The following abbreviations are used for the test sites: NNZ, northern Novaya Zemlya; SNZ, southern Novaya Zemlya; SEMI E, Semipalatinsk east; SEMI W, Semipalatinsk west; KAZ, Kazakh. NNZ and SNZ are situated roughly 300 km apart; SEMI E and SEMI W lie about 70 km apart. The approximate distances in degrees delta between the United States stations and the source regions are listed in Table IV.2. The United States is situated in the range  $60^{\circ}$  to  $80^{\circ}$  delta from the Novaya Zemlya sites, NNZ and SNZ. P waves at these ranges bottom in the smooth lower mantle and should be relatively free of propagational path effects. The KAZ and SEMI source regions lie in the  $80^{\circ}$  to  $100^{\circ}$  range, and thus the southern United States stations will experience amplitude effects due to diffraction at the core-mantle boundary.

There are several advantages in using nuclear explosions rather than earthquakes in an amplitude study of this nature. Earthquake amplitudes contain source radiation and directivity effects which must be corrected before amplitude effects due to the path or receiver can be ascertained. In contrast the explosion source is theoretically spherically symmetric, and thus is naturally free of this complication. Event locations within the Soviet test sites vary on the order of tens of kilometers. The several events in each site allow the amplitude measurement to be repeated, and afford us an opportunity to view the stability of the measurement. Short period vertical P waves are

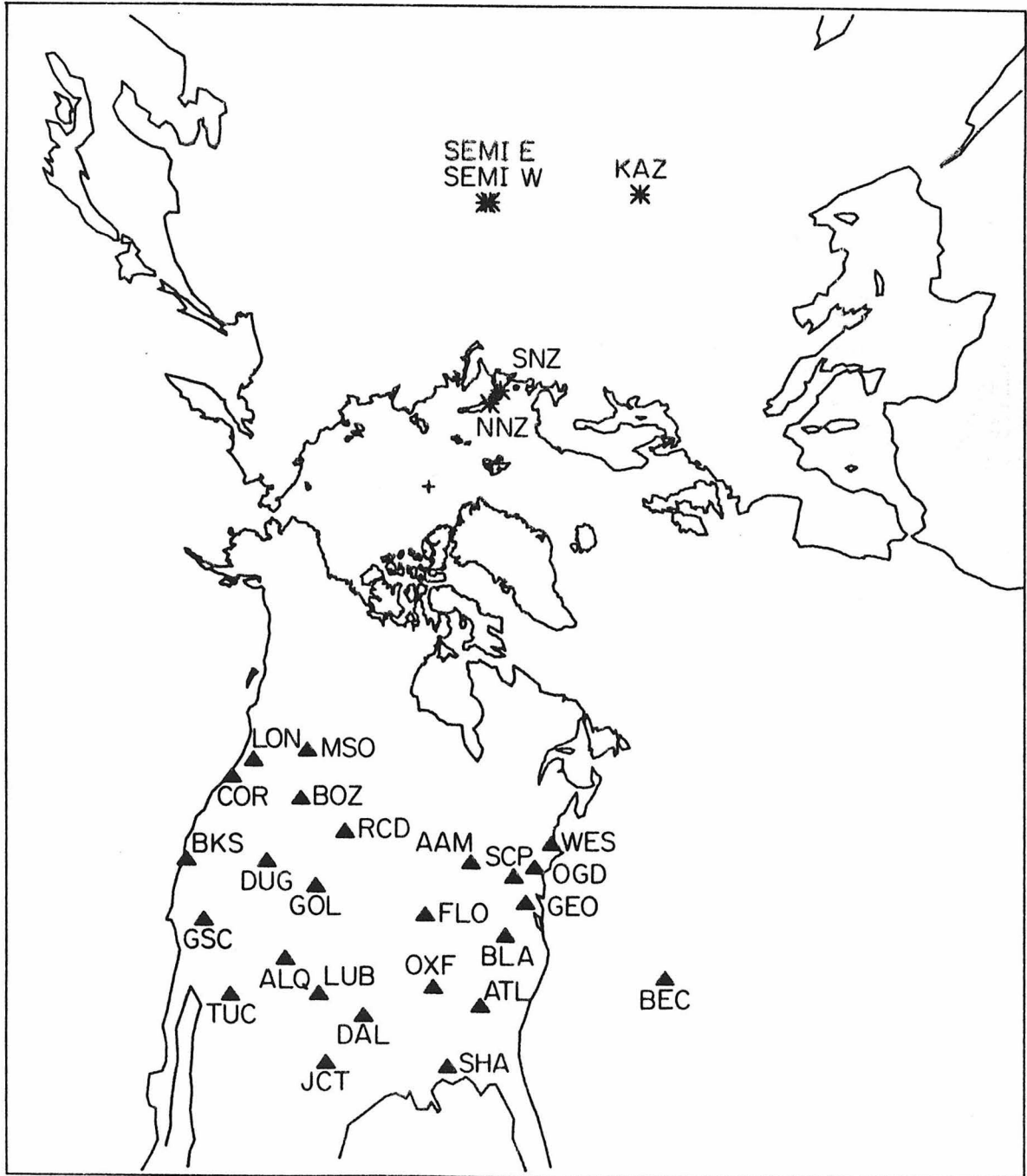


Figure IV.1 A gnomonic projection (all great circles are straight lines) showing the source regions in the Soviet Union and the WWSSN stations in the United States.

TABLE IV.1

## EXPLOSION DATA SET\*

## Northern Novaya Zemlya

27 Oct 66	5:57:58	73.44N	54.75E
21 Oct 67	4:59:58	73.37N	54.81E
7 Nov 68	10:02:05	73.40N	54.86E
14 Oct 69	7:00:06	73.40N	54.81E
14 Oct 70	6:02:57	73.31N	55.15E
27 Sept 71	5:59:55	73.39N	55.10E
28 Aug 72	5:59:57	73.34N	55.08E
12 Sept 73	6:59:54	73.30N	55.16E
29 Aug 74	9:59:56	73.37N	55.09E
23 Aug 75	8:59:58	73.37N	54.64E
21 Oct 75	11:59:57	73.35N	55.08E

## Southern Novaya Zemlya

27 Sept 73	6:59:58	70.76N	53.87E
2 Nov 74	4:59:57	70.82N	54.06E
18 Oct 75	8:59:56	70.84N	53.69E

## Semipalatinsk East

15 Jan 65	5:59:59	49.89N	78.97E
30 Nov 69	3:32:57	49.92N	79.00E
2 Nov 72	1:26:58	49.91N	78.84E
23 Jul 73	1:22:58	49.99N	78.85E
14 Dec 73	7:46:57	50.04N	79.01E
31 May 74	3:26:57	49.95N	78.84E
4 Jul 76	2:56:58	49.91N	78.95E
23 Nov 76	5:03:00	50.00N	79.00E

TABLE IV.1

(Continued)

## Semipalatinsk West

19 Oct 66	3:57:58	49.75N	78.03E
20 Apr 67	4:07:58	49.74N	78.12E
17 Oct 67	5:03:58	49.82N	78.10E
29 Sept 68	3:42:58	49.77N	78.19E
28 Jun 70	1:57:58	49.83N	78.25E
22 Mar 71	4:32:58	49.74N	78.18E
25 Apr 71	3:32:58	49.82N	78.09E
30 Dec 71	6:20:58	49.75N	78.13E
20 Feb 75	5:32:58	49.82N	78.08E

## Kazakh

6 Dec 79	7:02:57	43.83N	54.78E
12 Dec 70	7:00:57	43.85N	54.77E
23 Dec 70	7:00:57	43.83N	54.85E

\* Locations and origin times from Dahlman and Israelson (1977)

TABLE IV.2

APPROXIMATE DISTANCES BETWEEN U.S. STATIONS  
AND RUSSIAN TEST SITES  
(degrees delta)

	<u>NNZ</u>	<u>SNZ</u>	<u>SEMI</u>	<u>KAZ</u>
AAM	61.2	63.2	86.9	86.5
ALQ	71.2	73.6	95.4	99.8
ATL	69.9	71.9	95.7	94.5
BEC	67.0	68.4	91.9	86.2
BKS	69.0	71.6	90.6	98.6
BLA	65.6	67.5	91.3	89.7
BOZ	60.9	63.5	84.4	90.1
COR	62.3	64.9	83.9	91.9
DAL	72.3	75.6	97.5	99.4
DUG	66.4	68.9	89.6	95.6
FLO	65.6	67.8	91.1	91.9
GEO	63.3	65.2	89.1	86.8
GOL	66.4	68.8	90.7	94.9
GSC	71.4	74.0	94.0	100.9
JCT	75.0	77.3	99.9	102.5
LON	60.1	62.7	82.0	89.7
LUB	72.1	74.5	96.8	100.1
MSO	59.8	62.4	83.0	89.2
OCD	69.7	62.5	86.5	84.0
OXF	70.0	71.8	95.3	95.5
RCD	61.8	64.3	86.3	90.9
SCP	61.6	63.5	87.4	85.6
SHA	73.2	75.3	98.9	98.4
TUC	74.1	76.6	97.6	103.1
WES	58.8	60.6	84.5	81.5

shown in Figure IV.2 from four event source regions. The overall consistency and similarity of the initial waveforms from station to station and event to event represent another natural advantage of the explosion data set. The initial upswing and following larger downswing are characteristic of the explosion waveform. The coherency of waveforms diminishes after this initial portion due to different crustal effects at different stations. The relative amplitude of each station within each event is indicated. There is no apparent correlation between frequency content and amplitude in this data set. Synthetic waveforms computed for the von Seggern and Blanford (1972) theoretical explosion source are shown for comparison. The A and B swings are primarily controlled by the direct P wave, whereas the C peak is controlled by pP. The somewhat longer period waveform of the Kazakh event indicates a deeper depth of burial and slower rise time of the source.

The amplitude measure used throughout this study is indicated by the synthetic waveforms: the amplitude of first peak to first trough, or AB amplitude. This particular measure was chosen for several reasons. It may be consistently and unambiguously read at each station for all events. It is the portion of the waveform least contaminated by source effects due to variations in pP and source structure, and from the receiver effects of different station crustal structures. The AB amplitude measure also minimizes baseline problems in the presence of noise.

The quality of the explosion amplitude data is quite good. The amplitudes may read with a precision of better than 10%, except at low gain stations for smaller events where the error may be up to 30%.

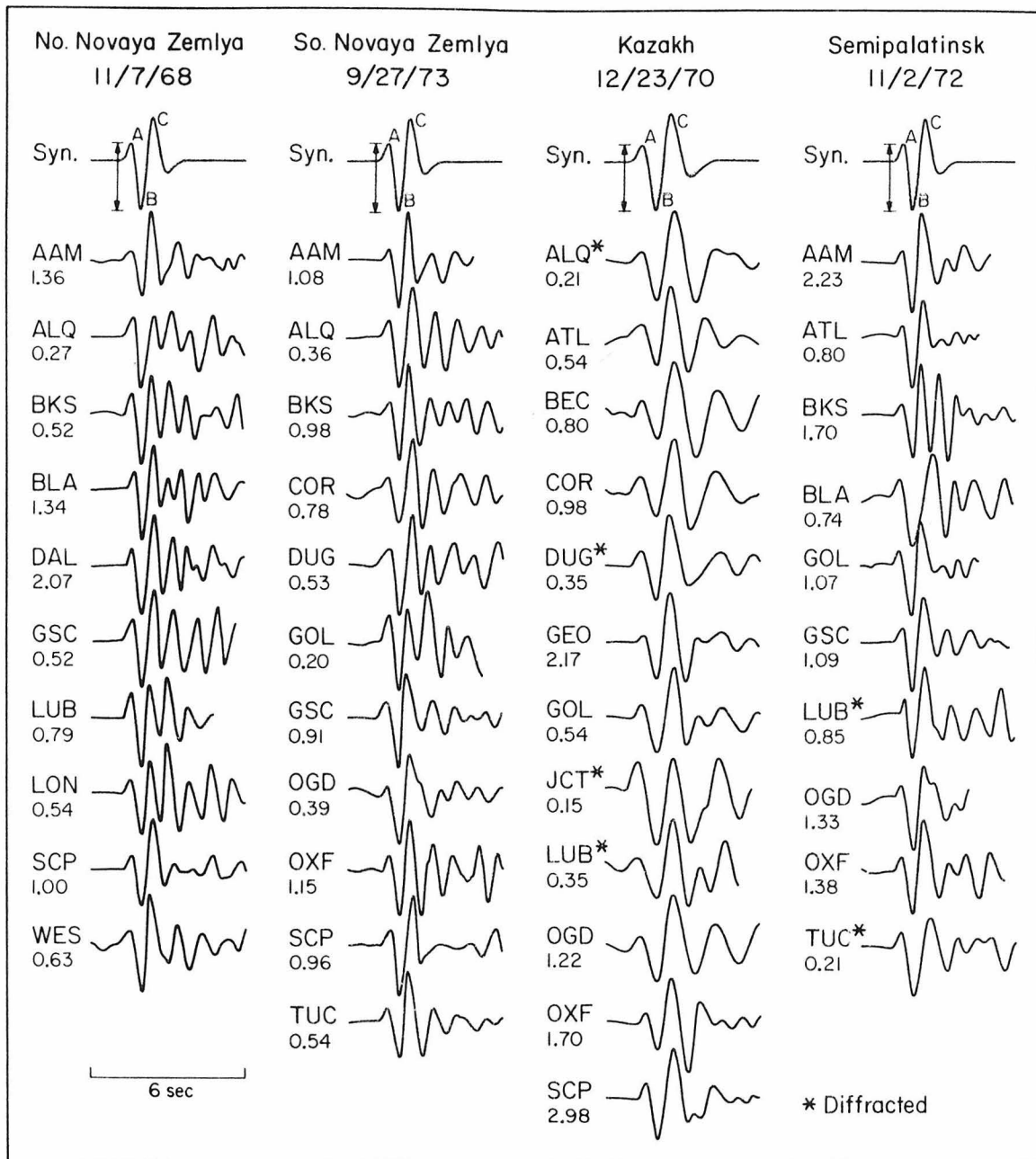


Figure IV.2 Short period P waves recorded at WSSN stations across the United States from four Russian nuclear events. The numbers beneath the station codes indicate the true relative amplitudes as defined by the AB measure indicated on the comparison synthetic waveform. Stations beyond 95.5° are noted as diffracted.

The data are measured, corrected to a common station gain of 100 k, and grouped by source region. In each source region we have amplitude observations  $o_{ij}$  for  $i$  events and  $j$  stations. While the relative amplitude relationship from station to station is similar from event to event, the absolute amplitudes of each event are different. A simple normalization procedure would be to choose one station as a reference, and then for each event divide all the station amplitude measurements by the amplitude at the reference station. In this way the events are normalized to a common scale but the reference station is always unity. However, this method forces whatever scatter that is characteristic of the reference station upon the rest of the stations. To improve this situation the following normalization procedure was used. From the  $i$  events choose a reference event  $k$ , to which the other events are to be scaled in a least squares sense. Scale factors  $\alpha_i$  are determined such that the least squares error is minimized for each event  $i \neq k$ :

$$\min \sum_j | \alpha_i o_{ij} - o_{kj} |^2 \quad (1)$$

Let  $\alpha_k$  be the average amplitude of the master event  $k$ :

$$\alpha_k = \frac{1}{j} \sum_j o_{kj} \quad (2)$$

The total error for all events  $i$  in the source region is then

$$\alpha_k \frac{1}{i} \sum_i \sum_j | \alpha_i o_{ij} - o_{kj} |^2 \quad (3)$$

we then iterate on the process, letting each event  $i$  in a source region be the master event  $k$ . The scale factors  $\alpha_i$  in each source are chosen for the event  $k$  which minimizes the total error in (3) the best.

### Data

The amplitude data for the five source regions are plotted in Figures IV.3 through IV.6. The ordinate of each plot is a log scale indicating relative amplitude. The stations of the WWSSN used in this study are listed in a west to east arrangement with respect to station location in the United States viewed from the Semipalatinsk test sites. Detailed intercomparisons of the source regions will be considered in the next section but some observations may be noted at this time. The results for NNZ are shown in Figure IV.3. The overall scatter at each individual station is quite low; less than a factor of 1.5 about the mean. The lowest stations are ALQ and GOL, followed by DUG and BEC. The amplitudes in the west are somewhat lower than those in the east. There is an amplitude differential of nearly a factor of 5 between GOL and ALQ and the higher amplitude stations, AAM, DAL and SHA. The data for SNZ plotted in Figure IV.4 are similar in overall pattern to NNZ, but different in detail. ALQ and GOL are still low, but OGD and WES are now among the lower values. The stations in the far west for SNZ have amplitudes comparable to the high values in the central United States. The relationship of BLA with other eastern stations is different for NNZ and SNZ. Figure IV.5 plots the data for both Semipalatinsk test sites. There appear to be no systematic differences between the SEMI E and SEMI W sites, in contrast to NNZ and SNZ. Figure IV.5 is considerably more complicated in appearance

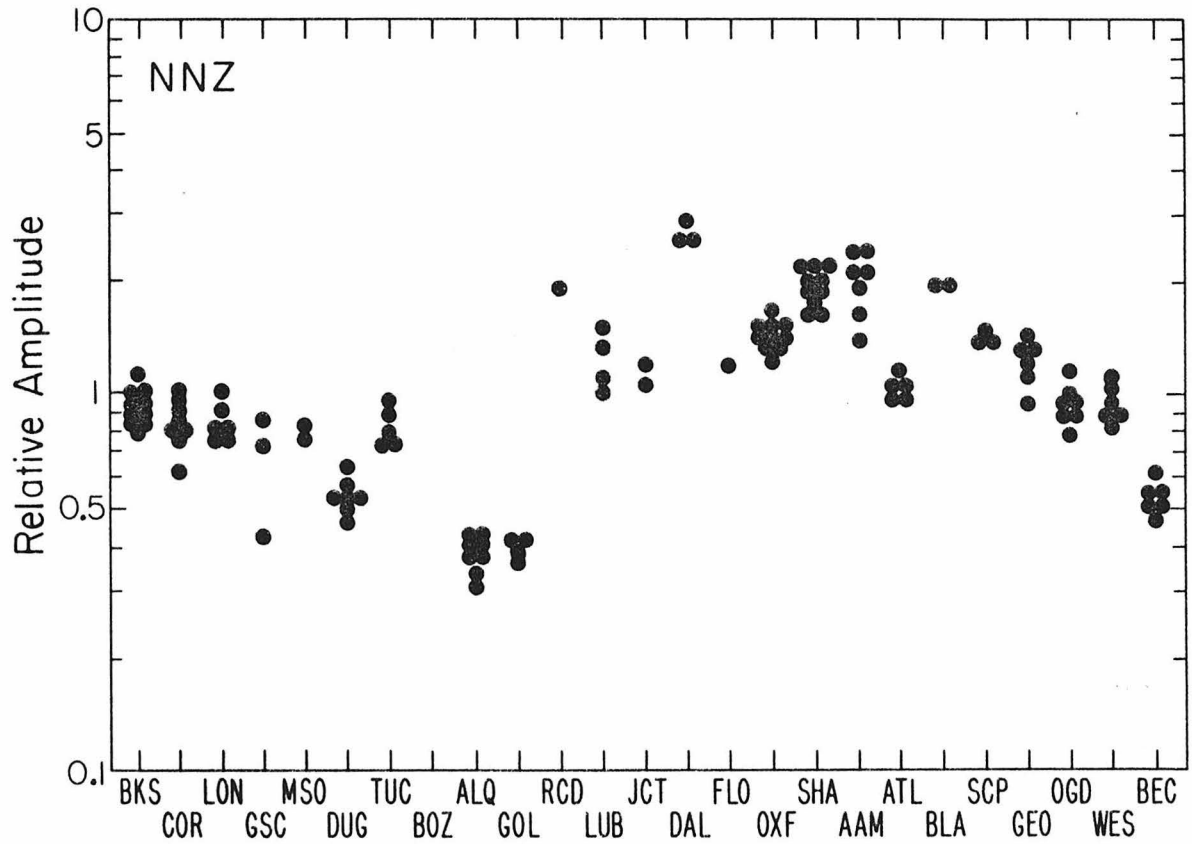


Figure IV.3 Relative amplitudes of short period P waves observed at WSSN stations across the United States from eleven nuclear explosions at the northern Novaya Zemlya site.

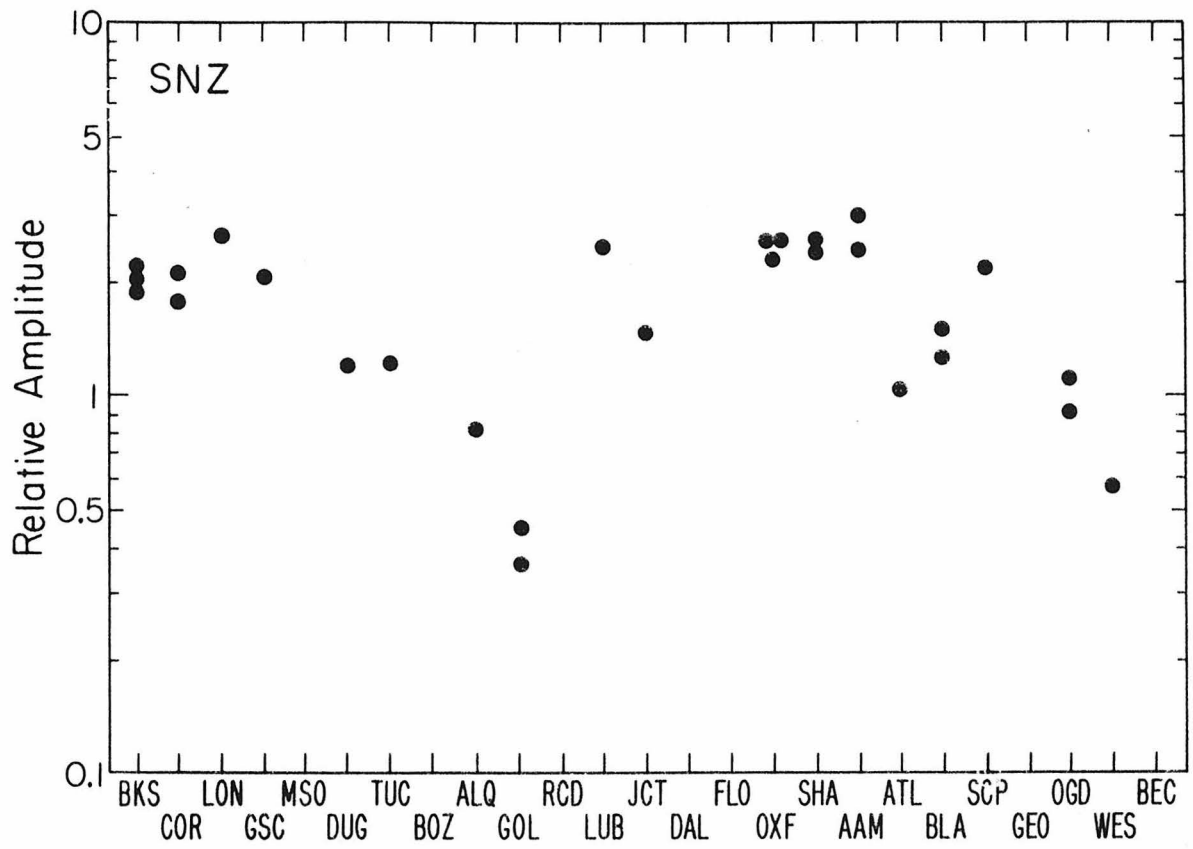


Figure IV.4 Relative amplitudes of short period P waves observed at WSSN stations across the United States from three nuclear explosions at the southern Novaya Zemlya site.

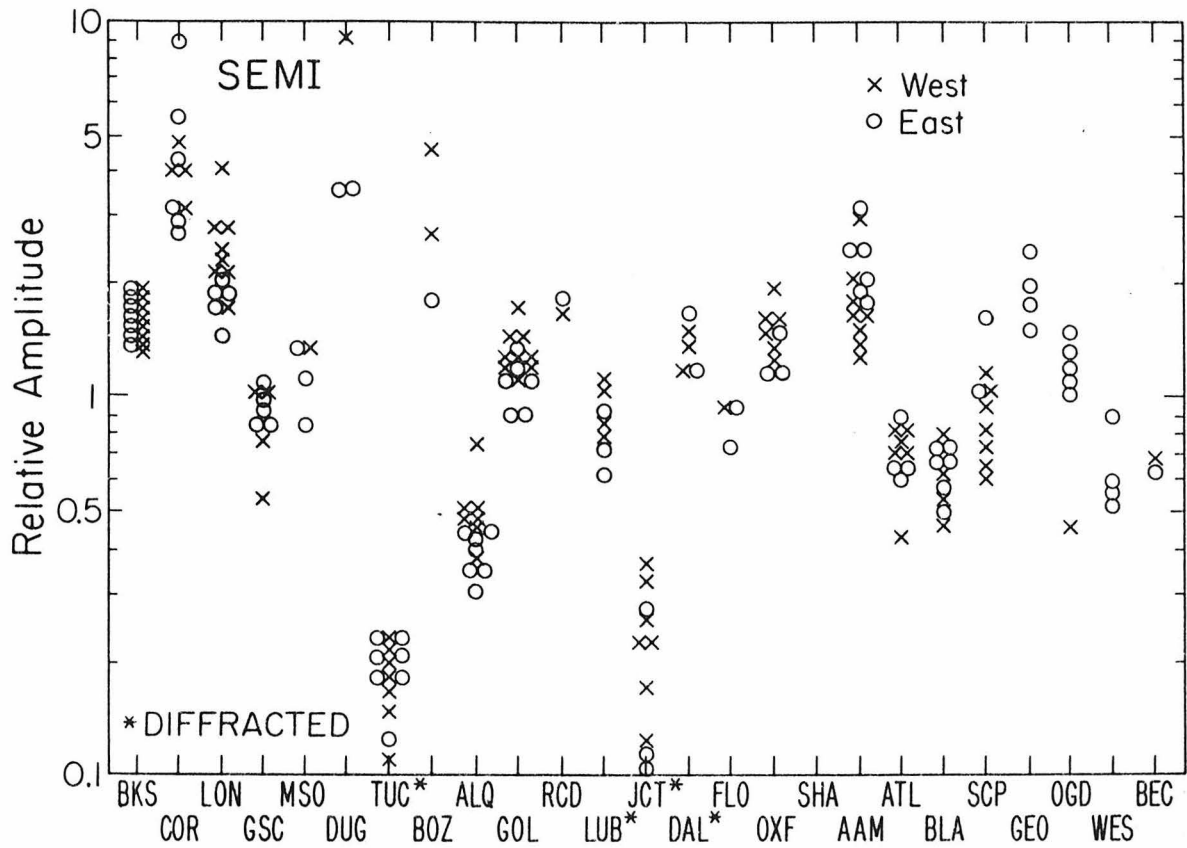


Figure IV.5 Relative amplitudes of short period P waves observed at WWSSN stations across the United States from seventeen nuclear explosions at the east and west Semipalatinsk test sites. Stations beyond  $95.5^\circ$  are noted as diffracted.

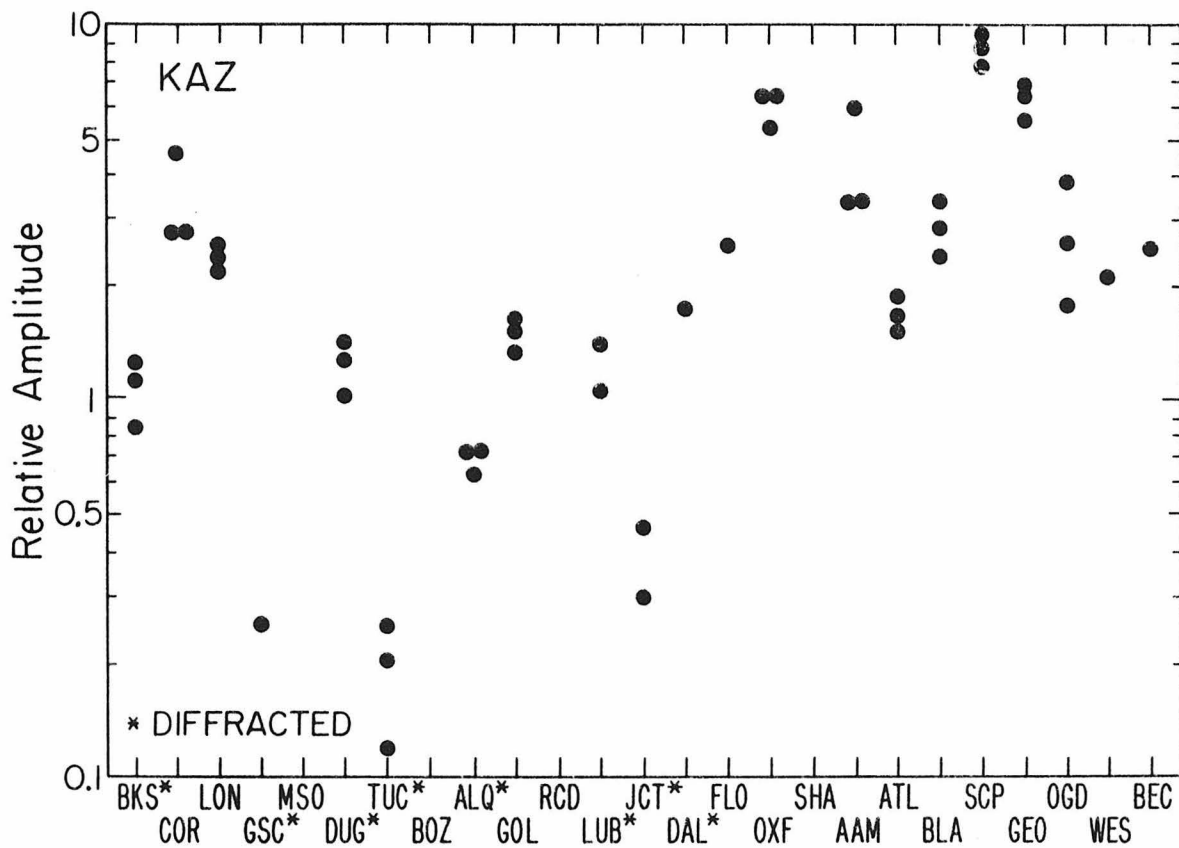


Figure IV.6 Relative amplitudes of short period P waves observed at WWSSN stations across the United States from three nuclear explosions at the Kazakh site. Stations beyond  $95.5^\circ$  are noted as diffracted.

than the plots for the Novaya Zemlya source regions. The greater scatter at the individual stations may come in part from including stations showing amplitude diffraction effects - TUC, DAL, LUB, JCT - in the data normalization procedure, and in part from larger reading errors in measuring the amplitudes of the smaller yield Semipalatinsk explosions. Stations COR, DUG, GOL show greater relative amplitudes at the Semipalatinsk sites than were observed for NNZ and SNZ. The three events for the Kazakh site are plotted in Figure IV.6. Low individual station scatter is observed for this site. A number of stations - BKS, GSC, DUG, TUC, ALQ, LUB, JCT, and DAL - show relative deamplification due to diffraction at the core-mantle boundary.

#### Source Comparisons

The amplitude patterns in Figures IV.3 through IV.6 represent a combination of source, path, and receiver effects. We may remove the effect of the receiver to look at the effects due to the source and the path if we assume the P waves emerging at a station in the United States from the different test sites experience a common receiver effect. As the azimuths and angles of incidence from the five source regions vary by only several degrees, this is a plausible assumption. The mean and standard error of the mean are calculated from the event data at each station for the different source regions and are used in further manipulation of the data. Dividing the station amplitude values for one test site by those of another cancels the common receiver and smaller geometric spreading effects. The resultant ratios may be plotted in the same fashion as Figures IV.3 through IV.6 and represent the relative source-path effects between the two source

regions. In the case of the two Novaya Zemlya sites, NNZ and SNZ, as the ray paths are similar and bottom in the rather smooth lower mantle, the ratio pattern represents primarily relative source effects. This ratio pattern is plotted in Figure IV.7 from the data in Figures IV.3 and IV.4. The figure shows an unmistakable trend of high in the west to low in the east, roughly a factor of 3 variation. As the ratios only indicate a relative pattern, the amplitude variation could originate at NNZ or SNZ, or a combination of both. To attempt to clarify this point, intercomparisons with the SEMI and KAZ sites are tried.

To utilize SEMI and KAZ for source and receiver consideration, stations suffering amplitude diminution due to diffraction at the core-mantle boundary must be separated. The diffraction effect is considered in detail in a separate paper (Ruff and Butler, in preparation) but may be briefly outlined. The SEMI and KAZ data are ratioed to the NNZ and SNZ data. The ratios are then plotted amplitude versus distance. The ratios hover about unity until the distances from SEMI and KAZ reach about  $95.5^\circ$  delta. Past this distance amplitudes systematically decline due to diffraction. Stations showing this amplitude diminution have been indicated in Figures IV.5 and IV.6 with an asterisk. These stations are largely deleted from further consideration in this chapter. Stations less than  $95.5^\circ$  shall be assumed to be free of diffraction amplitude effects.

An interesting contrast is observed between the two sites at Semipalatinsk and the two sites on Novaya Zemlya. The scatter observed at a station for the different events at the Novaya Zemlya sites in Figures IV.3 and IV.4 is low, and is somewhat greater for Semipalatinsk. This

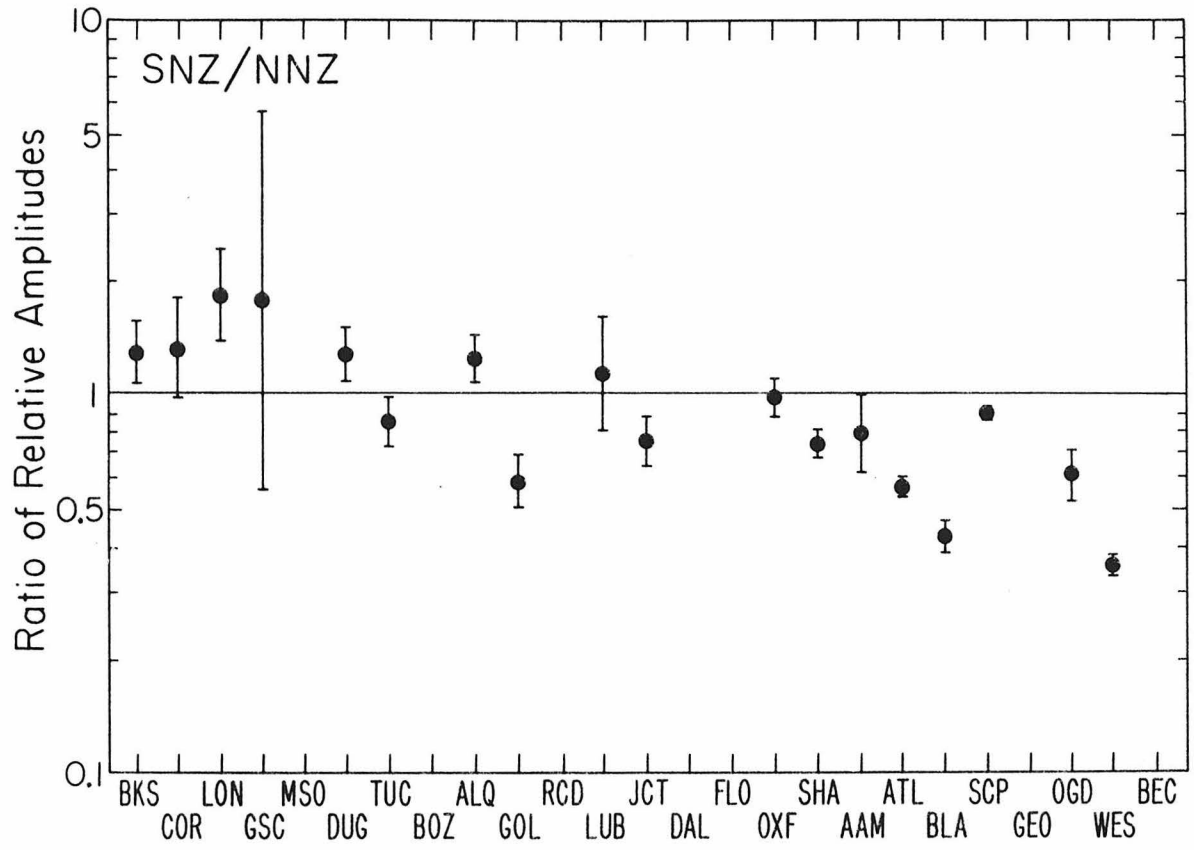


Figure IV.7 Ratio of the amplitude pattern for the southern Novaya Zemlya site to the amplitude pattern for the northern Novaya Zemlya site.

increased scatter in the SEMI values may be partly due to including the diffraction data in the normalization. More interesting, however, is the overall agreement of SEMI E with SEMI W, in marked contrast to the differences observed in the ratio plot of the SNZ to NNZ. The two SEMI sites lie about 70 km apart, while SNZ and NNZ are roughly 300 km apart. A ratio comparison among the combined SEMI data and NNZ and SNZ is shown in Figure IV.8. If we ignore COR, DUG, and GOL momentarily, the remaining SEMI stations fit the NNZ and SNZ data equally well with a scatter of less than a factor of two. This also appears to be the case in the KAZ data in Figure IV.9, although the control is more sparse. The scatter of the KAZ values in relation to NNZ and SNZ is of the same order as was observed in Figure IV.8 for Semipalatinsk, somewhat less than a factor of two.

The SEMI stations COR, DUG, GOL and the NNZ value for BLA show a considerably larger deviation than the other stations in Figure VI.8 and importune a momentary digression to consider these anomalous values further. For additional comparison a ratio plot of the KAZ data to NNZ and SNZ is shown in Figure IV.9. In this plot neither COR nor GOL show large deviations, and quite the contrary agree well the NNZ and SNZ values. DUG is included, though it may be somewhat diminished due to diffraction, to show that it does not stand greatly different than the NNZ or SNZ data. This suggests that the apparent amplification of COR, DUG, and GOL is a property of the SEMI data set. As this amplification is observed for only these three stations in both the SEMI E and SEMI W data, and as the two sites are situated 70 km apart, and ruling out coincidence as low probability, we may conclude that the apparent amplification is not due to the source regions,

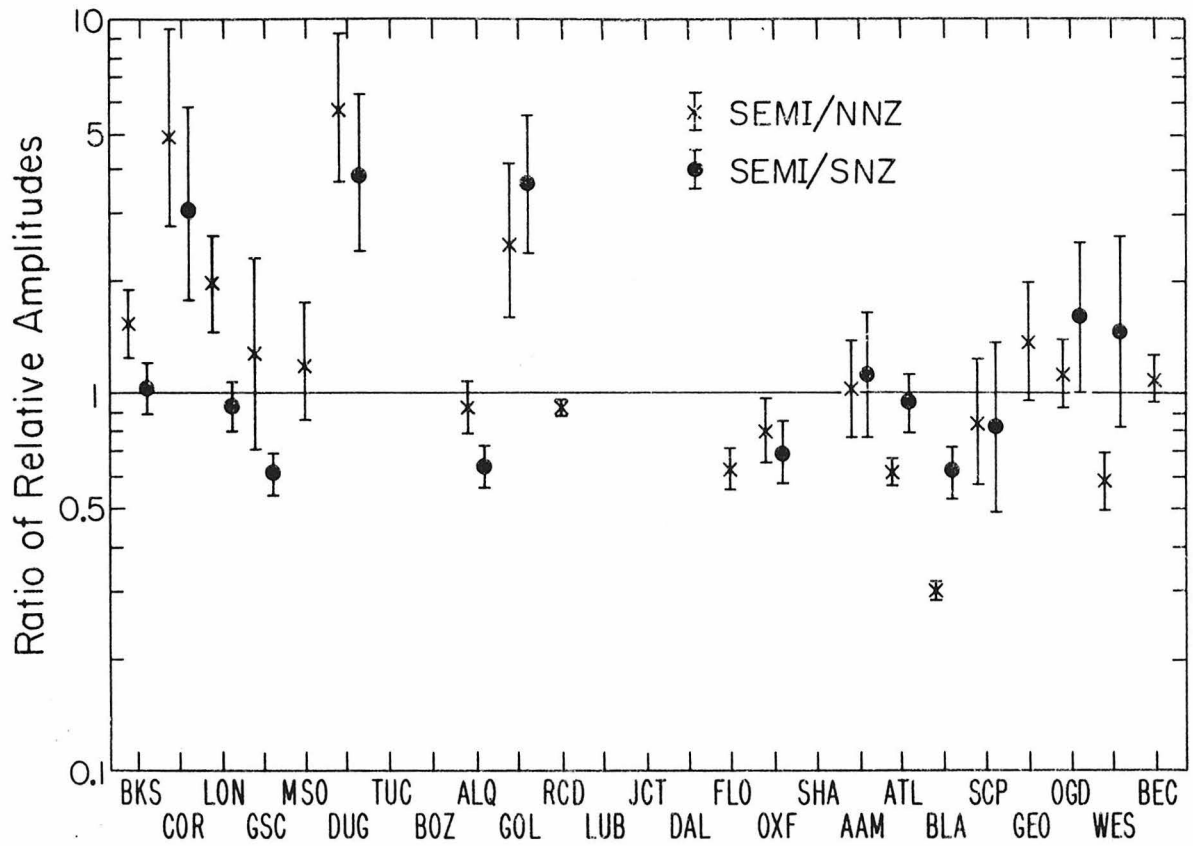


Figure IV.8 Ratios of the amplitude pattern for the combined east and west Semipaltinsk sites to the amplitude patterns for the northern and southern Novaya Zemlya sites. Diffracted data have been deleted.

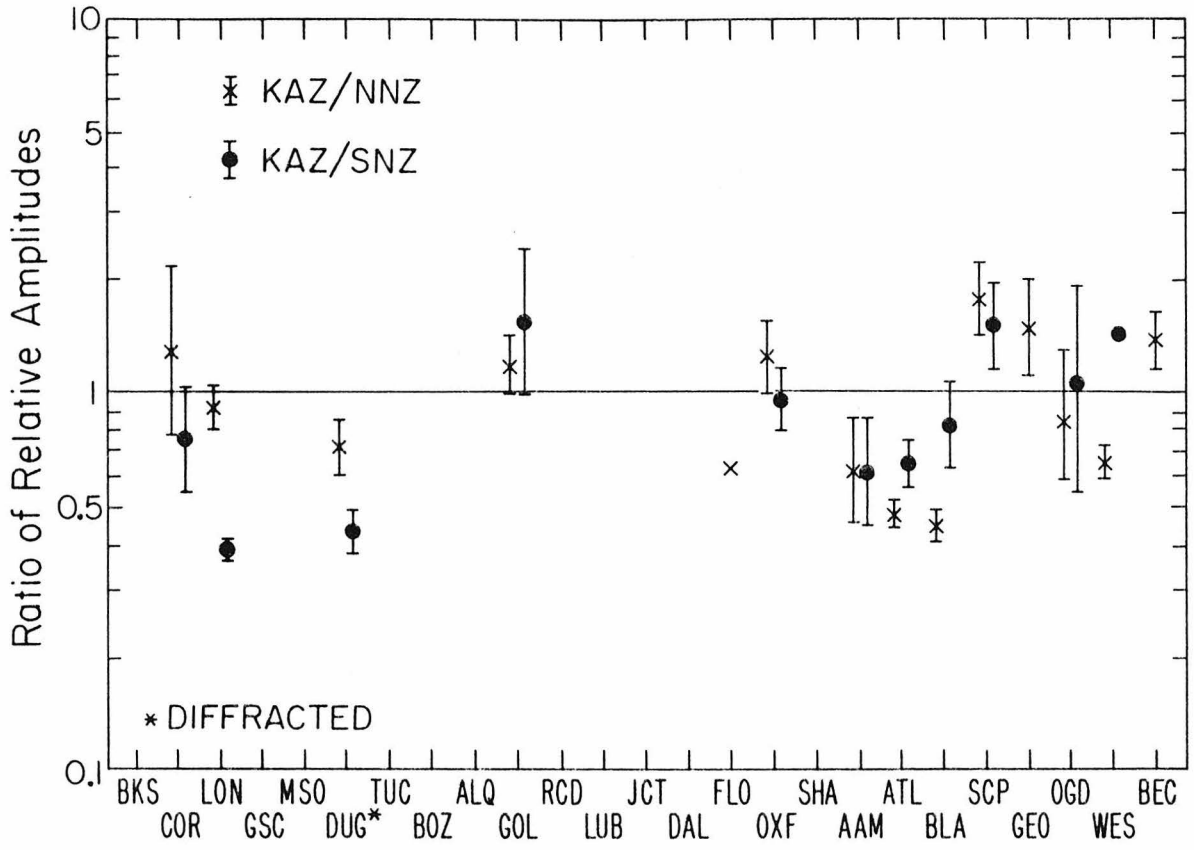


Figure IV.9 Ratios of the amplitude pattern for the Kazakh site to the amplitude patterns of the northern and southern Novaya Zemlya sites. Diffracted data - except DUG - have been deleted.

but rather rests in path or receiver effects. Other stations to be noted in Figure IV.9 are LON and BLA. LON has shifted from favoring SNZ at SEMI to favoring NNZ for the KAZ data. The amplitude value for BLA at NNZ is a factor of 2 or more greater than the values for BLA at the other test sites and most likely represents an anomaly in the NNZ source region.

Station COR at Corvallis, Oregon together with LON in Longmire, Washington have been studied by Burdick and Langston (1977), Langston and Blum (1977), and Langston (1977, 1978) who analyzed long period body waveforms in the determination of receiver structure. Both COR and LON have been found to show receiver anomalies which may be partly attributable to dipping structure. A comparison of the P waveforms of COR and LON with the other WWSSN stations in the United States for this explosion data set qualitatively reveals greater complexity for the vertical and horizontal components for both long and short period P waves at COR and LON. It seems likely then that the amplification at COR for the SEMI source regions, and possibly some of the scatter at LON, may be due to lateral heterogeneity at the receiver.

As DUC and GOL are adjacent stations such that their raypaths occur close together, the apparent amplification at these two stations may be caused by a common velocity anomaly affecting both paths. Otherwise, we would have to appeal to separate receiver anomalies that affected both stations in a similar fashion from the same approach azimuth. The discussion of a common velocity anomaly is deferred to the companion study.

On the basis of the intercomparisons of the test sites, we may summarize our qualitative results. The two sites at Novaya Zemla show a relative amplitude trend of a factor of three across the United States in their respective amplitude patterns. This is in contrast to the two test sites at Semipalatinsk, where they are in good relative agreement. This amplitude anomaly associated with Novaya Zemlya does not appear to be a local function of either NNZ or SNZ, as the amplitude patterns for KAZ and SEMI are intermediate between NNZ and SNZ. No information is available in the geophysical literature to help to resolve this issue. Geologically, the islands of Novaya Zemlya are a continuation of the Ural Mountains, and as such are part of a suture zone between ancient European and Asian plates. The complex geologic structure observed on geology maps of the Urals and Novaya Zemlya are circumstantially supportive, but offer no additional information to aid our interpretation.

#### Amplitude Variation at Receiver

In the previous section, amplitude data for the five test sites were inter-compared using a ratio technique which essentially eliminated common receiver effects. In this section the amplitude data from the five test sites are plotted together to look for systematics of the common receiver effect. Stations showing amplitude diffraction effects and the amplitude values of three anomalous stations for the Semipalatinsk data - COR, DUG and GOL - have not been included in the common plotting. Although some systematic differences among the various source regions were found in the previous sections we include the data from each site without any corrections, understanding that the source

region differences represent an inherent uncertainty in determining the effects common to the receiver. To plot the data from the different sites, the amplitude patterns in Figures IV.3 through IV.6 are characterized by the mean value of each station. The resultant amplitude patterns for the five sites are normalized in the same manner as was the event data at each site. Geometric spreading corrections have not been included as the effect is minor (about 15%) compared to the variations in the data.

The amplitude data from the five Russian nuclear test sites -- NNZ, SNZ, SEMI E, SEMI W, KAZ -- are plotted in Figure IV.10. The pattern represents apparent amplitude variations for the United States stations of the WWSSN for a northern azimuth of approach. This distinction is important as preliminary results (to be discussed in the next section) using earthquakes to view other azimuths indicate that the pattern is azimuthally dependent. However, even in accepting this narrowing distinction, several observations are important. The amplitudes in the western United States from BKS to GOL are not a consistent factor of three lower than amplitudes in the eastern United States. Stations ALQ and GOL are a factor of 4 to 5 lower than the higher stations, but the other low stations in the west, DUG and TUC, have amplitude values not dissimilar from JCT, FLO, ATL, BLA, OGD, WES and BEC in Bermuda. The values of BOZ are quite high, albeit they represent only three events from SEMI. The remaining stations in the west, BKS, COR, LON, GSC, and MSO, share a range of amplitude values with the higher stations in the east -- RCD, LUB, OXF, SHA, AAM, SCP, and GEO.

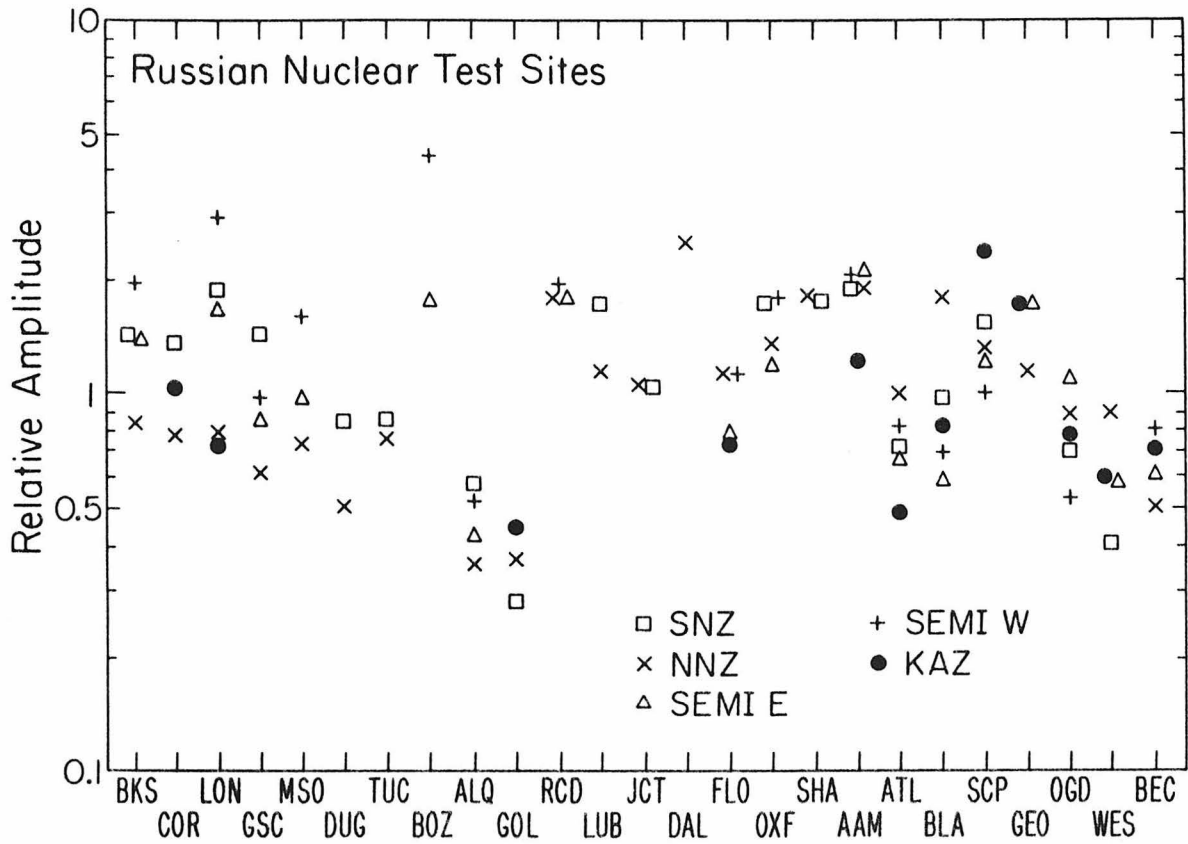


Figure IV.10 Combined plot of the amplitude data from the southern and northern Novaya Zemlya, east and west Semipalatinsk, and Kazakh sites for WWSSN stations across the United States. The mean of the amplitude data at each station for each site is plotted. Diffracted and anomalous (see text) data have been deleted.

Before comparisons of a more quantitative nature can be considered, effects due to differences in the geologic siting of the stations must be evaluated. Gutenberg (1956, 1957) and Borchardt (1970) have noted that stations situated on low velocity sediments are amplified relative to nearby stations situated on bedrock. Booth et al., (1974) invoked sediment amplification to explain high magnitude residuals for long period LRSM stations along the Gulf coast. This sediment amplification effect is illustrated in Figure IV.11. The receiver effect of a variety of different sediment structures overlying bedrock are compared to simple bedrock site (upper left) using Thomson-Haskell propagator matrices and a synthetic explosion waveform assuming Poisson's ratio for the shear velocity and a  $0.2 \text{ g/cm}^3$  bedrock-sediment density contrast. Sediment thicknesses of 300 meters show appreciable amplification. Near surface P wave velocities of 2 km/sec amplify a factor 1.6 to 1.8 relative to bedrock; surface velocities of 3 km/sec amplify by 1.4 to 1.5. As stations in the central United States (from RCD to AAM) are situated on slower sedimentary materials in contrast to the hard rock siting of the western and eastern coastal stations, some amplitude corrections must be made. The handbook of WWSSN contains a short description of the local geology at each station: RCD, 2700 feet of shale, sandstone and some limestone; LUB, Pleistocene terrestrial deposits; JCT, Cretaceous Edwards limestone; FLO, 50 to 60 feet of recent clay overlying Missippian bedrock; OXF, 2100 feet of Cenozoic and Mesozoic sediments; SHA, sands and gravels of Plio-Pleistocene age underlain by clays and sand of Miocene age; AAM, 200 feet gravel, 800 feet of shale, 4800 feet of limestone. Composing a velocity section from the the geologic descriptions is

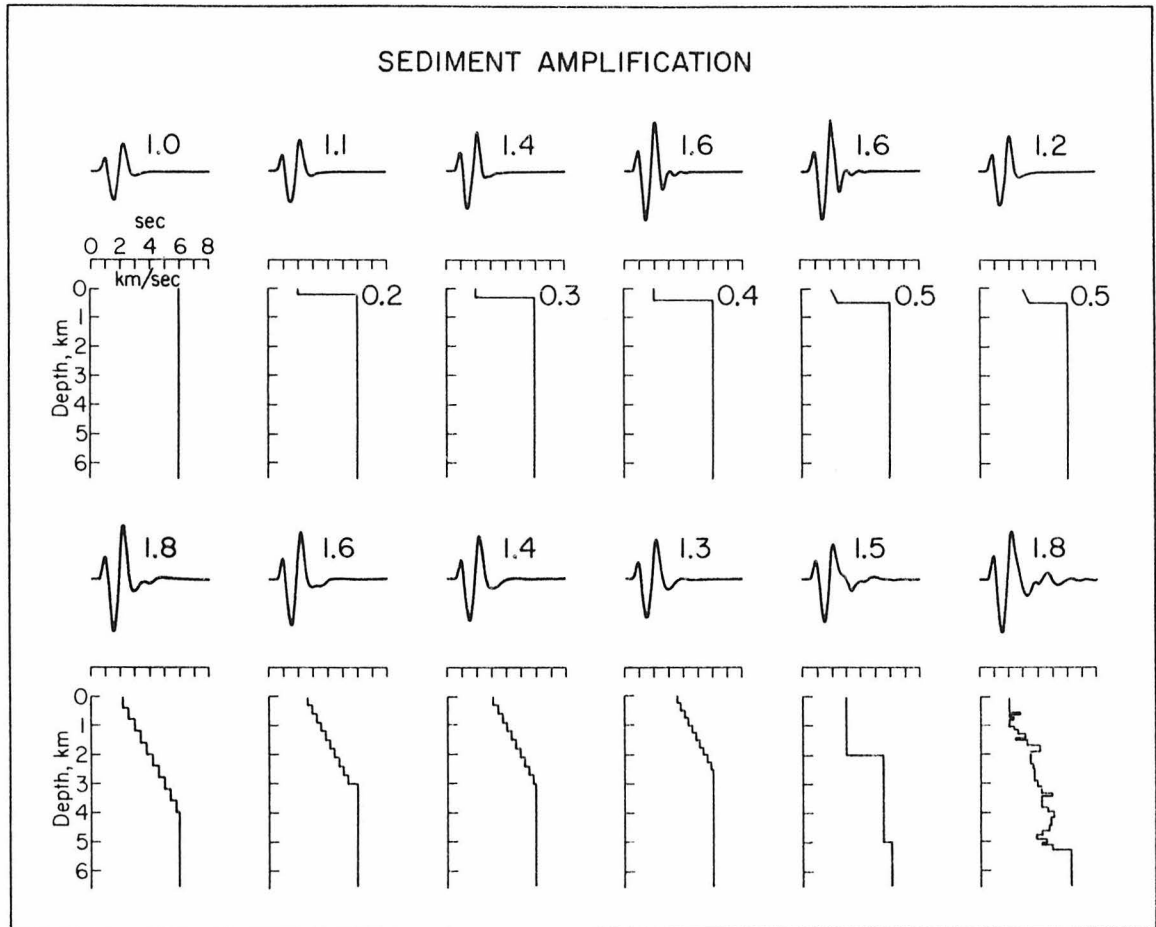


Figure IV.11 Amplification effects of shallow low velocity sediments upon crustal models. Amplitudes noted are relative to the bedrock model in upper left. Sediment thickness in kilometers is indicated in upper models.

somewhat arbitrary. Shallow lying sandstones and shales have compressional velocities from 1.4 to 3.3 km/sec. Limestone velocities are sensitive to the extent of crystallization and range between 1.7 and 6.1 km/sec. (Clark, 1966). Seismic refraction surveys provide only general control as sediments are grouped in a single layer characterized by the highest velocity arrival. Well log velocity depth data provide the only accurate control, but such information was obtainable only from SHA. The lower right velocity-depth section in Figure IV.11 was simplified from a well log 25 km from SHA, and shows a factor of 1.8 amplification relative to bedrock. Given the lack of velocity control in the surface layers at RCD, LUB, JCT, DAL, and AAM, only an approximate sediment amplification correction of a factor of 1.4 to 1.8 may be estimated.

Returning to Figure IV.10 and noting the stations in the central United States to be corrected for sediment amplification, we observe that no pervasive factor of three difference in amplitude is apparent between WSSN stations in west (left of RCD) and WSSN stations in the central and east (right of GOL). This factor of three variation between the east and west is based upon studies of earthquake magnitude variations for LRSM stations in the United States by Evernden and Clark (1970) and Booth et al. (1974).

The amplitude variations for receivers in the United States observed in Figure IV.10, whether or not the pattern is azimuthally dependent, may be attributed to a number of causes. Among the more likely are variations in attenuation properties, variations in scattering properties, and focusing or defocusing due to non-planar structure in the crust or uppermost mantle. While the focusing possibility is station specific

and cannot be modeled without more information, variations in attenuative and scattering properties may be tested for internal consistency with the data. A crude but simple test for variations of shallow crustal scattering can be made in the following manner. Let us consider the amplitude variations in the United States for the NNZ test site in Figure IV.3. For a simple scattering model we may assume the low amplitude stations are caused by energy scattered from the vertical component of motion. A large part of this scattered energy may manifest itself as large secondary arrivals on the horizontal components on the P wave train. This hypothesis was tested for the events at NNZ. Amplitudes of large secondary arrivals were measured from the north-south and east-west components of the P wave. These components are approximately radial and tangential, respectively, for geometry of source and receiver. The amplitudes are normalized by the value at OXF and plotted in Figure IV.12 in a fashion similar to the vertical data in Figure IV.3. If this simple scattering hypothesis was correct, we would expect the pattern of low and high amplitudes for the vertical arrivals in Figure IV.3 to be reversed for the horizontal secondary arrivals; that is, a high amplitude on the vertical would imply low amplitude on the horizontal and vice versa. This is clearly not the case in Figure IV.3. Thus, the amplitude variations observed for the vertical component are inconsistent with this simple scattering test. A more sophisticated test for scattering might be to compute the total power in the horizontal coda as opposed to a maximum amplitude, but this detailed effort is beyond the scope of the present investigation.

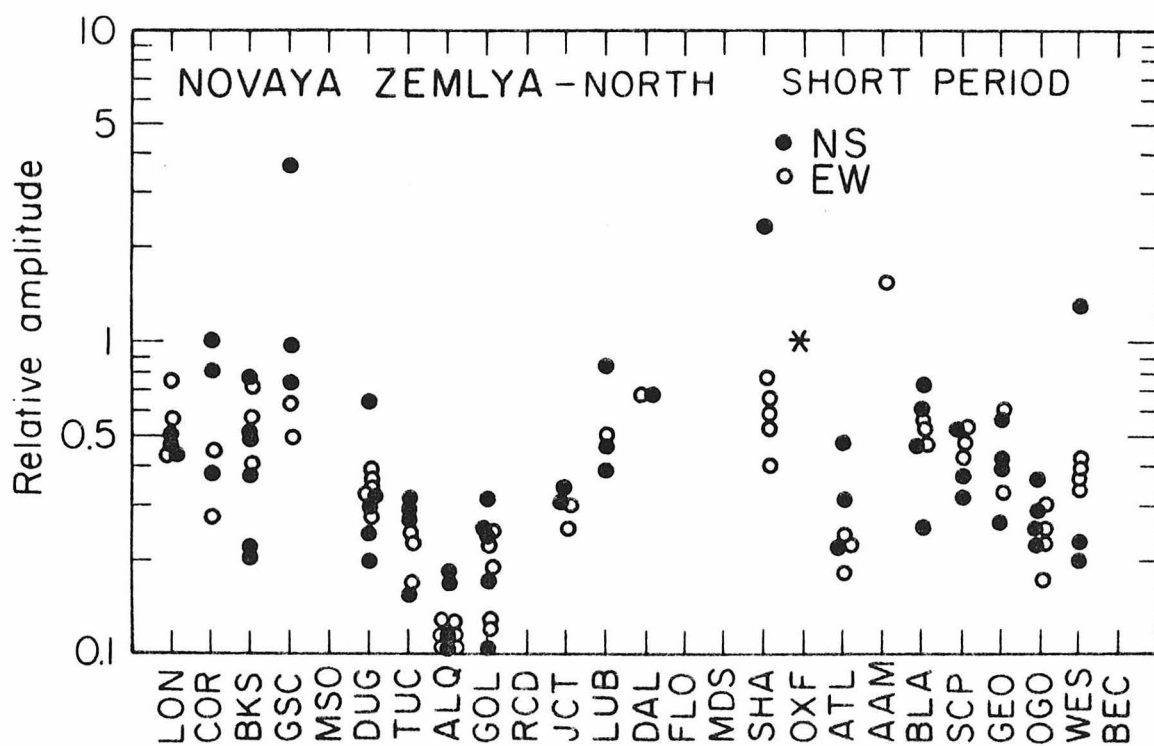


Figure IV.12 Relative amplitudes of horizontal P wave secondary arrivals (normalized to OXF) observed by WSSN stations across the United States from eleven nuclear explosions at the northern Novaya Zemlya site.

A second possible explanation for the amplitude variations in Figure VI.10 is from differences in the attenuative properties along the ray paths to the stations. If we assume that attenuation is independent of frequency in the band of the WWSSN short period instrument, we may characterize variations in attenuative properties by variations in  $t^* = T/Q$ , the ratio of travel time to path average  $Q$ . To verify the consistency of an attenuation explanation for the amplitude variation, a large amplitude waveform was carefully digitized and then attenuated using a Futterman (1962) attenuation operator. The results of the test are illustrated in Figure IV.13. The waveform and its relative amplitude are shown in the left column and the  $t^*$  and shape of the attenuation operator in the right column. A factor of five variation in amplitude is equivalent to a  $t^*$  variation of 0.5 units. It is somewhat surprising that the waveforms suffering different degrees of attenuation are quite similar. Restricting our attention to the first upswing and downswing - the part of the waveform used in this study and most free of crustal complications at the source and receiver - differences due to variation in attenuation are not appreciable resolvable to be of use as a criterion in accepting or rejecting attenuation as an explanation for the amplitude variations in Figure IV.10. Thus, the variations of amplitudes and lack of variation in the waveforms in the Russian explosion data set are consistent with an interpretation in terms of varying attenuative properties along the ray path to the receiver.

#### Preliminary Results for Earthquake Sources

The study of Russian nuclear explosions has provided an interesting pattern of amplitude variations in the United States ascribable to

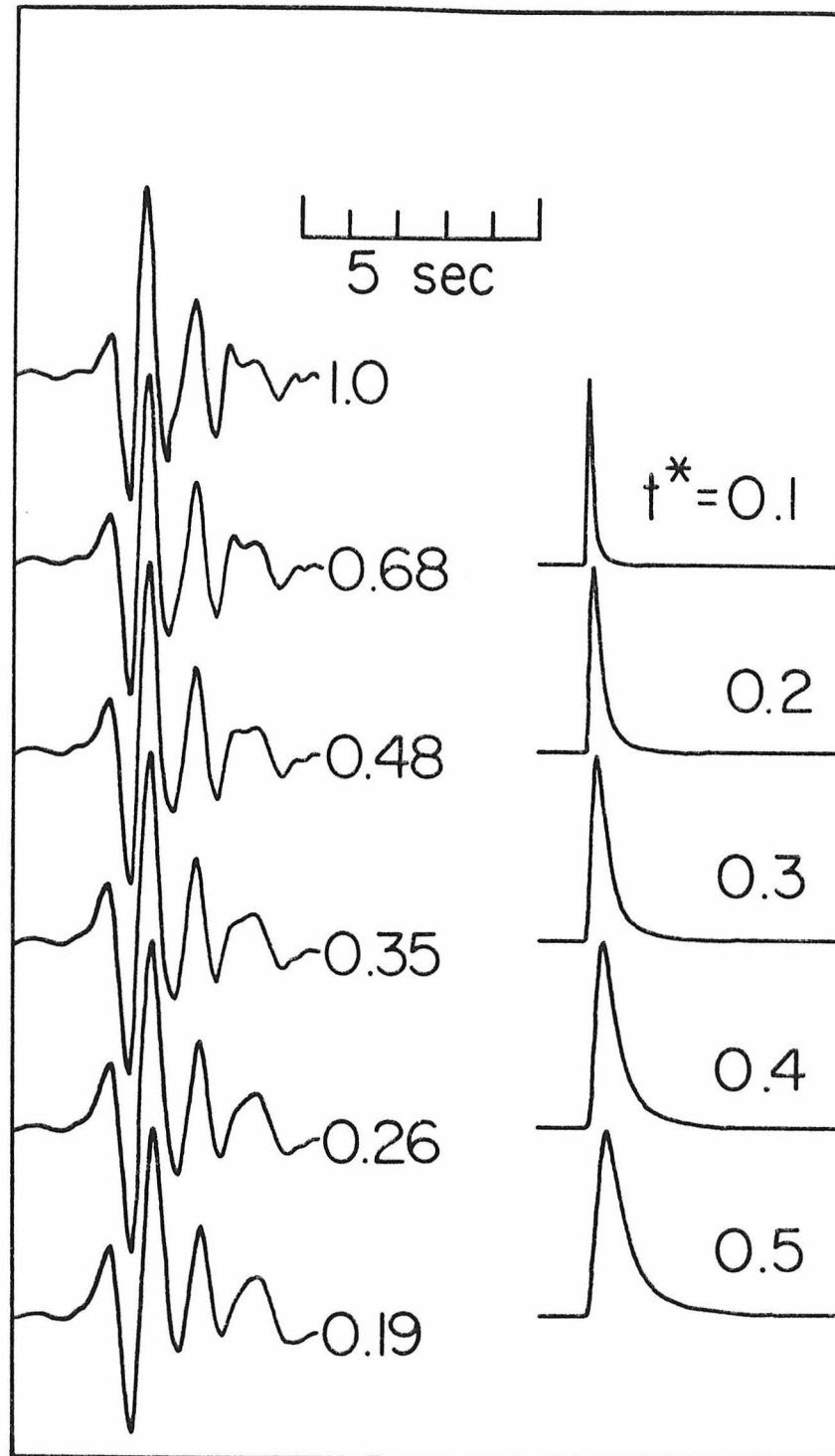


Figure IV.13 Result of numerical experiment in which a high amplitude short period P wave from a nuclear explosion is successively attenuated. The numbers following the traces indicate the signal amplitude normalized to the top trace at the left. The right-hand column shows the attenuation operators used to obtain each corresponding left-hand trace from the original record at top left.

receiver effects. However, as these data are solely from a northern azimuth of approach, it is particularly important to determine if the observed amplitude variations are azimuthally dependent. In view of the importance of this question and to temper premature speculation upon the interpretation of the explosion data, we shall briefly present preliminary amplitude data from earthquakes in the Kuriles and South America which suggest that the amplitude variations in the United States are indeed azimuthally dependent.

To simulate the study of the explosion data set and to overcome as best as possible the problems of earthquake source radiation and directivity, a selection of earthquakes were sought to satisfy the following criteria: the short period P waveforms must be simple, short duration, explosion-like in character, and must be similar at all stations recording the event in the United States. Two source regions were considered in the search: events in the Kurile Islands and South America.

A systematic search of earthquakes in the two regions occurring between 1965 and 1968 and between September, 1976 and May 1977 yielded six Kurile events and eight South American events of acceptable nature. Amplitudes were measured and normalized in the same manner as the Russian explosion study.

The earthquake data for the Kuriles is plotted in Figure IV.14 in the same manner as the explosion data. The low scatter of the event data at the individual stations suggests that source radiation and directivity effects are minimal. The azimuth to the Kurile earthquakes roughly lies N 45° W of the Russian test sites, and a good deal

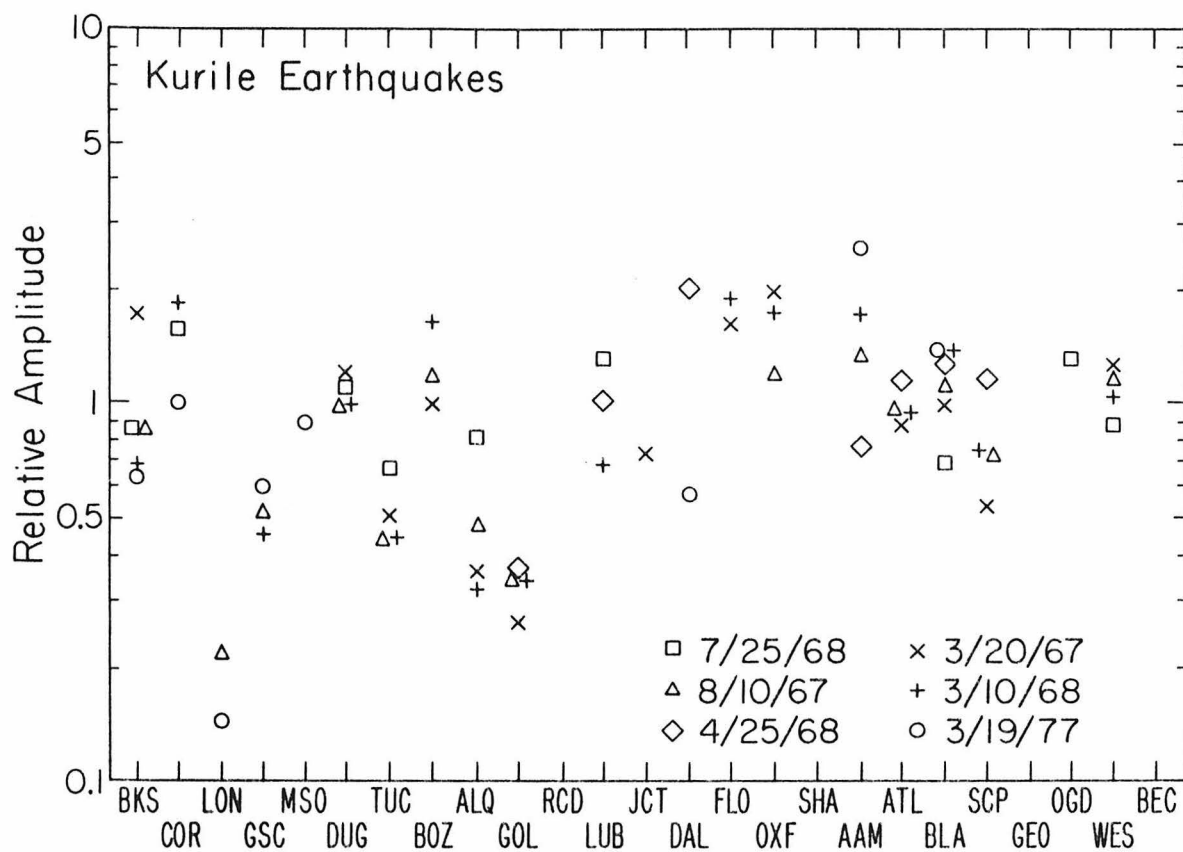


Figure IV.14 Relative amplitudes of short period P waves observed by WWSSN stations in the United States for six earthquakes in Kurile Islands. The events were selected to minimize earthquake source radiation and directivity effects.

of consistency is seen comparing Figure IV.10 and Figure IV.14.

Figure IV.15 plots the average values of Russian explosion data together with the Kurile earthquake data for better comparison. Except for LON which was noted earlier to be associated with anomalous receiver effects, the Kurile data lie within a factor of two of the Russian explosion data.

A plot of the eight South American earthquakes is shown in Figure IV.16. The scatter at the stations is again quite low. The South American events lie nearly opposite in azimuth to the Russian explosion data, and considerable differences between the two regions may be observed. ALQ and GOL are no longer the lowest amplitude stations, but now fall in the range of the other western and east coast stations. Amplitudes in the central United States are considerably larger than values east or west, but there are not enough data yet to preclude anomalous source effects. The amplitude data from earthquakes in the Kuriles and South America are quite interesting. The waveform criteria in selecting events yield amplitude data with low internal scatter and appear to minimize amplitude effects from the source radiation and directivity. The relative agreement between the Kurile data and the Russian explosion data indicates that the amplitude variation pattern in the United States is stable with moderate changes of azimuth. However, differences between the South American earthquakes and the Russian explosion data suggest that the total azimuthal variation is quite pronounced at some stations. Further discussion of azimuthal differences in the amplitude variations of WWSSN stations in the United States must await a more detailed study. However, the preliminary results presented herein suggest considerable promise in the ability to approach the azimuthally dependent amplitude variation problem.

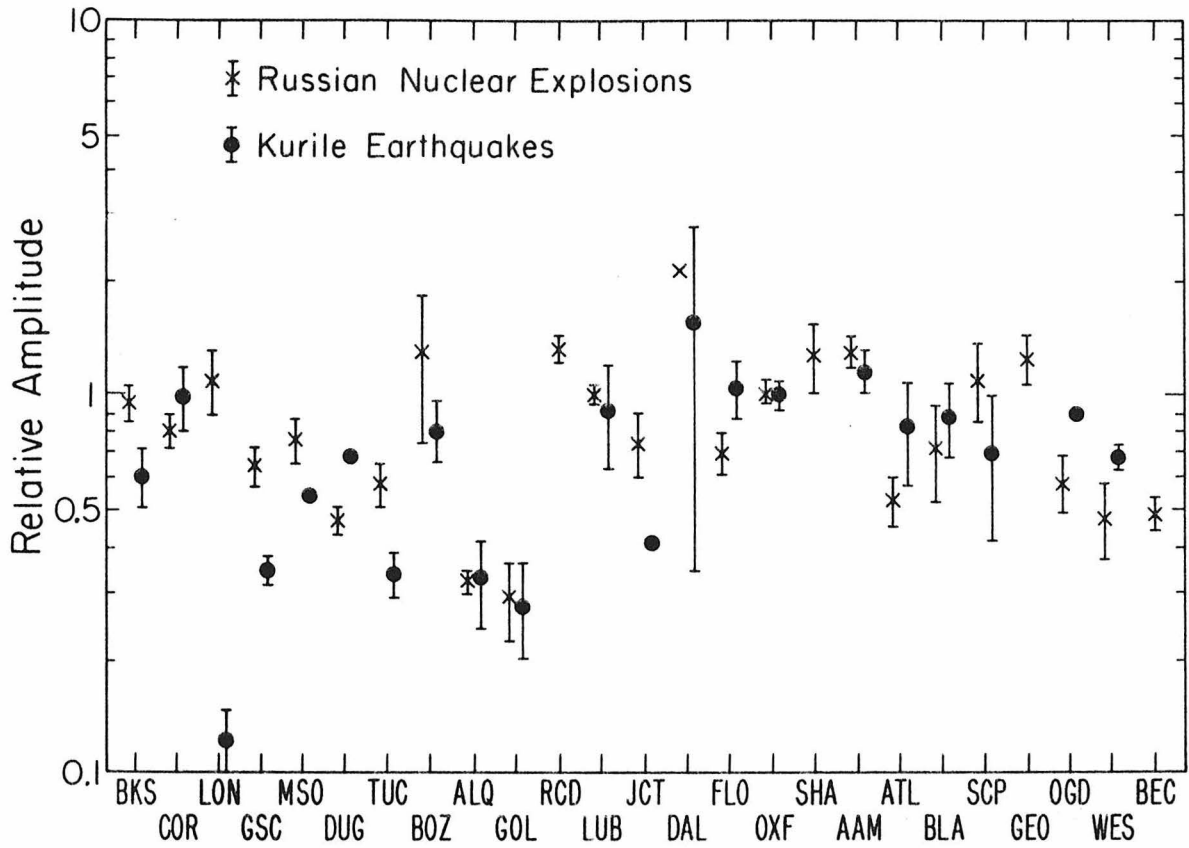


Figure IV.15 Comparison of the amplitude pattern from the combined Russian explosion data with the amplitude pattern from the Kurile Island earthquakes.

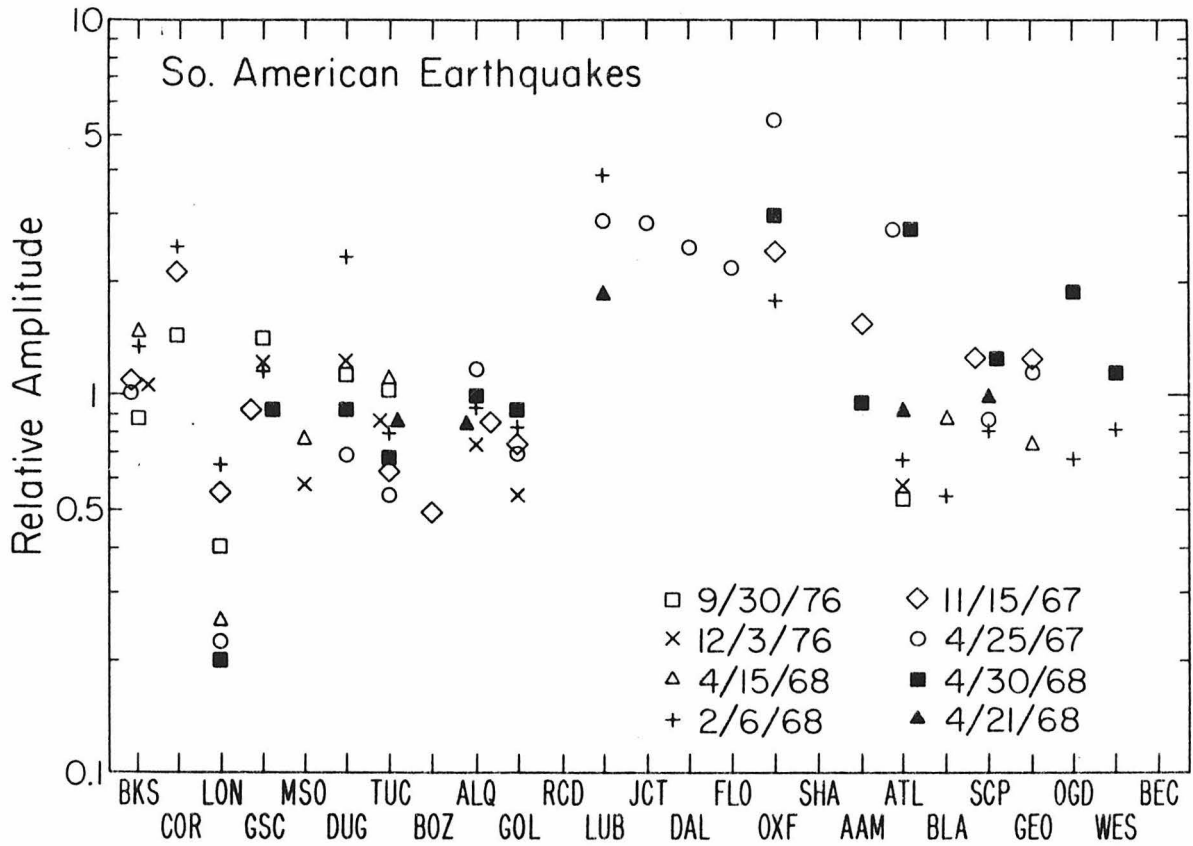


Figure IV.16 Relative amplitudes of short period P waves observed by WWSSN stations in the United States for eight earthquakes in South America. The events were selected to minimize earthquake source radiation and directivity effects.

SUMMARY

The study presented is an analysis of the short period amplitude behavior of WWSSN stations in the United States recording underground nuclear explosions in the Soviet Union. We have found that there is a well-defined relative amplitude pattern for any one Russian test site, and additionally, that the relative amplitude patterns observed at the U.S. stations are quite similar for the various test sites. This is an indication that the relative differences among the U.S. stations are primarily due to receiver effects. These initial results concerning the coherence of short period amplitudes and waveforms encourage a similar analysis be undertaken for all WWSSN stations.

This study may be considered a first step toward understanding the amplitudes and waveforms of short period seismograms. The observed short period seismograms are coherent from station to station for approximately 2 seconds after the initial onset. While the relationship between relative peak heights is maintained, the absolute amplitudes can vary by nearly an order of magnitude. Stability with regard to source region seems well demonstrated. There is an excellent agreement between the amplitude patterns of Semipalatinsk east and west, indicating a source coherence over 70 km. However, a systematic source azimuthal difference exists between southern and northern Novaya Zemlya, a distance of 300 km. For the purpose of defining an overall amplitude pattern from the northern approach, it is encouraging to note that the values for Semipalatinsk and Kazakhlie between the values for southern and northern Novaya Zemlya.

With regard to receiver effects, though there is a well defined relative amplitude pattern from the Russian test sites, this cannot be simply interpreted as regional differences in attenuation or scattering properties due to the evidence for an azimuthal dependence of the pattern. ALQ and GOL, which have the lowest amplitudes from the northern approach, have average amplitudes values from South American earthquakes. If we were to consider only the data from the Russian test sites, we might conclude that ALQ and GOL are inherently more attenuating than the other stations. This conclusion cannot be made in light of the South American data. Therefore, although relative amplitude differences may in fact be caused by varying seismic attenuation, before regions may be characterized as attenuating, the azimuthal amplitude effects must be understood and may yield valuable information on the nature and extent of an attenuating region. For example, if we note that ALQ and GOL, both located on the Rocky Mountain front, show low amplitudes from the north and northwest, but normal values from the southeast, then one interpretation is that a common localized attenuating region lies north and west of these stations. This interpretation is supported by azimuthal amplitude variations observed for explosions at the Nevada Test Site (Helmberger and Hadley, in preparation).

In conclusion, the principle results of this study are: (1) a demonstration of amplitude and waveform coherence of short period data from Russian nuclear explosions; (2) a preliminary result concerning the azimuthal variation in the effective radiation pattern from the Russian test sites; (3) the determination of a relative amplitude

pattern across the United States, though noting the azimuthal dependence of this pattern. Additionally, we have sought possible mechanisms for the amplitude variations and find that amplification due to sediment and diminution caused by intrinsic attenuation are viable processes in explaining the variations.

REFERENCES

- Booth, D. C., Marshall, P. D., and J. B. Young (1974) Long and short period P-wave amplitudes from earthquakes in the range  $0^{\circ}$ - $114^{\circ}$ , Geophys. J. R. astr. Soc., 39, 523-537.
- Borcherdt, R. D. (1970). Effects of local geology on ground motion near San Francisco Bay, Bull. Seism. Soc. Am. 60, 29-61.
- Burdick, L. J. (1978).  $t^*$  for S waves with a continental ray path, Bull. Seism. Soc. Am., 68, 1013-1030.
- Burdick, L. J. and C. A. Langston (1977). Modeling crustal structure through the use of converted phases in teleseismic body-wave forms, Bull. Seism. Soc. Am., 67, p 677.
- Cleary, J. (1967). Analysis of the amplitudes of short period P-waves recorded by long range seismic measurements stations in the distance range  $30^{\circ}$ - $102^{\circ}$ , J. Geophys. Res., 72, 4705-4712.
- Dahlman O. and H. Israelson (1977). Monitoring Underground Nuclear Explosions, Elsevier Scientific Publishing Company, New York, 1977.
- Der, Z. A., Masse, R. P. and J. P Gurski (1975). Regional attenuation of short-period P and S waves in the United States, Geophys. J. R. astr. Soc., 40, 84-106.
- Evernden, J. F. and D. M. Clark (1970). Study of teleseismic P. II amplitude data, Phys. Earth Planet. Int., 4, 24-31.
- Futterman, W. I. (1962). Dispersive body waves, J. Geophys. Res., 67, 5279.
- Gutenberg, B. (1956). Effects of ground on shaking in earthquakes, Transactions, A.G.U., 37 757-760.
- Gutenberg, B. (1957). Effects of ground on earthquake motion, Bull. Seism. Soc. Am., 47, 221-250.

- Langston, C. A. (1977). Corvallis, Oregon, crustal and upper mantle receiver structure from teleseismic P and S waves, Bull. Seism. Soc. Am., 67, 713.
- Langston, C. A. (1978). Structure under Mt. Ranier, Washington, inferred from body wave studies, EOS Transactions (abstract), 59, 1142.
- Langston, C. A. and D. E. Blum, (1977). The April 29, 1965, Puget Sound earthquake and the crustal and upper mantle structure of western Washington, Bull. Seism. Soc. Am., 67, 693.
- Solomon, S. and M. N. Toksoz (1970). Lateral variation of attenuation of P and S waves beneath the United States Bull. Seism. Soc. Am. 64, 1489-1498.
- von Seggern, D. and R. Blanford (1972). Source time functions and spectra for underground nuclear explosions, Geophys. J. R. astr. Soc., 31, 83.

Appendix A

Map of WSSN Stations



CODE	NAME	DATE OPEN	DATE CLOSED	STATE OR COUNTRY	LATITUDE	LONGITUDE	MAGNIFICATION (K)	
							SPZ	LPZ
AAE	ADDIS ABABA	62/05/14		ETHIOPIA	9 01 45.0N	38 45 56.0E	50.000	1.500
ADE	ADELAIDE	62/04/01		AUSTRALIA	34 58 01.0S	138 42 32.0E	25.000	.750
AFI	AFIAMALU	62/03/28		WESTERN SAMOA	13 54 33.6S	171 46 38.1W	12.500	.750
AKU	AKUREYRI	64/07/23		ICELAND	65 41 12.0N	018 06 24.0W	25.000	.750
ALQ	ALBUQUERQUE	61/10/03		NEW MEXICO	34 56 30.0N	106 27 30.0W	200.000	3.000
AAM	ANN ARBOR	62/10/08		MICHIGAN	42 17 59.0N	83 39 22.0W	25.000	1.500
ANP	ANPU	63/03/04		TAIWAN	25 11 00.0N	121 31 00.0E	6.250	.750
ANT	ANTOFAGASTA	62/12/04		CHILE	23 42 18.0S	70 24 55.0W	50.000	3.000
AQU	AQUILA	62/04/02		ITALY	42 21 14.0N	13 24 11.0E	50.000	3.000
ARE	AREQUIPA	62/01/18		PERU	16 27 43.5S	71 29 28.6W	50.000	1.500
ATU	ATHENS UNIVERSITY	62/03/16		GREECE	37 58 20.0N	23 43 00.0E	12.500	1.500
ATL	ATLANTA	63/06/14		GEORGIA	33 26 00.0N	84 20 15.0W	50.000	3.000
BAG	BAGUIO CITY	62/03/05		PHILIPPINES	16 24 39.0N	120 34 47.0E	25.000	3.000
BHP	BALBOA HEIGHTS	61/12/09		CANAL ZONE	8 57 39.0N	79 33 29.0W	12.500	.750
BEC	BERMUDA-COLUMBIA	61/12/28		BERMUDA	32 22 46.0N	64 40 52.0W	25.000	1.500
BLA	BLACKSBURG	62/08/26		VIRGINIA	37 12 40.0N	80 25 14.0W	100.000	.750
BOG	BOGOTA	62/04/09		COLOMBIA	4 37 23.0N	74 03 54.0W	12.500	3.000
BOZ	BOZEMAN	63/08/29	68/02/29	MONTANA	45 36 00.0N	111 38 00.0W	200.000	3.000
BOF	BRASILIA ARRAY	73/09/01		BRAZIL	15 39 49.5S	47 54 12.0W	100.000	1.500
BUL	BULAWAYO	63/01/10		RHODESIA	20 08 36.0S	28 36 48.0E	100.000	.750
BKS	BERKELEY (BYERLY)	62/05/28		CALIFORNIA	37 52 36.0N	122 14 06.0W	25.000	3.000
CCG	CAMP CENTURY	62/12/08		GREENLAND	77 10 00.0N	61 08 00.0W	100.000	1.500
CAR	CARACAS	62/04/16	63/04/28	VENEZUELA	10 30 24.0N	66 55 39.5W	25.000	3.000
CTA	CHARTERS TOWERS	63/02/20		AUSTRALIA	20 05 18.0S	146 15 16.0E	100.000	3.000
CHG	CHIENGMAI	63/03/02		THAILAND	18 47 24.0N	98 58 37.0E	200.000	3.000
COL	COLLEGE	64/01/01		ALASKA	64 54 00.0N	147 47 36.0W	100.000	1.500
COP	COPENHAGEN	62/01/04		DENMARK	55 41 00.0N	12 26 00.0E	12.500	.750
CMC	COPPER MINE	63/04/07	69/03/31	CANADA	67 50 00.0N	115 05 00.0W	200.000	3.000
COR	CORVALLIS	62/07/16		OREGON	44 35 08.6N	123 18 11.5W	25.000	.750
DAL	DALLAS	61/09/18		TEXAS	32 50 46.0N	96 47 02.0W	25.000	1.500
DAG	DANMARKSHAVN	72/09/01		GREENLAND	76 46 12.0N	18 46 12.0W	50.000	.750
DAV	DAVAO	64/09/01		PHILIPPINES	07 05 16.0N	125 34 23.0E	6.250	3.000
DUG	DUGHAY	62/05/02		UTAH	40 11 42.0N	112 48 48.0W	400.000	3.000
EIL	EILAT	69/01/01		ISRAEL	29 33 00.0N	34 57 00.0E	400.000	3.000
ESK	ESKDALEMUIR	64/03/16		SCOTLAND	55 19 00.0N	003 12 18.0W	12.500	.750
FLO	FLORISSANT	61/09/07		MISSOURI	38 48 06.0N	90 22 12.0W	50.000	3.000
FVM	FRENCH VILLAGE	74/05/10	71/08/31	MISSOURI	37 59 02.4N	90 25 33.6W	100.000	1.500
GIE	GALAPAGOS ISLANDS	64/05/14		GALAPAGOS ISLANDS	0 44 00.0S	90 18 00.0W	12.500	.750
GEO	GEORGETOWN	61/11/05		DISTRICT OF COLUMBIA	38 54 00.0N	77 04 00.0W	25.000	1.500
GDH	GODHAVN	62/11/15		GREENLAND	69 15 00.0N	53 32 00.0W	25.000	1.500
GOL	GOLDEN	61/12/08		COLORADO	39 42 01.0N	105 22 16.0W	400.000	1.500
GSC	GOLDSTONE	63/02/15		CALIFORNIA	35 18 06.0N	116 48 16.6W	100.000	1.500
GRM	GRAHAMSTOWN	67/10/22		SOUTH AFRICA	33 18 48.0S	26 34 24.0E	25.000	1.500
GUA	GUAM	63/04/07		MARIANA ISLANDS	13 32 18.0N	144 54 42.0E	12.500	.750
HLL	HALLETT	63/03/08	64/10/01	ANTARCTICA	72 18 50.0S	170 13 00.0E		



CODE	NAME	DATE OPEN	DATE CLOSED	STATE OR COUNTRY	LATITUDE	LONGITUDE	MAGNIFICATION (K)	SPZ	LPZ
PJA	PONTA UELGADA	62/02/03		AZORES	37 44 36.0N	25 39 42.0W	6.250		.750
PJO	POONA	64/11/01		INDIA	18 32 00.0N	073 51 00.0E	50.000		1.500
PMG	PORT MORESBY	62/06/21		PAPUA	9 24 33.0S	147 09 14.0E	25.000		1.500
PPO	PORTO	63/03/31		PORTUGAL	41 08 19.0N	8 36 08.0W	25.000		1.500
PRE	PRETORIA	62/05/30		SOUTH AFRICA	25 45 12.0S	028 11 24.0E	50.000		1.500
QUE	QUETTA	62/07/10		PAKISTAN	30 11 18.0N	66 57 00.0E	200.000		6.000
QUI	QUITO	63/01/28		ECUADOR	0 12 00.5S	78 30 01.8W	3.125		3.000
RAB	RABAU	62/02/12		NEW BRITAIN	04 11 28.6S	152 10 11.4E	12.500		.750
RCD	RAPID CITY	61/12/06	74/11/30	SOUTH DAKOTA	44 04 30.0N	103 12 30.0W	25.000		1.500
RAR	RAROTONGA	65/05/08		COOK ISLANDS	21 12 45.5S	159 46 24.0W	6.250		.375
RIV	RIVERVIEW	62/12/12		AUSTRALIA	33 49 45.7S	151 09 30.0E	12.500		.750
SDB	SA DA BANDEIRA	64/10/26	75/02/28	ANGOLA	14 55 33.0S	013 34 19.0E	100.000		1.500
SJG	SAN JUAN	64/10/12		PUERTO RICO	18 06 42.0N	66 09 00.0W	50.000		.750
SNA	SANAE	64/02/06		ANTARCTICA	70 18 56.0S	2 19 27.0W	50.000		1.500
SBA	SCOTT BASE	63/02/17		ANTARCTICA	77 51 01.0S	166 45 22.0E	25.000		.750
SEO	SEOUL	63/03/07		SOUTH KOREA	37 34 00.0N	126 58 00.0E	50.000		.750
SHL	SHILLONG	63/03/16		INDIA	25 34 00.0N	91 53 00.0E	200.000		3.000
SHK	SHIRAKI	65/12/22		JAPAN	34 31 48.0N	132 40 42.0E	12.500		1.500
SHI	SHIRAZ	63/05/04		IRAN	29 38 17.9N	52 31 11.8E	50.000		1.500
SOM	SOMREKO	64/10/06		CHILE	52 46 51.0S	69 14 32.0W	6.250		.375
SHG	SONGKHLA	65/11/04		THAILAND	7 10 24.0N	100 37 12.0E	25.000		3.000
SPA	SOUTH POLE	63/02/02		ANTARCTICA	90 00 00.0S	0 00 00.0E	100.000		.375
SHA	SPRING HILL	62/03/07		ALABAMA	30 41 41.1N	88 08 23.0W	6.250		1.500
SCP	STATE COLLEGE	61/12/05		PENNSYLVANIA	40 47 42.0N	077 51 54.0W	50.000		1.500
STU	STUTTGART	62/01/20		GERMAN FED REP	48 46 15.0N	009 11 36.0E	25.000		.750
TAB	TABRIZ	65/06/10		IRAN	38 04 03.0N	46 19 36.0E	6.250		1.500
TAU	TASMANIA UNIVERSITY	62/05/18		TASMANIA	42 54 35.7S	147 19 10.0E	25.000		.750
TOL	TOLEDO	62/03/20		SPAIN	39 52 53.0N	04 02 55.0W	25.000		1.500
TRI	TRIESTE	63/07/04		ITALY	45 42 32.0N	013 45 51.0E	50.000		3.000
TRN	TRINIDAD	62/01/08		TRINIDAD	10 38 56.1N	61 24 10.0W	25.000		1.500
TUC	TUCSON	62/12/06		ARIZONA	32 18 35.0N	110 46 56.0W	200.000		3.000
UME	UMEA	62/01/11		SWEDEN	63 48 54.0N	20 14 12.0E	50.000		5.500
UNM	UNIVERSIDAD NATIONAL	67/06/03	70/10/08	MEXICO	19 19 44.4N	99 10 41.1W	6.250		1.500
VAL	VALENTIA	62/10/16		IRELAND	51 56 22.0N	10 14 39.0W	25.000		1.500
WEL	WELLINGTON	62/04/05		NEW ZEALAND	41 17 10.0S	174 46 06.0E	6.250		.750
WES	WESTON	61/10/08		MASSACHUSETTS	42 23 04.9N	71 19 19.5W	50.000		3.000
WIN	WINDHOEK	62/11/13		SOUTH-WEST AFRICA	22 34 00.0S	17 06 00.0E	50.000		1.500
		TOTAL STATIONS OPEN =							
		110							